Thesis

High energy gamma-ray observations of active galactic nuclei

VOVK, Ievgen

Abstract

This thesis contains the results of the studies of Active Galactic Nuclei (AGNs) with modern gamma-ray telescopes. AGNs are among the most powerful and most variable object in the high-energy gamma-ray domain, while the location of their gamma-ray emitting sites remains unclear. In this thesis I study the properties of the AGN gamma-ray emission in order to infer the location of the emission site. The emitted gamma rays further illuminate the intergalactic space, which allows to study the properties of the latter. In particular, I use the gamma-ray observations of AGNs to estimate the strength of the extremely weak Intergalactic Magnetic Field. In order to facilitate this kind of analysis in the future, I also perform an all-sky search of the AGNs emitting in very high-energy gamma-ray domain, thus providing a list of targets for further observations with the highly sensitive ground-based gamma-ray telescopes.

Reference

VOVK, Ievgen. *High energy gamma-ray observations of active galactic nuclei*. Thèse de doctorat : Univ. Genève, 2013, no. Sc. 4602

URN : urn:nbn:ch:unige-309959
DOI : 10.13097/archive-ouverte/unige:30995

UNIVERSITÉ DE GENÈVE
Département d'astronomie

FACULTÉ DES SCIENCES
Professeur Andrii Neronov

High energy γ-ray observations of active galactic nuclei

THÈSE

présentée à la Faculté des sciences de l'Université de Genève
pour obtenir le grade de Docteur ès sciences
mention astronomie et astrophysique

par

Ievgen Vovk

d'Ukraine

Thèse №4602

GENÈVE
Atelier d'impression ReproMail
2013

UNIVERSITÉ
DE GENÈVE

FACULTÉ DES SCIENCES

Doctorat ès sciences
Mention astronomie et astrophysique

Thèse de *Monsieur Ievgen VOVK*

intitulée :

" High energy γ–ray observations of active galactic nuclei "

La Faculté des sciences, sur le préavis de Monsieur A. NERONOV, professeur assistant et directeur de thèse (Département d'astronomie), Madame R. DURRER, professeure ordinaire (Département de physique théorique), Messieurs T. COURVOISIER, professeur ordinaire (Département d'astronomie), D. SEMIKOZ, docteur (Centre national de la recherche scientifique, Laboratoire Astro particules et Cosmologie, Université Paris VII, Paris, France) et R. MIRZOYAN, docteur (Institut de Physique Max-Planck, Munich, Allemagne), autorise l'impression de la présente thèse, sans exprimer d'opinion sur les propositions qui y sont énoncées.

Genève, le 15 octobre 2013

Thèse - 4602 -

Le Doyen, Jean-Marc TRISCONE

N.B. - La thèse doit porter la déclaration précédente et remplir les conditions énumérées dans les "Informations relatives aux thèses de doctorat à l'Université de Genève".

Résumé en français

Cette thèse est basée sur le travail que j'ai effectué au cours des années de 2009 à 2013 au Centre de données ISDC Data Center for Astrophysics, rattaché à l'Observatoire Astronomique de Genève. Ce travail est consacré à l'étude d'un type particulier d'objets extragalactiques – les Noyaux Actifs de Galaxies (AGNs) – dans le domaine des rayons gamma, à hautes énergies. Dans le cadre de ce travail, j'ai utilisé les données du télescope spatial international Fermi/LAT, rendues disponibles juste avant le commencement de cette thèse. La sensibilité sans précédent du télescope Fermi/LAT a rendu possible la réalisation de plusieurs études qui n'auraient pu être faites avec les intruments de l'ancienne génération.

Bien que ce travail se concentre sur les AGNs actifs dans le domaine des rayons gamma, ils sont ici non seulement les cibles de l'étude, mais également les outils qui permettent d'étudier les régions vastes et peu peuplées de l'espace intergalactique. J'ai suivi la trace des rayons gamma à hautes énergies durant toute leur existence afin de tenter de répondre aux questions concernant l'origine des quanta de rayons gamma – Quels objets sont responsables de leur émission? Où sont situés les sites d'émission à l'intérieur de ces objets? – ainsi que d'étudier leur propagation à travers l'espace intergalactique jusqu'à ce qu'ils atteignent la Terre.

Dans cette thèse, j'aborde par la suite ces questions, en utilisant des techniques variées d'analyse et en comparant les résultats avec les attentes théoriques, de façon à tester différentes théories sur la structure des AGNs ainsi que les conditions dans l'espace intergalactique.

La première partie de cette thèse est consacrée à la recherche de sources extragalactiques émettant de très fortes radiations dans le domaine des rayons gamma à hautes énergies. Ici, je démontre comment Fermi/LAT peut être utilisé pour localiser la source de rayon gamma dans la bande d'énergie généralement utilisée comme champ de travail des télescopes Cherenkov sur Terre. Bien que le télescope Fermi/LAT soit bien plus petit que ces instruments au sol, son emplacement sur l'orbite terrestre lui donne l'avantage d'un bruit beaucoup plus faible, de sorte qu'il est capable d'atteindre une sensibilité comparable à celle de télescopes au sol plus larges. L'avantage de Fermi/LAT dans ce cas est qu'il possède un champ de vue plus large, permettant la recherche des sources émettrices en rayons gamma à très hautes énergies dans tout le ciel, ce qui est très difficile à faire avec les instruments Cherenkov. Je présente ici les résultats de cette étude, qui a permis de découvrir plusieurs dizaines de nouvelles sources de rayons gamma à hautes énergies. Le catalogue de ces sources, présenté dans cette section, fournit une liste de cibles pour instruments Cherenkov au sol – à la fois déjà existants et en cours de développement.

La question de l'emplacement de la zone d'émission des AGNs actifs dans le domaine des rayons gamma est abordée dans la deuxième partie de la thèse. Les distances énormes qui nous séparent de ces sources ne nous permettent pas d'obtenir une image directe de la structure du noyau actif avec les télescopes à rayons gamma actuels. En raison de cette limitation, j'utilise une approche indirecte: l'étude de la variabilité de ces sources dans le domaine des rayons gamma à hautes énergies. Cette approche permet d'extraire les informations concernant l'extension spatiale de la zone d'émission en raison de sa connexion avec la variabilité à la plus petite échelle de temps. Dans ma thèse, je démontre que cette méthode fournit une information parfois cruciale pour la compréhension de la structure du noyau actif. Suivant sa localisation à l'intérieur du noyau actif, la taille caractéristique de la zone d'émission varie, donc différentes valeurs de variabilité à plus petite échelle de temps sont attendues pour différents scénarios de production des rayons gamma dans les AGNs. Dans cette thèse, je présente les résultats de l'étude de variabilité aux échelles de temps minimales pour les AGNs actifs en rayons gamma détectés par Fermi/LAT. Bien que dans la grande majorité des cas, la sensibilité de cet observatoire spatial ne s'avère pas suffisante pour investiguer sur la taille du trou noir supermassif au centre de l'AGN, les résultats obtenus suggèrent que cette question peut être résolue par l'étude spécifique d'une population similaire de sources avec les télescopes Cherenkov au sol.

En raison de leur grande luminosité, les AGNs illuminent l'espace intergalactique autour d'eux dans différentes longueurs d'onde, et les rayons gamma ne sont pas une exception. Mais contrairement à l'émission optique, les rayons gamma à très hautes énergies sont efficacement absorbés dans le "vide" intergalactique. L'émission optique et infrarouge en provenance des galaxies remplit l'espace intergalactique de photons à basse énergie, qui interagissent avec les rayons gamma à haute énergie traversant ces régions. Cette interaction conduit à l'absorption des rayons gamma, rendant possible l'étude des propriétés du "fond" d'émission à basse énergie via l'investigation des caractéristiques d'absorption des

spectres gamma à très haute énergie d'AGNs distants. L'absorption des rayons gamma conduit à la production de paires electron-positron, qui peuvent être détectées grâce à la radiation secondaire qu'elles émettent. Comme le mouvement de ces paires est sensible au champ magnétique présent dans l'espace intergalactique, elles sont une opportunité intéressante pour mesurer ces champs. Cette opportunité est l'objet de la dernière partie de ma thèse: je présente pour la première fois les preuves de la présence d'un champ magnétique dans les vides de la Structure à Grande Echelle – un champ magnétique qui est bien plus faible que ceux habituellement observés dans les galaxies. Cependant, l'origine de ce champ n'est pas encore déterminée. Une possibilité intéressante serait que ce champ magnétique intergalactique est primordial et contient des informations sur les débuts de l'Univers. Si c'est le cas, l'étude des propriétés de ce champ magnétique ouvrira une fenêtre unique sur l'Univers primitif, en fournissant des informations inaccessibles par d'autres sources d'observation.

Pour résumer, la présente thèse contient les résultats de plusieurs études que j'ai réalisées et publiées au cours de ces dernières années. Elle aborde différentes questions concernant les processus qui se déroulent à l'intérieur et à l'extérieur des Noyaux Actifs de Galaxies, et démontre le potentiel des observations en rayons gamma à hautes énergies pour l'étude des différents aspects de la physique des AGNs. Bien que le phénomène d'AGN actif en rayons gamma ne soit pas entièrement compris, les résultats présentés ici ajoutent une information importante concernant notre compréhension de ces objets. Je suis sûr que les études à venir avec de nouveaux télescopes se baseront sur ces connaissances partielles afin de créer une image beaucoup plus complète des Noyaux Actifs de Galaxies.

Contents

1 Introduction

1.1 Active galactic nuclei

The phenomenon of Active Galactic Nucleus (AGN) was discovered in the 1943, when Carl Seyfert spotted the galaxies, which had unusually bright nuclei, demonstrating high-excitation spectral lines, usually found in planetary nebulae ([242]). These observations suggested, that something in the centre of active nuclei ionizes the gas, at the same time forcing it to orbit at the velocity of several thousand kilometres per second. Observations, carried out after that discovery, revealed the whole class of these galaxies, which were called the Seyfert galaxies.

Another impulse in the understanding of the physical picture of the AGN was obtained in the 1950-th with the discovery of quasars. The name "quasar" comes from the abbreviation for "quasi-stellar radio source" and serves as a perfect example of how puzzling the newly discovered sources could be. Discovered in the radio band as bright point-like sources of emission, quasars lacked identification with known sources in other domains – mainly because of poor angular resolution and corresponding poor localization ability of the radio telescopes of the time. Several techniques were used to improve the localization of quasars. Among them the Lunar occultation technique historically provided the first identification of a quasar with an optical source. This technique allows to determine the accurate coordinates of the source by timing the moment when the Moon in its movement around the Earth blocks and then unblocks the emission from the source. Using this technique, the first precise coordinates of quasar 3C 273 were determined ([129]), which allowed its identification with the stellar-like source in the optical domain, where the spectral analysis became a standard tool to determine the physical nature of the objects. 3C 273 was associated with what seemed to be a star, but, surprisingly, its spectra showed a bizarre set of spectral lines, which defied interpretation. The puzzle was solved with the assumption of a large redshift of 3C 273 ([240]), indicating that the source is located at a cosmological distance of approximately 500 Mpc. Together with the apparent small angular source size from the radio observations, this suggested a compact ($\lesssim 1$ Kpc) and unusually luminous (~ 100 times more than the galaxies associated with radio sources at that time) source. Soon after that interferometric observations in the radio band were used to get accurate coordinates and angular sizes of quasars ([178]). These observations associated observed quasars with star-like objects. Optical observations of these objects revealed, that they had peculiar colour indices and very broad emission lines ([178]). Detailed spectral analysis also suggested, they have large redshifts (e.g. [126]).

With the years, several different types of AGNs were defined. LINERs – low-ionization nuclei emission-line region galaxies – represent the class of AGNs with emission lines of O II, N II and S II and weaker lines of O III, Ne III and He III ([130]). The width of these lines is typically of 500 km/s, which is similar to the narrow-line gas in Seyferts. Seyferts themselves are the class of galaxies with unusually bright nuclei and emission lines, indicating fast movement of the gas in their centres ([242]). Emission lines in these galaxies are usually divided into two subgroups – broad emission lines (with the width corresponding to velocities of $\sim 1000 - 10000$ km/sec) and narrow emission lines ($\sim 100 - 1000$ km/sec). Seyfert galaxies, which have both these groups of lines in the spectra, are called Seyfet 1, and Seyfets with only narrow emission lines are classified as Seyfert 2 galaxies ([151]). A type of AGN with strong emission lines and nucleus so bright, that the host galaxy is barely visible is called quasars. Active nuclei with stellar-like nuclei, strong variability and almost featureless spectrum with very weak emission lines belong to the class of BL Lac objects – after the first discovered object of this type, believed to be a variable star – BL Lacertae ([255]).

A growing number of observations led to understanding that the AGNs constitute a "zoo" with different species in it. This species, or different kinds of AGN, still possessed some common features, or the features, that could have been translated from one kind to another, which led to the creation of unification schemes, combing all different types of AGNs into one phenomenon, with differences between separate types occurring due to different viewing conditions ([55, 267]). These schemes put in the centre of an AGN a supermassive black hole, surrounded by a hot accretion disk. The twisted magnetic field in the disk leads to the formation of the relativistic jets, oriented perpendicular to the plane of the disk. These jets carry energetic particles and are responsible for the non-thermal emission of the system. The supermassive black hole, disk and the jet launching region are embedded in the region with a highly-ionized gas, which orbits the black hole at the velocities of thousands kilometres per second, which causes

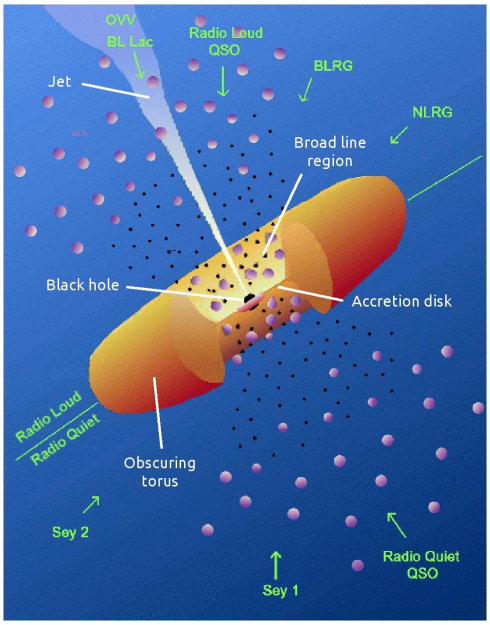

Figure 1: AGN unification scheme (based on http://www.integral.soton.ac.uk/science/AGN.html). Different types of AGN as an appearance of an active nucleus from different viewing angles.

the emission lines, produced here, to be broadened due to the Doppler effect – the so-called Broad Line Region (BLR). Further away from the centre, where the ionization of the gas, as well as the orbiting velocities, is lower, the Narrow Line Region is located. In the outer regions of the system, cooler gas forms a dust torus. Different types of AGN appear in this scheme as a result from observation of an active nucleus from a different angles (see Fig. 1).

Jets, although present not in all types of AGNs – only in those belonging to the "radio-loud" group, – became a real mark of the breed. Jets are the collimated relativistic outflows of plasma, coming out of the centre of an AGN. They span over kiloparsec and even megaparsec distances, transferring the energy from the active nucleus to the intergalactic medium. Jets emit non-thermal, synchrotron radiation, indicating a presence of energetic particles and magnetic fields. High-resolution observations in radio domain revealed that jets are not homogeneous and close to their base often split into separate parsec-scale blobs. This inhomogeneities move with different speed; when they collide, shocks are formed, accelerating particles and producing flares of radiation. Although jet launching mechanism is not yet determined, there is a general agreement that it has to do with the magnetic field in the accretion disk, that is twisted by the differential rotation of the disk to an helical structure, forcing the plasma to move along the beam, collimated towards the axis. Studies of the jet structure, dynamics and emission enable to better understand the physical processes in the very centre of an active nucleus.

Heart of the AGN – the region in the direct vicinity of the central supermassive black hole. The falling gas here forms a hot accretion disk, predominantly emitting in the optical/UV domain. X-ray observations revealed, that AGNs are powerful emitters in this domain too. In the case of Seyfert galaxies, seen from the edge, X-ray emission is thought to originate from the inverse Compton scattering of disk photons in the hot corona, surrounding the disk. Multiple scattering of soft photons within corona leads to the power law shape of the resulting spectrum. The X-ray photons, produced in corona, illuminate the disk. As this happens, the photons can undergo several possible interactions: Compton scattering off the particles in the disk, photoelectric absorption that would lead to the fluorescence and absorption followed by the de-excitation through the ejection of the Auger electron.

The reflected Compton component appears as a hump in the spectrum at the energies of several tens of KeV. On top of this component there is a fluorescence emission from heavy metals, most abundant in the disk. This fluorescence originates primarily from the K_α transitions, and the strongest emission comes from the iron K_α at 6.4 KeV. This fluorescence line is produced when one of the two electrons at

the ground state is ejected via the absorption of an X-ray photon, and an electron from the second level fills the vacancy.

As this line originates even at highest temperatures found in the inner part of the accretion disk, it became a powerful tool for the study of the accretion disk dynamics and central black hole properties ([96]). Indeed, the width of the K_α line is determined by the velocity of the gas movement around the black hole at the region, where the line is formed. Studying the emission in this line one can get an idea about the state of the matter in the innermost region of the accretion disk. The shape of the line is also complicated. As the material moves very close to the central black hole, it orbits at a velocity close the speed of light. As a result, the Doppler shift and boosting effects become very significant. Doppler boosting amplifies the intensity of radiation from the part of the accretion disk that moves towards the observer and dims the emission from the opposite side, and emission from this two sides becomes separated because of the Doppler shift. In addition to that the gravitational redshift shifts the whole line to a somewhat lower energy. It is expected, that the gas will form an optically thick disk and produce Fe K_α line down to the last stable orbit around the central black hole, the radius of which depends on its angular momentum. Due to this, the Fe K_α line profile depends both on the black hole mass and its rotation and observations of this line allow to determine these two quantities.

The AGNs observed in the gamma-ray domain (with the exclusion of a couple of nearby galaxies) belong to the class of blazars and have a completely different spectral appearance. The term "blazar" was first introduced by Ed Spiegel in 1978[1]. According to the Unification scheme of [267], these are the radio-loud AGNs with their jets oriented along the line of site (see Fig. 1). When viewed from other angles, these rare geometrical cases are seen as radio galaxies. In many ways, blazars are the most extreme of AGNs – the most luminous, the most polarized, the most variable. Enormous energy of their relativistic jets and their high collimation provides a direct indication of the energy extraction from the central black hole. In this way, blazars allow to study the black hole surrounding region though the study of the properties of their jets. Study of the jet emission and dynamics also allows to address the question of jet launching, which is not yet fully understood ([226]). Blazars can be defined in different ways – through their variability, compact flat-spectrum radio emission, their superluminal motion, their polarization and their gamma-ray brightness. Blazar spectra span over a very broad range of frequencies, from radio to the TeV domain, and consist of two distinct bumps – a lower-energy one is associated with the synchrotron emission, while the higher-energy bump is of the Inverse Compton origin. Based on the width of the observed spectral lines, blazar are divided in BL Lacs and Flat-spectrum radio quasars (FSRQs) – equivalent width of more than 5 Å is considered to be a signature of FSRQs ([267]). BL Lac in their turn can be divided into High-frequency peaked BL Lacs (HBL) and Low-frequency peaked BL Lacs (LBL). According to [217], the division here is done based on the ratio of the X-ray to radio fluxes, which anti-correlates with the frequency of the peak of their synchrotron emission – the ratio of fluxes at 5 GHz and 1 KeV is less than 0.75 for HBL and larger than this value for LBL type objects. Unification scheme of [267] associates BL Lacs with radio galaxies of FR I type and FSRQs – with FR II.

Fanaroff-Riley (FR I and FR II) types of radio galaxies were introduced back in 70th of the previous century ([100]). The original classification is based on the ratio of the distance from the center of the galaxy to the region of a brightest radio emission in the jet to the overall size of the extended radio source. If this ratio is less than 0.5, the sources is classified as FR I, in the other case – as FR II. In fact, this classification separates radio galaxies, which have the dominant radio emission coming from the central part of the jet from the galaxies, for which the emission of radio lobes takes over the emission of the inner jet regions.

Difference in the appearance of spectral lines in BL Lacs and FSRQs indicate another physical property, different in these two types of AGNs, which is the luminosity of the Broad Line Region. BL Lacs have on average lower BLR luminosity than FSRQs – a fact, which was suggested to be used to refine the relative definition of BL Lacs and FSRQs ([114]).

Studying a sample of blazars, [106] suggested that HBLs and LBLs/FSRQs actually represent a continuous population with the energy of the first and second spectral peaks gradually decreasing with the increase of the radio luminosity (see Fig. 2). Observations in the gamma-ray domain with the Fermi/LAT instrument (see section 1.2.2) revealed, that FSRQs and BL Lacs indeed form a continuous population in terms of their spectral indices in the LAT band, with BL Lacs having systematically harder

[1] http://www.nrao.edu/index.php/learnscienceprobingextremes

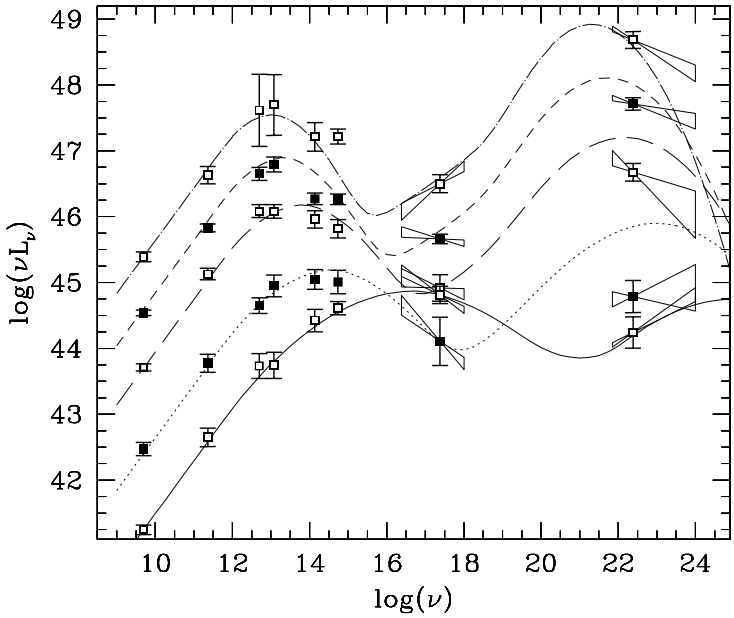

Figure 2: Averaged SED for a sample of FSRQs and BL Lacs, binned according to their radio luminosity. Curves show analytical models. Radio luminosity νL_ν is given in ergs/sec and frequency ν is in Hz. Ref: [106]

spectra ([10]), which is consistent with the assumption, that their spectra peak at higher energies. The same tendency is observed in the Fermi/LAT 2nd AGN catalogue [23] – FSRQs have softer spectral indices than BL Lacs. FSRQs in this catalogue are also detected at larger redshifts, indicating that they are more luminous than BL Lac objects.

Owing to their high luminosity, blazars constitute a half of the objects observed in the high energy GeV domain ([208]). Their extreme properties make them well-suited laboratories for the study of the physics of astrophysical jets and their connection to the central engines of AGNs. High luminosity of blazars even allow to probe the properties of the intergalactic medium this emission is coming through. All this made blazars the main sources of study of the present work.

1.2 γ-ray instrumentation

1.2.1 Previous γ-ray telescopes

SAS-2 mission

The first satellite, dedicated to γ-ray astronomy above several tens of MeV, was NASA Small Astronomy Satellite SAS-2 ([2]), launched in November 1972. It was designed to perform observations in the energy range between 20 MeV and 1 GeV and had a spark chamber for the detection of gamma-ray photons. Due to the failure of the low-voltage power supply, it stopped collecting the scientific data in June 1973.

SAS-2 provided the first detailed look at the γ-ray sky and studied the distribution of the γ-ray emission along the galactic plane. It has shown for the first time the strong correlation between the γ-ray radiation and galactic structural features, supporting the hypothesis that these gamma rays are produced through the interaction of cosmic rays with the interstellar gas. SAS-2 also detected discrete sources such as Crab and Vela pulsars.

Cos-B mission

Cos-B was ESA's first satellite dedicated to a single experiment and was launched in August 1975 ([8]). As SAS-2, Cos-B used a spark chamber and was sensitive to γ-rays between 30 MeV and 10 GeV. It was operational for more than 6.5 years, being switched off only in April 1982.

Most of the observations preformed by Cos-B were devoted to the study of the galactic plane emission, providing a detailed map of its spatial distribution. Cos-B also performed a thorough study of the binary system Cygnus X-3 and detected a quasar 3C 273. The extragalactic diffuse radiation, reported by SAS-2, turned out to be a hard target for Cos-B, as its highly elliptical orbit exposed it to bombardment by cosmic rays, which led to emission of secondary gamma rays in the spacecraft structure.

EGRET γ-ray telescope on board of CRGO

The second in NASA's program of orbiting "Great observatories", the Compton Gamma Ray Observatory (CGRO) was a sophisticated satellite observatory for the observations of the high-energy Universe ([3]). It was launched on April 5, 1991 and re-entered the Earth's atmosphere on June 4, 2000. CGRO had four instruments on board, that covered six decades of the electromagnetic spectrum – from 30 keV to 30 GeV. These instruments were the Burst And Transient Source Experiment (BATSE), the Oriented Scintillation Spectrometer Experiment (OSSE), the Imaging Compton Telescope (COMPTEL), and the Energetic Gamma Ray Experiment Telescope (EGRET).

The instruments on board of CGRO were designed for different purposes. BATSE served as the all-sky monitor in the energy range between 30 keV to over 1 MeV. It had eight detectors situated at the corners of the satellite, which allowed detection and localization of transient γ-ray sources, like gamma-ray bursts or other strong flaring sources over the sky. It has produced an all-sky map of gamma-ray bursts, showing they do not concentrate towards the galactic disk and thus providing evidence for their extragalactic origin. The spectrometer OSSE had four detectors, sensitive to gamma rays of energies from 60 keV to 10 MeV. These detectors could have been individually pointed, enabling measurement of the flux from the source and background regions at the same time. The higher energy resolution of OSSE (down to 4% at 5 MeV) allowed it to observe nuclear lines in solar flares and detect signatures of electron-positron annihilations in the Galactic centre region. The COMPTEL instrument illustrated the power of imaging in a narrow energy range. It was designed to perform observations from 0.8 to 30 MeV and produced an all-sky map in the light of radioactive aluminium 26, revealing regions of high concentration of this isotope.

EGRET was the highest energy telescope of CGRO, designed for observations at energies from 20 MeV to 30 GeV. EGRET is essentially a predecessor of the modern Fermi/LAT instrument. It used a spark chamber to measure the direction of the incoming γ ray and a calorimeter to measure its energy. Gamma-ray photons interacted with the foils in the spark chamber producing high-energy electron-positron pairs, whose trajectories were then tracked through the subsequent layers of the chamber. The pairs were then absorbed in the calorimeter at the bottom of the detector. Reconstruction of directions and energies of the pairs allowed to measure the energies and directions of the γ rays hitting the chamber. As cosmic rays were also detected by the spark chamber, EGRET had to deal with a large background – 10^5 times larger than the γ-ray signal of interest. For this reason EGRET was designed to be very efficient in terms of rejecting background events from the cosmic ray interaction within the spark chamber. From the top and sides the EGRET detector was protected by the anti-coincidence scintillator dome, which allowed to efficiently reject events from charged particles. Electrons and positrons resulting from the γ-ray interactions ionized molecules of the gas inside the chamber, which were afterwards accelerated by the high voltage, creating a number of secondary ionizations. The charges resulting from these interactions were then recorded in the tracking layers of the detector for further analysis on the ground.

The all-sky emission in the EGRET energy band is dominated by the emission from the cosmic rays interacting with the interstellar gas, concentrated in the plane of our Galaxy. This emission gives the primary contribution to the all-sky image, produced by EGRET. Apart from the galactic emission, EGRET also made a reliable measurement of the isotropic, presumably extragalactic, gamma-ray emission. EGRET also detected a number of point-sources. It detected 5 new gamma-ray pulsars and discovered, that certain Active Galactic Nuclei, known as blazars, emit most of their electromagnetic energy in the high-energy gamma-ray domain. EGRET discovered several dozens of these sources and showed, that their gamma-ray emission is extremely variable on the time scales as short as one day.

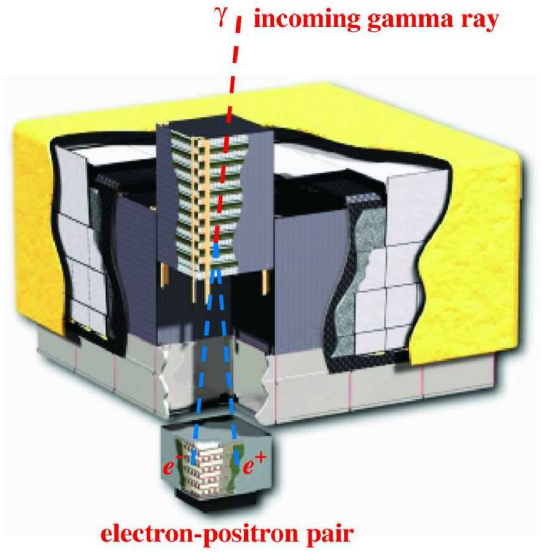

Figure 3: Schematic diagram of the Fermi/LAT ([57])

1.2.2 γ-ray telescope Fermi/LAT

The successor of EGRET, Large Area Telescope (LAT) on board of the Fermi satellite, was launched in June 2008. Originally the mission was called Gamma-ray Large Area Space Telescope (GLAST), but was later renamed after the famous physicist Enrico Fermi. The satellite was launched into a low-altitude orbit and makes one lap around the Earth in $\sim$ 95 minutes. The Fermi satellite carries on board two instruments dedicated for γ-ray observation in the broad energy range from several KeVs to more than 300 GeV – LAT and Gamma-ray Burst Monitor (GBM).

GBM is a low energy instrument with a large field of view, specifically designed for observations of gamma-ray bursts. Having a field of view of 9.5 sr, it consists of two sets of detectors – Sodium Iodide (NaI) and Bismuth Germanate (BGO) scintillators. Twelve Sodium Iodide detectors are designed to cover the lower energy range, detecting photons in the range between several keV and $\sim$ 1 MeV, whereas BGO detectors are responsible for catching higher energy γ rays, in the $\sim$ 150 KeV$-$ $\sim$ 30 MeV range, providing a good overlap with the LAT energy band.

Large Area Telescope (hereafter LAT or Fermi/LAT) is an instrument designed to perform observations of cosmic sources in the energy range between 20 MeV and 300 GeV, built by an international collaboration of France, Italy, Japan, Sweden and the United States [57]. As EGRET, LAT is a pair-conversion instrument and uses a similar design. It consists of 16 planes of high-Z material, in which γ-rays convert into the $e^+ - e^-$-pairs (see Fig. 3). This planes are interleaved by the detectors capable of recording the position of the passage of charged particles. In this way the trajectories of electron-positron pairs are tracked, which allows to reconstruct the direction the initial γ-ray photon came from. Photons converting in the first 12 layers are called "front", the ones that do convert in the last 4 layers are referred to as "back". This separation is a result of a trade-off between angular resolution and effective area of the instrument – first 12 layers are thinner, to provide better resolution, whilst the last 4 thick layers are to increase the effective area. Angular resolution of Fermi/LAT varies significantly with energy, ranging from 6˚at 100 MeV to 0.2˚at 100 GeV (68% containment radius, see Fig. 4). A calorimeter, which measures the energy of the produced electron-positron pair and thus allows to reconstruct the energy of the initial gamma ray, is located at the bottom of the detector. The anti-coincidence shield is surrounding the detector, allowing to reject the events associated with the passages of cosmic rays through LAT.

Although using a design, similar to EGRET, LAT hugely outperforms it in terms of effective area, which is several times larger – 7000 cm^2 at 1 GeV for LAT and $\sim$ 1500 cm^2 in the case of EGRET. LAT also has a larger field of view – 2.4 sr, which means that it observes 20% of the sky at any given moment of time. The orbit and self-rotation of the Fermi satellite were chosen in the manner that allows LAT to

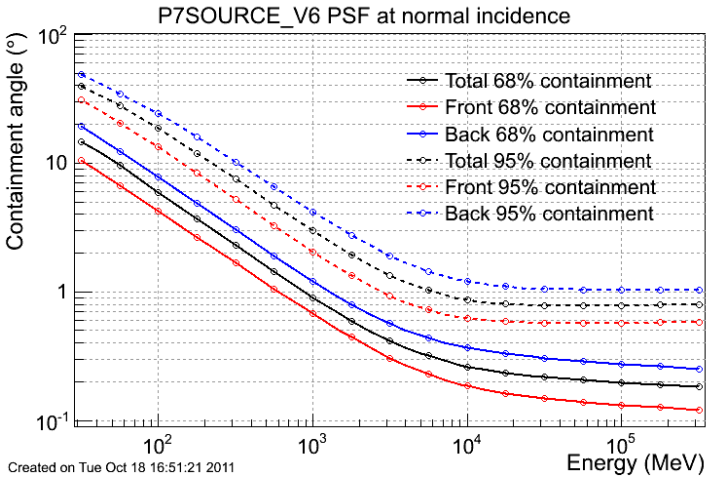

Figure 4: Fermi/LAT Point spread function (PSF) 68% and 95% containment radii ([230])

scan the entire sky in two orbital revolutions, or ~ 3.2 hours, which makes Fermi/LAT well-suited both for all-sky analysis and studies of individual sources.

1.2.3 Cherenkov telescopes

Opacity of the Earth atmosphere to the high energy photons forces us to put γ-ray telescopes into space, where the γ-ray photons can be detected directly. However, spectra of typical astrophysical sources are decreasing in the γ-ray domain, so that the amount of photons per unit area per unit time drop dramatically with increase of energy. Space-born instruments, that can not be too big in size, become inefficient due to their small effective area, requiring large exposure times in order to collect sufficient amount of γ-ray photons.

The alternative to sending expensive, but still small, missions to space is to build telescopes on the ground. Even though high-energy photons are absorbed in the atmosphere, they do not disappear without a trace. Their interaction with the atmosphere leads to the production of the avalanche of relativistic electron and positron pairs, called an electromagnetic shower. As these particles slow down, they emit Cherenkov light. Most of the shower develops at the altitudes ~ 10 km above the sea level. Radiated secondary photons, visible or ultraviolet, arrive on the ground at high quantities and illuminate the area of 10^4 square meters, becoming an indirect image of the air shower, thus allowing identification against the background and reconstruction of the energy and arrival direction of the original particle. In this way the atmosphere itself works as enormous detector, catching very high energy (VHE) γ rays and transforming them into something more easily detected on the ground.

The fact that the surface area, illuminated by the shower, is large, has two consequences. First of all, it means that the collection area of a Cherenkov telescope is huge compared to space-born instruments, as it will detect a γ ray if it happens to be anywhere within the shower illuminated patch of ground. The drawback of this is that the light intensity is low, which requires the detecting telescope to be sufficiently large and have high efficiency detectors, able to register single photons. As air showers typically last only several nanoseconds, the detectors have to be not only efficient, but also very fast.

Gamma rays of very high energies are rare events. Much more frequent optical/UV photons from the atmosphere glow, stars and other astrophysical sources constitute a large background, that Cherenkov telescopes have to deal with. But even with this complication, ground-based instruments such as MAGIC ([5]), VERITAS ([6]) and HESS ([9]) largely outperform capabilities of space observatories (e.g. Fermi/LAT) in the energy range between $\sim$ 100 GeV and $\sim$ 10 TeV, opening the window for the astrophysics of very high energies.

The first VHE γ-ray telescope was built at the Fred Lawrence Whipple Observatory in Southern Arizona in the United States ([4]) in 1968 and detected the its first γ-ray source – the Crab nebula – in 1989 ([277]). This telescope has a multi-segmented mirror with the total collective area of 75 m^2. The

telescope is still operational and observes in γ-ray sky in the energy range between 300 GeV and 10 TeV.

The Imaging Atmospheric Cherenkov Telescope technique was further developed in the HEGRA experiment ([1]). Started in 1992, this experiment, when completely constructed, consisted of 5 telescopes with 8.5 m^2 collective area each, arranged on a square with a side of 100 m with an additional telescope in the center. This configuration allowed to perform stereoscopic observations of air shower and provided a better discrimination between γ-ray and cosmic ray events, than one-telescope systems. Stereo views also enabled better reconstruction of the spatial development of air showers, improving the imaging capabilities of the system.

A similar setup is used in the High Energy Stereoscopic System, or H.E.S.S., built in Namibia, near the Gamsberg mountain ([9]). The H.E.S.S project was realized in two phases. In Phase I the initial four telescopes of 12 meters in diameter were constructed and arranged in the form of a square with the side of 120 m. The first telescope of the H.E.S.S. I system became operational in summer 2002, and all four telescopes of the system started to work in December 2003. In Phase II of the project a single much bigger telescope with the mirror of 32.6 m by 24.3 m was added in the center of the configuration in 2012, in order to increase the available energy range, overall sensitivity and angular resolution of the system.

The successor of the Whipple telescope, Very Energetic Radiation Imaging Telescope Array System (VERITAS), was build in the same Fred Lawrence Whipple Observatory in 2007. As HEGRA and H.E.S.S it consists of four atmospheric Cherenkov telescopes for stereoscopic view of the gamma-ray induced showers. Each telescope has an aperture of 12 m and the resulting configuration works in the energy range of 50 GeV to 50 TeV.

MAGIC ([5]) – another modern imaging atmospheric telescope – uses a slightly different approach. Instead of going for several small telescopes to improve the position of the photon impact, the MAGIC collaboration put the main emphasis on the detection of γ-ray photons of the lowest energies. This requires a larger collection area, so MAGIC telescopes feature 17 m mirrors. The system nowadays consists of two Cherenkov telescopes, which total collective area allowed to reduce the lower energy threshold of the instrument down to 25 GeV ([5]). The two telescopes MAGIC-I and MAGIC-II were finished in 2003 and 2009 correspondingly and are operational ever since.

The future of the VHE γ-ray astronomy is associated with the Cherenkov Telescope Array (CTA) ([7]). CTA is planned to consist of northern (1 km^2 in size) and southern hemisphere (3 km^2) arrays for a better sky coverage. Three different types of telescopes with different mirror sizes will be used in CTA to cover a broader energy range, than that of other Cherenkov telescopes – from few tens of GeVs to the energies well above 10 TeV. The low energy instruments will be represented by the telescopes of 24 m diameter and will have a field of view of 4-5 degrees. The medium energy telescopes will be 10-12 meters in diameter and will target the energy range of 100 GeV to 1 TeV, having a field of view of 6-8 degrees. At higher energies smaller size (with 4-6 meters aperture) telescopes will operate, covering energies above 10 TeV. The current design of the CTA arranges these telescopes on a circular area, with low energy instruments situated in the centre and high energy ones in the outer areas of the configuration. Compared to currently existing instruments, CTA will have much larger collective area, resulting in higher sensitivity. As in CTA the gamma-ray induced showers will be observed by a large number of telescopes, it should also outperform the existing instruments in terms of the angular resolution and cosmic ray background rejection. Apart from the studies of the astrophysical galactic and extragalactic sources, CTA will also study questions of fundamental physics through searches for the signatures of γ rays from Dark Matter decays, cosmic ray observations and tests of predictions of some quantum gravity theories.

1.3 Propagation of high energy γ ray through the Intergalactic medium

1.3.1 Extragalactic background light

The Extragalactic Background Light (EBL) is the combination of all the light emitted by the galaxies across the Universe along its history. As the primary sources of light in galaxies are stars, EBL is an important tool for the studies of stellar evolution. In particular, the knowledge of its dependence with redshift helps to trace star formation rates to earlier epochs.

A number of observational campaigns were carried out in an attempt to measure the energy density of the EBL as a function of wavelength. Emission from the stars and gas, which constitutes EBL, seats in the optical to far infra-red domain, and these campaigns utilized observations in different parts of it

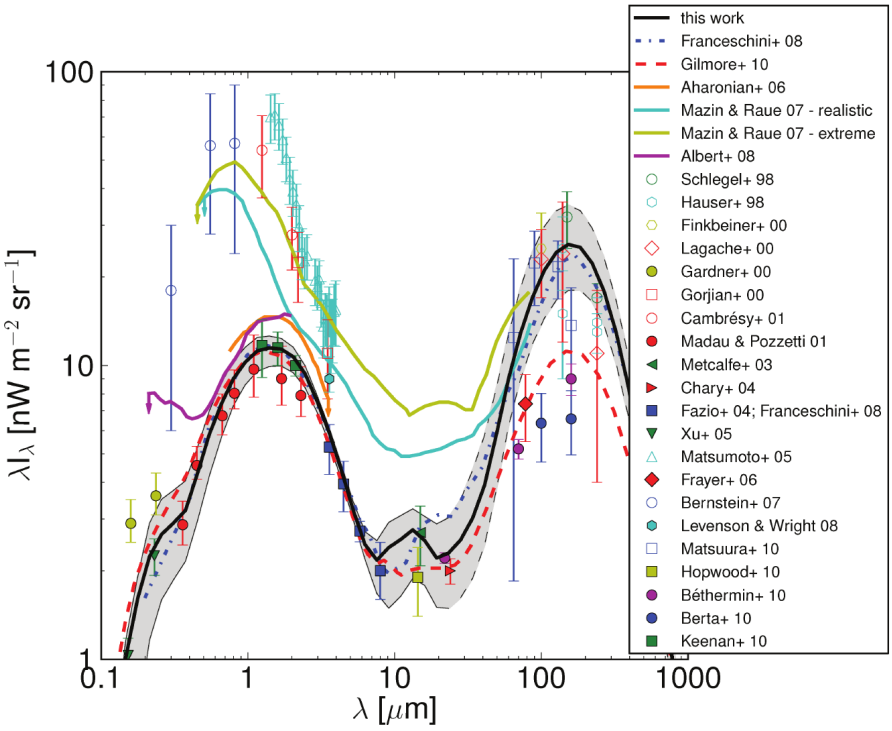

Figure 5: Summary of different theoretical models and observational upper and lower limits on the spectrum of the EBL, compiled by [91].

in order to constrain the multi-wavelength presence of the EBL emission. Part of these works focused on observing the flux from a given part of the sky, then subtracting the contribution from all known point-like and extended sources, in this way providing the measurements, which can be treated as the upper limits on the EBL energy density ([63, 72, 103, 121, 128, 158, 176, 177, 239]). Other campaigns counted the number of observed galaxies within a given patch of the sky in order to infer the level of the EBL they produce ([64, 65, 75, 102, 108, 110, 137, 149, 163, 166, 185, 219, 283]). As such measurement are always limited by the sensitivity, some fraction of faint galaxies remains uncounted, making these measurements rather lower limits on the EBL. Both these two kinds of EBL measurements are summarized in Fig. 5 along with several theoretical models.

In recent years, very-high-energy (VHE) γ-ray observations were also used to measure the EBL. VHE γ-ray flux from distant blazars is absorbed on the way from the source to the Earth through its interaction with the EBL photons ([123]). The measurement of the induced distortions of the VHE γ-ray flux from distant hard-spectrum blazars by the effect of absorption on the EBL was used to derive constraints on the EBL density ([33, 39, 216]).

The conventional derivation of the upper bound on the EBL from γ-ray observations adopts the assumption that the intrinsic power law type spectrum of the primary source (a distant blazar) is characterized by the slope $dN_\gamma/dE \sim E^{-\Gamma}$ with $\Gamma \geq 1.5$. This assumption appears reasonable in the framework of the most simple synchrotron-self-Compton (SSC) models for the broad band spectra of blazars. However, particular blazars considered for the derivations of EBL limits (the blazars with hardest intrinsic γ-ray spectra) may well not fit into this simplest SSC model framework, so that the assumption of $\Gamma \geq 1.5$ might be not applicable ([47, 70, 148, 160, 161, 195]). If the intrinsic spectra of the blazars used for the derivation of the upper bound on the EBL density are harder than $\Gamma = 1.5$, this upper limit is relaxed ([182]).

Constraints on the intrinsic slope of the spectra of blazars can be obtained from the observations by the Fermi/LAT ([57]) in the energy band below $\sim$ 100 GeV, where the effect of absorption on the EBL becomes negligible. However, the blazars used for the derivation of constraints on the EBL are characterized by the hard spectra, which makes it difficult to observe their flux below 100 GeV. In fact,

the blazar 1ES 0229+200, which until recent time was providing the tightest constraints on the EBL ([33]), is not listed in the catalogue of sources detected by LAT in the two-year exposure ([208]), with only upper limits on the source flux derived from the LAT data ([205, 258, 260]) and a weak detection reported by [216, 274].

An additional difficulty for such constraints is that the spectrum of hard blazars might be composed of two contributions. Apart from the direct γ-ray emission from the primary source, an additional contribution is expected from the γ-ray cascade initiated in the intergalactic medium (IGM) by the absorbed VHE γ rays ([46, 223]). The overall flux and the spectral shape of the cascade contribution are determined by the strength of the Intergalactic Magnetic Field (IGMF, see Sect. 1.3.2) ([49, 200, 201, 223]). Uncertainty of the IGMF strength introduces an uncertainty of the importance of the cascade contribution and prevents the measurement of the slope of the intrinsic γ-ray spectrum of the source. In fact, most of the limits on the EBL derived up to now are based on an underlying assumption about the IGMF strength (the IGMF should be strong enough to suppress the cascade contribution up to $\sim$TeV energies), which is not justified a-priori. In a recently published measurement of the γ-ray attenuation on the EBL [24] in addition to this assumption a sample of sources, the majority of which had a relatively low high energy cut-off ($\sim$ 1 TeV), was used, thus minimizing the amount of the expected cascade contribution and justifying the usage of the of the $\lesssim$ 10 GeV data as a proxy of the intrinsic blazar spectra. A different approach was used later on in the TeV domain: in [134] several different spectral models were used, including those accounting for in the intrinsic curvature of the source spectra. Even without considering $\lesssim$ 100 GeV data to infer the intrinsic source spectrum, a combined fit of several, brightest in the TeV domain, sources enabled to clearly measure the effect of the γ-ray absorption on the EBL photons.

If the assumption on the IGMF strength is relaxed, the γ-ray data can be used to measure the IGMF strength (see Sect. 4.1 for details). The electron-positron pairs, created as a result of the absorption of multi-TeV photons, up-scatter the Cosmic microwave background (CMB) as they cool, creating secondary emission in the GeV domain ([201]). With the mean-free-path of TeV γ rays being $D_\gamma \simeq 100\ (E_\gamma/10\ \mathrm{TeV})^{-1}$ Mpc, the production of these multi-TeV energy e^+-e^- pairs occurs predominantly in extragalactic space. Furthermore, if non-negligible magnetic fields are present in the region these pairs are born into, they deflect significantly from their initial directions, resulting in secondary GeV photons having a reduced probability of reaching the observer. Thus, the apparent flux is suppressed at low energies. Observational evidence for the presence of such a suppression places constraints on the IGMF strength to be $\gtrsim 10^{-17}$ G ([84, 89, 205, 258, 260]) and is discussed in Section 4.

1.3.2 Intergalactic magnetic field

The problem of the origin of 1- to 10-μG magnetic fields in galaxies and galaxy clusters is one of the long-standing problems of astrophysics and cosmology (see [124, 155, 157, 279] for reviews). It is commonly assumed, that these fields originate from the amplification of a much weaker seed field. However, the seed magnetic fields escaped detection until recently and their nature remains unclear. It is possible that these fields were generated in galaxies in the early stages of their evolution and afterwards amplified by the dynamo mechanism; an alternative hypothesis is that the seed fields originate from phase transitions in the Early Universe. Magnetic fields produced in the Early Universe may have survived till our days in the voids of the Large-Scale Structure, whereas the fields, generated in galaxies, should concentrate around the latter.

It is possible, however, that magnetic fields generated and amplified in galaxies were brought out of them with the outflows, powered either by star formation or AGN activity. Volume filling factor of these outflows in simulations varies from 20% to 100%, depending on the assumptions made in the simulation set up (see e.g. [111, 165, 222]). Some observations suggest that galaxies are surrounded by metal-enriched halos of the size of $\sim$ 100 Kpc ([69, 225, 250], see also [184] for a review). As these halos are remnants of the outflows, they suggest, that the volume filling factor of outflows is small. The detection of the galactic-origin magnetic field in the voids would serve as an important tool to constrain the power of this galactic outflows.

Role of the Intergalactic magnetic field (IGMF) in the astrophysical picture of our Universe is not limited to serving as a seed for the currently existing galactic fields. Sufficiently strong IGMF could have influenced the structure formation by affecting the evolution of density perturbations ([124, 276]). If

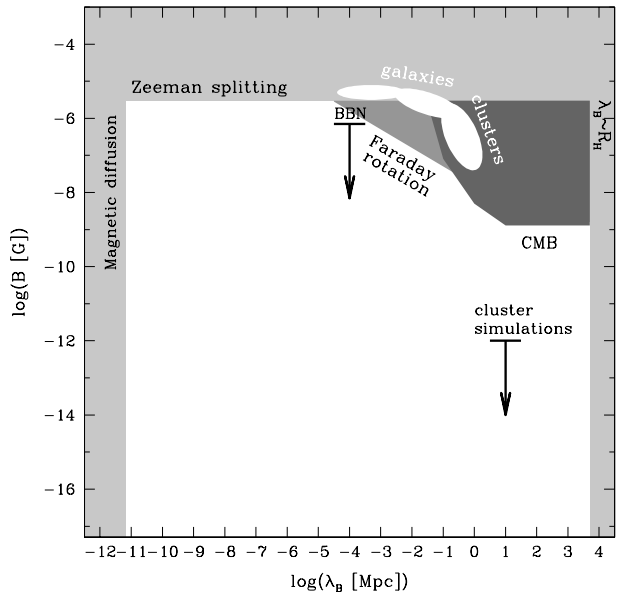

Figure 6: The summary of known observational bounds on the strength and correlation length of IGMF (from [201]). The bound from Big Bang Nucleosynthesis marked "BBN" is from [124]. White ellipses show the range of measured magnetic field strengths and correlation lengths in galaxies and galaxy clusters.

IGMF was inhomogeneous, it could have modulated the formation of galaxies by giving baryons streaming velocity with respect to the dark matter ([77]). As a result, some of the baryons will not fall into the gravitational potential well and galaxy formation will be inhibited on small scales.

From the observational point of view, there is a number of methods to detect the IGMF, which were summarized in [201]. Perhaps the most direct way to detect the IGMF would be to measure it through the Zeeman splitting of lines in the spectra of the different galaxies. Observations of Zeeman splitting of the 21 cm hydrogen line in spectra of distant blazars are used to measure the $\gtrsim 10^{-6}$ G magnetic fields in the Milky Way ([133]) and other galaxies (e.g. [280]). Observations of the Faraday rotation of the polarized radio emission from distant galaxies allows to probe a lower IGMF strengths and limits at the level of $\sim 10^{-6} - 10^{-11}$ G were derived ([68, 156]), depending on the assumption on the correlation length of IGMF and electron density along the line of sight of the observation. The overall conclusion from these non-detections is that IGMF should be weaker than $\sim 10^{-8}$ G in case if its correlation length is larger than 1 Mpc ([201]). Apart from these, direct methods, indirect procedures have been used to further constrain the IGMF. For example, a sufficiently strong IGMF could have affected the structure formation on different scales ([77, 276]). If IGMF was produced in the Early Universe before the epoch of recombination, it might have left various imprints in the CMB, such as temperature anisotropies ([61]) and the Faraday rotation of the polarized CMB emission ([146, 154]). Another cosmological implication of the IGMF is related to the fact, that in the presence of a strong magnetic field the rates of weak reactions are changed, so a strong cosmological IGMF could have affected the Big Bang nucleosynthesis ([125, 174, 175], also see [124] for a review).

The expected correlation lengths λ_B of the IGMF is bounded from the top and the bottom. Small-scale magnetic fields in the intergalactic medium decay due to magnetic diffusion, so the requirement that it would have survived till our days imposes a lower limit on λ_B ([124]). A natural upper bound on λ_B is set from the requirement that it wouldn't be larger than the visible part of the Universe – $\lambda_B \leq R_H$, where R_H is the Hubble radius.

All these limits are summarized in Fig. 6 in terms of the strengths of the IGMF and its correlation length.

As it is seen from this figure, the correlation lengths of the IGMF is constrained both both sides, whereas its strength is constrained only from the top. This leaves a lot of freedom for the theoretical modelling of the generation of the IGMF and its further role in the evolution of the Universe. In Section 4

I present the results, which for the first time provide the *lower* bound on the strength of the IGMF, thus significantly constraining existing theoretical models.

2 Fermi/LAT very high energy sources

The number of known astronomical sources of very-high-energy (VHE) γ-rays grew ten-fold over the last five years[2]. A large part of the newly discovered sources lies in the Galaxy and were revealed via a systematic scan of the inner Galactic Plane by the HESS telescope [32, 40]. The HESS survey has covered an area 0.1 sr in a strip $|l| < 30^\circ$, $|b| < 3^\circ$. This covers less than 1% of the sky. Surveys of larger regions on the VHE γ-ray sky with the existing ground based Cherenkov γ-ray telescopes are difficult because the size of the field of view is too small (5° for HESS, 3.5° VERITAS telescopes and 3° for MAGIC telescope). A previous survey of the northern hemisphere using the Cherenkov telescope Whipple has resulted only in derivation of upper limits on the flux of persistent VHE γ-ray sources [278]. The wide field of view MILAGRO [56] and Tibet [53] arrays have produced a systematic survey of the VHE γ-ray sky. However, the energy threshold of the air shower arrays like MILAGRO and TIBET is rather high (in the multi-TeV band) so that only sources with spectra extending well above 1 TeV can be detected.

Contrary to the ground-based Cherenkov γ-ray telescopes, *Fermi* has a wide field-of-view and continuously surveys the whole sky on a time scale of 3.2 hr. Over the first year of operation *Fermi* has detected some 1.5×10^3 Galactic and extragalactic sources of γ-rays with energies above 1 GeV ([12]). In two years only the number of detected AGNs grew up to almost a thousand ([23]). In fact, the Fermi/LAT 2nd AGN catalogue [23] lists 395 BL Lacs, 310 FSRQs, 157 blazars of unknown class, 8 misaligned AGNs, 4 Seyfert 1 galaxies and 10 AGNs other types. Blazars, detected by Fermi/LAT, span over a wide range of luminosities – from 10^{44} to 10^{49} ergs/sec – and are located at redshifts up to 3. Out of 54 blazars, detected in TeVs to date[1], 39 are in in the Clean Sample of the Fermi/LAT 2nd AGN catalogue. The mean spectral index of AGNs in this catalogue is larger than for its subsample, corresponding to the sources, also detected in TeV band. This indicates, that GeV-TeV AGNs have harder spectra than the majority of GeV-bright AGNs, detected in the LAT band ([23]). Since its launch, Fermi/LAT was implied in the detection of 9 AGNs in the TeV band ([136, 168, 171, 170, 209, 210, 211, 213, 214]). This demonstrates the power of Fermi/LAT in providing candidates for the future observations with TeV instruments. However, some TeV blazars, like 1ES 0229+200 and 1ES 0347-121 elude detection in the GeV band, as their spectra peak far above 100 GeV and, thus, emission in the multi-GeV band is weak. To improve the detection efficiency in all-sky observation of LAT one has to go to energies above 100 GeV.

However, the smaller collection area of *Fermi* (~ 1 m^2, compared to $\sim 10^5$ m^2 for the ground-based γ-ray telescopes) prevents an extension of the all-sky monitoring with *Fermi* to the VHE γ-ray band. At the same time, at the energies above 100 GeV the *Fermi* signal is almost background-free (in contrast to the ground based telescopes in which the signal has to be identified on top of the strong background created by cosmic rays and optical/UV night sky background).

The collection area of *Fermi* is still sufficient for detecting the brightest γ-ray sources at the energies above 100 GeV. The power of the all-sky monitoring capabilities of *Fermi* at the highest energies was clearly demonstrated by discoveries of new VHE γ-ray sources motivated by *Fermi* detections of these sources above 10 GeV ([212, 214, 136, 168, 171, 170, 209, 210, 211, 213, 214]). The all-sky survey capabilities of space-based γ-ray telescope EGRET at the energies above 10 GeV were used for the search of new VHE γ-ray blazars by [86, 120] via cross-correlation of arrival directions of highest energy EGRET photons with positions of known sources.

In the following sections I present the work I've performed on the search of the VHE sources using the all-sky capabilities of the Fermi/LAT. In section 2.1, based on my publication [198], I show how the correlation of the arrival directions of > 100 GeV photons led to the detection of a new VHE source – a radio galaxy IC 310. Cross-correlation analysis of the arrival directions of the highest energy photons, detected by the LAT, with the position of known blazars, is presented in section 2.2 ([199]). The power of the Fermi/LAT with respect to the detection of high-redshift VHE-emitting blazars is demonstrated in section 2.3 ([203]).

[2] **See e.g.** `http://http://tevcat.uchicago.edu/, http://www.mppmu.mpg.de/~rwagner/sources/`

2.1 Very high-energy gamma-ray emission from IC 310

2.1.1 Introduction

As it was said before, the scanning observation mode of the Fermi/LAT is well-suited for the all-sky surveys of the gamma-ray sky in the VHE domain – a task, which the ground-based Cherenkov telescopes with small fields of view have troubles to realize. Here we use *Fermi* data to produce a survey of the extragalactic sky at energies above 100 GeV, i.e. in the energy range accessible for the ground-based γ-ray telescopes. The majority of the sources we find with *Fermi* at energies above 100 GeV are known TeV blazars. The only source which has not been previously reported as a VHE γ-ray source turns out to be IC 310, which is a head-tail radio galaxy [244] with possibly a BL Lac type nucleus [232].

Two radio galaxies have been previously reported to be the sources of γ-rays with energies above 100 GeV: M87 ([20, 42, 50]) and Cen A ([31]). These two sources are the two closest Fanaroff-Riley type I (FR I) radio galaxies. The FR I radio galaxies form the "parent" population of BL Lac type blazars ([267]). They are expected to be weak VHE γ-ray emitters, because the γ-ray flux from these sources is not boosted by the relativistic Doppler effect. In this respect it is not surprising that only the two nearest FR I radio galaxies have been seen in the VHE γ-ray band so far. Both Cen A and M87 are too weak to be detected at 100 GeV in the 1.5 yr exposure of *Fermi*.

IC 310 is situated in Perseus galaxy cluster at the distance of 80 Mpc, which is a factor of 22 and 5 larger than the distances of Cen A and M 87 respectively. IC 310 is, therefore, by 1-2 orders of magnitude more luminous than that of Cen A and M87. Besides, IC 310 is not classified as a FR I type radio galaxy. Instead, it is a head-tail radio galaxy ([244]), the type of galaxies usually found in galaxy clusters. It possesses an extended "tail" of the angular size $\sim 15'$ aligned along the direction connecting the centre of Perseus cluster and the galaxy. This tail is believed to be produced as a result of the fast motion of the galaxy through the intra-cluster medium ([237]). The detection of IC 310 in the VHE band looks less surprising if the hypothesis that the source hosts a low-luminosity BL Lac is adopted ([232]). In this case the mechanisms of VHE γ-ray emission from the source can be the same as in the majority of extragalactic VHE γ-ray sources.

2.1.2 Survey of extragalactic sky above 100 GeV with *Fermi*

We used the data of Large Area Telescope (LAT) on board the *Fermi* satellite to generate an all-sky map of arrival directions of γ-rays with energies above 100 GeV. The entire list of the Pass 6 diffuse class photons, detected by *Fermi* in this energy range, included 4145 events, collected over the period from August 4, 2008 till February 14, 2010. A substantial fraction of the events is produced by emission from diffuse and point sources along the plane of the Galaxy. In our analysis of extragalactic sources we exclude the region $|b| < 10^\circ$ from the point source search. This leaves 2603 photons available for the analysis.

To identify significant point sources we first selected clusters of three and more events within circles of the radius 0.1°, corresponding to the 68% containment radius of the LAT point spread function at energies above 100 GeV [3]. For each cluster we calculated the probability to find the observed number of events within the angular resolution circle by chance. To do this, we calculated the overall number N_{10} of events within a circle of 10 degrees radius around the cluster. The chance probability to find a second event within a 0.1° around the first event is $p = (1 - \cos(0.1^\circ))/(1 - \cos(10^\circ)) \simeq 10^{-4}$. The chance probability to find a cluster of at least $K_{0.1}$ events within a circle of the radius 0.1° is then $P(N_{10}, K_{0.1}) = \sum_{k=K_{0.1}-1}^{\infty} p^k (N_{10}-1)! / (N_{10}-k-1)!k!$

The chance probability $P_{100-300}$ of finding clusters of $K_{0.1} \geq 3$ events in the 100-300 GeV energy band is less than 10^{-5} everywhere in the extragalactic sky. The list of $K_{0.1} \geq 3$ excesses found at Galactic latitudes $|b| > 10^\circ$ is given in Table 1. In the same table we also give the number of γ-rays within the circle of the radius 0.2°, which corresponds to the 95% containment radius of LAT PSF above 100 GeV. In principle, the estimate of the chance probability of finding a cluster of ≥ 3 photons in the background events could be improved if known *Fermi* sources are removed from the background. However, the only $< 10^2$ photons with energies above 100 GeV could be associated to the known *Fermi* sources ([199]), which

[3] `http://www.slac.stanford.edu/exp/glast/groups/canda/archive/pass6v3/lat_Performance.htm`

	Name	RA	DEC	$K_{0.1}$	$K_{0.2}$	$P_{100-300}$
1	3C 66A	35.67	43.06	4	5	$< 5 \times 10^{-7}$
2	**IC 310**	**49.14**	**41.30**	**3**	**3**	6×10^{-6}
3	1ES 0502+675	77.15	67.61	3	3	7×10^{-6}
4	Mrk 421	166.11	38.20	20	24	$< 5 \times 10^{-7}$
5	PG 1553+113	238.90	11.24	3	5	$< 5 \times 10^{-7}$
6	Mrk 501	253.49	39.77	10	10	$< 5 \times 10^{-7}$
7	PKS 2005-489	302.37	-48.85	4	4	$< 5 \times 10^{-7}$
8	PKS 2155-304	329.74	-30.23	8	9	$< 5 \times 10^{-7}$

Table 1: Catalog of γ-ray sources detected by LAT at energies above 100 GeV at $|b| > 10°$.

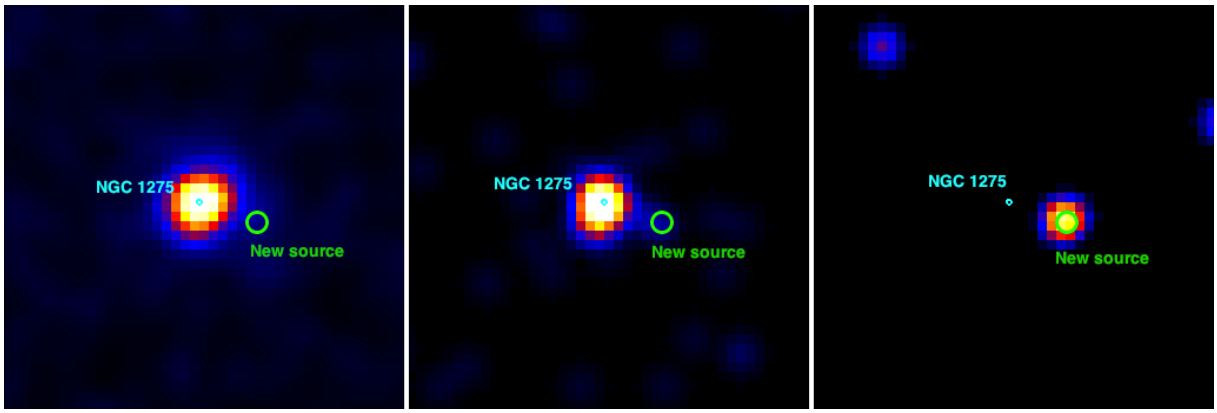

Figure 7: *Fermi* count maps of the sky region around the centre of Perseus cluster in 1-10 GeV (left), 10-100 GeV (centre) and 100-300 GeV (right) energy bands. The position of *Fermi* source 1GFL J0319.7+4130 is marked by the ellipse corresponding the uncertainty of the source position (95% confidence level). The green circle of the radius 0.1° marks the position of additional source detected at the energies above 100 GeV. The colour scale is linear, from 0 (black) to the maximal number of counts (white).

means that the correction introduced by "masking" the known sources in the background estimates would be small.

All but one detected clusters of $K_{0.1} \geq 3$ events listed in Table 1 could be identified with the known TeV blazars. The only source that does not belong to the blazar class and was not previously detected in the VHE energy band is the source #2 at $RA = 49.14 \pm 0.08$, $Dec = 41.30 \pm 0.06$.

2.1.3 VHE γ-ray emission from IC 310

The excess at the position of source #2 has three photons at energies above 100 GeV. The chance probability that such an excess is due to a chance coincidence is ruled out with probability $(1-P_{100-300}) \simeq 99.9994\%$, which corresponds to a 4.5σ significance of the source detection above 100 GeV.

Fermi images of the sky region around source #2 are shown in Fig. 7. The new source is situated approximately 0.6° to the south-west from the bright *Fermi* source 1FGL J0319.7+4130, which is identified with the radio galaxy NGC 1275 in the centre of Perseus galaxy cluster. The spectrum of the new source is harder than the spectrum of NGC 1275, so that emission from NGC 1275 dominates in the 1-10 GeV energy band, while emission from the new source dominates the signal above 100 GeV.

At energies above 30 GeV, 95% of events from a point source are contained in a circle of the radius 0.3°. This means that events from the bright source 1FGL J0319.7+4130 do not affect the signal from the newly detected source 0.6° away. Taking this into account, we included events with energies above 30 GeV in the analysis. We found two more events from the source within the 0.1° search circle in the 30-100 GeV band. To calculate the probability P_{30-100} of finding two additional events at the source position one can use modification of the expression for the 100-300 GeV band with a substitution $K_{0.1} - 1 \to K_{0.1}$ and $N_{10} - 1 \to N_{10}$. Doing this we find $P_{30-100} = 1.1 \times 10^{-4}$. The probability to find ≥ 2 additional photons

in the 30-100 GeV to a cluster of ≥ 3 photons in the 100-300 GeV band is $P_{100-300}P_{30-100} \simeq 6.6 \times 10^{-10}$ (which corresponds to 6σ for Gaussian statistics). Equivalently, the combined probability to find a 3.9 and 4.5σ excess in the two bands is $\simeq 2 \times 10^{-8}$, which corresponds to the significance of source detection at the level of 5.6σ (integrating the probability density outside constant likelihood contour for Gaussian statistics).

In order to verify the detection of the source with *Fermi*, we performed a standard Fermi analysis[4] for the sky region containing IC 310. In this analysis we used photons of the Pass 6 diffuse class with energies between 10 GeV and 300 GeV, collected from a circular area with a radius of 5 degrees around the position of IC 310. We included all sources mentioned in the Fermi first year catalogue ([12]) for this region of the sky. All the sources had freely varying normalizations and spectral indices. We assumed that the spectra of all the sources included in the likelihood analysis had power-law shape.

The likelihood analysis has resulted in the detection of IC 310 with the Test Statistic (TS) ([179]) value of 53, which corresponds to approximately 7σ source detection significance and is compatible with the 6σ source detection significance found from the direct photon counting above 30 GeV. Figure 8 shows the map of TS values generated with *gtlike* tool by varying the position of the source on the grid of 12 by 12 positions with a 0.1 degree step. The uncertainty of the source position found from the TS map is also compatible with the one found from the direct photon counting.

Figure 9 shows a comparison of the Fermi image above 100 GeV with the images of the same region of the sky in X-ray (*ROSAT* all sky survey[5]) and radio (WENSS survey [234]) bands obtained through the SkyView interface[6]. The radio and X-ray source at the position of the new γ-ray source is the galaxy IC 310, which is a part of Perseus cluster. There are no other bright radio or X-ray sources within the 0.1° degree circle around the position of the γ-ray source. This provides an unambiguous identification of the source with IC 310.

In order to estimate the flux from the source in the 30-300 GeV energy range, we calculated the exposure of *Fermi/LAT* in the direction of the source in this energy band with the *gtexposure* tool. Collecting the photons from the 95% containment circles of the energy-dependent point spread function for the front and back-converted photons ([14]), we find the estimates of the source flux in two energy bins, 30-100 GeV and 100-300 GeV are $F_{30-100} = 2.3^{+2.3}_{-1.2} \times 10^{-11}$ erg/(cm^{2}s) and $F_{100-300} = 1.4^{+1.1}_{-0.6} \times 10^{-11}$ erg/(cm^{2}s), respectively. These estimates are shown in Fig. 10 together with the multi-wavelength data on IC 310 collected from the NASA Extragalactic Database[7].

At energies below 30 GeV, the signal from NGC 1275 could give a non-zero number of photons at the position of the new source. In order to estimate the background at the source position we adopted the following procedure. We have chosen three "background" circular regions of the radius 0.3° situated at the same angular distance from NGC 1275 as the new source, but at the position angles 90°, 180° and 270°, with respect to the direction from NGC 1275 toward the new source. The signal of NGC 1275 should give approximately the same number of counts in the three "background" regions and in the "source" region, which we choose to be a circle of the radius 0.3° around the source position. We found that the signal in the source circle is compatible at $\leq 3\sigma$ level with the signal in the background regions in the energy bins 1-3 GeV, 3-10 GeV and 10-30 GeV, see Fig. 10.

2.1.4 Discussion

Known VHE γ-ray loud Active Galactic Nuclei (AGN) are divided into several classes. Most of the sources are BL Lacs, which are relativistically beamed versions of Fanaroff-Riley type I radio galaxies. Two of the detected sources are the nearest FR I radio galaxies themselves (M87 and Cen A). One source, 3C 279, belongs to the Flat Spectrum Radio Quasar (FSRQ) class. Unless IC 310 proves to be a weak BL Lac type object, the detection of VHE γ-ray emission from a head-tail radio galaxy provides a new class of extragalactic VHE γ-ray sources. If the interpretation of the source as a weak BL Lac ([232]) is adopted, the source still has unusual properties due to its unusual for BL Lacs radio morphology and host galaxy (lenticular, instead of a giant elliptical) ([207]).

[4] `http://fermi.gsfc.nasa.gov/ssc/data/analysis/scitools/`
[5] `http://www.xray.mpe.mpg.de/cgi-bin/rosat/rosat-survey`
[6] `http://skyview.gsfc.nasa.gov/`
[7] `http://nedwww.ipac.caltech.edu/`

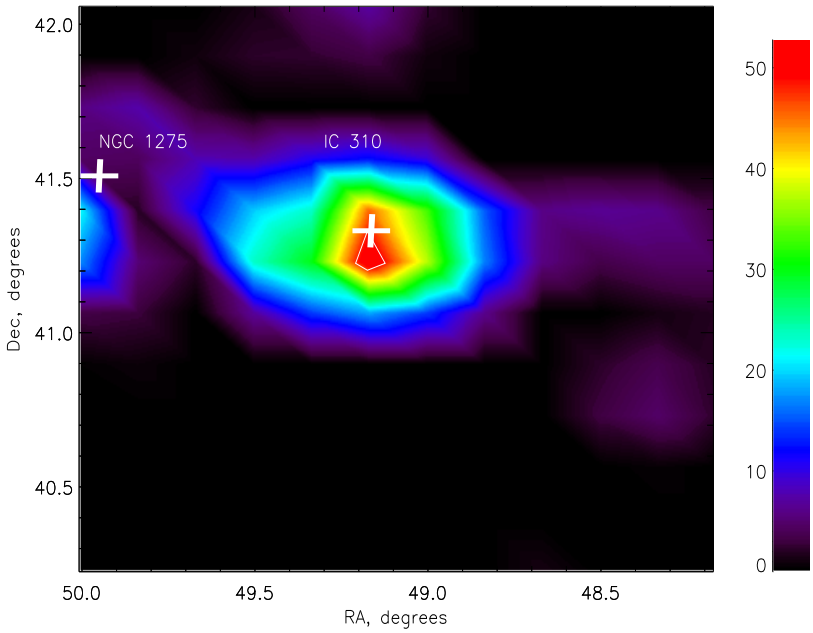

Figure 8: Map of the TS values for an additional source near NGC 1275 at energies above 10 GeV. The white contour corresponds to the 95% uncertainty of the source position.

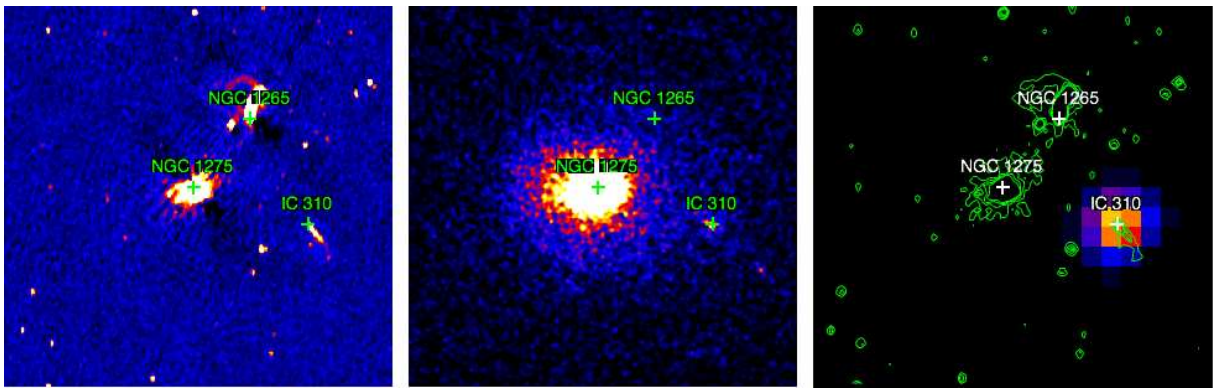

Figure 9: Image of Perseus galaxy cluster in radio band from WENSS sky survey (left), in the X-ray band from the *ROSAT* all sky survey (middle) and the *Fermi* image in the 100-300 GeV energy band (right). The green contours on the right panel correspond to the radio image from the left panel.

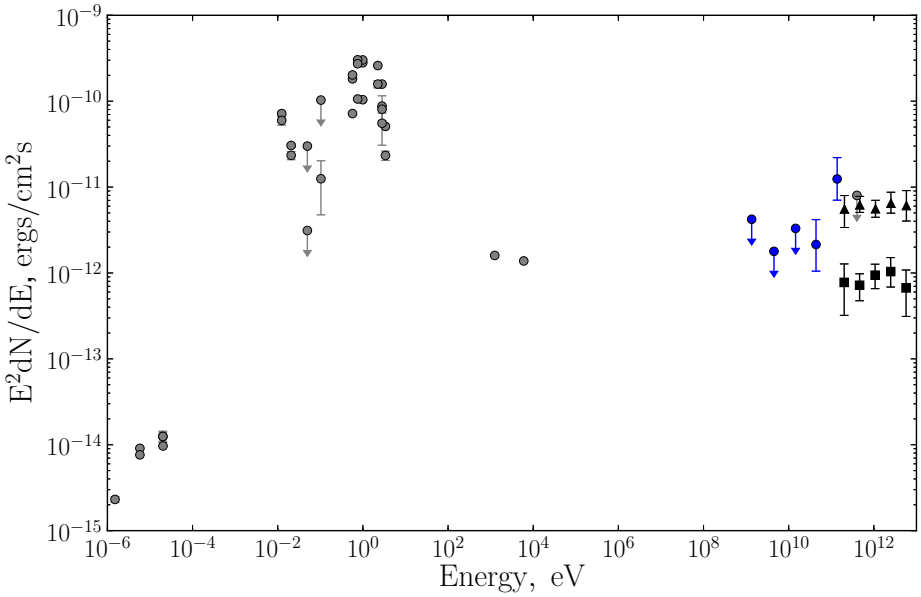

Figure 10: Spectral energy distribution of IC 310. Grey points are taken from NED, black points are MAGIC measurements from [261] for the high (triangles) and low (squares) flux states. Blue points are *Fermi* measurements (this work).

In FR I radio galaxies and BL Lacs the VHE γ-ray emission is most probably produced in the innermost part of the jet that is ejected by the supermassive black hole. For IC 310, it is not clear a priori if the γ-ray emission is powered by the same mechanism. An alternative possibility is that γ-rays are produced at the bow shock formed in interaction of relativistic outflow from the fast moving galaxy with the intra-cluster medium. In this respect, the IC 310 – Perseus cluster system might be similar to a much smaller scale PSR B1259-63 system, in which γ-ray emission is produced at the bow shock formed in interaction of relativistic outflow from a pulsar moving through a dense wind of a companion star ([256]).

Angular resolution of γ-ray telescopes is only marginally sufficient to resolve the bow shock surface in the IC 310 – Perseus cluster system. The angular length of the "tail" of the bow shock visible in the radio band is $\sim 15'$. The uncertainty of the *Fermi* source position is $\sim 4'$, which is smaller than the length of the tail. The *Fermi* data indicate that most of the γ-ray emission is produced in the "head" part of the source (see Fig. 9). At the same time, the *Fermi* angular resolution is not sufficient to distinguish between emission from the "head" of the bow shock and the emission from the base of the jet near the supermassive black hole, which powers the source activity.

The crucial test, which would allow to distinguish between the two mechanisms would be the (non) detection of variability of γ-ray emission from the source. Indeed, in the BL Lac type models the γ-ray emission is expected to be variable at different time scales, down to the time scale of the light-crossing of the central supermassive black hole. On the other hand, if the observed γ-ray emission is produced at the bow-shaped contact surface between the AGN outflow and the intra-cluster medium, the γ-ray source has $\sim$kpc scale size. This means that the γ-ray emission could not be variable on time scales much shorter than $\sim 10^3$ yr.

Variability of the γ-ray signal from IC 310 could not be studied with *Fermi*, which has detected only five γ-rays from the source at energies above 30 GeV. We verified that the five detected events did not come within a narrow time window, which would indicate the possibility of a strong flare from the source.

The presence or absence of the variability of the VHE γ-ray emission from IC 310 could be readily verified by observations with ground based γ-ray telescopes. A previous observation of the region around Perseus cluster with Whipple telescope has resulted in an upper limit one the source flux ([220]). However, this upper limit is comparable with the *Fermi* measurement of the source flux, so no conclusion about the presence or absence of long-term variability of the source could be drawn from the comparison of Whipple and *Fermi* observations. It is clear that observations of the source with the new generation

of ground-based γ-ray telescopes VERITAS or MAGIC (the source is in the northern hemisphere, not easily accessible for HESS) would give much higher signal statistic at energies above 100 GeV, so that the hypothesis of the flux variability could be easily tested. Indeed, following the discovery of IC 310 above 100 GeV with *Fermi*, the detection in the same energy band was confirmed by the MAGIC telescope ([170]). Recent observations with MAGIC revealed that the source is variable on daily time scales, suggesting that the γ-ray emission of IC 310 is of a blazar nature ([261]).

From Fig. 9 it is immediately clear that not every head-tail radio galaxy in the Perseus cluster emits in the VHE γ-ray band at the *Fermi* sensitivity level. The image of the cluster, shown in this figure, includes another prototypical head-tail galaxy, NGC 1265. This source is clearly identified in the radio band, but, contrary to IC 310, does not show significant X-ray and VHE γ-ray emission. A comparison of the physical parameters of IC 310 and NGC 1265 (e.g. velocity through the intra-cluster medium, overall power of relativistic outflow etc.) could help to clarify the conditions under which particle acceleration and VHE γ-ray emission in this type of sources occurs.

2.2 High Galactic latitude Fermi sources of gamma rays with energies above 100 GeV

2.2.1 Introduction

The all-sky search of the point sources above 100 GeV, presented in section 2.1, became possible owing to the large field of view of the Fermi/LAT and its small background above this energy. This search resulted in eight significant excesses with at least three photons within a 0.1° circle corresponding to the 68% containment radius of the point spread function (PSF) of the LAT. Seven excesses were associated with known VHE γ-ray sources, while the remaining one was identified with the head-tail radio galaxy IC 310. Detection of IC 310 in the VHE band was later confirmed by the MAGIC telescope ([170]). Owing to the moderate collection area of *Fermi*, only the brightest VHE γ-ray sources were detected individually in the *Fermi* VHE γ-ray sky survey. All other known VHE γ-ray sources at Galactic latitudes $|b| \geq 10^\circ$ gave ≤ 2 photons within the LAT PSF circle and could not be found from the analysis of the data above 100 GeV alone.

A complementary method for identifying the sources of $E \geq 100$ GeV photons detected by *Fermi* is to use prior knowledge of source positions on the sky and to verify which of the already known sources could have produced the highest energy γ-rays detected by the LAT telescope. In other words, sources of $E \geq 100$ GeV γ-rays could be identified also via cross-correlation of arrival directions of the $E \geq 100$ GeV γ-rays with the source positions on the sky. This approach to the identification of the sources was previously applied to the analysis of EGRET data above 10 GeV by [86] and [120].

Here we perform the cross-correlation analysis of the arrival directions of γ-rays with energies above 100 GeV detected by *Fermi* at Galactic latitudes $|b| \geq 10^\circ$ with the first year *Fermi* source catalogue ([12]). Our analysis results in a catalogue of 50 high Galactic latitude sources that correlate with the arrival directions of 100 GeV $\leq E \leq$ 300 GeV γ-rays within a 68% containment circle of LAT PSF. Among these 50 sources, seven sources that correlate with ≥ 3 VHE γ-rays (considered previously in Sect. 2.1; see also [198]) are detected above 100 GeV with significance $\geq 8\sigma$. Six sources that correlate with two photons are detected with a significance of around $4 - 5\sigma$. Each individual source that correlates with just one VHE γ-ray has a significance of around 3σ in this energy band; the overall significance of the detection of the entire source set is very high. The chance coincidence probability of $E > 100$ GeV γ-ray arrival directions to correlate with the source positions is $< 10^{-40}$ (excluding the seven high significance sources from the previous Section), which corresponds to the significance of detection of the entire set of $50-7 = 43$ sources $> 13\sigma$. The sources correlating with only one $E > 100$ GeV photon should be considered as "VHE source candidates". A simple analysis indicates that most of the sources contributing to the correlation signal are real VHE γ-ray sources, only three of them are expected to be false detections. Taking into account that most of the sources in the list are BL Lac type objects, we extend our cross-correlation analysis to the catalogue of BL Lacs [272] and find eight more sources that correlate with the arrival directions of 100 GeV $\leq E \leq$ 300 GeV γ-rays and are not listed in the first year *Fermi* catalogue. For completeness, we list sources from the first year *Fermi* catalogue for which the $E \geq 100$ GeV γ-rays are found within a circle of the radius at which the correlation signal is the strongest. This radius is somewhat larger than the 68% containment circle of LAT PSF. There are 25 sources of this kind, six of them are expected to

be false detections because of the chance coincidence of the arrival direction of the VHE γ-ray with the source position. For energies $E > 300$ GeV, we found correlations with four known sources, one possible new source and one false detection.

2.2.2 Data selection and data analysis

For our analysis, we use the LAT data collected in the period between August 4, 2008 and June 25, 2010. The data were filtered using the *gtselect* tool provided by Fermi Science Tools[8], so that only Pass 6 Clean γ-ray events (`evcls=3` filter for the Pass 6 dataset) with energies above 100 GeV were retained in the analysis. The resulting list of photons has 6376 events. A fraction of the $E \geq 100$ GeV photons comes from directions close to the Galactic plane, which is a source of significant diffuse γ-ray emission even at photon energies higher than 100 GeV. Presence of strong diffuse emission complicates the analysis of the point source contribution. Taking this into account, we consider only photons coming from Galactic latitudes $|b| \geq 10^\circ$. This cut on the Galactic latitude leaves 4086 photons for the analysis.

For energies $E < 300$ GeV, photons are thought to be clearly distinguishable from cosmic rays in *Fermi*, while at $E > 300$ GeV (`evcls=3`) the sample contains an unknown number of misidentified cosmic rays ([57]). We therefore split the data in two energy bins with a separation energy of $E = 300$ GeV. There are 3186 photons with energies 100 GeV $\leq E \leq 300$ GeV, for which we perform our main analysis in the following sections, and there are in addition 900 photons with energies $E > 300$ GeV, which we discuss separately in Section 2.2.6[9].

The set of photons considered in the analysis includes the list of photons studied in the previous Section (see also [198]). Here we exclude the high-confidence sources of VHE γ-rays identified in Sect. 2.1. We also exclude 75 γ-ray photons associated with these eight sources from the *Fermi* $E \geq 100$ GeV photon list, i.e. found within 0.2 degrees around these sources. Otherwise, these sources would dominate the correlation signal. Nevertheless, we include the high-confidence sources in the final source list given in the Table 2, to obtain a complete catalogue of sources of VHE γ-rays found by *Fermi*. The final photon list used in the analysis includes 3111 photons with $|b| \geq 10^\circ$.

Photons detected by *Fermi*/LAT are divided in two types – *front*- and *back*-converting. Photons that pair-convert in the top 12 layers of the tracker are classified as front-converting, and are otherwise back-converting ([15]). At the same energy, front-converting photons have a somewhat sharper PSF ([230]). We take this into account by considering the sets of 1179 front- and 1934 back-converted photons separately in our correlation analysis.

If the sky region around the source is not too crowded, the point spread functions of individual *Fermi* sources do not overlap at the energies above $\sim$ 1 GeV. At high Galactic latitudes, the strength and complexity of the diffuse Galactic γ-ray background at energies above 1 GeV is far lower than the low-latitude / low-energy background. We calculate the spectra of the sources using two methods, one the unbinned likelihood analysis performed using the *gtlike* tool in narrow energy bins (see `http://fermi.gsfc.nasa.gov/ssc/data/analysis/scitools/likelihood_tutorial.html`) and the other using the aperture photometry method for the same energy bins. In each case, we verify that the two analysis methods provide consistent results. The aperture photometry method is most useful at the highest energies, at which the photon statistics is low. In this method, we first calculate for each source and each energy the number of source counts within a circle of the radius equal to the 95% containment circle of the LAT PSF and calculate the LAT exposure within this circle using the *gtexposure* tool. The errors in the measurements are calculated based on a Poisson distribution, which provides the correct description of the data at low photon statistics. To estimate the diffuse sky background at the position of the source, we calculate the number of background counts in a ring with the outer radius 3° and the inner radius equal to the 95% containment radius of the LAT PSF, centred on the source. We verified that the results obtained using such an intuitively simple spectral extraction procedure are consistent with those obtained via spectral extraction using likelihood analysis in narrow energy bins and/or likelihood analysis in the wide energy range using a specific broad-band spectral model.

[8] http://fermi.gsfc.nasa.gov/ssc/data/analysis/

[9] For the method discussed below, it does not matter whether the background consists of photons or misidentified cosmic rays. We are grateful to I.Tkachev and P.Tinyakov, who pointed out that we can use photons with $E > 300$ GeV in our analysis.

2.2.3 Correlation between arrival directions of $E \geq 100$ GeV photons and sources from the first year *Fermi* catalogue

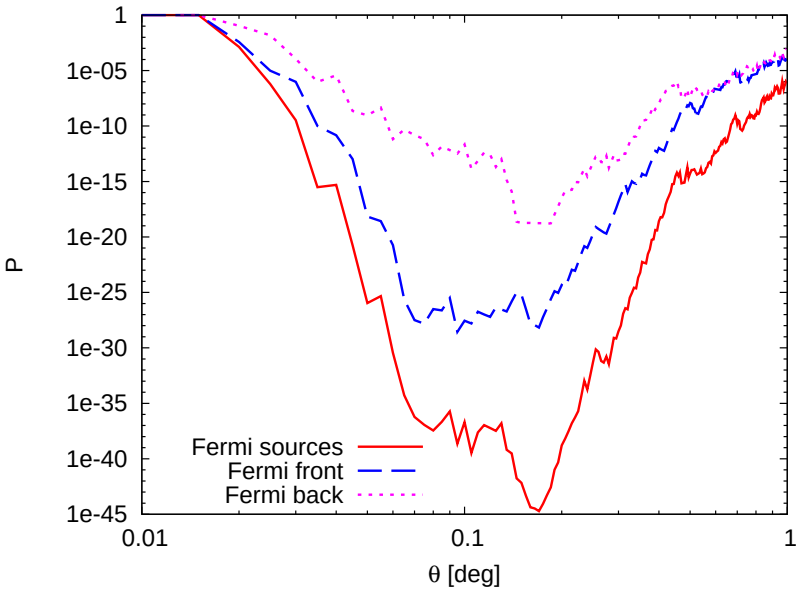

Figure 11: Dependence on the chance probability of correlation between arrival directions of $E \geq 100$ GeV photons and positions of *Fermi* sources as a function of the radius of the search circle. Solid curve corresponds to all photons. Dashed and dotted curves correspond to, respectively, front- and back-converted photons.

To find sources of $E \geq 100$ GeV γ-rays that cannot individually be recognized in the *Fermi* data in this energy band, we apply a method similar to the one discussed in [86] and [120]. Using this method, sources producing just a few photons could be identified. A fraction of identified sources might be false detections because of a chance coincidence of the source position with the arrival direction of a background photon. The fraction of positive-to-false detections could be readily estimated. Real sources should largely outnumber the false source detections. This makes the list of sources contributing to the correlation a valuable "input catalogue" for the observations with ground-based γ-ray telescopes that are more sensitive than *Fermi* in the VHE γ-ray band, but, in contrast to *Fermi*, do not have all-sky survey capabilities.

As a first choice, we took the first year *Fermi* catalogue [12] as an input catalogue for the correlation analysis. The catalogue contains 1451 sources, 1043 of which are objects with $|b| \geq$10 degrees. Removing seven confirmed VHE γ-ray sources from the list from the Sect. 2.1 (IC 310 is not in the *Fermi* catalogue), we obtain an input catalogue of $N_{\rm source} = 1036$ sources.

The probability that a γ-ray photon originates within a given distance θ from one source in the catalogue is estimated as the ratio of the area of the circle of radius θ to the part of the sky at $|b| \geq 10^\circ$

$$p_1 = \frac{\pi\theta^2}{4\pi(1-\cos(80^\circ))} \simeq 9.2 \cdot 10^{-7} \left[\frac{\theta}{0.1^\circ}\right]^2. \quad (1)$$

The total probability of a photon originating within an angle θ of one of the catalogue sources is then

$$p = N_{\rm source} \cdot p_1 = 9.5 \cdot 10^{-4} \left[\frac{N_{\rm source}}{1036}\right] \left[\frac{\theta}{0.1^\circ}\right]^2. \quad (2)$$

The probability that K or more photons from $N_\gamma = 3111$ γ-rays come within the angle θ from any of the sources in the catalogue by chance is given by the binomial probability

$$P(\theta) = \sum_{k=K}^{N_{tot}} p^k (1-p)^{N_\gamma - k} \frac{N_\gamma!}{(N_\gamma - k)!k!}. \quad (3)$$

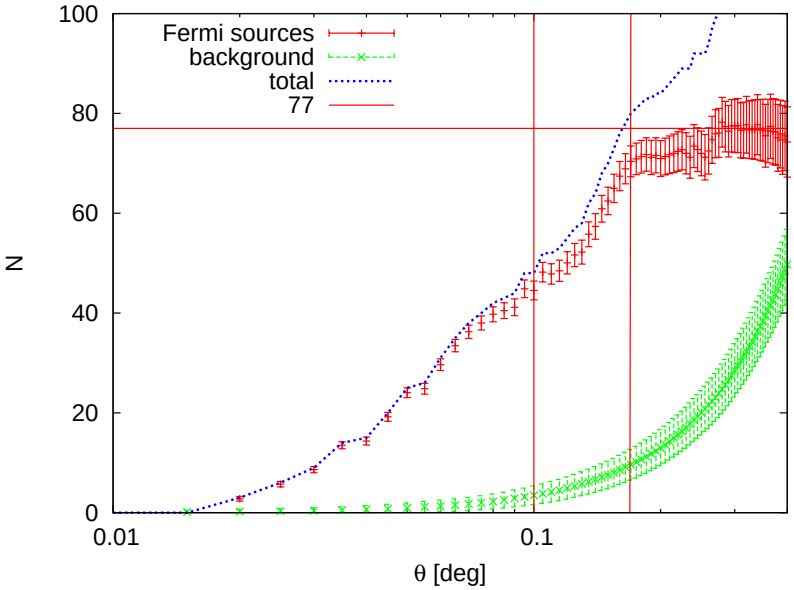

Figure 12: Number of events that come from *Fermi* sources as a function of the radius of the search circle (red data points). Error bars indicate fluctuations in the background when determining the signal from the sources. Average number of background photons is shown with green line. Vertical line at 0.1 degree is the radius of the 68 % containment circle of *Fermi* PSF. The vertical line at 0.17 degree shows the position of the dip in the probability shown in Fig. 11. The horizontal line indicates the asymptotic number of photons from all the sources.

In Fig. 11, we plot this probability as a function of angle θ. The probability, that our association of the arrival directions of the gamma rays with energies above 100 GeV with the positions of *Fermi* sources is by chance, we estimate to be $P < 10^{-45}$, i.e. the chance coincidence hypothesis is firmly ruled out.

The function $P(\theta)$ has two minima at around 0.1 degrees and 0.17 degrees. This is explained by the difference in the precision, with which the arrival direction is determined, for the front and back converted γ-rays. To verify this, we divide the whole photon list into two parts corresponding to the front and back converted γ-rays and plot the contributions of those photons separately. From Fig. 11, one can see that the minimum at 0.1 degree is due to front photons, while the minimum at 0.17 degrees is due to both front and back photons.

In Fig. 12, we plot the number of source photons with arrival directions within the angle θ from the catalogue of Fermi sources and compare it to the expected number of background events within the same distance from the sources. To estimate the number of background events, we used two alternative methods. First, we estimated the expected background near each source counting all photons within 10 degrees from it and estimating the fraction of photons that originate within the angle θ. This method can be used only for $\theta \lesssim 0.5°$. For $\theta \gtrsim 0.5°$, circles around the *Fermi* sources cover a significant fraction of the sky and overlap. In the second method, we estimated the background by generating 3111 photons in the sky outside the Galactic plane $|b| > 10°$. We followed the *Fermi* exposure which had been estimated using the *gtexposure* tool by keeping Galactic b-values of events and generating randomly l-values. This takes into account the remaining contribution of the Galaxy for $|b| > 10°$. After that, we average over many Monte Carlo simulations. Both methods gave similar results for small angles.

Vertical lines in Fig. 12 show the angular positions of the two minima of probability seen in Fig. 11. The minima correspond to the places where the steep rise in the number of signal events changes to a plateau. The asymptote of the distribution of signal counts at large θ gives an estimate of the total number of γ-rays contributing to the correlation. One can see that only ~ 77 out of 3111 events come from known *Fermi* sources. 48 for these 77 events are displaced by less than 0.1° from the catalogue source position. In this circle, one expects only $N_{B,\,0.1} \simeq 3$ background events. No more than seven background photons are expected at the 95% confidence level and no more than nine background photons

are expected at the 99.5% confidence level. The number of events contributing to the correlation within $\theta = 0.17^\circ$ circle is $N_{S,\ 0.17} \simeq 71$, while the expected number of background events is $N_{B,\ 0.17} \simeq 7.7$ (13 at the 95% confidence level, 15 at the 99% confidence level).

2.2.4 Catalogue of extragalactic VHE γ-ray sources

The list of sources contributing to the correlation signal within $\theta = 0.1^\circ$ is given in Table 2. There are $N_{\mathrm{Source},\ 0.1} = 50 - 7 = 43$ sources, if the sources from the list from Sect. 2.1 are excluded. For $N_\gamma = 3111$, only $p \cdot N_\gamma \simeq 3$ photons on average can be at the distance $\theta \leq 0.1^\circ$ from a catalogue source by chance. This means that 3 out of 43 new VHE γ-ray sources listed in Table 2 are expected to be false detections (and no more than 7(9) sources are false detections at the 95%(99.5%) confidence level).

It is not possible to know in advance which of the 43 sources from Table 2 are false detections. In principle, the ten sources that have more than one photon within the 95% containment circle of the LAT PSF are not expected to be false detections, because the probability that two background photons come close to the same source is much smaller than the same probability for just one background photon. Additional information that might help us to single out the false detections could be obtained by comparison of the estimate of the source fluxes, expected from the extrapolation of the measured spectral characteristics of the sources in the 1-100 GeV energy band, with the simple estimates of the flux that produces one photon at $E \geq 100$ GeV within 1.8 year exposure with *Fermi*. In principle, a false detection might be spotted if the source contributing to the correlation has low flux and/or a soft spectrum. This is illustrated in Fig. 13 where the distribution of fluxes and photon indices of the AGN from the *Fermi* AGN catalogue [11] is compared to the distribution of fluxes and photon indices of the sources from Table 2. Dashed lines show the combinations of the spectral parameters that are expected to give a fixed number of photons in the 100-300 GeV band, assuming no high-energy cut-off in the spectrum.

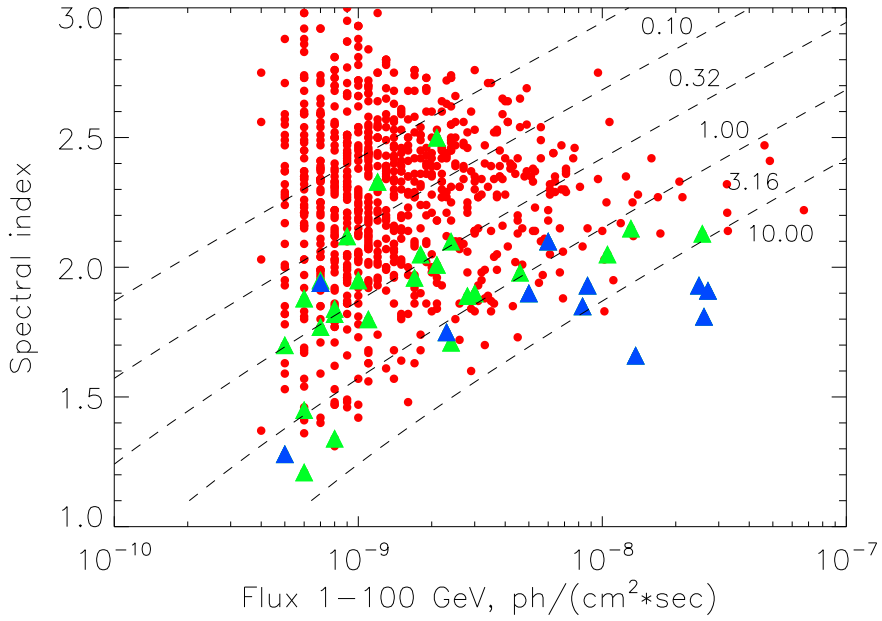

Figure 13: Comparison of the distribution of fluxes and photon indices of *Fermi* sources of $E \geq 100$ GeV γ-rays (triangles) with those of all sources from the *Fermi* AGN catalogue. Blue triangles mark known TeV γ-ray sources.

Fig. 14 shows the measurements of the source fluxes in 0.3-1 GeV, 1-3 GeV, 3-10 GeV, and 10-100 GeV for the entire 1.8 yr Fermi/LAT exposure in addition to the estimates of the source fluxes in the 100-300 GeV band based on the number of $E \geq 100$ GeV photons detected from each source.

	1FGL	N_{68} $_{30-100}$	P_{68} $_{30-100}$	N_{68} $_{100-300}$	N_{min} $[N_{95}]$	P $_{100-300}$	TS	Type[1]	Name	z
1	J0033.5-1921	6	$2.1 \cdot 10^{-14}$	1b	1	$2.3 \cdot 10^{-5}$	21	BL V	RBS 76	0.61
2	J0054.9-2455	0	–	1f		$3.2 \cdot 10^{-3}$	18			
3	J0110.0-4023	1	$1.3 \cdot 10^{-2}$	1f		$2.4 \cdot 10^{-3}$	12			
4	J0209.3-5229	2	$1.1 \cdot 10^{-4}$	1f		$3.5 \cdot 10^{-3}$	12	BL Vf	RBS 285	
5	J0213.2+2244	2	$1.6 \cdot 10^{-4}$	1b		$2.6 \cdot 10^{-3}$	13	QSO	1RXS J021252.2+22	
6	J0222.6+4302	16	$4.6 \cdot 10^{-40}$	3f1b	1	$1.4 \cdot 10^{-13}$	75	BL V	**3C 66A**	0.444
7	J0237.5-3603	3	$2.3 \cdot 10^{-7}$	1b		$2.4 \cdot 10^{-3}$	15	BL V	RBS 334	
8	J0303.5-2406	9	$2.0 \cdot 10^{-23}$	2f	[1]	$1.8 \cdot 10^{-6}$	39	BL Vf	PKS 0301-243	0.26
9	J0315.9-2609	1	$1.4 \cdot 10^{-2}$	2b		$3.5 \cdot 10^{-6}$	28	BL V	RX J0316.2-2607	0.443
10	J0316.3-6438	0	–	1b		$1.5 \cdot 10^{-3}$	13			
11	J0322.1+2336	2	$2.0 \cdot 10^{-4}$	1f		$4 \cdot 10^{-3}$	16	BL Vf	RGB J0321+236	
12	J0325.9-1649	0	–	1b		$2.5 \cdot 10^{-3}$	12	BL V	RBS 421	0.29
13	J0338.8+1313	0	–	1b		$3.1 \cdot 10^{-3}$	13			
14	J0416.8+0107	0	–	1f		$2.5 \cdot 10^{-3}$	14	BL Vf	**2E 0414+0057**	
15	J0428.6-3756	9	$3.4 \cdot 10^{-22}$	1f		$2.9 \cdot 10^{-3}$	18	BL	PKS 0426-380	1.11
16	J0505.9+6121	1	$1.9 \cdot 10^{-2}$	1f	[2]	$1.6 \cdot 10^{-6}$	21			
17	J0507.9+6738	12	$2.7 \cdot 10^{-29}$	2f2b	3	$3.8 \cdot 10^{-19}$	96	BL V	**1ES 0502+675**	0.341
18	J0543.8-5531	1	$2.0 \cdot 10^{-2}$	1f1b		$5.3 \cdot 10^{-6}$	34	BL V	RBS 679	
19	J0650.7+2503	1	$1.0 \cdot 10^{-2}$	1f		$2.2 \cdot 10^{-3}$	15	BL V	1ES 0647+250	0.203
20	J0710.6+5911	3	$2.3 \cdot 10^{-6}$	1f		$2.0 \cdot 10^{-3}$	17	BL	**RX J0710.4+5908**	0.125
21	J0721.9+7120	9	$6.3 \cdot 10^{-21}$	1f		$3.6 \cdot 10^{-3}$	13	BL Vf	**S5 0716+71**	0.3
22	J0745.2+7438	0	–	1b		$3.9 \cdot 10^{-3}$	10	BL V	1ES 0737+746	0.315
23	J0809.4+3455	0	–	1f		$2.5 \cdot 10^{-3}$	14	BL Vf	B2 0806+35	0.0825
24	J0809.5+5219	5	$3.1 \cdot 10^{-11}$	1f1b		$5.9 \cdot 10^{-6}$	25	BL Vf	**1ES 0806+524**	0.138
25	J0816.4-1311	5	$5.5 \cdot 10^{-13}$	1f		$1.8 \cdot 10^{-3}$	13	BL Vf	PMN J0816-1311	
26	J0905.5+1356	1	$1.5 \cdot 10^{-2}$	1b		$4.0 \cdot 10^{-3}$	14	QSO?	SDSS J090513.28 +140240.3	1.12
27	J0915.7+2931	3	$8.6 \cdot 10^{-7}$	1f		$2.7 \cdot 10^{-3}$	13	BL Vf	B2 0912+29	
28	J0953.0-0838	2	$9.5 \cdot 10^{-5}$	1f		$2.6 \cdot 10^{-3}$	15	BL Vf	PMN J0953-840	
29	J0957.7+5523	6	$2.1 \cdot 10^{-13}$	1b		$3.6 \cdot 10^{-3}$	12	QSO	4C +55.17	0.8955
30	J1015.1+4927	5	$2.9 \cdot 10^{-11}$	1b	2	$2.6 \cdot 10^{-7}$	35	BL V	**1ES 1011+496**	0.212
31	J1104.4+3812	57	0	14f8b	3[1]	0	494	BL V	**Mkn 421**	0.03
32	J1117.1+2013	3	$5.5 \cdot 10^{-7}$	1f		$2.9 \cdot 10^{-3}$	12	BL Vf	RBS 958	0.1
33	J1133.1+0033	0	–	1f		$2.9 \cdot 10^{-3}$	11	BL V	PKS B1130+008	1.223
34	J1217.7+3007	2	$2.0 \cdot 10^{-4}$	1b		$3.0 \cdot 10^{-3}$	8	BL V	B2 1215+30	0.13
35	J1224.7+2121	6	$7.3 \cdot 10^{-14}$	1f1b		$1.7 \cdot 10^{-6}$	31	FSRQ	4C +21.35	0.432
36	J1309.5+4304	3	$8.8 \cdot 10^{-7}$	1f		$2.9 \cdot 10^{-3}$	13	BL Vf	B3 1307+433	0.69
37	J1337.7-1255	0	–	1f		$1.5 \cdot 10^{-3}$	15	FSRQ	PKS 1335-127	0.539
38	J1437.0+5640	4	$5.7 \cdot 10^{-9}$	1f		$3.4 \cdot 10^{-3}$	17	BL	RBS 1409	0.15
39	J1555.7+1111	25	0	3f2b	1[1]	$3 \cdot 10^{-16}$	124	BL V	**PG 1553+113**	
40	J1653.9+3945	17	$1.1 \cdot 10^{-44}$	9f1b	1	$1.5 \cdot 10^{-32}$	214	BL V	**Mkn 501**	0.0336
41	J1722.5+1012	0	–	1f		$2.3 \cdot 10^{-3}$	17	FSRQ	TXS 1720+102	
42	J1744.2+1934	1	$2.1 \cdot 10^{-2}$	1b		$2.5 \cdot 10^{-3}$	13	BL V	1ES 1741+196	0.083
43	J1824.6+1013	0	–	1f		$1.9 \cdot 10^{-3}$	10			
44	J2000.0+6508	7	$2.1 \cdot 10^{-15}$	1f	[1]	$1.9 \cdot 10^{-4}$	20	BL Vf	**1ES 1959+650**	0.048
45	J2000.9-1749	1	$2.2 \cdot 10^{-2}$	1b		$4.0 \cdot 10^{-3}$	11	FSRQ	PKS 1958-179	0.65
46	J2004.8+7004	0	–	1b		$4.3 \cdot 10^{-3}$	13			
47	J2009.5-4849	7	$1.3 \cdot 10^{-15}$	4f1b	[1]	$7.5 \cdot 10^{-15}$	82	BL V	**PKS 2005-489**	0.071
48	J2158.8-3013	23	0	5f3b	1[1]	$2.2 \cdot 10^{-24}$	164	BL V	**PKS 2155-304**	0.117
49	J2314.1+1444	1	$1.8 \cdot 10^{-2}$	1f		$3.1 \cdot 10^{-3}$	13	AGN	SDSS J231405.46 +143904.6	1.319
50	J2322.6+3435	1	$2.0 \cdot 10^{-2}$	1f		$3.4 \cdot 10^{-3}$	14	BL	TXS 2320+343	0.098

Table 2: List of *Fermi* sources for which a 100 GeV $\leq E \leq$ 300 GeV photon is found within the 68% containment circle of radius 0.1°. First column: *Fermi* source ID; 2-th column: number of photons in the 68% containment circle in 30-100 GeV band; 3-th column: chance coincidence probability to find given number of photons in the 68% containment circle in 30-100 GeV band; 4-th column: number of photons in the 68% containment circle in 100-300 GeV band; "f" marks front photons, "b" marks back photons; 5-th column: number of photons in the $\theta \leq 0.17°$ circle around the source or in the 95% containment circle of the radius 0.3° (square brackets); 6-th column: chance probability to find given number of background photons within 0.1° and 0.17° [0.3°] circles around the source position; 7-th column: TS value in 100-300 GeV energy bin, found with our analysis; 8-th column: source type; 9-th column: alternative name of the source; 10-th column: source redshift. Bold marks the sources which have been previously detected in the VHE band by ground-based γ-ray telescopes. Underlined are sources detected with Fermi in 100-300 GeV band with $TS > 25$. The updated version of this table is available online at http://www.isdc.unige.ch/vhe/.

[1] BL – BL Lac type object; QSO – quasi-stellar object, AGN – active galactic nucleus, FSRQ – flat spectrum radio quasar; FR I – Fanaroff-Riley type I radio galaxy; V – also found from the correlation analysis with the BL Lac catalogue; Vf – front photon contributes to the correlation signal with the BL Lac catalogue.

	1FGL	N_{68} $_{30-100}$	P_{68} $_{30-100}$	N_{min} $_{100-300}$	P_{min} $_{100-300}$	Type	Name	z
51	J0043.6+3424	1	$2 \cdot 10^{-2}$	1f	$7.7 \cdot 10^{-3}$			
52	J0203.5+7234	0	–	1f	$7.2 \cdot 10^{-3}$	BL	CGRaBS J0203+7232	
53	J0440.6+2748	0	–	1f	$5.2 \cdot 10^{-3}$		B2 0437+27B	
54	J0442.7-0019	0	–	1f	$7.5 \cdot 10^{-3}$		PKS 0440-00	
55	J0449.5-4350	12	$6.5 \cdot 10^{-30}$	1f	$7.8 \cdot 10^{-3}$		PKS 0447-439	
56	J0536.2-3348	2	$1.6 \cdot 10^{-4}$	1f	$8.1 \cdot 10^{-3}$	BL Vf	FRBA J0536-3343	
57	J0803.1-0339	1	$1.1 \cdot 10^{-2}$	1f	$3.1 \cdot 10^{-3}$			
58	J0856.6+2103	1	$1.4 \cdot 10^{-2}$	1b	$7.8 \cdot 10^{-3}$	FSRQ	OJ 290	2.106
59	J0909.2+2310	1	$1.7 \cdot 10^{-2}$	1b	$8.3 \cdot 10^{-3}$	BL V	RX J0909.0+2311	
60	J1101.3+1009	1	$1.6 \cdot 10^{-2}$	1f	$7.7 \cdot 10^{-3}$			
61	J1112.8+3444	0	–	1b	$1.2 \cdot 10^{-2}$	FSRQ	CRATES J1112+3446	1.9556
62	J1125.5-3559	0	–	2b	$2.5 \cdot 10^{-5}$	AGN	CRATES J1125-3557	
63	J1136.9+2551	2	$1.5 \cdot 10^{-4}$	1f	$1.1 \cdot 10^{-2}$	BL V	BZB J1136+2550	0.2
64	J1154.0-0008	0	–	1b	$7.8 \cdot 10^{-3}$			
65	J1253.0+5301	1	$1.9 \cdot 10^{-2}$	1b	$8.6 \cdot 10^{-3}$	BL V	CRATES J1253+5301	
66	J1328.2-4729	3	$1.8 \cdot 10^{-6}$	1f	$5.6 \cdot 10^{-3}$			
67	J1345.4+4453	0	–	1b	$7.7 \cdot 10^{-3}$	FSRQ	B3 1343+451	
68	J1426.9+2347	16	$7.5 \cdot 10^{-43}$	2b	$2.6 \cdot 10^{-5}$	BL V	**PKS 1424+240**	0.16
69	J1428.7+4239	6	$1.3 \cdot 10^{-14}$	1b	$7.8 \cdot 10^{-3}$	BL V	**1ES 1426+428**	0.129
70	J1553.9+4952	2	$1.3 \cdot 10^{-4}$	1b	$9.8 \cdot 10^{-3}$			
71	J1923.5-2104	0	–	1f	$9.4 \cdot 10^{-3}$	FSRQ	OV -235	0.874
72	J2014.5-0047	1	$2 \cdot 10^{-2}$	1b	$7.9 \cdot 10^{-3}$			
73	J2250.1+3825	3	$1.6 \cdot 10^{-6}$	1b	$7.3 \cdot 10^{-3}$	BL V	B3 2247+381	0.1187
74	J2323.5+4211	5	$2.1 \cdot 10^{-11}$	1b	$7.0 \cdot 10^{-3}$	BL V	1ES 2321+419	
75	J2325.8-4043	1	$1.4 \cdot 10^{-2}$	1b	$8.0 \cdot 10^{-3}$	BL V	RXS J23247-4040	

Table 3: List of *Fermi* sources for which a 100 GeV $< E <$ 300 GeV photon is found within the radius $\theta = 0.17°$, but not within $\theta = 0.1°$. Notations are the same as in Table 2.

Although the significance of the detection of individual sources with 1(2) photons in the 100-300 GeV band in Table 2 is around $3\sigma(4\sigma)$, some of the sources are detected with a significance higher than 5σ in the adjacent 30-100 GeV energy band. The 5-th and 6-th columns of Table 2 show the numbers of photons and the chance coincidence probabilities derived by comparing the expected number of background photons within $\theta \leq 0.12°$ circles (corresponding to the 68% containment circle at 30 GeV) around the sources with the number of the source photons in the 30-100 GeV band. For the sources which are detected with more than 5σ significance in the 30-100 GeV band we show more detailed spectra above 1 GeV, calculated using all publicly available data of *Fermi* collected from August 2008 to June 2010 (rather than the 11 month data used for the analysis of the first year *Fermi* catalogue). One can see that for most of the sources the estimates of the source flux in the 100-300 GeV energy bin agree well with the extrapolation of the power-law spectrum from lower energies.

The maximum of the correlation signal (minimum of the chance probability) shown in Fig. 12 is achieved at the angle $\theta = 0.17°$, corresponding to the maximum correlation signal in the back-converted events. The improvement in the correlation achieved with the increase of θ from 0.1° to 0.17° means that there are more real events within the rings $0.1 \leq \theta \leq 0.17°$ around their sources, than there are background events in these rings.

Table 3 lists the sources contributing to the correlation signal within $\theta \leq 0.17°$ but not within $\theta \leq 0.1°$. The number of background events in the ring $0.1° \leq \theta \leq 0.17°$ is estimated to be 6. This implies that 6 out of the 25 additional sources listed in Table 3 might be false detections.

We note that only 16 out of 75 sources listed in Tables 2 and 3 are already known sources of VHE γ-rays detected by the ground-based γ-ray telescopes. The majority of the sources from Tables 2 and 3 are the new real sources in the VHE band. Taking into account that only 9 out of the 75 sources listed in Tables 2 and 3 are possible false detections, the *Fermi* all sky survey at the energy $E_\gamma \geq 100$ GeV reveals 75-9-16=50 new extragalactic VHE γ-ray sources. This doubles the number of already known extragalactic VHE γ-ray sources[10].

Another important point is that the $E \geq 100$ GeV γ-ray sources listed in Tables 2 and 3 are distributed over a broad range of redshifts. The "record" redshift of the VHE γ-ray source so far was $z \simeq 0.5$ for the possible detection of 3C 279 during a short several hour flare by MAGIC ([167]). In our Table 2, several sources have redshifts larger than 0.5.

[10] See http://tevcat.uchicago.edu/

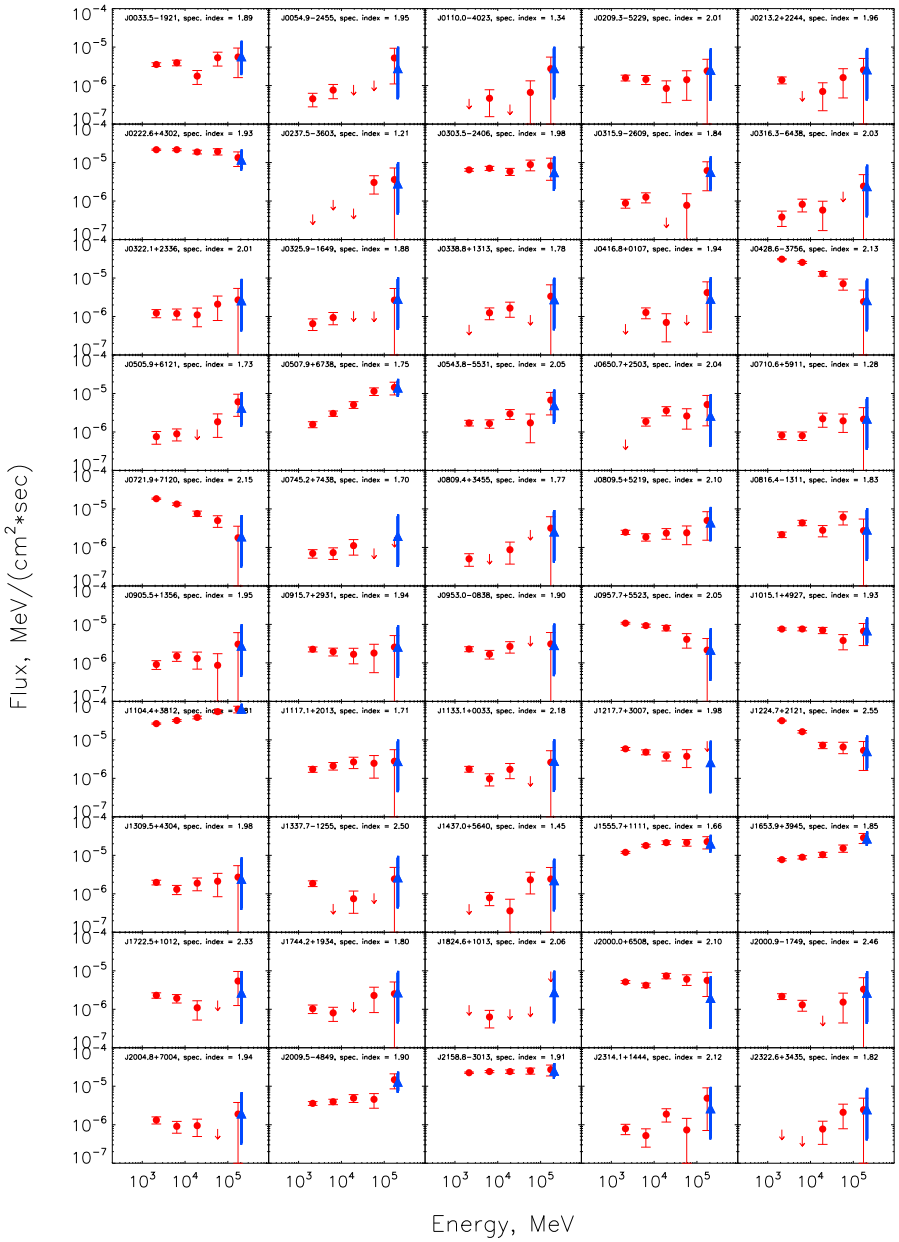

Figure 14: Comparison of the spectra of the sources from Table 2 in the 1-300 GeV band, obtained with the standard Fermi analysis procedure (red circles represent the flux measurements, red arrows - upper limits), and the estimated source fluxes in the 100-300 GeV band, obtained using aperture photometry technique (blue triangles). Aperture photometry data points in the 100-300 GeV band are artificially shifted to slightly higher energy to ensure that they are visible, and displayed with the measurements from the likelihood analysis in the same energy band.

2.2.5 Correlation between arrival directions of 100 GeV $\leq E \leq$ 300 GeV photons and sources from the 13th Veron catalogue

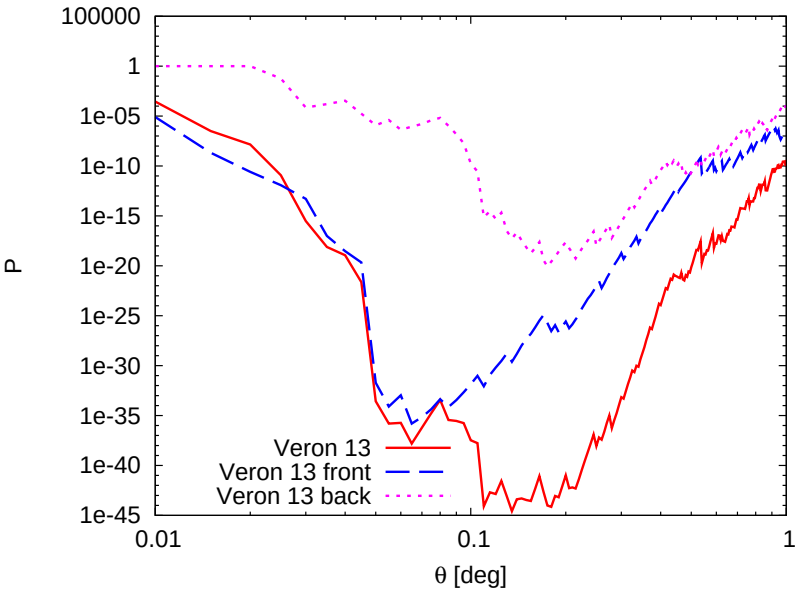

Figure 15: Dependence on the chance probability of correlation between arrival directions of 100 GeV $\leq E \leq$ 300 GeV photons and positions of BL Lacs from [272] catalogue as a function of the radius of the search circle. Notations are the same as in Fig. 11.

Most of the 100 GeV $\leq E \leq$ 300 GeV sources listed in Tables 2 and 3 are BL Lac objects. These sources are known to be characterized by relatively hard spectra in the GeV energy band ([11]). It is therefore possible that some of the VHE γ-ray emitting BL Lacs escape detection in the GeV band, while being bright VHE γ-ray sources.

To search for the VHE γ-ray emitting BL Lacs with very hard spectra, we performed a correlation analysis, similar to the one reported above for the first year *Fermi* catalogue, also for the 13th Veron catalogue of BL Lacs [272]. To select a complete sample of BL Lacs, we adopted the prescription of [120] and applied a cut to magnitude of objects $V < 18.0$, which leaves 316 BL Lacs. This set of objects includes six out of seven known VHE γ-ray sources identified in the $E \geq 100$ GeV *Fermi* data in Sect. 2.1. As in the analysis of the first year *Fermi* catalogue, we removed these objects and associated photons from analysis. We also removed the three photons associated with IC 310. This leaves $N_{\rm source} = 310$ BL Lac objects and 3111 photons.

The probability that a single photon comes by chance near one of the selected BL Lacs is $p = N_{\rm source} \cdot p_1 = 2.7 \cdot 10^{-4} \cdot (\theta/0.1^\circ)^2$. The probability that K or more photons fall within an angle θ from one of the sources is calculated using Eq. 3. Fig. 15 shows this chance probability as a function of θ. As for the analysis of first year *Fermi* source catalogue, the probability has a minimum at the angular resolution of the LAT at the energies $E \geq 100$ GeV. From our correlation analysis we find that 39 BL Lac out of 310 correlate with Fermi data within the angle $\theta \lesssim 0.17^\circ$ corresponding to the minima of $P(\theta)$ from Figs. 11 and 15.

In Fig. 16, we compare the number of source photons to the number of background photons as functions of the angular distance to the BL Lacs. The asymptotic value of the signal events $N = 54$ is reached at the angular distance $\sim 0.2^\circ$. At the angle 0.1°, 31 photons come from 28 sources, while only 0.9 of them are on average caused by the background. At 95 % C.L., there are two background photons. At the angular distance 0.17°, 47 photons come from 39 sources, and, on average, 2.6 of them correspond to the background. There are 5(6) background photons at the 95%(99%) confidence level. Eight of these 35 sources are not present in Tables 2 and 3. These seven sources are listed in Table 4. Other sources

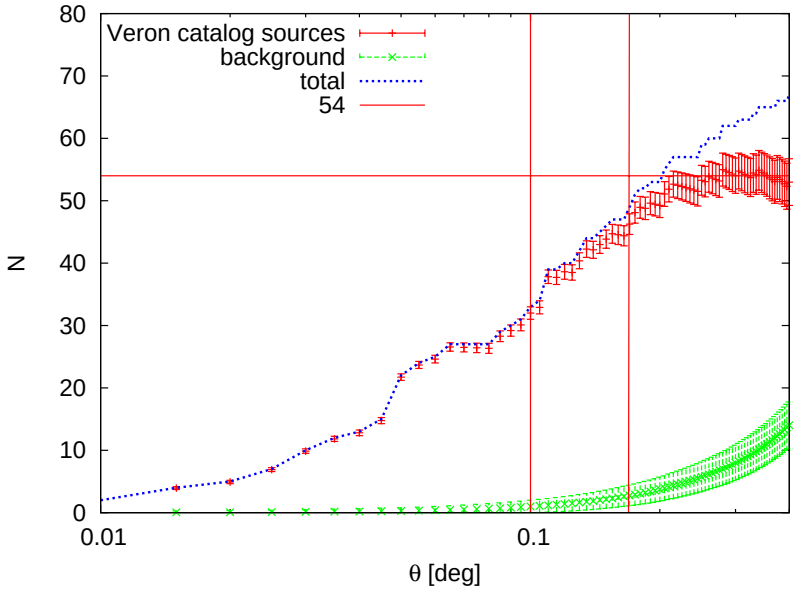

Figure 16: Number of events which come from BL Lac sources as a function of the radius of the search circle. Notations are the same as in Fig. 12.

contributing to the correlation signal in both the first year *Fermi* and [272] catalogues are marked by an "V" in Tables 2 and 3.

We also performed a special analysis with only front photons and a BL Lac catalogue. In this case, the correlation signal is maximal at $\theta \simeq 0.07^\circ$ (see Fig. 15). At this angle, there are 21 front photons, which correlate with 20 BL Lac sources. PKS 0301-243 has two photons, which can occur by chance in only $P = 10^{-7}$ cases. This means that this source is discovered by *Fermi*. Only 0.18 background photons are expected at this angle, which means that all of the 19 remaining sources are most probably real. At the 99% confidence level, two of the 20 sources might be false detections. Sixteen of these 20 sources are marked as "Vf" in Tables 2 (15 sources) and 3 (1 source) and the remaining six are those that have front photons marked "f" in Table 4.

2.2.6 Sources at energies $E > 300$ GeV

We discuss correlations between 900 *Fermi* photons with $E > 300$ GeV and the sources from the first year *Fermi* catalogue together with BL Lacs from [272] catalogue. We note that this energy is exactly in the range of sensitivity of the TeV gamma-ray telescopes.

We first consider correlations with sources from the first year *Fermi* catalogue. Using the analysis identical to the one presented in Section 2.2.3, we study correlations of $E > 300$ GeV photons with the sources within a $\theta = 0.1^\circ$ angular distance. There are four sources correlated within this angle, while only 0.7 photons are expected to be found in the direction of *Fermi* sources in the case of random coincidences. Those sources are presented in the first four lines of Table 5. All of them are known TeV sources.

We next consider correlations of photons with $E > 300$ GeV with sources from the first year *Fermi* catalogue within $\theta = 0.17^\circ$ in analogy with Table 3. There is one more source (source #5 in Table 5) which correlates with $E > 300$ GeV photons within this angle but does not correlate within $\theta = 0.1^\circ$. We expect 2.3 background events within this angle. The $E > 300$ GeV photons from the direction toward source #5 are, most probably, a random coincidence, because this source is a blazar at the redshift $z > 1$. Photons with $E > 300$ GeV cannot reach the Earth from a source at such a high redshift because of the interactions with the infra-red background.

We can finally repeat the analysis of Section 2.2.5 and consider correlations with BL Lacs from [272] catalogue. We find that there are photons correlating with four out of 317 bright BL Lac sources with

	Name	RA deg	Dec deg	$N_{0.1}$ $[N_{min}]$	z
1	**NPM1G +01.0067**	28.165	1.788	1f	0.08
2	V Zw 326	48.210	36.256	1b	0.071
3	B3 0651+428	103.682	42.799	1f	0.126
4	RXS J09130-2103	138.252	-21.054	1f[1b]	0.198
5	RXS J10162+4108	154.070	41.137	1b	0.281
6	SDSS J114023.48 +152809.7	175.098	15.469	1f	0.244
7	MS 1221.8+2452	186.101	24.607	1f	0.218
8	MS 1312.1-4221	198.764	-42.614	1f	0.105

Table 4: List of BL Lac sources from [272] catalogue for which a 100 GeV $\leq E \leq$ 300 GeV photon is found within the circle of radius 0.1° and are not the first year *Fermi* catalogue sources. Underlined source is detected by *Fermi* in 100-300 GeV band with $TS > 25$. Column 5 gives the number of photons in the circles of the radius 0.1° and 0.17° around the source ($N_{0.1}$ and N_{min}, respectively). Column 6 is the source redshift.

	Name	RA	Dec	$N_{0.1}$	N_{min}	z
1	**1ES 0502+675**	76.99	67.64	1f 1b	1b	0.341
2	**Mkn 421**	166.1	38.21	1f 3b	1f	0.03
3	**B2 1218+30**	185.3	30.18	1f	1f	0.184
4	**1ES 1959+650**	300.0	65.13	1b		0.048
5	RGB J0250+172	42.66	17.20		1b	1.1
6	SHBL J10102-3119	152.6	-31.32	1b		0.143

Table 5: List of *Fermi* and BL Lac sources from [272] catalogue for which a $E > 300$ GeV photon is found within the circle of radius 0.17°. Underlined sources are detected with Fermi at $E > 300$ GeV energies with $TS > 25$. Notations are the same as in Table 4.

magnitude $V < 18$ within $\theta = 0.1°$. Those are sources 2, 3, 4, and 6 in Table 5. In this case, only 0.27 background photons are on average expected. The only new source is the source number 6, which is more probably a real source rather than a random coincidence (with probabilities 0.73 vs. 0.27 for the two cases). At the same time, the source is located at a moderate Galactic latitude, 20°, so that the possibility that an excess at the position of the source is due to the diffuse emission from the Galaxy cannot be ruled out.

2.2.7 Comments on individual sources

High-redshift sources

Several sources in Table 2 have redshifts higher than the redshift of 3C 279, $z \simeq 0.5$, which is the furtherest known VHE γ-ray source ([167]). The study of high-redshift sources in the VHE band is interesting for the measurements of the density and cosmological evolution of the extragalactic background light (EBL) [107, 123, 152, 182, 248] and the cosmological magnetic fields [201, 205]. In this subsection, we provide some details about the high-redshift sources from Table 2.

RBS 76 at $z = 0.61$ has two photons within the distance 0.17° from the catalogue source position. It is detected with a significance of more than 4σ in the 100-300 GeV band. The source is also detected with a significance of more than 7σ in the 30-100 GeV energy band. Broad band spectrum of the source is shown in Fig. 17. The historical multiwavelength data are taken from the NASA Extragalactic Database (NED)[11].

PKS 0426-380 at $z = 1.11$ is a bright source in the GeV energy band, with the flux reaching 10^{-10} erg/cm^{2}s.

[11] http://nedwww.ipac.caltech.edu/

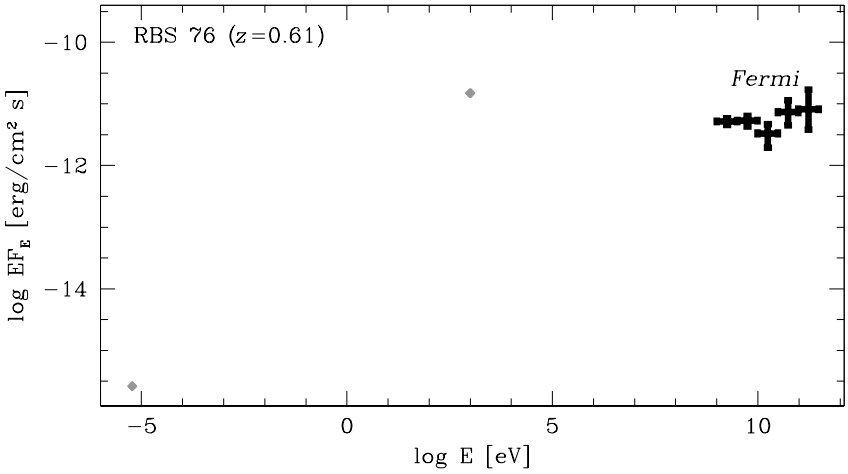

Figure 17: Broad-band spectrum of RBS 76. Grey data points are historical data from NED.

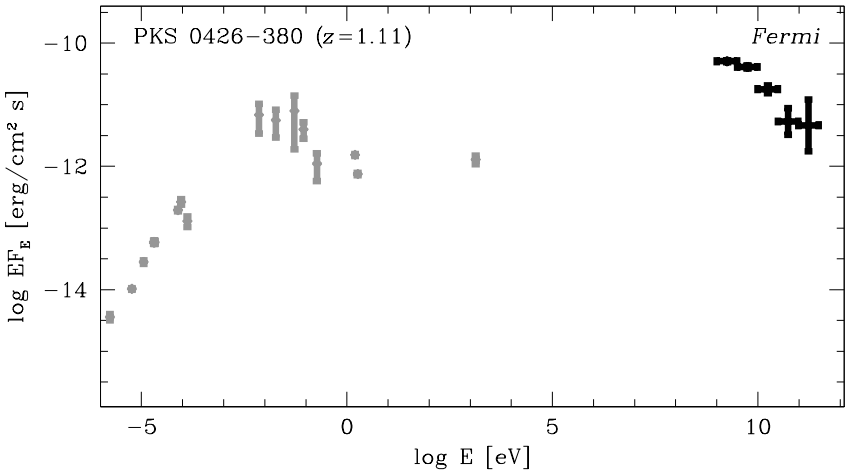

Figure 18: Broad band spectrum of PKS 0426-380. Grey data points show historical data taken from NED.

Its γ-ray spectrum is relatively soft and consistent with a power-law with photon index $\Gamma \geq 2.5$. The γ-ray measurements are compared to the multiwavelength data for the source in Fig. 18. As in the case of RBS 76, the overall spectrum of the source could be interpreted in terms of the synchrotron self-Compton or synchrotron external-Compton type models where the radio-to-optical emission is produced by means of the synchrotron mechanism and X-ray-to-γ-ray emission by inverse Compton scattering. The extremely high redshift of the source and possible presence of the high-energy cut-off in the spectrum might increase the difficulty of the source detection with ground-based γ-ray telescopes at energies significantly higher than 100 GeV.

SDSS J090513.28+140240.3 at $z = 1.12$ has a flat (E^{-2}) spectrum in the 1-300 GeV band. It was previously observed only in the optical domain. A comparison of γ-ray measurements and historical data is presented in Fig. 19. The extrapolation of the source spectrum from energies below 100 GeV agrees well with the estimated flux in the 100-300 GeV band, giving no indication of a cut-off. Despite the low statistics in the data in this band obtained with *Fermi/LAT*, this means that the source should be observable with ground-based Cherenkov telescopes.

4C +55.17 at $z = 0.8955$ also has a relatively soft spectrum in the 1-300 GeV band. The γ-ray measurements are compared to the broad-band data in Fig. 20. The source was previously detected in the

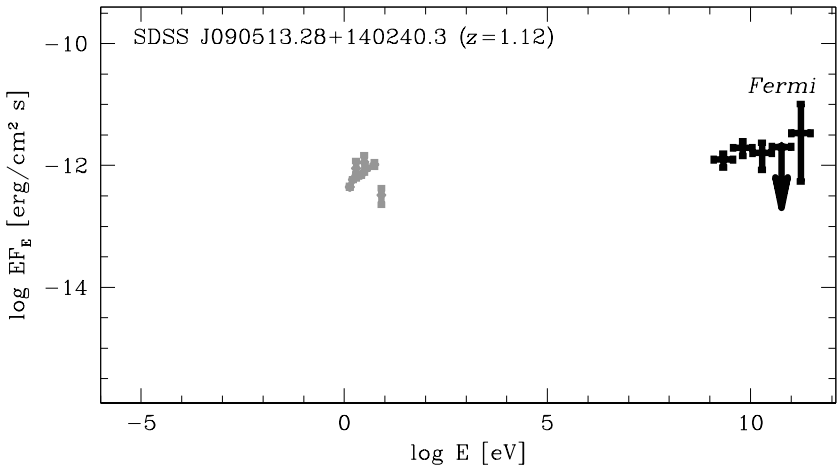

Figure 19: Broad-band spectrum of SDSS J090513.28+140240.3. Grey data points show historical data from NED.

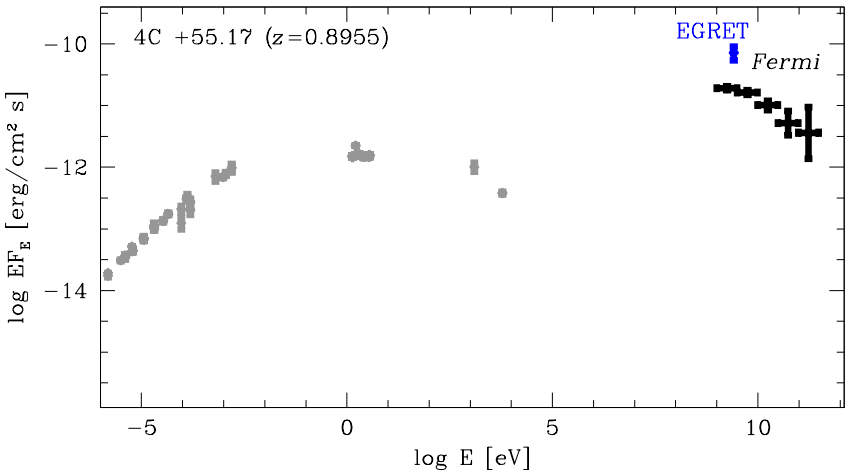

Figure 20: Broad-band spectrum of 4C +55.17. Grey data points show historical data from NED. The measurement of γ-ray flux by EGRET [262] is also shown.

0.1-1 GeV band by EGRET. There are no other sources from the first year Fermi catalogue within a distance 4° of the source. This means that an EGRET measurement most probably refers to the same blazar, rather than to a possible nearby higher flux source. A comparison of the historical EGRET measurement with the *Fermi* measurement of the source flux shows that the source is variable on a 10 yr timescale.

PKS B1130+008 at $z = 1.223$ has the second highest redshift among the sources listed in Table 2. It has an associated front-converted photon with energy 128 GeV. An estimate of the source flux above 100 GeV based on this one photon is above the extrapolation of the source spectrum from the lower energies; we refer to Fig. 21 which possibly indicates that this high-redshift source is a false detection. Otherwise, if the source spectrum is flat at energies up to 100 GeV, as indicated by the detection of the $E > 100$ GeV γ-ray, its observation with the ground-based Cherenkov telescopes should provide valuable constraints on the EBL at redshifts $z \sim 1$.

B3 1307+433 at $z = 0.69$ has a harder than E^{-2} spectrum up to the highest energies accessible to *Fermi* (see Fig. 22). The estimate of the flux based on the detected $E > 100$ GeV photon agrees well with the extrapolation of the source spectrum from lower energies. This indicates that the source should be

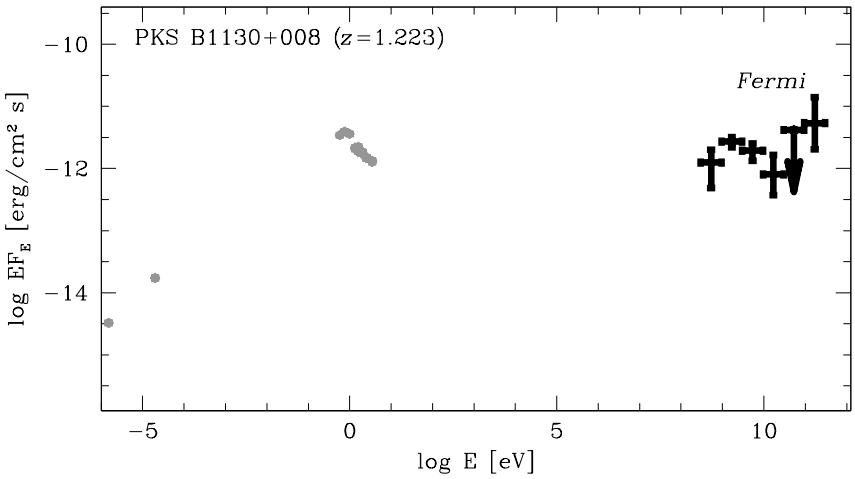

Figure 21: Broad-band spectrum of PKS B1130+008. Grey data points show historical data from NED.

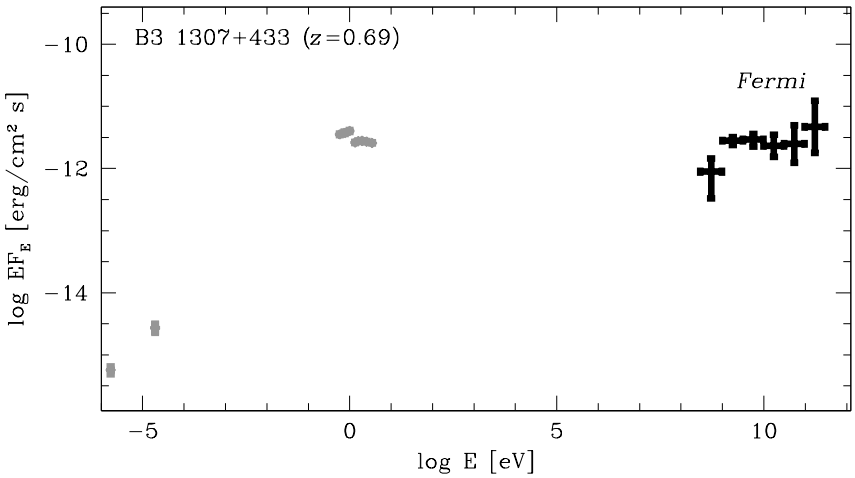

Figure 22: Broad-band spectrum of B3 1307+433. Grey data points indicate historical data from NED.

readily detectable with ground-based γ-ray telescopes, despite its high redshift.

PKS 1958-179 at $z = 0.65$ is also characterized by an excess of high-energy ($E > 30$ GeV) emission above the extrapolation of the lower energy spectrum with $\Gamma = 2.46 \pm 0.07$ reported in the first year Fermi catalogue. No photons are indeed detected from the source in the energy range 10-30 GeV (see Fig. 23). However, at the energies above 30 GeV the source is clearly identifiable in Fermi count maps (see Fig. 24). Standard likelihood analysis gives TS value $TS = 32$, which formally corresponds to $> 5\sigma$ detection in this energy range. This indicates that the source spectrum hardens at the energies above 30 GeV. Unfortunately, the statistic of the Fermi signal at the highest energies is insufficient to clarify the nature of the 100 GeV excess in the source spectrum.

BZU J2313+1444 is formally the highest redshift source in Table 2, with $z = 1.319$. The source is relatively weak. In contrast to the other high-redshift sources, the significance of source detection in the 30-100 GeV band is less than 5σ. From Fig. 25, one can see that the source spectrum does not exhibit a signature of a high energy cut-off. This implies that the source might be an ideal candidate for the study of EBL evolution with redshift.

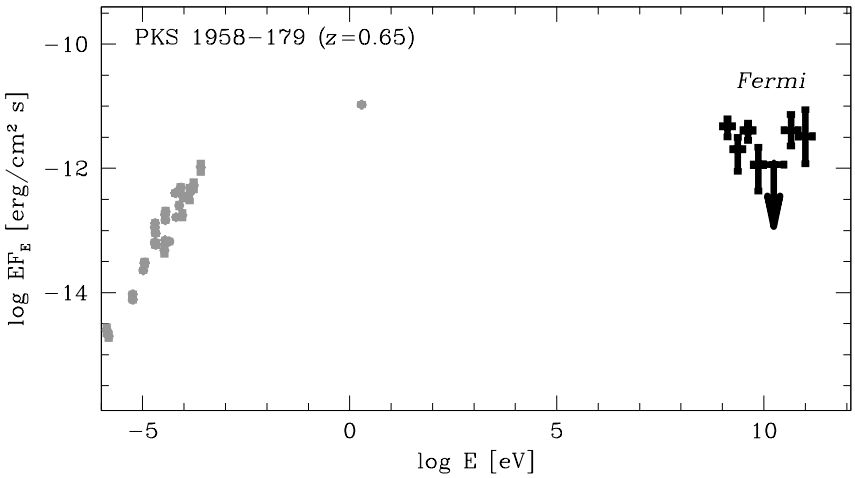

Figure 23: Broad-band spectrum of PKS 1958-179. Grey data points show historical data from NED.

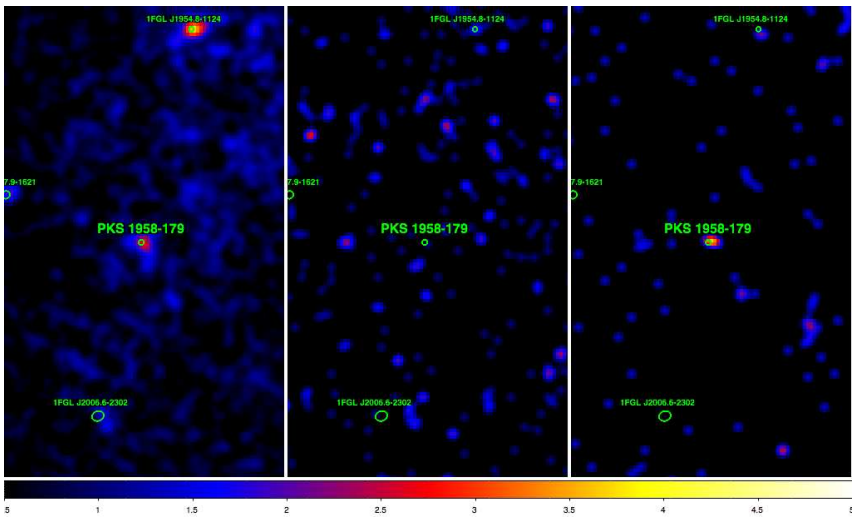

Figure 24: LAT count maps smoothed by 0.3° around the position of PKS 1958-179 in 1-10 GeV (left), 10-30 GeV (center), and 30-300 GeV (right) bands. Color scales are linear, from 0.5 to 5 counts per pixel (left panel), from 0.04 to 0.4 cts/pixel (center), and from 0.03 to 0.3 cts/pixel (right panel).

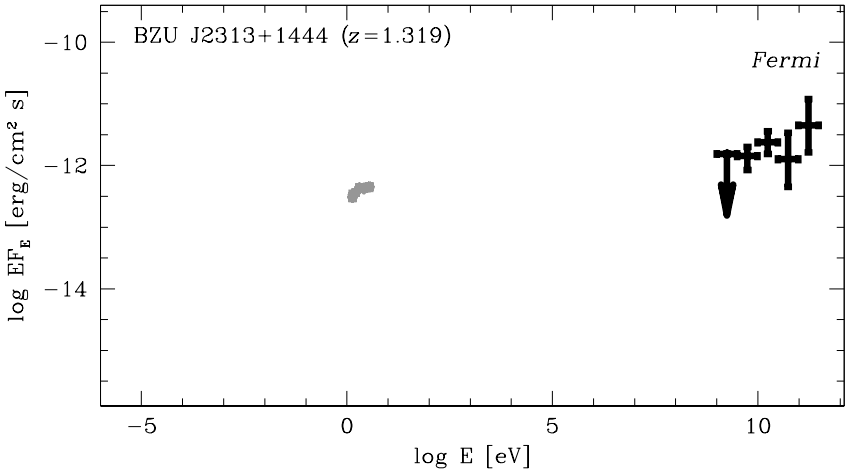

Figure 25: Broad-band spectrum of BZU J2313+1444. Grey data points show data from NED.

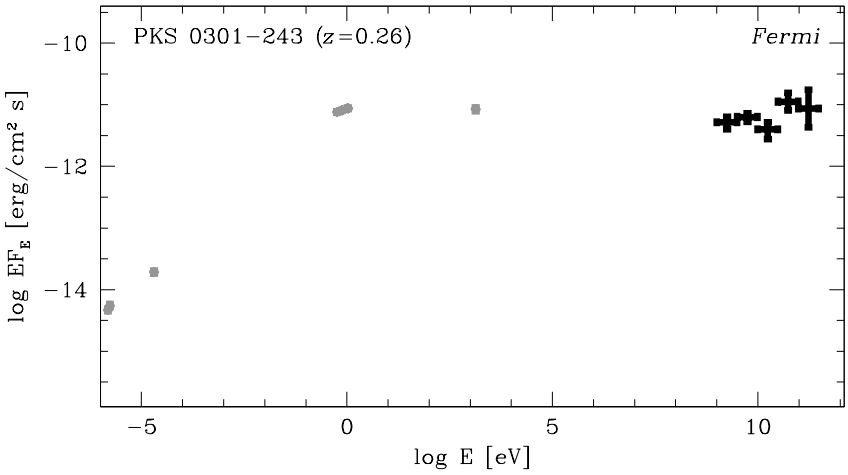

Figure 26: Broad-band spectrum of PKS 0301-243. Grey colour shows historical data from NED.

Sources detected at $\geq 4\sigma$ level at $E \geq 100$ GeV

Apart from the eight high-confidence sources at $E \geq 100$ GeV found in Sect. 2.1 and the bright high-redshift sources discussed above, several other sources in Tables 2 and 3 have detection significances higher than 4σ above 100 GeV. We list below these sources and discuss some details of their broad-band spectral energy distributions.

PKS 0301-243 at $z = 0.26$ has one back- and two front-converted photon associated with the source above 100 GeV. The back photon is within the 95% containment circle of the radius $\theta = 0.3°$. Taken together, the two photons represent a $\simeq 5.2\sigma$ detection of the source above 100 GeV. At the same time, the source is also detected with high significance in the 30-100 GeV band. Both $E > 100$ GeV photons came during the flaring activity of the source in April-May 2010 ([73, 197]). The broad-band spectrum of PKS 0301-243, shown in Fig. 26, is consistent with the possibility that radio-to-X-ray emission is produced via the synchrotron mechanism and the 1-300 GeV emission via the inverse Compton mechanism.

RX J0316.2-2607 is a relatively high-redshift ($z = 0.443$) source, which has two back γ-rays within the distance $\theta = 0.1°$. The chance coincidence probability of finding two photons within this distance from the source is 2.5×10^{-6}, which implies a detection significance 4.7σ above 100 GeV. From Fig. 27, one can see that the source has a hard γ-ray spectrum without a signature of a high-energy cut-off. The

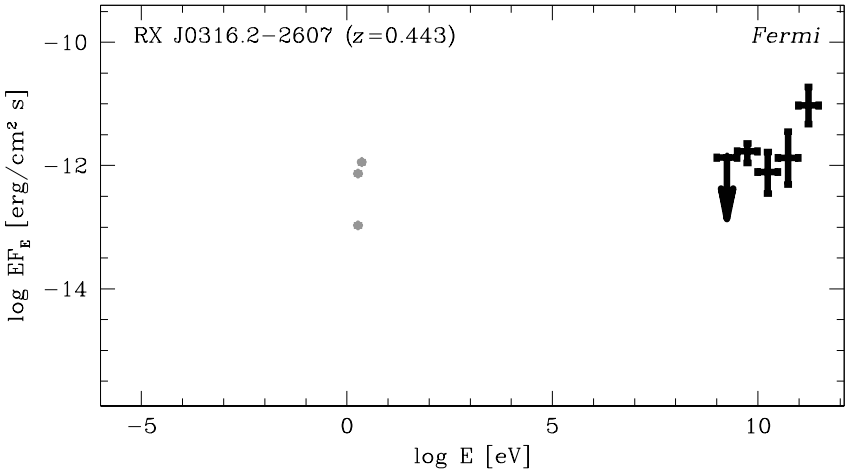

Figure 27: Broad-band spectrum of RX J0316.2-2607. Grey colour shows historical data from NED.

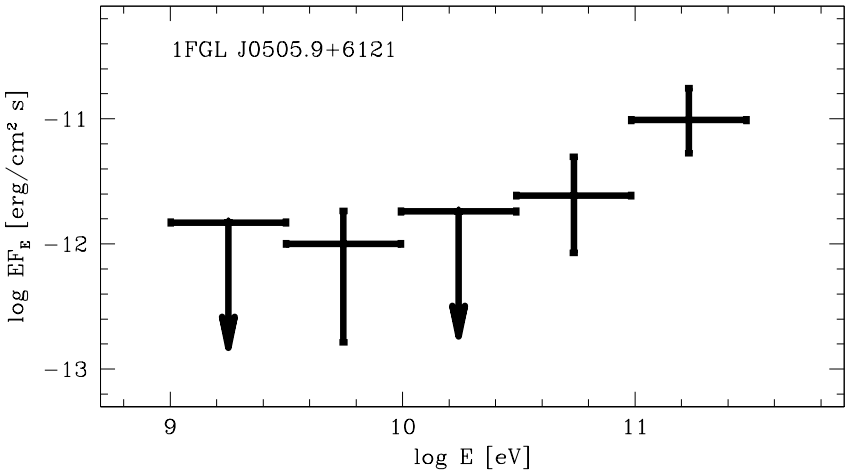

Figure 28: *Fermi* spectrum of 1FGL J0505.9+6121.

γ-ray energy flux from the source is comparable to the optical flux. Similarly to BZU J2313+1444, this source might also be an ideal candidate for the study of both EBL and cosmological magnetic fields.

1FGL J0505.9+6121 has three adjacent photons within 0.22°. Formally, the chance probability of finding three photons inside this distance is $P = 8 \cdot 10^{-8}$; however, since the detection angle was not defined a priori, it has to be penalized for this and the final probability is just 5σ (see Table 2), still implying that the source is detected at $E \geq 100$ GeV individually, and not only within the population of *Fermi* sources from Table 2. It is also detected with a significance higher than 5σ in the 30-100 GeV band. The spectrum of the source shown in Fig. 28 is consistent with a hard power-law (photon index harder than 2) up to the highest energy.

The object is located near the Galactic plane at $b = +12°$, so it can be of Galactic origin. The high level of Galactic diffuse γ-ray background around the location of the source prevents its detection at lower energies $E \leq 1$ GeV. The small value of the test-statistics (TS) value[12] for this source in the Table 2 could indicate that this source is not point-like. A standard *Fermi/LAT* analysis procedure, which was used to calculate the value of TS, does not work in this case.

Detailed multiwavelength observations are needed to constrain its nature. A possible candidate for the source identification is the radio- and X-ray loud AGN RX J0505.9+6113 ([71]) situated at the distance

[12]See http://fermi.gsfc.nasa.gov/ssc/data/analysis/scitools

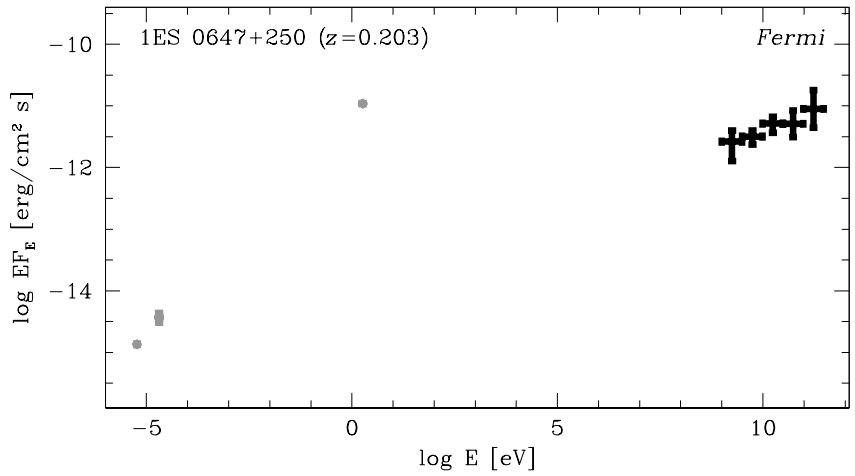

Figure 29: Broad-band spectrum of 1ES 0647+250. Grey colour shows historical data from NED.

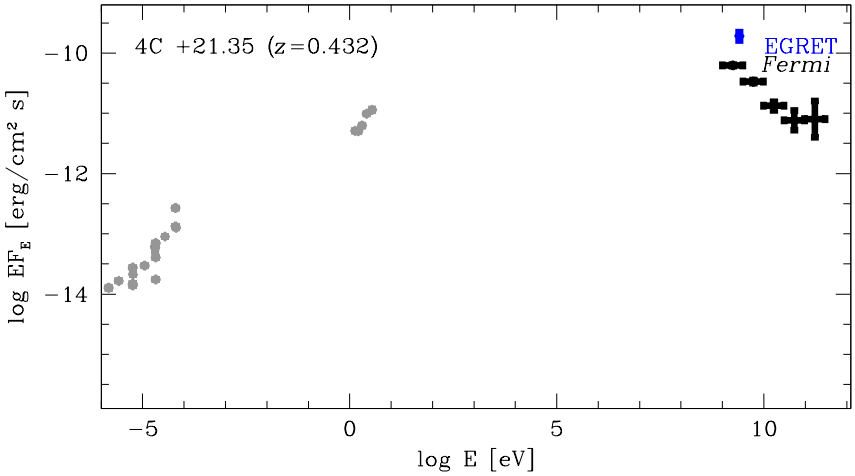

Figure 30: Broad-band spectrum of 4C +21.35. Grey colour shows historical data from NED. The EGRET measurement is also shown.

7.6′ from the catalogue source position and the distance 0.06° from the front-converted $E \geq 100$ GeV photon.

1ES 0647+250 at $z = 0.201$ was already mentioned as a "candidate" TeV blazar in the analysis of [79], based on its broad-band spectra properties. Fig. 29 demonstrates that the source has a hard γ-ray spectrum, with no signature of a cut-off up to 300 GeV. This ensures that it should be readily detectable with ground-based γ-ray telescopes.

4C +21.35 at $z = 0.432$ is an intermediate redshift BL Lac that exhibited a γ-ray flare in April-May 2010 ([92]) during which both $E > 100$ GeV photons associated with the source were detected, resulting in the detection of the source with 5.6σ significance above 100 GeV ([196]). The detection of the source above 100 GeV was recently confirmed with MAGIC observations of the source ([169]). A time-averaged spectrum of the source in the 1-300 GeV band is shown, together with the historical data, in Fig. 30. The previous EGRET measurement of the source flux is characterized by a somewhat higher source flux. This indicates that the source is variable not only on the short (days to month) timescale, but also on decade-long time scales.

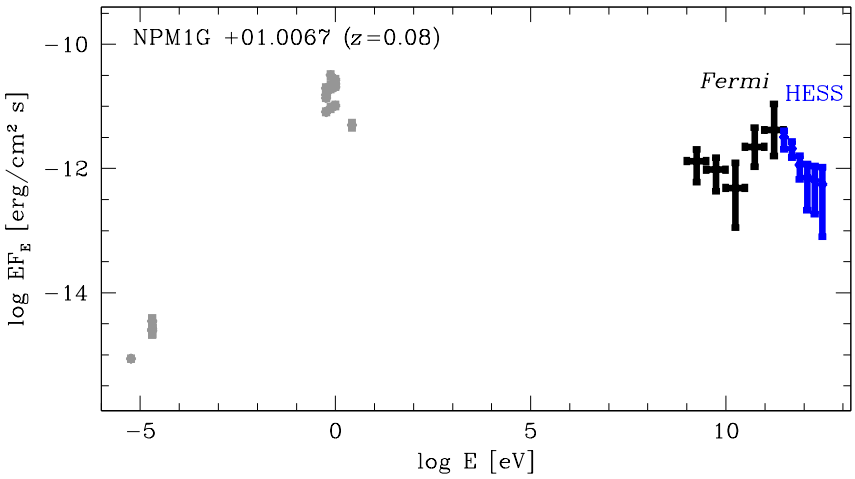

Figure 31: Broad-band spectrum of NPM1G +01.0067. Grey colour shows historical data from NED.

Sources from the BL Lac catalogue

NPM1G+01.0067 at $z = 0.08$ was previously detected in the VHE band by HESS ([36]). The *Fermi* spectrum of the source, shown in Fig. 31 is in good agreement with the HESS measurements. In spite of the source not being reported in the first year *Fermi* catalogue, it is detected in the 1.9 yr exposure with a TS value of $TS = 108$ above 1 GeV.

RX J09130-2103 has two γ-rays with energies $E \geq 100$ GeV within 0.1° distance. One of the γ-rays is a front-converted γ-ray, for which the 68% containment circle has a smaller radius. The front-converted γ-ray is at the distance 0.01° from the catalogue source position and a back photon at 0.03°. The field of the radius 10° around the source contains 20 photons at the energies above 100 GeV. The overall chance probability of finding front- and back-converted photons within the 68% containment circles of the front-converted and back-converted photons is $\simeq 10^{-5}$.

Despite the source not being reported in the first year *Fermi* catalogue, it is also detected with *Fermi* at energies below 100 GeV. A standard likelihood analysis in the energy range 1-300 GeV gives the TS value 80, which corresponds to a source detection significance $\simeq 9\sigma$.

The map of TS values in the region $2° \times 2°$ around the source is shown in Fig. 33. The TS values were calculated for the model of source distribution in the region 14° around RX J09130-2103 in which all the first year *Fermi* source catalogue sources apart from 1FGL J0908.7-2119 were included and one additional source was allowed to have a variable position. One can see that the TS value at the position of RX J09130-2103 is much larger than that at the position of 1FGL J0908.7-2119, which is only marginally detected above 1 GeV.

The broad-band spectrum of the source is shown in Fig. 32. One can see that the γ-ray spectrum of the source is hard, which explains its non-detection in the first 11 months of operation of *Fermi*.

MS 12218+2452 has a front-converted photon at the distance 0.04 from the catalogue source position. The source is also not reported in the first year Fermi catalogue, but is detected in the 1.9 yr exposure with TS value 80, which corresponds to the $\simeq 9\sigma$ significance of the source detection.

The map of TS values in the region of size $1° \times 1°$ at energies $E \geq 1$ GeV around the source position is shown in Fig. 35. To construct this map, we included all the sources from the first year *Fermi* catalogue situated at the distance $\theta \leq 14°$ from the source position into the model of source distribution on the sky. One can clearly see the source in the TS map.

Fermi data are compared to the broad-band archival data in Fig. 34. The γ-ray flux from the source is comparable to its optical flux intensity. The γ-ray spectrum does not display any signatures of a high-energy cut-off.

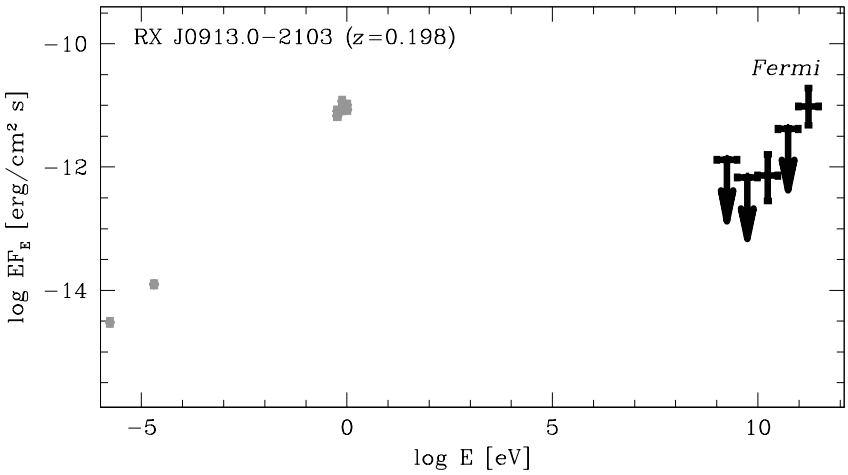

Figure 32: Broad-band spectrum of RX J0913.0-2103. Grey data points show historical data from NED.

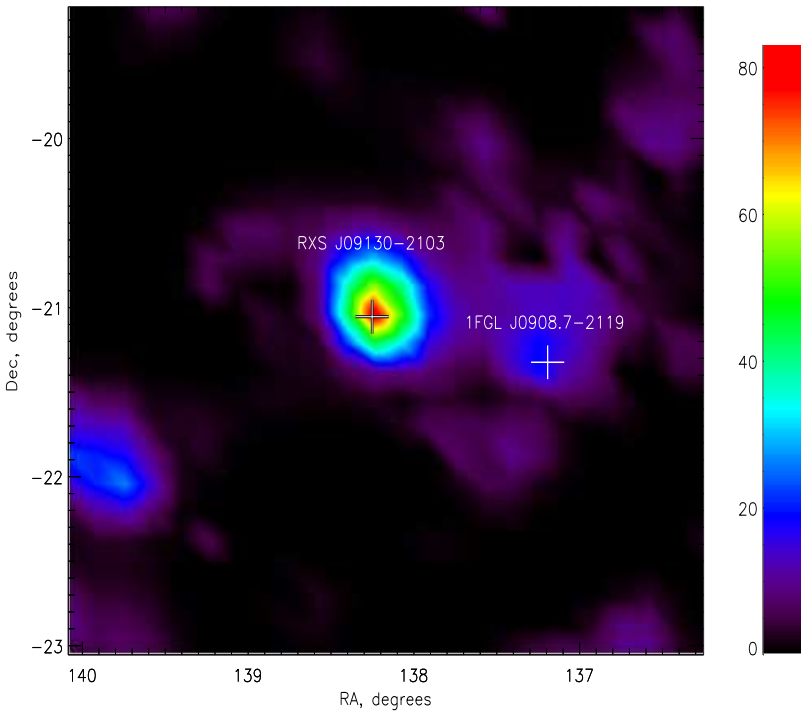

Figure 33: TS map of the region 2° × 2° in the energy band above 1 GeV around the position of RX J0913.0-2103.

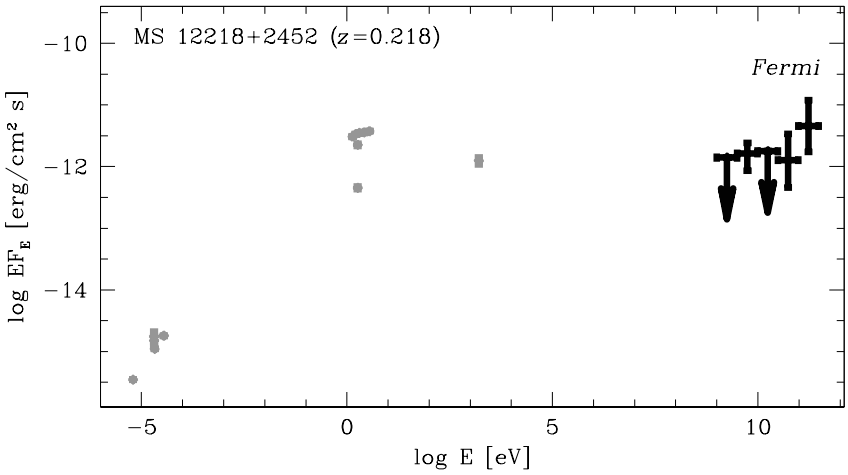

Figure 34: Broad-band spectrum of MS 12218+2452. Grey data points show historical data from NED.

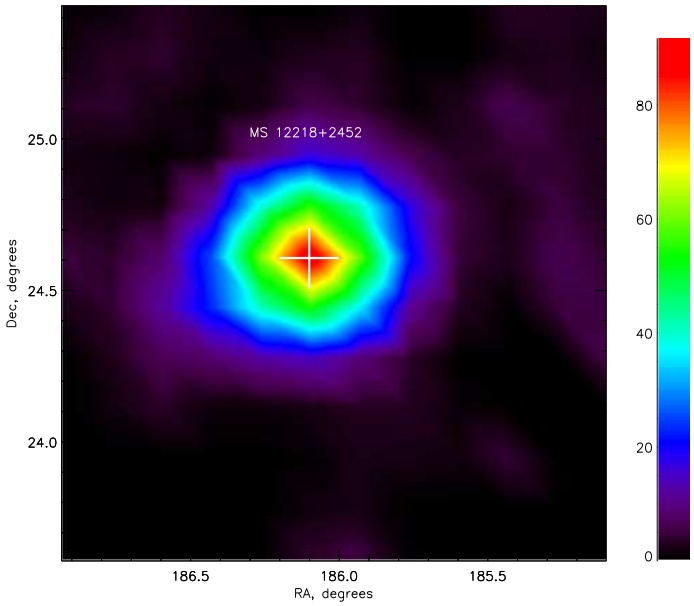

Figure 35: TS map of the region $1^\circ \times 1^\circ$ in the energy band above 1 GeV around the position of MS 12218+2452.

2.2.8 Discussion and conclusions

The study of cross-correlation of the arrival directions of the highest energy photons ($E \geq 100$ GeV) detected by *Fermi* with the catalogue of sources detected at lower energies $E < 100$ GeV has proven to be an efficient way of finding new γ-ray sources observable in the VHE γ-ray band. This study complements the pointed observations of selected γ-ray sources with the ground-based γ-ray telescopes because it results in an all-sky survey of the high Galactic latitude VHE γ-ray sky.

The high Galactic latitude sky survey above 100 GeV has revealed a large number of new VHE γ-ray sources. Adding the list of new sources to that of all sources previously detected with the ground-based γ-ray telescopes doubles the number of known extragalactic VHE γ-ray sources. As for all known VHE γ-ray sources, most of the new sources reported in Tables 2-4 are BL Lac type objects, a special type of AGN with jets closely aligned to the line of sight.

The majority of the sources listed in Table 2 are the real, new VHE γ-ray sources; only three sources are expected to be false detections caused by the chance coincidence of arrival directions of γ-rays with the source position. Several sources in Table 1 have more than one photon associated with them. These sources are detected with high significance in the 100-300 GeV energy range. Sources correlating with only one $E > 100$ GeV photon should be considered as "VHE source candidates". Apart from the known VHE γ-ray sources, the unidentified *Fermi* source 1FGL J0505.9+6121, as well as PKS 0301-243 and 4C +21.35, is detected with a significance close to 5σ above 100 GeV. In addition, BL Lacs with an associated front-converted photon, which are found to correlate with the catalogue of [272] (marked by "Vf" in Table 2), should also be considered as high-confidence detections.

Table 3 lists 21 lower significance sources, among which five or six are most probably false detections. As it was for Table 2, the source marked "Vf" (#56), which contributes with a front-converted photon to the correlation with the BL Lac catalogue, should be considered as a higher significance detection. For the sources listed in this table, it is reasonable to accumulate longer exposure to single out false detections.

Table 4 lists VHE γ-ray emitting BL Lacs that were not listed in the first year *Fermi* catalogue, but contribute to the correlation of the *Fermi* VHE γ-rays with the BL Lac catalogue of [272]. Their absence from the *Fermi* catalogue might be caused by the hard spectra of these sources. We have demonstrated that three of the eight sources listed in Table 4, the sources #1, 4, and 7 are, in fact, detected with a significance $> 5\sigma$ in the 1-300 GeV band. The other three sources, which have a front-converted photon associated with them, should also be considered as probable true detections.

Table 5 lists six sources, which have photons with energies above 300 GeV, including four known TeV sources and two possible new sources which are, however, consistent with random coincidences with background photons. Among the TeV sources, only B2 1218+30 does not contain photons in the 100-300 GeV energy range within a region $\theta \leq 0.2^\circ$ around its centre. However, it has 2 back-converted photons at $0.2^\circ < \theta < 0.3^\circ$.

Tables 2-5 list 86 VHE source candidates, our of which 17 are known sources of the TeV emission. After the completion of this work, 10 more sources listed in these tables were detected with the ground-based Cherenkov telescopes[13]: PKS 0301-243, 1ES 0647+250, B2 1215+30, 4C +21.35, 1ES 1741+196 – from Table 2, PKS 0447-439 and B3 2247+381 – from Table 3, MS 1221.8+2452 and MS 1312.1-4221 – from Table 4 and SHBL J10102-3119 from Table 5. This way, one third of the sources presented in Tables 2-5 has been detected up to now in the VHE domain, while the other two thirds are still awaiting for their discovery with the Cherenkov telescopes.

Some of the new VHE γ-ray sources listed in Table 2 are situated at high redshifts $z \sim 1$. Our analysis of the γ-ray spectra of the high-redshift sources indicates that at least several of them do not display any signatures of a high-energy cut-off up to 300 GeV. The typical fluxes of the sources listed in Tables 2-4 are at the level $EF_E(E \geq 100 \text{ GeV}) \geq (few) \times 10^{-12}$ erg/(cm^{2}s), i.e., at the level of 0.1 Crab units. These sources should be readily detectable by ground-based Cherenkov telescopes at energies of several hundreds of GeV. The larger collection area of the ground-based telescopes should result in much higher quality signal statistics, which should allow a study of the detailed spectral properties of these new bright VHE γ-ray sources. We anticipate that a detailed high sensitivity study of high-redshift VHE γ-ray sources with ground-based γ-ray telescopes will enable us to study the cosmological evolution of the BL Lac properties,

[13] http://tevcat.uchicago.edu/

the EBL, and the associated evolution of galaxies producing the EBL ([107, 123, 152, 182, 248]), as well as cosmological intergalactic magnetic fields ([201, 205]).

2.3 Very high-energy gamma-ray emission from high-redshift blazars

2.3.1 Introduction

As it was mentioned earlier in section 2.2, the study of the cosmological evolution of the EBL would require an observation of a sample of high-redshift blazars with the ground-based Cherenkov telescopes. However, most of the VHE γ-ray loud blazars, detected by these telescopes, are situated in the local Universe, at (several) hundred megaparsec distances, in the redshift range $z \sim 0 - 0.2$[14]. Only one source at redshift $z > 0.5$, 3C 279, was possibly detected by the MAGIC telescope during a flaring activity ([167]). Another source at redshift 0.444, 3C 66A, was detected by VERITAS ([21]). One more relatively high-redshift source, PG 1553+113 (at $z > 0.4$, reported by [81]) has been detected by MAGIC and VERITAS ([51, 215]). Accumulation of a larger sample high-redshift blazars is complicated by the fact that γ-ray emission from distant blazars is suppressed by the effect of pair production through interactions of these γ-rays with the low-energy photons forming the EBL ([107, 117, 122, 152, 182, 248]). This prevents observations of high-redshift sources using the technique of imaging of the Cherenkov emission produced through γ-ray induced air showers, used by the ground-based Cherenkov telescopes HESS, MAGIC and VERITAS ([44]).

Measurement of the effect of suppression of the VHE γ-ray flux from low-redshift blazars is commonly used for the estimation of the density of the EBL in the local Universe ([107, 117, 152, 248, 182]). Constraints on the EBL density and spectral characteristics, extracted from the VHE blazar observations, are useful for understanding the cosmological evolution of galaxies. Observations of the suppressed VHE γ-ray emission from blazars at non-negligible redshifts can provide a measurement or constraint not only of the EBL density in the local Universe, but also new information on the cosmological evolution of the EBL, which is largely uncertain.

Observations of high-redshift sources in the VHE band would also provide valuable information on the cosmological evolution of the VHE γ-ray loud blazars (and, more generally, γ-ray emitting active galactic nuclei, AGN), which is also highly uncertain. This information is important, in particular, for the understanding of the origin of Extragalactic γ-ray background ([16, 202]). Most of the VHE γ-ray emitting blazars at zero redshift belong to a High-energy peaked BL Lac (HBL) sub-class of the blazar population. Negative cosmological evolution of this sub-class was reported based on the observations in the visible and X-ray band ([118]). Such puzzling evolution is, apparently, opposite to the general positive evolution of blazars and radio galaxies (BL Lac parent AGN population) with the cumulative power of the sources increasing as $(1 + z)^k$, $k > 0$ ([135, 236, 247]). Independent verification of this hypothesis using γ-ray observations would be possible only if a significant amount of VHE emitting blazars could be detected in the redshift range $z \sim 0.5 - 1$.

Taking into account the importance of the study of the VHE γ-ray emission from distant AGN, in this section I present the detection of VHE γ-ray signals from sources at redshifts $z > 0.5$ by the Fermi/LAT (see also [203]). Small effective area of LAT, when compared to that of the ground-based γ-ray telescopes, allows it to detect only one-to-several photons from the brightest extragalactic VHE γ-ray sources in ~ 4 years of observations. At the same time, an extremely low level of the background (including the residual cosmic ray background and Galactic / extragalactic γ-ray background) makes even a several-photon signal in the energy band above 100 GeV significant. Similarly to the analysis in section 2.2, here we use the correlation of arrival directions of VHE γ-rays detected by Fermi with the positions of high-redshift blazars to identify high-redshift sources of VHE γ-rays and to study their spectral characteristics.

2.3.2 Data selection and data analysis

For our analysis we have used Fermi Pass 7 data within the time window from August 4, 2008 till June 11, 2012. We have considered two sub-classes of the "ULTRACLEAN" events ("evclass=4" in the photon selection routines): the event from the classes 65311 and 32543. Those classes have the best angular

[14] `http://tevcat.uchicago.edu`

resolution in Fermi, corresponding to a "superclean class" in the Pass 6 data for $E > 100$ GeV. Using the method of [120] we correlated the arrival directions of photons with $E > 100$ GeV with positions of the sources listed in the two-year Fermi catalogue ([208]) with high Galactic latitude $|b| > 10^\circ$. This analysis is similar to the one performed for the 1FGL catalogue in section 2.2 ([199]), where a catalogue of 75 objects with $E > 100$ GeV was obtained.

There are 1036 front and 888 back converted photons at high Galactic latitude $|b| > 10^\circ$ and $E > 100$ GeV in the selected data.

We have measured the PSF for the selected events via the correlation of photon arrival directions with the sky positions of known gamma-ray blazars. The size of the 68% containment circle for the event classes 65311 and 32543 is 0.08° for front photons and 0.21° for back photons with energies above 100 GeV. In order to keep the analysis methods consistent with those used by [199], we use 0.1° and 0.2° distance bins for correlation analysis using front and back photons.

We took all high Galactic latitude Fermi LAT sources with known redshifts and selected high-redshift sources with $z > 0.5$. The original two-year Fermi catalogue [208] does not contain information on the redshift of the sources. Instead, we have considered the redshifts listed in the 13th Veron catalogue of BL Lacs ([272]) and in the Rome blazar catalogue of [173]. We cross-checked the information on the source redshifts with the Fermi AGN catalogue [15] and with the information given in the NED[15] and SIMBAD[16] databases. In this way out of 414 Fermi BL Lacs we selected 55 with $z > 0.5$.

For the 55 selected BL Lacs we found six photons correlating with six objects within 0.1 degree, while a total background of 0.06 was expected. The probability that this signal occurred by chance was $P \sim 6 \cdot 10^{-11}$. The six sources contributing to the correlation are listed in the upper part of the Table 6. Within 0.2 degrees from the source positions, (but outside the 0.1 degree region of the sources) the expected background was 0.14 photons, while 4 photons were observed from 3 additional BL Lacs.

One of these three additional sources was KUV 00311-1938, with two associated photons. The chance coincidence probability for the two photons to arrive within 0.2 degrees from the source position was 8×10^{-6}, which corresponds to a 4.5σ detection of the source above 100 GeV. The chance coincidence probability for the remaining two photons to arrive within 0.2° from two other BL Lacs was $P \sim 10^{-2}$. We list these sources in the lower part of the Table 6 (two last lines), but one should remember that they might, in principle, be "fake detections" due to the chance coincidence of the background photon arrival directions.

From the 351 Flat Spectrum Radio Quasars (FSRQ) we selected 269 objects with $z > 0.5$. Within 0.1 degree from these objects we found four photons from four different sources, while a total background of 0.4 was expected. The probability that this happened by chance was $P \sim 8 \cdot 10^{-4}$. Again, these objects were given lower priority in Table 6, similar to that for the case of BL Lacs with photons only associated within 0.2 degrees. We did not consider correlations with FRSQ objects within larger angles because of the high level of chance coincident background.

The complete list of sources with redshift $z > 0.5$ which correlate with the arrival directions of the VHE γ-rays in LAT is shown in Table 6.

For the spectral and timing analysis presented in Figs. 36-48, we have used the Fermi Science Tools[17]. We have calculated the source spectra using two complementary techniques: the likelihood analysis and the aperture photometry methods. These two methods give consistent results. The likelihood method is more reliable at low energies ($0.1 - 10$ GeV) where the LAT instrument has a relatively wide point spread function. The aperture photometry method enables to properly take into account the Poissonian statistics of the signal at low photon count rates in the 10-300 GeV range.

2.3.3 Properties of individual high-redshift sources

In this section we study in more detail the spectral and timing properties of the high-redshift VHE γ-ray sources listed in Table 6, to understand if some of the lower significance sources in Table 6 among the FSRQs and the two BL Lacs listed in the last two rows of the table could possibly be random coincidences of arrival directions of the VHE γ-rays with the source positions on the sky. We also investigate the possibility for the detection of these sources using ground-based γ-ray telescopes.

[15] http://ned.ipac.caltech.edu/
[16] http://simbad.u-strasbg.fr/simbad/
[17] http://fermi.gsfc.nasa.gov/ssc/data/analysis/

	Name	Type	z	N_{30-100}	$N_{0.1}$	$N_{0.2}$	E_{max}	$L/L_{\rm Mrk421}$	P
1	TXS 0138-097	BL	0.733	2	1f	0	138	44.5	1.1e-3
2	PKS 0426-380	BL	1.11	13	1f	0	134	151	0.9e-3
3	B2 0912+29	BL	1.521	5	1f	0	126	405	0.7e-3
4	Ton 116	BL	1.065	11	1b	0	114	133	0.7e-3
5	PG 1246+586	BL	0.847	9	1b	0	104	67.5	1.2e-3
6	B3 1307+433	BL	0.69	4	1f	0	104	37.5	0.8e-3
7	4C +55.17	FSRQ	0.8955	14	1b	0	141	84.0	1.6e-3
8	TXS 1720+102	FSRQ	0.732	0	1f	0	168	46.8	1.9e-3
9	PKS 1958-179	FSRQ	0.65	2	1b	0	118	33.5	2.3e-3
10	PKS 2142-75	FSRQ	1.139	1	1f	0	135	173	1.5e-3
11	KUV 00311-1938	BL	0.61	11	0	2b	152	53.2	8e-6
12	RGB J0250+172	BL	1.1	3	0	1b	358	147	7.6e-3
13	PKS 1130+008	BL	1.223	1	0	1f	140	204	4.4e-3

Table 6: List of high-redshift blazars emitting in the energy band $E > 100$ GeV. Columns $N_{0.1}$ and $N_{0.2}$ give the numbers of VHE photons within an angular distance of 0.1° and 0.2° from the source position. P is the chance coincidence probability for the VHE photons to be found within the 0.1° or 0.2° circles from the source, labels "f" and "b" mark photons pair converted in the front- and back- layers of the LAT detector. Column N_{30-100} gives the number of photons associated to the source in the lower energy band $30 - 100$ GeV. E_{max} is the maximal energy of photon associated to the source. $L/L_{Mrk\ 421}$ is the source luminosity in units of Mrk 421 luminosity at $E > 100$ GeV.

2.3.4 Firm detections

TXS 0138-097

The redshift of this source has been obtained through spectroscopic measurements ([254]). At the same time, the SIMBAD database entry for the source gives a redshift of 1.03, based on the data from the SDSS photometric catalogue [27]. The detection of absorption lines at redshift $z = 0.5$ ([253]) for this source imposes a lower limit on its redshift, so that in any case the source belongs to the $z > 0.5$ source sample in which we are interested here.

The upper panel of Fig. 36 shows the light curve of the source in the energy band above 1 GeV. From this light curve, one can see that the source behaviour is stable on the time scale of almost four years of Fermi exposure. The lower panel of the same figure shows the source spectrum in the 0.3-300 GeV energy range. The spectrum is well described by a simple power law of the form $dN/dE \sim E^{-\Gamma}$ with spectral slope $\Gamma \simeq 2$, suppressed at high-energies through the absorption on the EBL. The model spectrum shown in Fig. 36 is calculated assuming a source redshift of 0.733 and using the EBL model of [107]. The 100-200 GeV band source flux is consistent with the expectation based on the Franceschini et al. model [107].

Of course, the statistics of the Fermi signal is largely insufficient for a sensible study of the details of the shape of the spectrum in the 100 GeV band, which is determined by the effects of propagation through the EBL. Such study would be possible only with a ground-based γ-ray telescope, which provides a much larger collection area for γ-rays and, consequently, much higher source signal statistics. The lower panel of Fig. 36 shows a comparison of the measured source spectrum with the sensitivity limits of different existing and future ground-based γ-ray telescopes. Unfortunately, the model source flux is below the sensitivity limit of the HESS-II telescope, which has started operation in 2012. The estimate of the HESS-II sensitivity shown in this plot has been taken from [172]. The sensitivity curve found in [172] is given in terms of the integral flux. Conversion of the sensitivity into the differential flux sensitivity depends on the slope of the source spectrum. Fig. 36 shows three different differential sensitivity curves corresponding to three different values of the slope of the source spectrum. One can see that within the energy range covered by HESS-II, the spectrum is steep, with a slope close to $\Gamma = 4$, so that the source flux is below the HESS-II sensitivity level and, thusly, the source is not expected to be detectable.

The expected performance of the next-generation ground-based γ-ray telescope CTA is not better than that of HESS-II for energies below 100 GeV. Because of this, the prospects for the source detection with CTA are also not promising. Contrary to this, however, the sensitivity of a ground-based γ-ray

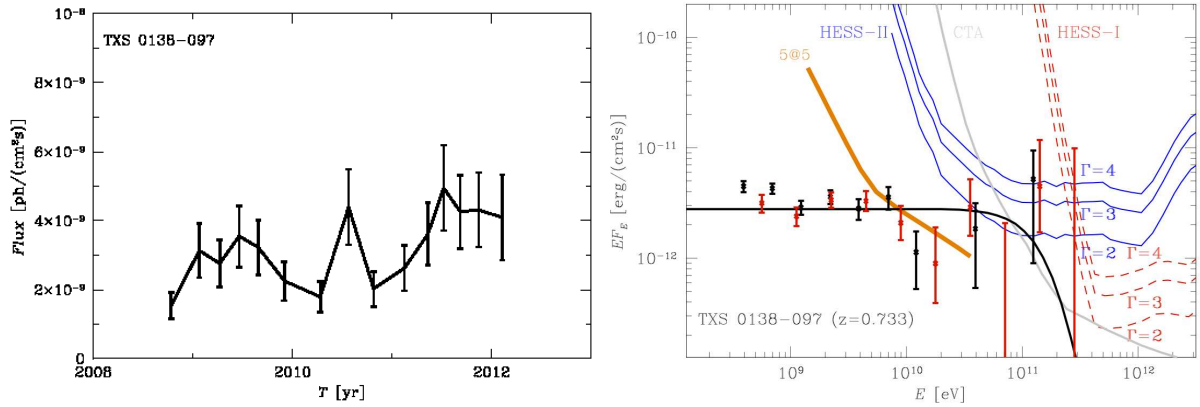

Figure 36: Light curve (top) and spectrum (bottom) of TXS 0138-097 at redshift $z = 0.733$. Black curve in the bottom panel shows a power law type model spectrum absorbed on the EBL from [107]. Also shown in the bottom panel are sensitivity curves of different ground based γ-ray telescopes: 5@5 ([48]), HESS-I and HESS-II ([172]) and CTA ([25]). Black and red data points in the lower panel show the spectrum extracted using the likelihood analysis and aperture photometry method, respectively.

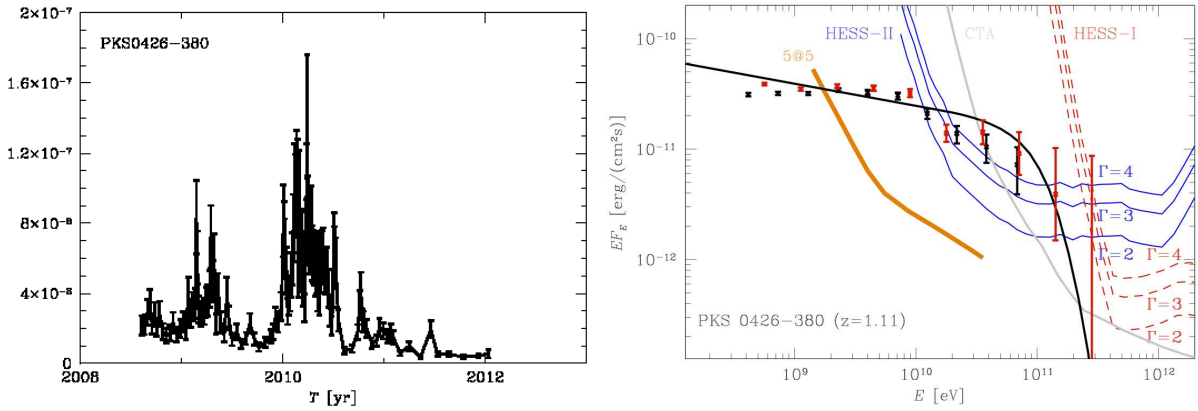

Figure 37: Lightcurve (top) and spectrum (bottom) of PKS 0426-380 at the redshift $z = 1.11$. Notations are the same as in Fig. 36.

telescope optimized for the 10 GeV energy band, 5@5 ([48]) is sufficient for the source detection in the energy range above 10 GeV and up to the sharp EBL-induced cut-off at 100 GeV. The difference in the performance of 5@5 and CTA in the 10-100 GeV energy band turns out to be crucially important for the possibility of the study of VHE γ-ray emission from this high-redshift source.

PKS 0426-380

This bright BL Lac is situated at a redshift of $z = 1.11$ [132]. The source is strongly variable in the GeV energy band, see upper panel of Fig. 37. Several active episodes, during which the flux increased by up to an order of magnitude, have been observed during the four years of Fermi's operation.

The source spectrum averaged over the whole observation period extends as a soft power law with $\Gamma > 2$ well into the 100 GeV energy band at the level of $\sim 10^{-11}$ erg/cm^{2}s, see lower panel of Fig. 37. At this flux level, the source should be readily detectable in the 30-100 GeV energy range with the HESS-II telescope and, in the future, with CTA.

We have verified that the source flux did increase by a factor of $\sim 2-3$ during the flaring activities, without any significant change in its spectral shape. This implies that the detectability of the source from the ground should be facilitated if the next ground-based observations are triggered during the next increased activity episode (which could be traced based on the Fermi monitoring of the source).

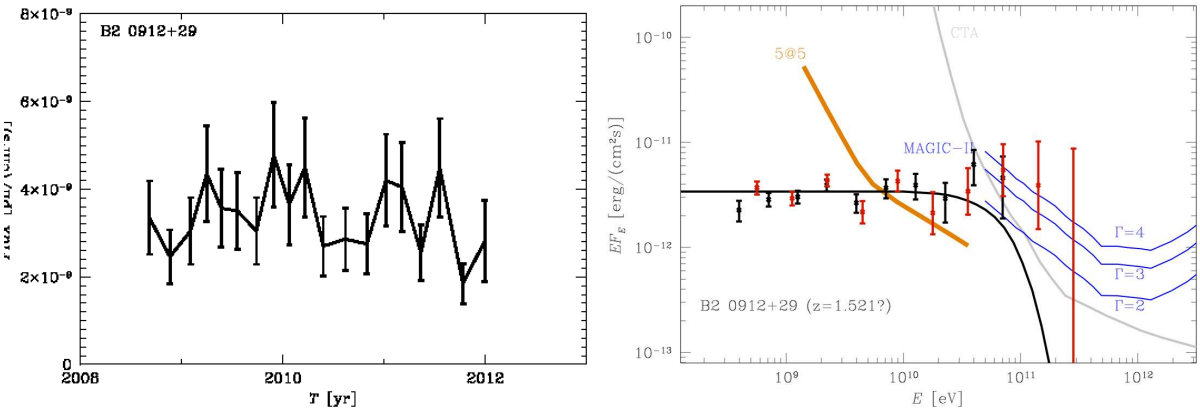

Figure 38: Lightcurve (top) and spectrum of B2 0912+29 at the supposed redshift $z = 1.521$. Notations are the same as in Fig. 36. Blue curves show the sensitivity of the MAGIC telescope in the stereo observation mode, from [78].

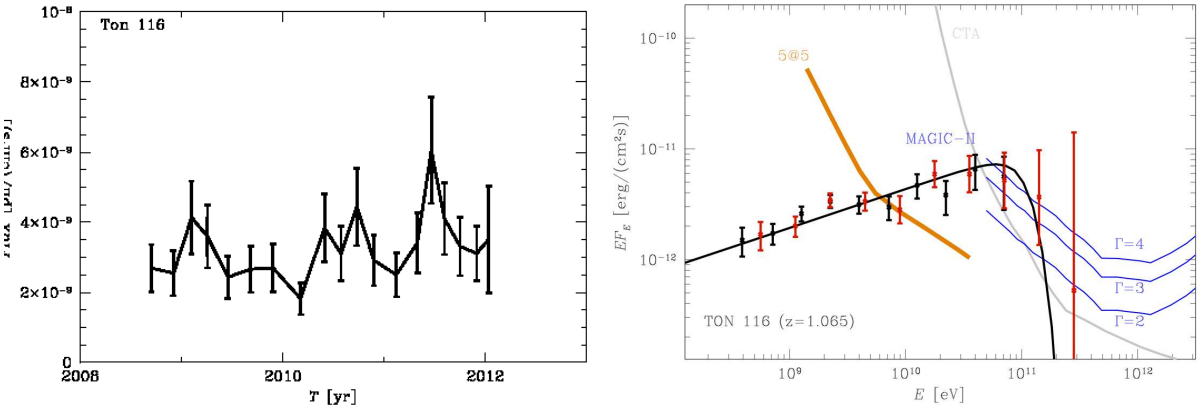

Figure 39: Lightcurve (top) and spectrum of Ton 116 at the redshift $z = 1.065$. Notations are the same as in Figs. 36 and 38.

B2 0912+29

The SIMBAD database ascribes a redshift $z = 1.521$ to the source, with a reference to the SDSS photometric survey [27], but stating that the redshift is spectroscopic. At the same time, the NED database does not ascribe a redshift to the source.

The source spectrum can be described by a relatively hard power law with slope $\Gamma \simeq 2$ up to ~ 200 GeV energy, showing no sign of suppression by the EBL. Such unabsorbed power law shape of the spectrum would pose a problem for modelling of the source if it is indeed at a redshift of $z = 1.5$. At this redshift, the suppression of the flux due to absorption on the EBL should start already below 100 GeV, so that the flux measurements in both 50-100 GeV and 100-200 GeV bands would be in tension with the model, see Fig. 38.

The bottom panel of Fig. 38 shows a comparison of the sensitivity of the MAGIC telescope in stereo operation mode ([78]) with the level of the source flux for different assumed values of the slope of the power law spectrum Γ. One can see that if the source flux is indeed at the level measured by Fermi, rather than the theoretically expected flux from a source at the redshift 1.521 suppressed by the absorption on EBL, this source should be detectable by MAGIC.

Ton 116

The redshift of the source cited in the NED database is $z = 1.065$, with a reference to the SDSS measurement [26]. At the same time, the Fermi AGN catalogue [15] list this source as having an unknown redshift. The source has a hard spectrum with slope $\Gamma \simeq 1.7$ (see Fig. 39), so that in spite of the high

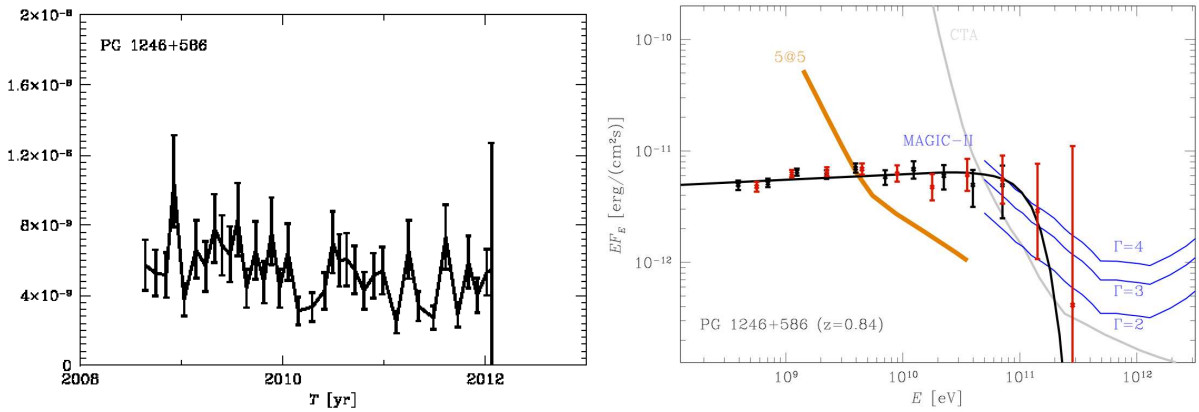

Figure 40: Lightcurve (top) and spectrum of PG 1246+586 at the redshift $z = 0.847$. Notations are the same as in Figs. 36 and 38.

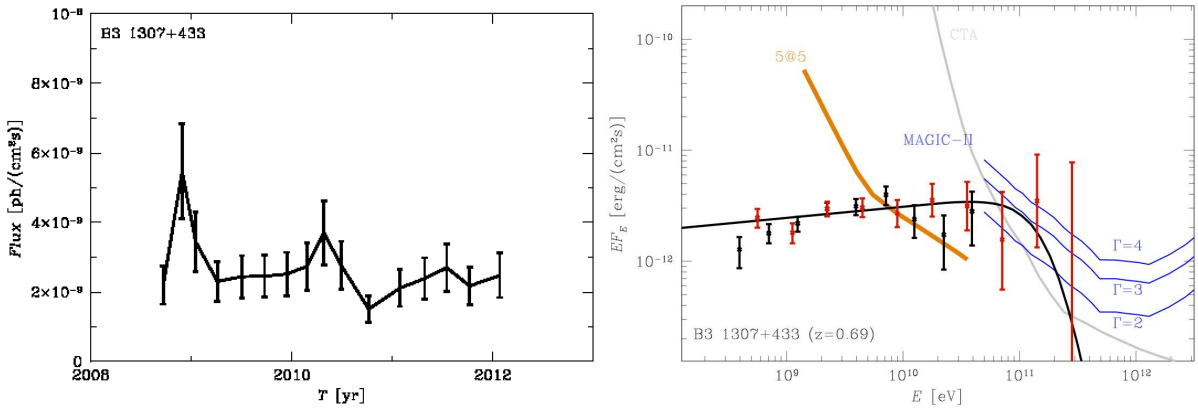

Figure 41: Lightcurve (top) and spectrum (bottom) of B3 1307+433 at the redshift $z = 0.69$. Notations are the same as in Figs. 36 and 38.

redshift of the source, the flux in the 100 GeV energy range should be at the level detectable by MAGIC and, in the future, by CTA. The source spectrum is expected to become very steep just above 100 GeV, so that its signal in MAGIC and CTA would be dominated by the contribution from the lowest energy bin just at the threshold energy of the instrument. It is not clear what quality of measurement of the shape of the spectrum in the VHE band could be achieved for such a situation. A proper study of the shape of the spectrum and of the effect of the EBL on it could be done only with a dedicated instrument with a very low energy threshold, like 5@5. From Fig. 39 one can see that the 5@5 instrument would be able to detect the source starting from an energy of $\simeq 10$ GeV.

PG 1246+586

The source redshift listed in both the NED and SIMBAD databases is $z = 0.847$ with a reference to SDSS ([26]). In the Fermi AGN catalogue the source redshift is considered as unknown ([15]). The source exhibits a steady behaviour, remaining stable over the four-years of Fermi monitoring (see the top panel of Fig. 40) and the source spectrum is hard with a slope slightly harder than $\Gamma = 2$ up to energies above 100 GeV, where the spectrum starts to be affected by the effect of suppression on the EBL (bottom panel of Fig. 40). The sensitivity of the MAGIC telescope would be sufficient for the detection of the source, as would the sensitivity of CTA. Similar to the case of Ton 116, a proper study of the shape of the VHE γ-ray spectrum could be done only with a dedicated low energy threshold instrument, like 5@5, which would be able to detect the source starting from an energy ~ 10 GeV.

B3 1307+433

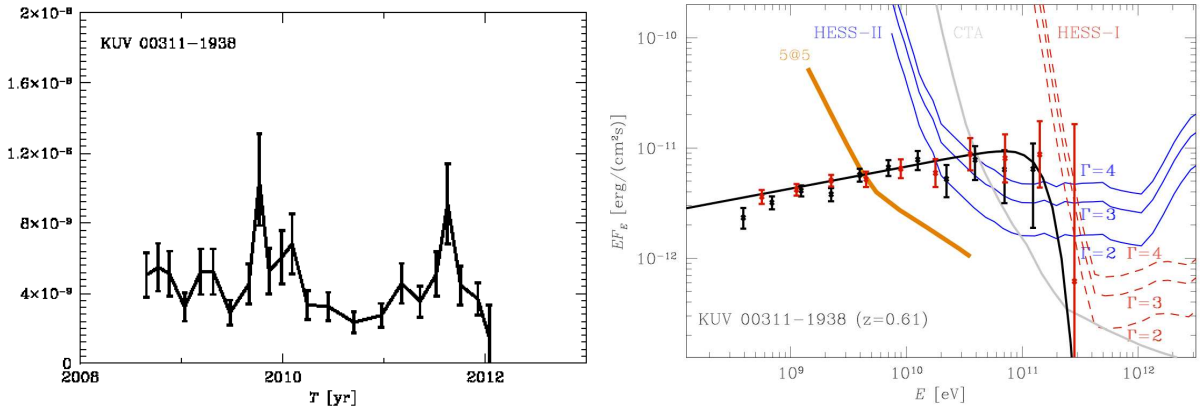

Figure 42: Lightcurve (top) and spectrum of KUV 00311-1938 at the redshift $z = 0.61$. Notations are the same as in Fig. 36.

The redshift quoted for this source in the NED database is $z = 0.69$, based on the SDSS measurement [224]. At the same time, SIMBAD quotes a redshift of $z = 2.159$, also based on the SDSS data ([27]). The spectrum of the source, shown in Fig. 41, is a hard ($\Gamma < 2$) power law up to ~ 200 GeV. If the source was at a redshift of 2.159, as stated in the SIMBAD, the detection above 100 GeV would be in contradiction with the expected level of suppression of the source flux due to the interactions of γ-rays with the EBL photons. At a redshift of 0.69, however, the Fermi measurement is consistent with the theoretical expectation (see Fig. 41).

Verification of the source spectral properties in the 100 GeV band, therefore, would allow clarification of the issue of the source redshift via observations with the existing ground based telescopes (MAGIC and Veritas). However, high quality measurements of the shape of the spectrum would require a next generation instrument, like CTA and 5@5.

KUV 00311-1938

As is mentioned in the previous section, this source is individually detected above 100 GeV with significance 4.5σ. The redshift of this BL Lac is $z = 0.61$ ([119]). Its spectrum is characterized by a hard power law type with $\Gamma < 2$ from 0.3 up to ~ 200 GeV. The VHE data point in the 100-200 GeV band matches exactly that expected from an extrapolation of the low-energy spectrum, with no signature of the EBL suppression noticeable at this energy at the Fermi data quality level. The Fermi measurement, however, is consistent with the assumption of a power law suppressed by the absorption on EBL. The EBL effect is expected to appear mostly above 200 GeV, in the energy band readily accessible by the HESS telescope. The source flux above 100 GeV is sufficiently high for the detection with HESS-II and, possibly, HESS (see Fig. 42).

2.3.5 Possible detections

In this subsection we provide the details on the sources for which the correlation of the arrival directions of $E > 100$ GeV photons with their source positions is less significant. We notice that some "chance coincidence" sources can possibly be singled out based on their spectral characteristics (the extrapolation of the low-energy spectrum to the VHE band being not consistent with the source flux level in the VHE band implied by the detection of the VHE photon). However, this criterion alone can not be used to firmly reject the source due to the possible existence of peculiar source spectra (e.g. due to the presence of different emission components in different energy bands).

4C +55.17

4C +55.17 is a source from the FSRQ subclass of blazars, i.e. from the subclass which gives only a minor contribution to the set of known VHE γ-ray sources in the local Universe. The appearance of this source, along with the three other FSRQs in the $z > 0.5$ VHE source sample is, perhaps, important, since it may provide an indication of the higher FSRQ contribution to the VHE γ-ray source population

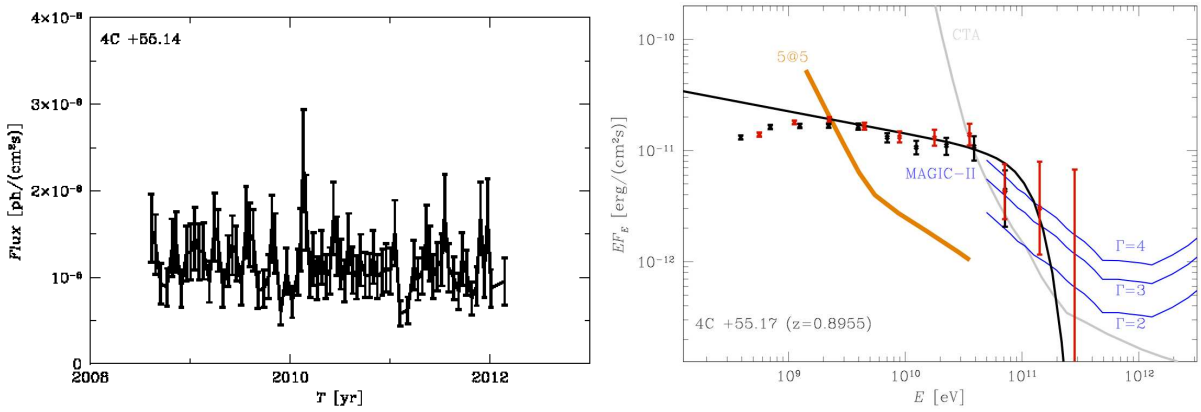

Figure 43: Lightcurve (top) and spectrum (bottom) of 4C +55.17 at the redshift $z = 0.8955$. Notations are the same as in Figs. 36 and 38.

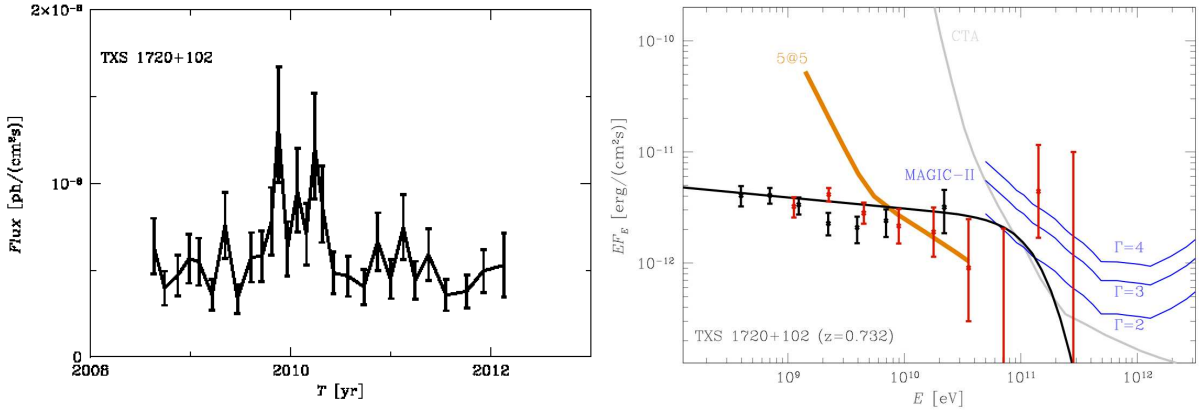

Figure 44: Lightcurve (top) and spectrum (bottom) of TXS 1720+102 at the redshift $z = 0.732$. Notations are the same as in Figs. 36 and 38.

in the cosmological past.

The source's redshift is $z = 0.8955$ ([26]). The source spectrum is softer than $\Gamma = 2$ for GeV energies and above, as expected from FSRQs which have on average softer spectra than BL Lacs (see Fig. 43). An extrapolation of the $E < 100$ GeV band spectrum into the VHE band is consistent with the estimate of the VHE flux of the source based on the detected VHE photon. This indicates that the VHE γ-ray emission from the source is real. However, detection of the source from the ground would be a challenging task for the existing ground-based telescopes like MAGIC (see Fig. 43). At the same time, the source should be readily detectable by the next-generation instruments CTA and 5@5 (Fig. 43).

TXS 1720+102

This is another representative of the FSRQ sub-population in the high-z VHE source sample. The source is at a redshift $z = 0.732$ ([28]). Its spectrum is softer than $\Gamma = 2$ in the energy band below 100 GeV. The overall source flux level is somewhat lower compared to e.g. 4C +55.17, so that the source would hardly be detectable by MAGIC, VERITAS and/or CTA (see Fig. 44), unless the spectrum has a "bump"-like feature in the 100 GeV band. The quality of Fermi data is not sufficient to judge whether this is the case or the Fermi detection in the $E > 100$ GeV band is due to the up-fluctuation of the photon count rate. The $E > 100$ GeV data are well consistent with the extrapolation of the lower energy power law attenuated by the EBL (see Fig. 44).

PKS 1958-179

The spectral characteristics of this FSRQ at a redshift of $z = 0.65$ ([60]) appear somewhat peculiar

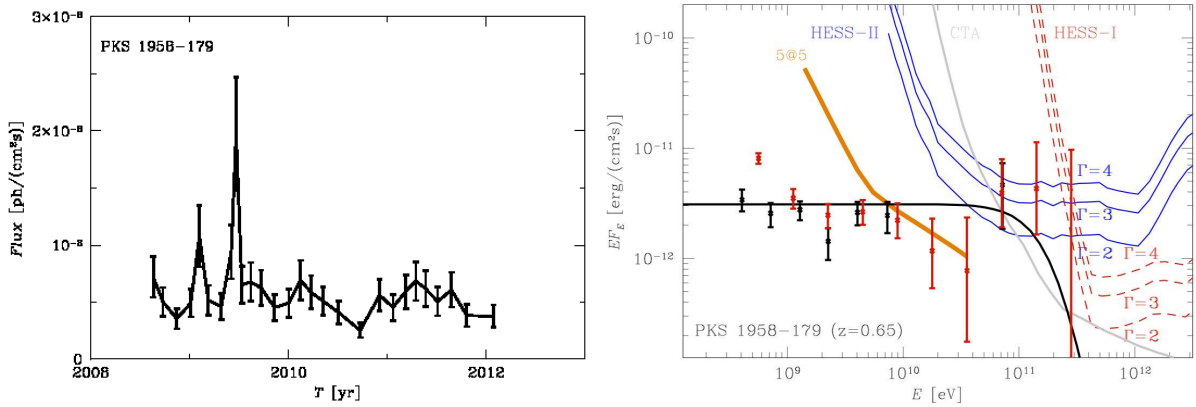

Figure 45: Lightcurve (top) and spectrum of PKS 1958-179 at the redshift $z = 0.65$. Notations are the same as in Fig. 36.

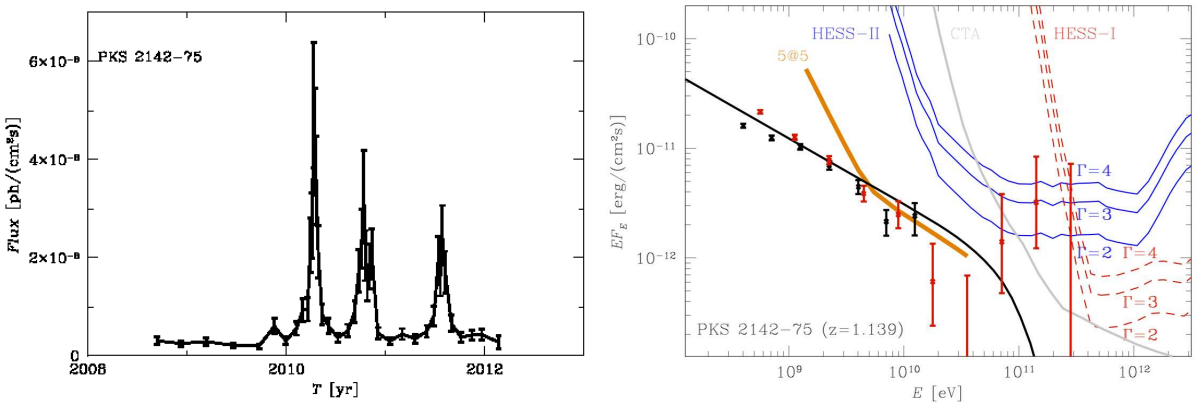

Figure 46: Lightcurve (top) and spectrum of PKS 2142-75 at the redshift $z = 1.139$. Notations are the same as in Fig. 36.

with a soft spectrum below an energy ~ 30 GeV and a possibly a new hard component appearing above the 30 GeV band, see Fig. 45. The statistics of the Fermi data is not sufficient to draw definitive conclusions about the existence of two separate components in the spectrum. In principle, a single power law with a photon index of about $\Gamma = 2$ provides a satisfactory fit to the data above an energy of 1 GeV. Within such a spectral model, the detection of the source in the energy band above 100 GeV is consistent with the assumption that the power law extends up to the VHE band, if the absorption of the VHE γ-rays through interactions with the EBL photons is taken into account. The source could be marginally detectable with the ground based γ-ray telescopes, including both existing and future facilities (see Fig. 45).

PKS 2142-75

This FSRQ at $z = 1.139$ ([143]) also has a peculiar time-average spectrum in the 0.3-300 GeV energy band, with a soft component dominating at energies below 30 GeV and possibly a new hard component appearing above 30 GeV, see Fig. 46. If not for this hard component, the source would not be detectable at energies above 100 GeV. During the period of Fermi observations, the source has exhibited several pronounced flares (Fig. 46 upper panel). The complicated shape of the spectrum might be due to the fact that different components contribute to the source flux during the flare and quiescent periods. However, with only two photons above 30 GeV, one could not make any firm conclusions on the reality and possible nature of the "hard excess". It is well possible that the VHE photon coming from within 0.1° of the source is a background photon falling coincident to the source (as discussed in the previous section, one among the four FSRQs listed in Table 6 could possibly be a false detection in the VHE band).

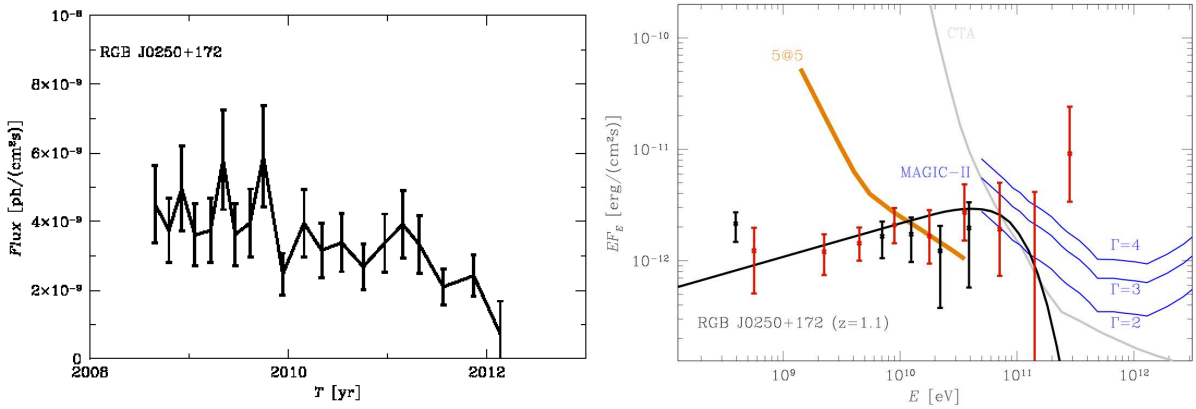

Figure 47: Lightcurve (top) and spectrum of RGB J0250+172 at the redshift $z = 1.1$. Notations are the same as in Figs. 36 and 38.

RGB J0250+172

Contrary to the soft spectra FSRQs, RGB J0250+172 at $z = 1.1$ ([62]) is characterized by a hard γ-ray spectrum and is a good candidate for being a real VHE γ-ray source. However, due to the lower overall flux normalization, the source should only be marginally detectable by both Fermi, current and next-generation ground-based γ-ray telescopes (see Fig. 47). Unexpectedly, a photon with energy 358 GeV is detected from the source direction. This detection is somewhat puzzling. On one side, the estimate of the source flux in the 200-400 GeV band, based on this photon, is consistent with the power law extrapolation of the lower-energy spectrum, without an account of the EBL-induced suppression of the source flux (see Fig. 47). On the other side, if the EBL suppression is taken into account, the measured source flux is orders of magnitude above the expected flux from a source at redshift 1.1. Resolution of this inconsistency might be: (a) that the VHE photon from the source direction is a background photon, with a chance probability of 0.8%, (b) that the energy of this particular photon is over-estimated by the LAT data analysis software or (c) that the redshift of the source has not been correctly measured.

This contradiction could be easily resolved via observation of the source with existing ground-based γ-ray telescope(s) like MAGIC. If the source flux in the 200-400 GeV band is indeed at the level of $\sim 10^{-11}$ erg/(cm^{2}s), it should be readily measurable by MAGIC. If the flux is at the level expected based on the estimate of the model calculation taking into account the EBL suppression, the source is likely not detectable neither by MAGIC nor by CTA. It would be, however, detectable by 5@5 due to the lower energy threshold of the instrument.

PKS 1130+008

The redshift of this source is quoted in SIMBAD to be $z = 1.223$ (from Ref. [27]). The Fermi AGN catalogue [15] ascribes the redshift 0.678 to the source. The source has a power law type spectrum in the energy range 0.3-30 GeV with photon index $\Gamma \simeq 2$. Significant suppression of the source flux above ~ 30 GeV is expected taking into account the high redshift of the source. In this respect, the estimate of the source flux in the 100-200 GeV band, based on the photon detected by the LAT from the source direction, is somewhat surprising, because it lies at the extrapolation of the power law from the lower energies and is above the expected flux level taking into account the expected EBL suppression. At the same time, the inconsistency is still very mild due to the large uncertainty of the Fermi flux estimate.

A relatively low level of the source flux makes its detection in the $E > 100$ GeV band with MAGIC and CTA difficult if not impossible, if the redshift is $z = 1.223$ (it is, however, detectable if the redshift is $z = 0.678$, as in the Fermi AGN catalogue [15]). At the same time, a dedicated low-energy-threshold ground-based γ-ray telescope, like 5@5, would be able to study the details of the EBL effects on the source spectrum, because the source would be detectable from an energy of $\sim$10 GeV.

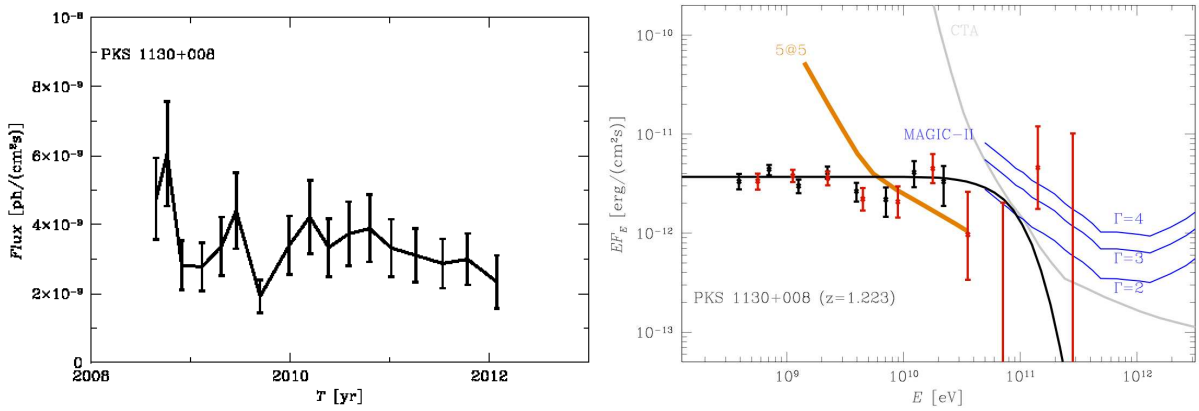

Figure 48: Lightcurve (top) and spectrum of PKS 1130+008 at the redshift $z = 1.223$. Notations are the same as in Figs. 36 and 38.

2.3.6 Discussion

Detection of the VHE γ-ray emission at energies above 100 GeV from blazars with redshifts beyond $z = 0.5$ carries important implications for the possibility of studying the cosmological evolution of the blazar population and the overall energy output from the galaxies, in the form of the EBL.

Fermi/LAT, being able to discover the VHE γ-ray signal from the high-redshift sources, does not have a capability of studying the details of the spectral characteristics of these high-redshift sources. At the same time, Fermi's detections of these sources provide a clear indication for the selection of the high-redshift targets for observations with the existing and next-generation ground-based γ-ray telescopes.

Above we have compared the Fermi flux measurements in the $E > 100$ GeV band with the sensitivity of the ground-based γ-ray telescopes. The results from such comparisons indicate that the flux levels of sources listed in table 6 are already at or below the sensitivity limit of the current generation ground-based telescopes and are, in fact, just at the sensitivity limit of the next generation facility CTA. This means that Table 6 provides a more or less exhaustive list of the high-redshift sources accessible for detection using ground-based γ-ray telescopes.

The situation with the limited capabilities for the detection of high-redshift sources from the ground could, nevertheless, change if a telescope system specially optimized for the reduction of the low-energy threshold, like 5@5, would be realized. In this case most of the sources listed in Table 6 would be detectable by 5@5 already at energies of about 10 GeV, with very high signal statistics. This would allow a high-quality study of the details of the spectral characteristics of the VHE γ-ray emission from high redshift sources. Lowering the energy threshold with 5@5 would open the possibility for detecting a much larger number of the high-redshift sources, compared to the just thirteen sources listed in Table 6.

Low statistics of the VHE γ-ray signal from the Fermi high redshift blazars does not allow to study the effect of absorption of γ-rays through their interactions with EBL photons on a source-by-source basis. However, the significance of this effect for different models of cosmological evolution of EBL could be evaluated collectively for all thirteen sources from Table 6, following the method discussed by [13]. Fig. 49 shows the energies of VHE γ-rays from distant blazars as a function of the source redshift. The data from the previous analysis at lower energies, reported by [13], are shown in grey in the same figure for comparison. The black/grey curves show the energies at which the optical depth with respect to pair production on the EBL is $\tau = 1$ and $\tau = 3$, respectively. This implies a flux suppression by a factor of $\simeq 3$ and $\simeq 20$. A naive expectation is that there should be no VHE photons from the sources in the upper part of the plot, far beyond the corresponding $\tau = 1$ or $\tau = 3$ curves. From Fig. 49 one can see that this trend of decreasing photon counts beyond the $\tau = 1$ curve holds in the redshift range $z = 0.5 - 1$, with only one photon beyond the solid black curve corresponding to $\tau = 1$ for the [107] model of EBL evolution. At the same time, the trend seems to be broken for redshifts of about $z \gtrsim 1$, where a large number of photons beyond the $\tau = 1$ curve appears. This large number of photons beyond the $\tau = 1$ curve is definitely not due to the larger source number in this redshift range. Table 6 contains seven

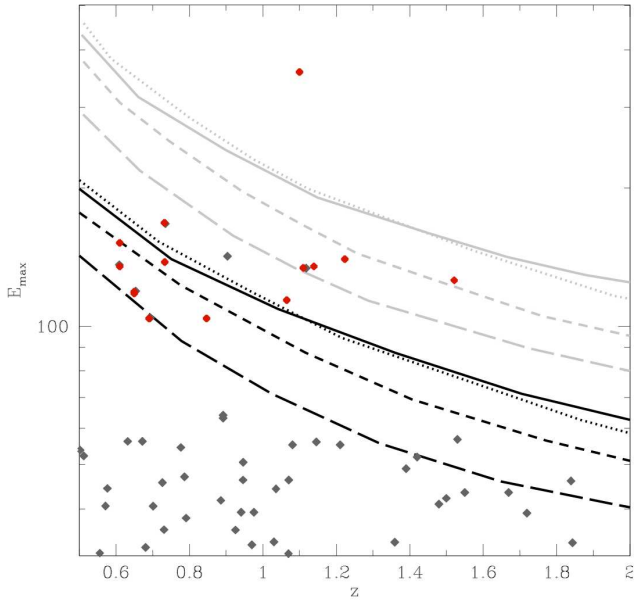

Figure 49: Energies of VHE photons from BL Lacs and FSRQ as a function of redshift. Curves correspond to the optical depth $\tau = 1$ (black) and $\tau = 3$ (grey) with respect to absorption on the EBL. Solid line: EBL from [107]; dotted line: EBL from [117]; short-dashed line: EBL from [104]; long-dashed line: EBL from [152]

sources at $z < 1$ and six sources at $z \geq 1$. Thus, the larger statistics of photons beyond the $\tau = 1$ curve should be due to a different reason.

One possibility is that the determination of redshifts of the $z \geq 1$ sources listed in the table 6 is not reliable and, in fact, the sources are at lower redshifts. In the previous section it is mentioned that this might be the case for B2 0912+29. Another possibility is that at least one or two photons in the $z > 1$ part of the diagram might still be from the background and not from the high-redshift sources. This might be the case for the highest energy photon beyond $\tau = 3$ curves, which came from the direction of RGB J0250+172. This photon has a 0.8% probability of being from the background.

If none of these possible explanations holds (this needs to be checked with more data and verification of the redshift measurements), then the over-abundance of the VHE photons beyond the $\tau = 1$ curves in the redshift range $z > 1$ in Fig. 49 should be due a physical effect. One possibility is that the EBL level at high redshifts is lower, so that the Universe is more transparent to the VHE photons, than what is implied by the currently existing models. Otherwise, new propagation effects, such as origin of the γ-ray emission in the ultra-high-energy (UHE) cosmic ray induced cascade ([45, 95, 187]) or even by new physics, like axions ([186]), should be considered.

In the scenario of [95], UHE protons with energies in the EeV range propagate cosmological distances and lose energy primarily through the proton pair production process. In this case secondary TeV gamma-rays are produced by such protons at distances 100-300 Mpc and easily reach the Earth. For this model to be valid, one needs a relatively low extra-galactic magnetic field with values 1-10 pG everywhere on the way of the protons, not only in the voids of large scale structure. Apparently, a support for such a scenario is found in a recent work of [159], in which absorption lines at the redshift beyond $z = 1$ were found in the spectra of two BL Lacs, PKS 0447-439 and PMN J0630-24. One of these BL Lacs has been recently observed in the VHE band by HESS ([285]). Explanation of the detection of PKS 0447-439 in the VHE band within conventional models would be challenging if the source redshift is indeed $z > 1$ ([45]). Thorough verification of the redshift measurement for both PKS 0447-439 and for the $z \geq 1$ sources listed in the Table 6 is extremely important for the clarification of consistency / inconsistency of the VHE band detections of the high-redshift sources with the current understanding of the mechanisms of formation of the VHE γ-ray spectra of the sources and of the cosmological evolution of the EBL.

3 AGN variability in the GeV domain

Historically, the class of blazars was defined, among other features, by their prominent variability across different wavelengths ([255, 266]). In fact, blazar variability is the fastest and of the largest amplitude among AGN ([54, 251]), so it's a remarkable phenomenon on its own.

The studies of variability of blazars and AGNs in general are crucial for understanding the physical processes, taking place in their central regions. Correlations between different wavelengths, variability time scales and spectral changes allow to get information about the state of the matter in regions of AGN, not resolvable with existing optical/infra-red interferometers. Although recent observations with radio interferometers show significant progress here (for instance, jet-launching structure was resolved in M87 ([87])), they still allow to resolve these regions only for the nearby AGNs.

Early observations in radio and X-ray band provided good evidences for the relativistic beaming in blazars ([138, 144, 145]). Optical variability of these sources extends down to intra-day time scales, and LBLs (see Sect. 1.1) are systematically more variable at these wavelengths than HBLs ([131]). Stronger variability of LBLs in optical domain is connected to the fact that in this case they are observed above the synchrotron peak of their spectra ([266] and references therein). An opposite situation is observed in soft X-rays, where there declining part of the synchrotron peak is observed for HBLs and rising part of the Inverse Compton peak is seen for LBLs.

After the launch of EGRET on board of CGRO ([3]) it became clear, that many blazars emit in the γ-ray domain ([262]). Almost all blazars detected by EGRET, at least those bright enough for the instrument to collect enough statistics, were found to be variable on the time scales of months ([127]); for some blazars, that were bright enough to permit a search of faster variability, variations on the time scales of few days were found (3C 279: [153], 1633+382: [180], PKS 0528+134: [141]). In some cases bright flares from blazars were observed, reaching hight fluxes and showing evidences for variability time scales even shorter than a day ([181]). Not only blazars were found variable in γ rays, EGRET also found that their energy output in this domain is often larger than what is emitted in lower energy domains (see, for instance, [141, 180]).

In the TeV domain Whipple cherenkov telescope ([4]) in early 90s has detected two blazars – Mrk 421 ([227]) and Mrk 501 ([229]). These observations indicated, that the emitter power in TeVs is comparable to that of other domains. Whipple has also revealed that Mrk 421 is variable at TeV energies on a several-day ([150]) or even less than a day ([109]) time scales. Later observations with HESS ([9]) detected very fast variability from PKS 2155-304 – variability time scales as short as several minutes were seen ([17, 43]). Mrk 501 was re-observed with MAGIC ([5]) in 2005, detecting flux doubling times down to 2 minutes ([52]). Observations of 1ES 1218+304 with VERITAS ([6]) telescope also have shown that the source is variable on a daily time scales ([142]).

Early GeV-TeV observations have led to several conclusions ([265]): (a) from the requirement, that γ-ray emitting region should be transparent with respect to the pair production it followed that γ rays are relativistically beamed; (b) blazars emit a significant fraction of their luminosity at very high energies – power output in γ rays is comparable to the of all other wavelengths; (c) the energy of the second peak of blazar spectra is higher for the sources whose first peak is also at higher frequencies.

The successor of EGRET, Fermi/LAT, adds more data to the picture of the blazar variability at high energies. In fact, blazars, constitute almost half of all sources and the majority of AGNs, detected in the GeV domain with LAT ([208]). The Second Catalogue of Active Galactic Nuclei Detected by the Fermi/LAT [23] states that for 348 blazars out of 705 presented in the catalogue the variability is detected with significance greater than 99%. The more variable sources in this catalogue were found to have softer spectra, indicating that they are observed above the the second, Inverse Compton, peak of their spectra, where the variability amplitude is larger. The analysis of this source sample also indicate that FSRQ objects are on average more variable than BL Lacs. It also indicates that less luminous blazars have lower level of variability than more luminous ones.

High sensitivity of Fermi/LAT enables the searches of very fast variability on the time scales of several hours ([105, 238]) – a quality which will be used in this section. In what follows I present two my publications [206, 273] aiming to study the fastest blazar variability accessible to Fermi/LAT. I start with one of the most interesting blazars on the sky – OJ 287.

3.1 Fast variability of γ-ray emission from supermassive black hole binary OJ 287

3.1.1 Introduction

Blazar OJ 287 ($z = 0.306$ ([252])) provides a unique laboratory for the study of the mechanism of AGN activity, because this is one of the few AGN known to host binary black hole system ([162, 271]). In this system, a lighter black hole of the mass $M_{\rm BH1} \simeq 1.3 \times 10^8 M_\odot$ orbits a heavier black hole of the mass $M_{\rm BH2} \simeq 1.8 \times 10^{10} M_\odot$ with a period $P_{\rm orb} \simeq 11.65$ yr ([245, 271]). Separation of the components of the system at periastron is just about 10 Schwarzschild radii of the heavier black hole, so that the orbital motion is strongly affected by the relativistic gravity effects ([269]).

OJ 287 is known to belong to the BL Lac sub-class of AGNs, which means that it emits a relativistic jet whose direction is aligned with the line of sight. It is not clear a priori, which of the black holes ejects the observed relativistic jet. Following a simple argument, which does not take into account the relativistic beaming of the jet emission, one would assume that the observed relativistic jet is the one ejected by the heavier black hole, simply because the bigger black hole accretes more matter and, therefore, could produce a more powerful jet. Most of the existing studies of multi-wavelength blazar activity of OJ 287 adopt this assumption (see e.g. [271]). However, relativistic jets in BL Lacs are known to have Doppler factors $\delta \gg 1$. This results in boosting of the apparent luminosity of the jets by a factor δ^4, when the jets are viewed face-on. Thus, if the less powerful jet emitted by the smaller black hole is aligned with the line of sight, while the jet from the larger black hole is not, the jet from the smaller black hole might give dominant contribution to the source flux.

Here I present the results of my publication [206] and show, that variability properties of γ-ray emission from the source indicate that the relativistically beamed emission comes from the jet produced by the smaller black hole. Independently of the value of the Doppler factor of the jet δ, the shortest observed variability time scale ΔT_{min} imposes a constraint on the size of the jet's "central engine", $R_{\rm CE} \lesssim c\Delta T$ ([74, 194]). In the case of OJ 287, $R_{\rm CE}$ turns out to be much smaller than the Schwarzschild radius of the more massive black hole, but compatible with the size of the smaller mass black hole.

Observation of γ-ray emission from the base of the jet of the smaller black hole in the system makes OJ 287 a unique laboratory for the study of mechanisms of jet production. Regular orbital modulation of the physical parameters of the ambient medium around the $1.3 \times 10^8 M_\odot$ black hole provides a unique possibility to study the response of the jet to the changes of the properties of the accretion flow and of the external medium in which the jet propagates. In this respect, the OJ 287 system provides a scaled-up analogue of Galactic γ-ray-loud binaries, in which orbital modulation of γ-ray emission enables a study of the response of the relativistic outflow from a compact object (a neutron star or a black hole) to the changes of the properties of the external medium (stellar wind and radiation field of a companion star) (see e.g. [284]).

3.1.2 Fermi/LAT observations

In order to study the variability of the γ-ray signal during the flaring activity, we have processed publicly available data of the Fermi/LAT instrument, using the Fermi Science Tools provided by the Fermi Science Support Centre. The data were selected using *gtselect* tool. The light curves were produced with the help of *gtbin* and *gtexposure* tools as it is explained in the Fermi data Analysis Threads[18].

Fig. 50 shows the long-term light curve of the source at the energies above 0.1 GeV over the August 2008 – September 2010 period, binned to achieve signal to noise ratio S/N=5 per time bin. Photons were collected from the circle 2° in radius and centred on OJ 287. The flaring activity period, which started on October 5 2009, could be readily identified. The detailed light curve of the flaring period, shown in Fig. 51, reveals several well separated flares. The brightest flare which happened on October 22, 2009 was reported by [76]. Follow up observations of the October 22 flare by the Swift/XRT have revealed an increase of the X-ray flux accompanying the γ-ray flare ([80]).

The direction towards OJ 287 is situated close to the plane of Ecliptic. The light curve of the source could be affected by the passage of the Sun through the field of view of the telescope. The periods of the Sun passage within the region of the radius 15° centred on OJ 287 (the sky region chosen for the

[18] `http://fermi.gsfc.nasa.gov/ssc/data/analysis/scitools/`

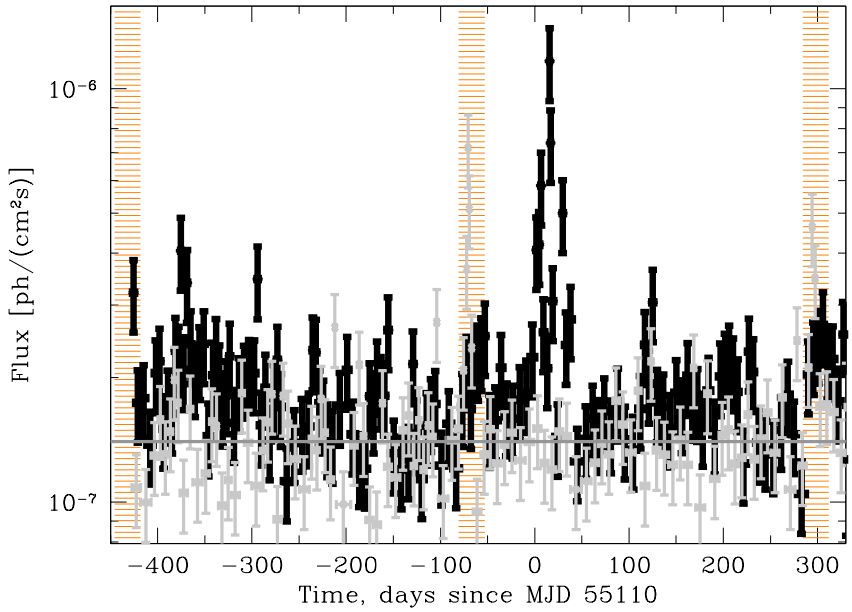

Figure 50: August 2008 – January 2010 light curve of OJ 287 (black) and background region (grey). Orange bands mark the periods of the passage of the Sun through the region of observation.

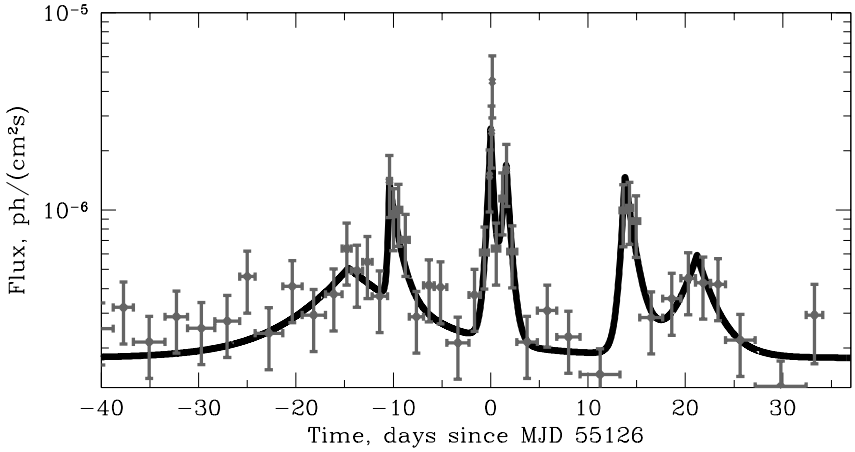

Figure 51: Light curve of October-November 2009 flare of OJ 287 in the $E > 0.1$ GeV energy band, binned in time bins with S/N ratio equal to 3. Black curve shows model fit to the light curve, Eq. (4) with parameters given in Table 7.

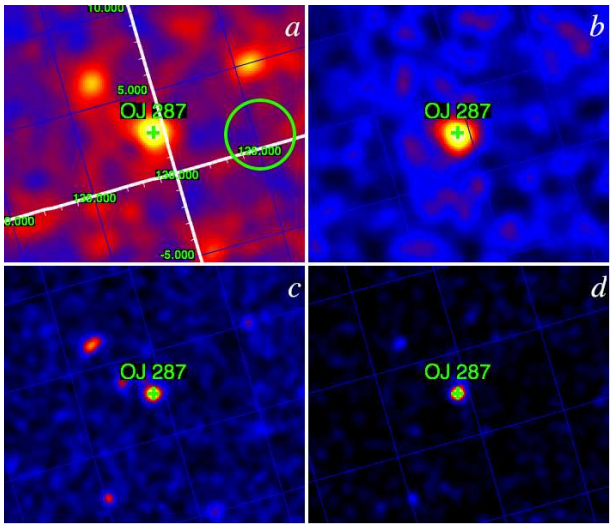

Figure 52: Images of sky region around OJ 287. Panels *a* and *c* show 0.3-1 GeV and 1-300 GeV band images for the entire observation period. Panels *b* and *d* show 0.3-1 GeV and 1-300 GeV band images during the flaring activity of OJ 287. Coordinate grid show ecliptic coordinates. Green circle shows the region from which the background light curve was extracted. Images in the 0.3-1 GeV band are smoothed with a Gaussian of the width 1°. Images in the 1-300 GeV band are smoothed with the Gaussian with 0.5° width.

analysis) are shown by the orange-shaded strips in Fig. 50. Possible effect of the Sun passage on the source light curve is most clearly seen in the light curve produced for the region of the radius 2° displaced by $\sim 5°$ from the position of OJ 287 to the position RA=127.11, DEC=19.89. No source is detected at this position, so the light curve of this region (shown by grey data points in Fig. 50) can be considered as a measure of the diffuse background level close to the position of OJ 287. One could notice a flare in the background light curve, associated with the Sun passage close to the background extraction region. The effect of the Sun passage on the light curve of OJ 287 is less pronounced (see Fig. 50), because the source is situated higher above the Ecliptic plane, compared to the background region.

Analysis of the images of γ-ray sky around OJ 287 show that, apart from OJ 287, the region of the radius 15° centred on OJ 287 contains several other sources (most clearly visible in the 1-300 GeV band image in the panel *c* of Fig. 52). However, these sources are quite weak, so that they are not detected on one month exposure time scale corresponding to the duration of the flaring activity of OJ 287(see the right panel of Fig. 52). Absence of strong sources near OJ 287 ensures that the observed variability of the signal from the source during the flaring period is not affected by possible variable emission from a nearby source for which the tail of the point spread function overlaps with that of OJ 287.

The $E > 0.1$ GeV light curve of the flare consists of several well separated pulses with quite sharp rise and decay. To find the rise and decay times we have fitted the light curve with a phenomenological model of a sum of exponentially rising and decaying pulses

$$F(t) = B + \sum_{k=1}^{3} \begin{cases} A_k \exp\left((t-t_k)/t_{rk}\right), & t < t_k \\ A_k \exp\left(-(t-t_k)/t_{dk}\right), & t > t_k \end{cases} \tag{4}$$

where $B = const$ is the background level. The background level was found from the circle of the radius 2° displaced by 5 degrees from the position of the source. Parameters of the model function (4), derived from the fitting, are given in Table 7.

One can see from Fig. 51 and Table 7 that brightest flares are characterized by the quite sharp rises and decays, with the rise/decay times of several hours. At this time scales measurement of the rise/decay times of the flares is complicated by the fact that Fermi/LAT telescope observes a given patch of the sky once in 3.2 hours (once per two rotation periods of $\simeq$ 96 min). This is clear from Fig. 53 in which light curve for the time interval of several hours around the brightest flare from the source is shown in

k	t_k d	t_{rk} d	t_{dk} d	A_k $\times 10^{-6}$ cm$^{-2}s^{-1}$
1	1.4 ± 0.5	$5.0^{+10.0}_{-2.5}$	$7.0^{+4.0}_{-3.5}$	$0.33^{+0.07}_{-0.08}$
2	$5.6^{+0.2}_{-0.3}$	$0.15^{+0.37}_{-0.14}$	$1.0^{+0.6}_{-0.4}$	$1.0^{+0.4}_{-0.3}$
3	$16.02^{-0.05}_{+0.07}$	$0.33^{+0.19}_{-0.09}$	$0.30^{+0.15}_{-0.1}$	$2.3^{+0.6}_{-0.6}$
4	$17.6^{+0.18}_{-0.15}$	$0.5^{+0.4}_{-0.25}$	$0.46^{+0.25}_{-0.18}$	$1.5^{+0.5}_{-0.5}$
5	$29.8^{+0.4}_{-0.3}$	$0.4^{+0.3}_{-0.23}$	$1.0^{+0.5}_{-0.4}$	$1.3^{-0.3}_{+0.3}$
6	$37.2^{+1.3}_{-1.0}$	$2.0^{+1.8}_{-1.0}$	$1.9^{-0.9}_{-2.2}$	$0.41^{-0.14}_{+0.12}$

Table 7: Parameters of the model fit (see Eq. (4)) to the light curve of the γ-ray flare of OJ 287 together with their 68% confidence ranges.

more details. The upper panel of the figure shows the $E \geq 0.1$ GeV light curve of the source. The lower panel shows the energies of photons collected from the circle of the radius 2° centred on the source (black points) and photons collected from a background extraction circle displaced of the same radius displaced by 5 degrees from the source position. Photons from the source and background regions come only within periodic time intervals spaced by 3.2 hr marked by vertical grey strips in the two panels of the Figure 53. It is clear that the Fermi/LAT pointing pattern does not allow to constrain the rise/decay time of the flares to accuracy better than 3.2 hr. The apparently abrupt end of the flare (12 photons from the source are detected between t = MJD55126.0 + 3 hr and t = MJD55126.0 + 4 hr, while no photon is detected within the subsequent observation period MJD55126.0 + 6.2 hr < t < MJD55126.0 + 7.2 hr) limits the decay time of the flare to be less than 3.2 hr. Assuming that the source flux did not change in the time interval following the peak of the flare, one could estimate the chance probability of detecting zero photons in this time bin to be 7×10^{-4}, taking into account the exposures in the two adjacent time intervals with maximal and zero count rates, 3.3×10^6 cm^{2}s and 2×10^6 cm^{2}s, respectively.

To summarize, both fitting of the light curve profile with a phenomenological exponential rise / exponential decay model and and direct photon counting in the individual 1 hr long Fermi/LAT exposures indicate that the flux from the source is significantly variable on time scales shorter or comparable to 3-10 hr. This fact has important implications for the physical model of the origin of the γ-ray emission from the OJ 287 system.

3.1.3 Origin of the relativistic jet in OJ 287

Constraint on the variability time scale of the γ-ray flares $T_{\rm var} = \min(t_{rk}, t_{dk}) \leq 3.2$ hr, derived above, enables to identify the γ-ray emission site within the binary black hole system of OJ 287.

It is commonly accepted that γ-ray emitting jets are generated by the AGN "central engines", the supermassive black holes, on the distance scales of the order of gravitational radius of supermassive black hole

$$R_g = \frac{G_N M_{\rm BH}}{c^2} = 2 \times 10^{13} \left[\frac{M_{\rm BH}}{1.3 \times 10^8 M_\odot} \right] \ {\rm cm}, \tag{5}$$

where $M_{\rm BH}$ is the black hole mass. The minimal variability time scale of the electromagnetic emission originating from the AGN central engine is expected to be not shorter than the light crossing time of the supermassive black hole,

$$\begin{aligned} T_{\rm lc} &= (1+z) 2R_{\rm BH}/c = 2(1+z) \left(R_g + \sqrt{R_g^2 - a^2} \right) /c \\ &\simeq \begin{cases} 0.5 \left[M_{\rm BH}/1.3 \times 10^8 M_\odot \right] \ {\rm hr}, & a = R_g \\ 0.9 \left[M_{\rm BH}/1.3 \times 10^8 M_\odot \right] \ {\rm hr}, & a = 0 \end{cases} \end{aligned} \tag{6}$$

where $R_{\rm BH}$ is the size of the black hole horizon and $0 < a < R_g$ is black hole rotation moment per unit mass. Variability of X-ray emission at time scale $T \sim T_{\rm lc}$ is observed in the X-ray emission from Galactic sources powered by black holes with masses $M_{\rm BH} \sim 10 M_\odot$ ([233]). Variability at the time scale $T_{\rm var} \sim T_{\rm lc}$ is observed in the γ-ray emission from blazars as well ([37, 42, 52, 109, 191, 194]).

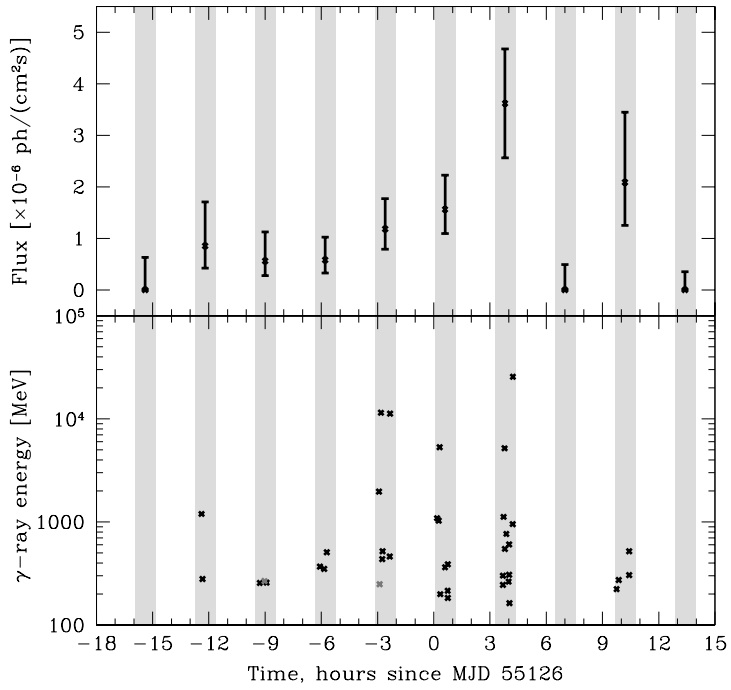

Figure 53: Upper panel: light curve of the brightest episode of the October-November 2009 flare of OJ 287 in the $E > 0.1$ GeV energy band. Lower panel: energies and arrival times of the γ-rays from the source (black points) and from the background region (grey points). Vertical grey strips show the periods when the source was in the field of view of the LAT telescope.

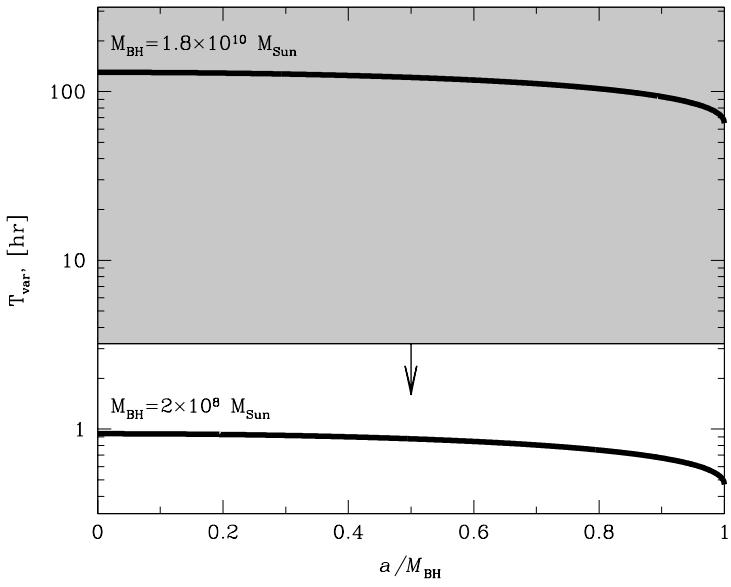

Figure 54: Comparison of the upper bound on the variability time scale of OJ 287 flares (grey shaded region) with the light crossing times of the two supermassive black holes in the system.

Fig. 54 shows a comparison of the upper limit $T_{\rm var} \leq 3.2$ hr on the variability time scale of the flares from OJ 287 with the light crossing time of the two supermassive black holes in the OJ 287 system. One can see that the upper bound is much lower than the light crossing time of the more massive black hole with $M_{\rm BH} \simeq 1.8 \times 10^{10} M_{\odot}$, independently of the black hole rotation moment a. At the same time, the limit on the variability time scale is larger than the light crossing time of the smaller black hole. This implies that the observed γ-ray emission is generated by the jet emitted by the lower mass companion black hole in the system.

Note, that the above result does not depend on the assumptions about relativistic motion of the γ-ray emission region. Indeed, the minimal possible time scale ΔT_{min} of emission from relativistic jet moving with bulk Lorentz factor Γ does not depend on Γ and is instead determined by the size of the non-moving "central engine" which ejected the jet ([74, 194, 193]). In the jet co-moving frame, the minimal variability time scale $\Delta T'_{min} \sim \Gamma \Delta T_{min}$ is the light crossing time of the smallest size γ-ray emitting "blobs", $\Delta T'_{min} \sim R'_{min}/c$. γ-ray emitting blobs which were ejected by the jet's "central engine" of the size $R_{\rm CE}$ could not have size smaller than $R'_{min} \geq R_{\rm CE}\Gamma$ in the co-moving frame. This implies that $\Delta T_{min} \sim \Delta T'_{min}/\Gamma \sim R'_{min}/c\Gamma \geq R_{\rm CE}/c$, independently of Γ.

At the first sight, such conclusion looks counter-intuitive. Indeed, since the two black holes accrete matter from the same reservoir, the accretion rate onto the more massive black hole should be much higher. In general, a higher accretion rate should lead to production of a more powerful jet.

However, the above argument does not take into account possible relativistic beaming effects, which are usually very significant in BL Lacs. γ-ray flux from a relativistically beamed jet, moving with the bulk Lorentz factor Γ at an angle θ with respect to the line of sight, is boosted by a factor δ^4, where $\delta = (\Gamma(1 - \beta\cos\theta))^{-1}$ is the Doppler factor and β is the bulk velocity of the jet. A constraint on the bulk Lorentz factor of the jet produced by the $M_{\rm BH} \simeq 1.3 \times 10^8 M_{\odot}$ black hole could be found under assumption that the observed X-ray emission from the system ([241]) originates from the same jet region as the GeV emission.

The highest energy of the γ-ray photons coming from the source is $E_{\gamma,max} \geq 30$ GeV (see Fig. 53). γ-rays of such energies can produce e^+e^- pairs in interactions with X-ray photons of the energy

$$E_X \geq \frac{\Gamma^2 m_e^2 c^4}{(1+z)^2 E_\gamma} \simeq 0.5 \left[\frac{\Gamma}{4}\right]^2 \left[\frac{E_{\gamma,max}}{30\ {\rm GeV}}\right]^{-1}\ {\rm keV} \tag{7}$$

where we have assumed that the typical collision angles for photons emitted from the jet are $\alpha \simeq \Gamma^{-1}$. Apparent (relativistically beamed) luminosity of OJ 287 in the soft X-ray band is $L_{\rm app} \simeq 3 \times 10^{44}$ erg/s, which corresponds to the observed flux $F_X \simeq 10^{-12}$ erg/cm^{2}s ([241]). Calculating the optical depth of γ-ray emission region of co-moving size $R' \simeq \delta c T_{\rm var}/(1+z)$ and luminosity $L' \simeq \delta^{-4}(1+z)^2 L_X$ one finds

$$\tau_{\gamma\gamma} \simeq 0.5 \left[\frac{\delta}{4}\right]^{-6} \left[\frac{L_X}{10^{44}\ {\rm erg/s}}\right] \left[\frac{T_{\rm var}}{3.2\ {\rm hr}}\right]^{-1} \tag{8}$$

High energy γ-rays could escape from the source if $\tau_{\gamma\gamma} < 1$. This condition imposes a restriction on the Doppler factor $\delta \gtrsim 4$.

Thus, the observed γ-ray flux from the jet is Doppler boosted by a factor of at least $\delta^4 \gtrsim 3 \times 10^2$. It is interesting to note that even if emission from the higher mass black hole is not relativistically beamed toward observer on the Earth, it might be noticed in the spectrum of the source. Indeed, assuming a simple Eddington-like scaling of the accretion rate and jet luminosity with the black hole mass, $L_i \sim M_{{\rm BH}i}$, one finds that the relativistically beamed luminosity of the jet from the lighter black hole $L \sim \delta^4 L_1 \geq 10^2 L_1$ could, in fact, be comparable to the overall luminosity of the heavier black hole, $L_2 \sim (M_{\rm BH2}/M_{\rm BH1})L_1 \simeq 1.4 \times 10^2 L_1$. Fast variability of the emitted radiation can, therefore, serve as a tool for identification of the contribution of the emission from the lighter black hole in the overall source spectrum.

A common feature of all models of the jet production by black holes is that matter ejection into the jet is associated with rotation of matter around the black hole and/or with rotation of the black hole ([66, 67]). This implies that the characteristic time scale at which the properties of the jet could change is given by the period of rotation of the black hole itself or by the orbital period of the accretion flow.

Period of rotation around a circular orbit at a distance r from the black hole is given by ([59])

$$P(r) = 2\pi(1+z)\frac{r^{3/2} \pm aR_g^{1/2}}{cR_g^{1/2}} \,, \tag{9}$$

The + (−) sign corresponds to the prograde (retrograde) orbit. Stable circular orbits exist only down to certain distance $r_{\rm ms}$ from the black hole. The period of rotation along the last prograde stable orbit at the distance $r_{\rm ms}$ is

$$P(r_{\rm ms}) \simeq \begin{cases} 3\left[\dfrac{M_{\rm BH}}{1.3\times10^8 M_\odot}\right] \text{ hr}, & a = R_g \\ 22\left[\dfrac{M_{\rm BH}}{1.3\times10^8 M_\odot}\right] \text{ hr}, & a = 0 \end{cases} \tag{10}$$

Upper bound on the variability time scale $T_{\rm var} \leq 3.2$ hr is much shorter than period of rotation around the non-rotating black hole and is comparable or smaller than the period of rotation around maximally rotating black hole with $a = R_g$. This means that the relativistic ejections into the jet, responsible for the observed flares, are produced by the matter moving in the direct vicinity of the black hole horizon, well inside the $R = 6R_g$ radius of the last stable orbit around the non-rotating black hole.

3.1.4 Conclusions

To summarize, we find that observations of OJ 287 in the $E > 0.1$ geV energy band constrain the minimal time scale of the flux variations of the source to be shorter than 3.2 hr. The upper limit on the minimal variability time scale imposes a restriction on the size of the jet formation region. We find that the size of the jet formation region in the OJ 287 system is much smaller than the size of the horizon of the more massive black hole in the binary black hole system powering the source. This means that the observed γ-ray emission is produced by the jet ejected from the smaller mass black hole. Higher apparent luminosity of the smaller mass companion is explained by the effect of the relativistic beaming of the γ-ray emission. Combining the X-ray and γ-ray data, we find a restriction on the Doppler factor of the γ-ray emitting part of the jet, $\delta \gtrsim 4$. The observed variability time scale indicates that relativistic jet from the smaller mass black hole is formed close to the black hole horizon, well inside the last stable orbit around non-rotating supermassive black hole.

γ-ray data provide a new insight in the physical model of the unique binary supermassive black hole system in OJ 287. The γ-ray flaring activity is produced in a connection with the passage of the smaller mass black hole through the accretion disk around the larger mass black hole during the periods of close approach of the two black holes in the periastron of the binary orbit. Interaction of the smaller mass black hole with the larger mass black hole accretion disk leads to the transient episodes of ejection into the relativistic jet from the smaller mass black hole. It appears that the transient jet from the small mass black hole happens to be aligned with the line of sight, the fact responsible for the BL Lac type appearance of the source. It is not clear *a priori* if the jet from the smaller mass black hole forms only during the periastron passage or if it exists throughout the binary orbit. If the jet is powered by the transient accretion onto the black hole, it would be natural to expect that the small mass black hole jet (and the associated γ-ray emission) should disappear soon after the periastron passage on a characteristic time scale of accretion. Otherwise, if the jet is powered by the rotation energy stored in the small mass black hole, it is natural to expect that the jet and the γ-rays from it would be persistent throughout the binary orbit. The systematic monitoring of the source evolution in γ-rays on the orbital (11.7 years) time scale, which is now possible with Fermi/LAT, might clarify this question. It is interesting to note that if the jet from the smaller mass black hole is directed along the black hole spin axis, its alignment with the line of sight might be destroyed by the precession of the black hole spin axis (see [270] for detailed discussion of the orbital evolution of the system). This would mean that the BL Lac appearance of the source might be time-dependent. An immediate consequence of the misalignment of the smaller black hole jet with the line of sight should be the loss of the strong Doppler boosting of the flux. In the absence of the Doppler boosting, the emission from the smaller mass black hole might become sub-dominant compared to the emission from the larger mass black hole. Study of the details of the overall time evolution and the short time scale variability properties of the source along the orbit and from periastron to periastron should clarify the transient/permanent nature of the BL Lac appearance of the source.

3.2 Variability of γ-ray emission from blazars on the black hole time scales

3.2.1 Introduction

As it was shown in the previous section, analysis of the variability is a powerful tool for the study of the physical properties of AGNs. In the same way as it was done in the section 3.1 for single source, this kind of analysis can be extended on a sample of sources to infer some of their common properties. An example of such application of the variability searches for a ~ 100 blazars is given in this section. Here I will focus on the location of γ-ray emission site within a blazar jet, based on my publication [273].

Jets of the radio-loud AGNs are known to span over many orders of magnitude in distance, from the astronomical unit scale of the AGN central engine – the supermassive black hole (SMBH) – up to the parsec to megaparsec scales. The exact location of the "blazar emission zone" in the jet is not known. If the γ-ray flux originates within the broad-line region (BLR), where the radiation fields are intense, interactions of the γ-rays with low energy background photons lead to $e^{\pm}$-pair production, thus preventing the γ-rays from escaping the source ([164]). This problem could be avoided if the site of production of the γ-rays is located outside the BLR, parsecs away from the central SMBH.

However, the possibility of the emission region being located at large distances poses a problem for the explanation of the observed variability time scales. Over the last few years, a number of blazars were found to exhibit variability on very short time scales, down to several minutes ([17, 43, 52, 105, 206, 238], see also section 3.1). Simple causality arguments indicate that the short variability time scales could be best explained by the compactness of the γ-ray emission regions, which appears natural if the blazar emission zone is situated close to the central engine. In fact, γ-ray emission produced at the distances $D \sim \Gamma^2 R_{\rm CE}$, where $\Gamma \sim 3 - 30$ is the bulk Lorentz factor of the jet and $R_{\rm CE}$ is the size of the blazar central engine, could be still variable on a time scale as short as the light crossing time of the central engine, $t_{\rm CE} = R_{\rm CE}/c \sim 10^3\,[R_{\rm CE}/2\ {\rm AU}]$ seconds ([74]).

Although fast variability provides a strong argument in favour of γ-ray production within the BLR, close to the central engine, alternative possibilities, usually invoking very compact emission regions embedded in the larger-scale jet, have been considered to explain the fast variability phenomenon ([112, 113, 115, 190]).

Accumulation of a larger sample of fast variable blazars is needed to distinguish between the two possibilities. If the fast variability is due to the γ-ray emission region being located close to the blazar central engine, one generally expects that the shortest variability time scale is determined by the central engine's size. In this case, the minimum variability time scales of blazars are expected to scale proportionally to the mass of the central SMBH. Otherwise, if the shortest time scales are related to the compact emission regions at large distances, formed as a result of the development of instabilities intrinsic to the jet, the minimum variability time scales are not expected to depend on the size of the SMBHs powering the jets.

In this work we focus on the investigation of the minimum variability time scales of a large number of blazars observed by the Large Area Telescope (LAT) on board of the Fermi satellite ([57]) (see section 1.2.2). LAT is operating in the all-sky survey mode and is well suited for the monitoring blazar activity at different time scales in the 0.1–100 GeV energy band. At the same time, the relatively small effective area of LAT limits the photon statistics at the shortest minute–hour–day time scales, expected if the fastest variability scale is determined by the SMBH. Below we study the variability properties of a large number of blazars which were detected by LAT over a two-year exposure ([208]) and for which estimates of the mass of the SMBH exist. We demonstrate that although the minimum detected variability time scales are generally limited by the LAT sensitivity, for ~ 10 of the brightest sources LAT sensitivity is sufficient to probe the fundamental SMBH time scale. For these brightest sources, the variability at the time scale comparable to the period of rotation around the last stable orbit is in fact observed. For three sources among these, the detected minimum variability time scales are found to be truly minimum, intrinsic to the sources. At the same time, we find that LAT sensitivity is currently not sufficient to confirm or rule out the correlation of the minimal variability time scales with the SMBH mass. We argue that accumulation of a larger exposure with LAT will increase the statistics of the bright blazar flares when the sources exhibit a short time scale variability. This should open a possibility for testing the "minimum variability time scale – black hole mass" correlation.

3.2.2 The blazar sample

Fermi/LAT is a space-borne detector, sensitive to γ rays approximately from 100 MeV to 300 GeV (see section 1.2.2). This instrument operates in all-sky scanning mode, completing the survey in two revolutions ($\sim$ 3.2 hours). The Fermi/LAT two-year source catalogue [208] contains $\sim$ 1800 sources, among which $\sim$ 1000 are associated with AGNs.

For the purpose of this work, we select blazars from the LAT two-year catalogue for which estimates of the black hole masses exist. The mass estimates mainly come from observations in the optical domain, where several alternative methods for the mass estimates are used. One possibility is to use the observed correlation between the SMBH mass and velocity dispersion in the central stellar bulge observed in the nearby galaxies. Measuring the bulge velocity dispersion through spectroscopic observations of the blazar host galaxy, one could estimate the SMBH mass ([263]). Otherwise, the black hole mass could be estimated from a combination of measurement of the width of the atomic line emission from the BLR and the time delays between the continuum and line emission (reverberation mapping technique; [147]).

	Source name	Type	RA	Dec	z	$\log\left(\frac{\tau_{min}}{1\ \mathrm{s}}\right)$	$\log\left(\frac{M_{\mathrm{BH}}}{M_{\odot}}\right)$	Ref.
1	1ES 0033+595	bzb	8.964	59.854	0.086	—	7.25 ± 0.70	1
2	1ES 0120+340	bzb	20.665	34.420	0.272	—	8.69 ± 0.70	1
3	**1Jy 0138-097**	bzb	25.396	-9.481	1.034	6.03	9.63 ± 0.70	1
4	4C +15.05	agu	31.256	15.235	0.405	5.78	7.91 ± 0.70	3
5	**PKS 0208-512**	agu	32.696	-51.035	0.999	5.61	8.78 ± 0.70	3
6	**3C 66A**	bzb	35.662	43.036	0.444	5.10	8.30 ± 0.70	3
7	4C +28.07	bzq	39.472	28.778	1.207	—	7.98 ± 0.70	3
8	AO 0235+164	bzb	39.675	16.624	0.940	5.94	7.98 ± 0.70	3
9	1H 0323+022	bzb	51.545	2.413	0.147	—	8.36 ± 0.70	1
10	PKS 0336-019	bzq	54.871	-1.744	0.852	6.02	7.21 ± 0.70	3
11	1H 0414+009	bzb	64.209	1.092	0.287	—	9.05 ± 0.70	1
12	PKS 0420-01	bzq	65.807	-1.342	0.915	5.37	8.04 ± 0.70	3
13	PKS 0440-00	bzq	70.686	-0.293	0.844	4.95	7.23 ± 0.70	3
14	**PKS 0454-234**	bzq	74.268	-23.427	1.003	4.83	8.05 ± 0.70	3
15	PKS 0454-46	bzq	74.041	-46.218	0.853	—	8.05 ± 0.70	3
16	4C -02.19	bzq	75.319	-1.931	2.286	5.73	8.50 ± 0.70	3
17	**PKS 0521-36**	agn	80.769	-36.469	0.055	4.57	8.68 ± 0.12	2
18	PKS 0528+134	bzq	82.714	13.553	2.070	—	7.66 ± 0.70	3
19	1Jy 0537-286	bzq	84.846	-28.697	3.104	6.21	7.78 ± 0.70	3
20	PKS 0537-441	bzb	84.706	-44.084	0.894	6.04	8.02 ± 0.70	3
21	1ES 0647+250	bzb	102.699	25.096	0.203	—	7.73 ± 0.70	1
22	EXO 0706.1+5913	bzb	107.629	59.139	0.125	—	8.67 ± 0.70	1
23	S5 0716+714	bzb	110.476	71.350	0.300	4.80	7.74 ± 0.70	1
24	PKS 0735+17	bzb	114.524	17.703	0.424	6.05	8.08 ± 0.70	1
25	PKS 0754+100	bzb	119.288	9.963	0.266	—	8.21 ± 0.70	1
26	1ES 0806+524	bzb	122.460	52.308	0.137	—	8.65 ± 0.70	1
27	S4 0814+425	bzb	124.573	42.398	1.073	—	8.01 ± 0.70	1
28	PKS 0823+033	bzb	126.478	3.144	0.506	—	8.55 ± 0.70	1
29	B2 0827+24	bzq	127.646	24.122	0.940	—	8.41 ± 0.43	4
30	PKS 0829+046	bzb	127.987	4.486	0.174	6.06	8.52 ± 0.70	1
31	4C +71.07	bzq	130.420	70.880	2.172	4.41	7.22 ± 0.70	3
32	**OJ 287**	bzb	133.713	20.098	0.306	5.11	8.50 ± 0.70	1
33	S4 0917+44	bzq	140.236	44.697	2.189	5.08	7.88 ± 0.70	3
34	4C +55.17	bzq	149.433	55.382	0.895	5.50	8.42 ± 0.70	3
35	S4 0954+658	bzb	149.652	65.557	0.368	5.67	8.37 ± 0.70	1
36	1H 1013+498	bzb	153.788	49.432	0.212	—	8.94 ± 0.70	1
37	1ES 1028+511	bzb	157.761	50.895	0.360	—	8.70 ± 0.70	1
38	MKN 421	bzb	166.120	38.213	0.030	—	8.23 ± 0.70	1

39	1ES 1106+244	bzb	167.349	24.240	0.460	—	8.64 ± 0.70	1
40	PKS 1127-145	bzq	172.580	-14.803	1.187	—	7.75 ± 0.70	3
41	MKN 180	bzb	174.178	70.164	0.045	—	8.10 ± 0.70	1
42	4C +29.45	bzq	179.878	29.247	0.724	5.59	8.56 ± 0.21	4
43	ON 231	bzb	185.374	28.239	0.102	—	8.01 ± 0.70	1
44	**4C +21.35**	bzq	186.226	21.380	0.432	3.64	8.18 ± 0.70	3
45	**3C 273**	bzq	187.277	2.042	0.158	4.70	9.38 ± 0.17	5
46	PG 1246+586	bzb	192.063	58.350	0.847	—	9.15 ± 0.70	1
47	3C 279	bzq	194.042	-5.794	0.536	5.48	7.82 ± 0.70	3
48	1Jy 1418+546	bzb	215.067	54.376	0.153	—	8.74 ± 0.70	1
49	PG 1424+240	bzb	216.760	23.795	0.160	—	6.42 ± 0.70	1
50	PG 1437+398	bzb	219.802	39.536	0.344	6.25	8.95 ± 0.70	1
51	1ES 1440+122	bzb	220.688	11.996	0.162	—	8.55 ± 0.70	1
52	BZB J1501+2238	bzb	225.275	22.639	0.235	—	8.55 ± 0.70	1
53	**PKS 1510-089**	bzq	228.207	-9.103	0.360	3.84	8.31 ± 0.27	4
54	1H 1515+660	bzb	229.517	65.437	0.702	—	9.36 ± 0.70	1
55	AP Lib	bzb	229.435	-24.360	0.049	—	8.64 ± 0.14	2
56	RGB J1534+372	bzb	233.861	37.335	0.143	6.42	8.13 ± 0.70	1
57	PG 1553+113	bzb	238.942	11.190	0.360	—	7.25 ± 0.70	1
58	PKS 1604+159	bzb	241.770	15.876	0.357	—	8.25 ± 0.70	3
59	4C +10.45	bzq	242.148	10.494	1.226	—	8.07 ± 0.70	3
60	OS 319	bzq	243.372	34.159	1.397	—	8.22 ± 0.70	3
61	4C +38.41	bzq	248.809	38.171	1.814	4.81	7.54 ± 0.70	3
62	MKN 501	bzb	253.481	39.763	0.034	—	8.72 ± 0.70	1
63	**NRAO 530**	bzq	263.279	-13.128	0.902	4.90	8.07 ± 0.70	3
64	4C +51.37	bzq	265.060	52.201	1.375	5.70	7.97 ± 0.70	3
65	S4 1738+476	bzq	265.089	47.645	0.316	—	8.22 ± 0.70	1
66	1ES 1741+196	bzb	266.044	19.579	0.083	—	8.93 ± 0.70	1
67	**1Jy 1749+701**	bzb	267.217	70.111	0.770	4.68	9.90 ± 0.70	1
68	**OT 081**	bzb	267.876	9.640	0.322	5.47	8.64 ± 0.70	1
69	**S5 1803+784**	bzb	270.147	78.483	0.680	4.95	8.82 ± 0.70	1
70	B2 1811+31	bzb	273.395	31.722	0.117	6.26	8.82 ± 0.70	1
71	4C +56.27	bzb	276.001	56.838	0.663	6.60	9.10 ± 0.70	1
72	**PKS 1830-210**	bzq	278.413	-21.075	2.507	4.44	8.05 ± 0.70	3
73	PKS 1933-400	bzq	294.320	-39.933	0.966	—	8.06 ± 0.70	3
74	1ES 1959+650	bzb	300.020	65.157	0.047	—	8.14 ± 0.70	1
75	1Jy 2005-489	bzb	302.375	-48.834	0.071	6.48	8.57 ± 0.14	6
76	PKS 2052-47	bzq	314.068	-47.255	1.489	5.57	7.88 ± 0.70	3
77	**4C -02.81**	bzb	323.466	-1.906	1.285	5.88	9.96 ± 0.70	1
78	S3 2141+17	bzq	325.879	17.720	0.211	5.45	8.14 ± 0.34	4
79	PKS 2149+173	bzb	328.102	17.590	0.000	—	7.78 ± 0.70	1
80	PKS 2155-304	bzb	329.715	-30.219	0.117	6.69	7.60 ± 0.70	3
81	**BL Lac**	bzb	330.707	42.268	0.069	4.96	8.58 ± 0.70	1
82	PKS 2201+04	bzb	331.164	4.705	0.027	—	7.76 ± 0.13	2
83	B3 2247+381	bzb	342.512	38.419	0.119	6.15	8.64 ± 0.70	1
84	**3C 454.3**	bzq	343.497	16.153	0.859	2.94	6.76 ± 0.70	3
85	BZB J2322+3436	bzb	350.672	34.588	0.098	—	6.76 ± 0.70	3
86	1ES 2344+514	bzb	356.759	51.705	0.044	—	8.57 ± 0.70	1

Table 8: List of the sources used in this work. Boldface marks sources found to be variable on the timescales comparable with the light crossing time of the central black hole and/or the period of the last stable orbit. Source classification is that of [208]. References: (1) [281]; (2) [97]; (3) [99]; (4) [282]; (5) [218]; (6) [275].

For blazars, which form the majority of the AGNs observed in the GeV domain, it is often the case that the velocity dispersion of the bulge cannot be measured due to a strong contamination from the emission of the AGN itself. In this case, less direct estimates are used to infer the mass of the SMBH. These estimates are based on the so-called Fundamental plane, which gives the relation between the effective radius, average surface brightness and velocity dispersion of early-type galaxies ([97]). A similar correlation was found between the optical R-band luminosity of the bulge and the mass of the central SMBH ([183]).

For the purpose of this work, we combined from the literature ([97, 98, 218, 281, 282]) a list of 195 AGNs with SMBH masses measured using different methods. We further selected those sources, that were observed by the Fermi/LAT telescope. Among those, only the sources without bright companions within a 2°-radius around their positions were chosen for analysis. Such selection criterion assures that the variability properties of the source of interest are not affected by the variability of the nearby sources (the point-spread function of LAT is several degrees wide in the energy range below ~ 1 GeV – see Fig. 4). The resulting list of 86 AGNs, used in the present work, is given in Table 8.

3.2.3 Data analysis: light curves

For our analysis we used *Fermi Science Tools v9r23p1*[19] – a standard software package provided by the Fermi collaboration to reduce the data obtained by Fermi/LAT. We also made use of the Pass 7 version of the photon files, which the Fermi collaboration calls the best dataset for the Fermi/LAT analysis.[20] We selected the class 2 photons and applied the cut on the zenith angle of 105°.

To produce the light curves, we used the *gtbin* tool, and computed exposures, corresponding to each bin, with the help of *gtexposure*. We fixed the spectral indices of the sources at the values, presented in the Fermi/LAT two-year source catalogue [208]. The energy range in our analyses was set to 100 MeV – 300 GeV. As we were not interested in the absolute flux normalization, but were rather keen to detect variability, we set the software to collect photons within a small, 1° circle. This is much smaller than the 68% photon containment radius for 100 MeV, and is roughly equal to the same containment radius at 1 GeV. This way, the analysis uses only the central, core part of the PSF, omitting its wings, thus minimizing contribution from nearby sources. We built the light curves with signal-to-noise ratio (S/N) binning, with the value of S/N in each bin fixed at 4. Reducing the noise when the flux is low, such binning allows us to resolve the finest details in the light curve during the flares and, thus, to probe the fastest variability of the source.

The above-mentioned procedure is equivalent to the usual aperture photometry with two exceptions. First is that we do not collect all photons from the source, since we select only narrow central core of the PSF for our analysis. The second difference comes from the fact that we do not perform background subtraction. As the background is not expected to be variable, this should not introduce any additional time scales into our results, but might limit the sensitivity to the fast variability of weak sources.

3.2.4 Data analysis: variability search

To search for variability, we utilized the structure function (SF) approach ([246]). The SF of the light curve $x(t)$ with the time lag τ is defined as

$$SF_x(\tau) = \langle (x(t+\tau) - x(t))^2 \rangle \tag{11}$$

and represents the amount of variability at a given time scale τ. It was first introduced in astronomy by [246], and was afterwards successfully used to measure the variability of AGNs (e.g. [101]). The advantage of the SF is that it works in the time domain, making it less sensitive than the Fourier analysis to windowing problems.

There are a few important properties of the structure function, that are crucial to this work. First of all, for very small values of τ, far below the shortest variability time scale, the SF is dominated by noise in the signal and, as the noise is independent of any time scale, the structure function here is constant. For larger τ, but still below the minimum variability time scale, the SF represents the small-scale linear

[19] http://fermi.gsfc.nasa.gov/ssc/data/analysis/software/
[20] http://fermi.gsfc.nasa.gov/ssc/data/analysis/documentation/Pass7_usage.html

trends in the signal and grows as τ^2. For the time scales where the variability occurs, the change in the SF is defined by the type of the variability itself (for example, if a periodicity is present in the signal, the SF will show a dip at the corresponding period). Finally, for the largest values of τ, larger than any variability time scale present in the signal, the structure function forms a plateau at the value corresponding to the variance of the incoming signal. Thus, the overall look of the structure function for a particular light curve is defined by the combination of the minimum and maximum variability time scales, the level of noise and the particular binning used to produce the light curve. A deeper discussion of the SF properties and caveats is given in [94].

The structure function also provides a direct way of measuring the amplitude of the variability at a given time scale. The ratio of values of SF at two different time scales is the square of the ratio of the corresponding amplitudes (see Eq. 11). Probably the most convenient way of quantifying the variability amplitude is to compare the corresponding value of the SF with its plateau value in the limit of large τ, which represents the overall variance of the light curve.

To find the variability one has to compare the observed inclination slope of the logarithmically scaled SF (that is to say $\alpha{=}d\log(SF)/d\log(\tau)$) with 2 (linear growth) and 0 (below the minimum or above the maximum variability time scale). Linear growth, which is not considered to be a type of variability here, may come out for two different reasons. First, expansion of almost any signal into a Taylor series leads to a dominant linear term for sufficiently small values of τ, so generally one expects the slope of the SF to be 2 for these values of τ for any light curve. If, on the other hand, the light curve itself is a simple linear increase of flux, than there is no time scale that can be associated with this growth, and the minimum variability time scale cannot be derived. The apparent slope of the SF is affected by the noise, introduced due to the limited number of photons in each bin of the light curve. Before checking the slope of the SF one has to remove the contribution from this noise. In this work we assumed that the noise is purely Poissonian and corresponds to the amount of counts in each time bin. To calculate its influence on the resulting SF, we produced a number of simulated light curves for which the time bins were taken as in the initial one, and the number of photons in each bin was taken from the Poisson distribution with the mean equal to the initial number of photons in this bin. This way, we expected to add to the light curve the very same noise as the one already present there, and, as a result, to double the value of the noise plateau of the SF. The resulting difference between the SF averaged over the simulations and the initial SF should be equal to the value added to the SF by the noise. Having subtracted this value from the initial SF, we obtained the noise-subtracted structure functions for each source. At the same time, the distribution of the values of simulated SFs for every given τ defined the uncertainties of the structure function derived from the original light curve.

Uncertainties of the logarithmic inclination indices α of the structure function were also derived from these simulations. Because the computed error bars of the SF are correlated (as every simulation resembles the original light curve), we computed the inclination indices for each simulated SF and then used their distribution for each value of τ to compute the 95% confidence error bars for the indices of the initial structure function.

We then compared all the indices of the SF with 2 and 0, as described above. The value of τ in the first bin, that, accounting of the error bars, would have an index different from these two reference values, was considered to be an estimate of the minimum variability time scale, present in the light curve.

As an example, the light curve, structure function and structure function indices of 4C +21.35 obtained in this way are shown in Fig. 55.

The minimum variability time scale derived in this manner may depend on the particular way the bins were chosen. Binning with a constant S/N essentially collects the photons in groups of $N = S/N^2$, which is 16 in our case (S/N=4). Thus, in principle, we have a freedom to choose these bins in 16 different ways. To account for this, for each source we produced 16 different light curves, each starting from the second photon of the previous one, and in this way going over all the possible combinations. The time scales, derived for these light curves, then gave us the uncertainty to which the minimum variability is determined. If for any of those light curves variability was not found, we assumed that the source was not variable over the time interval covered by our analysis.

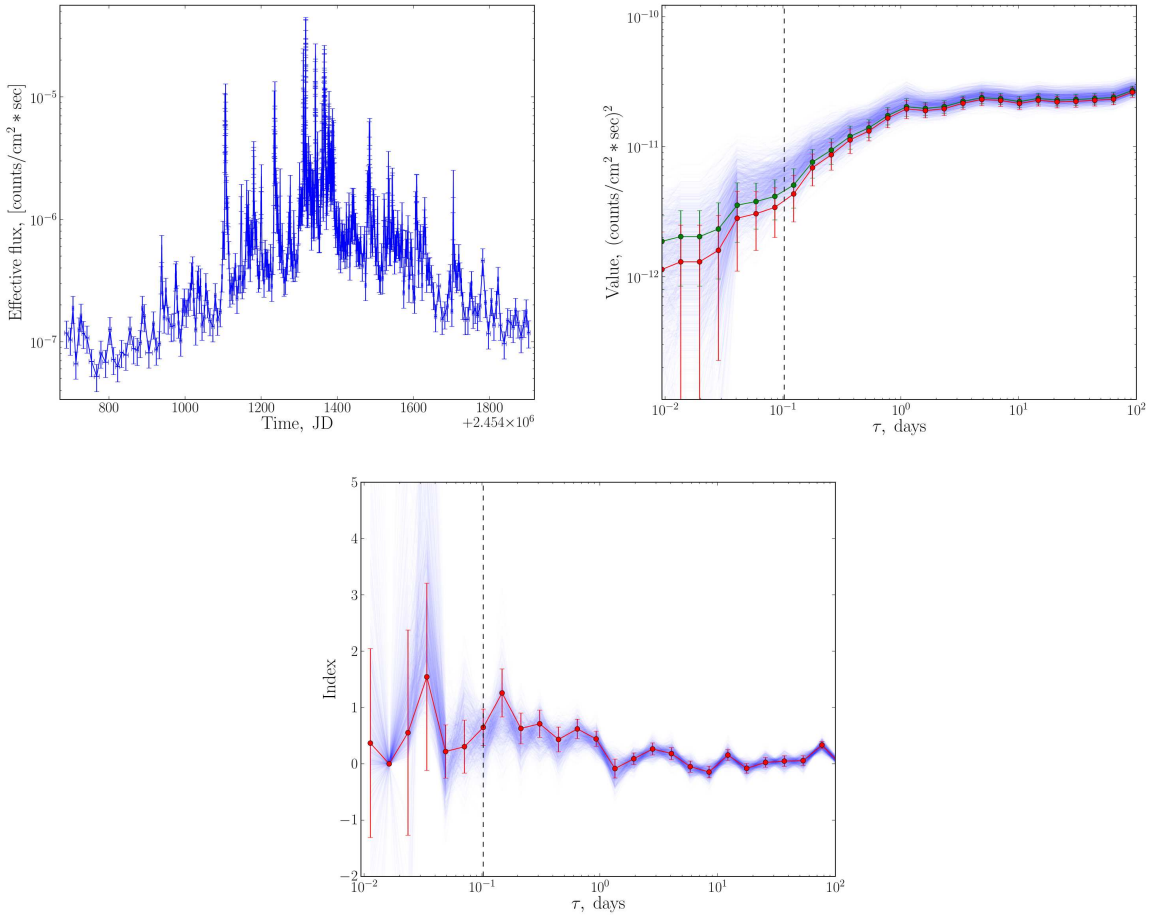

Figure 55: Example of the complete analysis cycle – 4C +21.35. Top left panel: the S/N-binned light curve. Top right panel: structure function before (green) and after (red) noise removal. Bottom panel: structure function logarithmic inclination index. Light blue lines represent the distribution of simulated SFs (top right panel) and their indices (bottom panel) used to compute the error bars (95% confidence range). Minimum present variability time scale, marked with the dashed vertical line, is 0.1 days.

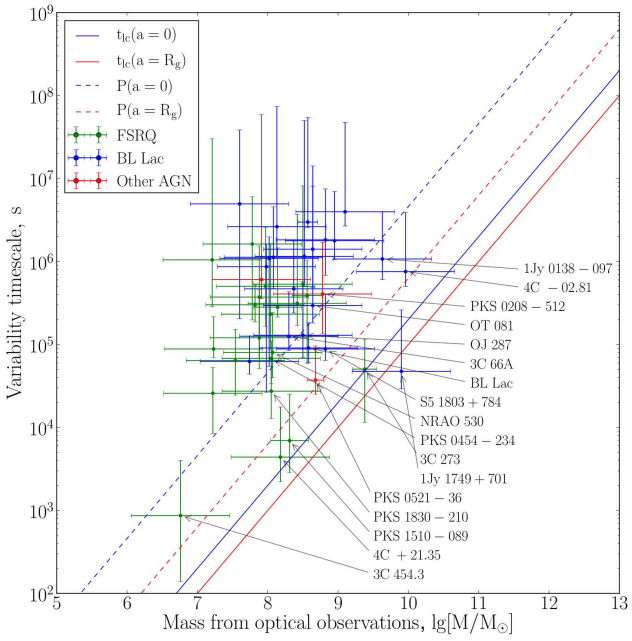

Figure 56: Measured minimum variability time scales vs. mass of the central black hole for the AGNs from table 8. Solid lines represent the light crossing times for maximally rotating (red) and non-rotating (blue) black holes, dashed lines – the same for the period of the last stable prograde orbit.

3.2.5 Results

The derived minimum variability time scales, plotted versus the corresponding SMBH mass, are shown in Fig. 56. As can be seen from this figure, the majority of blazars in our sample vary on time scales significantly longer than the light crossing times of their SMBHs, shown by the solid straight lines (see Eq. 6):

$$T_{lc} \simeq (1+z) \begin{cases} 10^3 \left(\frac{M_{BH}}{10^8 M_\odot}\right) s, & a = R_g \\ 2 \times 10^3 \left(\frac{M_{BH}}{10^8 M_\odot}\right) s, & a = 0 \end{cases} \tag{12}$$

where $R_g = GM_{BH}/c^2$ and $a = J_{BH}/M_{BH}c^2$ is defined by the angular momentum J_{BH} of the black hole and lies in the range $0 \leq a \leq R_g$.

A small fraction (some $\sim$ 10%) of the sources demonstrate variability time scales as small as the period of the last stable prograde orbit (shown by the dashed lines in Fig. 56, see Eq. 9)

$$P(r_{min}) = \begin{cases} \frac{4\pi R_g}{c} \simeq 6 \times 10^3 \left(\frac{M_{BH}}{10^8 M_\odot}\right) s, & a = R_g \\ \frac{12\sqrt{6}\pi R_g}{c} \simeq 5 \times 10^4 \left(\frac{M_{BH}}{10^8 M_\odot}\right) s, & a = 0 \end{cases} \tag{13}$$

From Fig. 56 one can note that different blazar types, BL Lac objects and flat spectrum radio quasars (FSRQs) exhibit variabilities at different time scales, with FSRQs being systematically variable at shorter time scales. It is not clear a priori if this reflects the difference in the mechanisms of γ-ray emission in these types of objects or is related to a selection bias or is an instrumental effect in LAT.

It is also not clear a priori if the sources which do not reveal variability on time scales as short as the black hole light crossing time and/or the period of rotation around the last stable orbit are just not

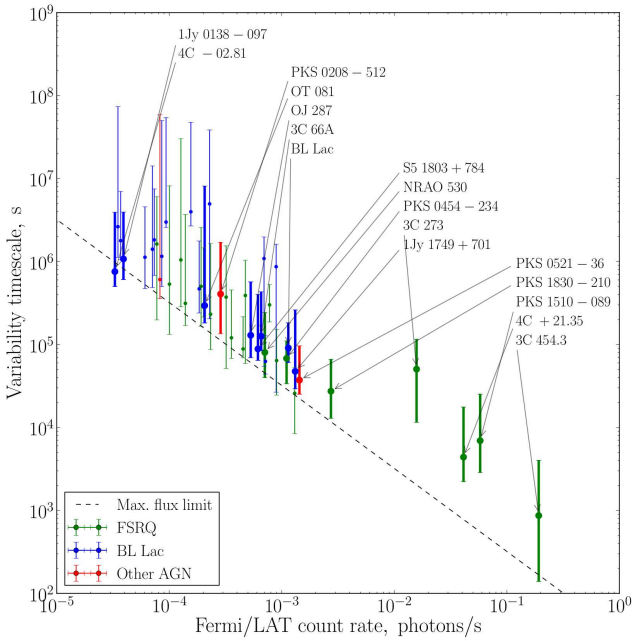

Figure 57: Measured minimum variability time scales vs. maximal count rate found in the present analysis. Dashed line represents the minimum variability time scale measurable with a given count rate. Sources found to have variability on the time scales comparable to/shorter than the period of the last stable orbit are in bold.

variable on these time scales or the sensitivity of the LAT is not sufficient to detect variability on such short time scales.

In order to investigate the sensitivity limit of the LAT, we plot in Fig. 57 the dependence of the minimum variability time scale on the peak count rate in the LAT. From this figure one can see the trend that the minimum measured variability time scale decreases with increasing peak count rate. This can be readily explained by the fact that detection of variability at a given time scale requires sufficient signal statistics. The minimum statistics in our case is 16 photons in one time bin. The minimum detectable variability time could not be shorter than the time necessary for the collection of 32 photons (there should be at least two time bins to compare the fluxes). This minimum detectable scale is shown by the dashed line in Fig. 57. One could see that the detected variability time scales follow the minimum detectable time scale line. Thus, the non-detection of variability of the signal from most of the blazars on SMBH time scales is not related to the absence of such variability, but is rather due to the sensitivity limit of the LAT.

From the same figure one could see that the difference in the variability time scales of FSRQs and BL Lac objects is due to the fact that FSRQs are on average brighter than BL Lac objects in the LAT energy band. Higher count rates of FSRQs allow the detection of shorter variability time scales for these sources.

One can also note from Fig. 57 that for three blazars, namely, 3C 273, 4C +21.35 and PKS 1510-089, the sensitivity of Fermi/LAT allows the detection of a variability that is an order of magnitude faster than actually observed. This suggests that the minimum variability time scales obtained for these sources correspond to truly minimum time scales, defined by the physics of their emission regions. Analysis results for these sources are briefly summarized below.

3C 273 was variable by a factor of ~ 100 in terms of flux over the period of the Fermi/LAT observations. This highly variable source is also one of the brightest in our sample, thus allowing us to study the variability at the smallest time scales. This is demonstrated in Fig. 58, where one of the bright flares,

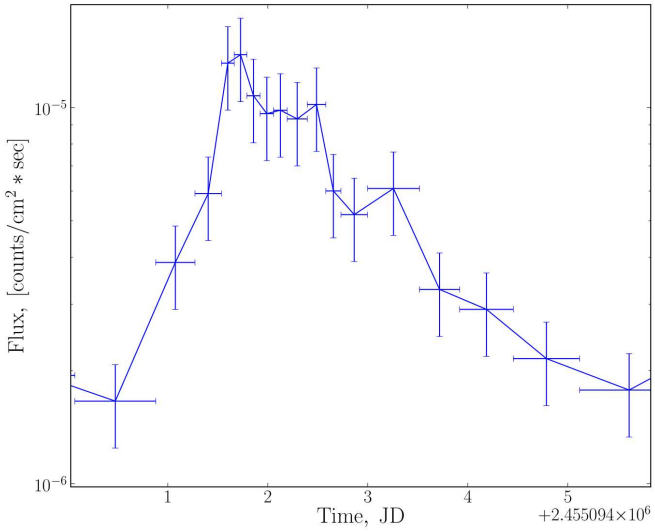

Figure 58: Part of the light curve of 3C 273 around the 21th of September 2009 (JD 2455096) with the bright flare in it.

which occurred on the 21th of September 2009, is shown. As can be seen from this figure, the brightness of this flare ensures that a sufficient number of photons per bin is achieved even for several hours long intervals, so variability down to a few hours could be, in principle, detectable for this particular light curve if the variability amplitude is large enough, whereas our analysis indicated, that only $\sim$ day time scales are present (Fig. 57). This can be seen from Fig. 59, which shows the structure function for this particular light curve. The minimum variability time scale, found from our analysis of the entire light curve, is $0.58^{+0.76}_{-0.45}$ days. The corresponding light-crossing time of the central black hole and period of rotation at the last stable orbit can be estimated from Equations (12) and (13): $t_{lc} \approx 0.3 - 0.6$ days and $P(r_{min}) \approx 1.7 - 14$ days, depending on the black hole rotation momentum.

A curious feature seen in Fig. 59 is a dip at the time scale of $\sim$ 5 days, which may indicate (quasi)periodic changes in the light curve. Indeed, this behaviour is seen in the light curve, with the most prominent episode shown in Fig. 60. If this is associated with the emission of some blobs of gas just about to fall onto the black hole, this gives us the period of rotation on the last stable orbit around the central SMBH. As the exact value of this period depends on the black hole's rotation momentum, similar measurements (with better statistics) could be used to measure the latter.

4C +21.35 is another highly variable source with bright flares (see Fig. 55). The minimum variability time scale, determined by our analysis, is $0.050^{+0.022}_{-0.024}$ days or $1.20^{+0.53}_{-0.58}$ hr. Visual inspection of the light curve suggests that it took place during the brightest flare on the 30th of April 2010. As Fermi/LAT operates in the all-sky scanning mode with the scanning period of 3.2 hr, this measurement of the variability time scales below 3 hr may be affected by the fact that the telescope did not observe the source constantly. Consequently, it would be more conservative to say that the minimum detected variability time scale lies between 0.5 hr, which is the average duration of the observation of a given patch of the sky, and 3.2 hr.

PKS 1510-089 has produced a number of bright flares during the period of the Fermi/LAT operation, with the strongest one taking place on the 19th of October 2011. The minimum variability time scale, derived through the SF analysis, is $0.11^{+0.18}_{-0.06}$ days or $2.6^{+4.4}_{-1.5}$ hr. Similarly to the case of 4C +21.35, we visually inspected the light curve and concluded that this estimate corresponds to the above-mentioned flare. As the derived time scale is smaller than 3.2 hr, this estimate is subject to the same uncertainty, as the estimate for 4C +21.35. At $\tau \simeq 50$ days, the structure function exhibits a dip, that continues up to the time scales comparable with the duration of the light curve, which is the longest time scale we can test with our analysis.

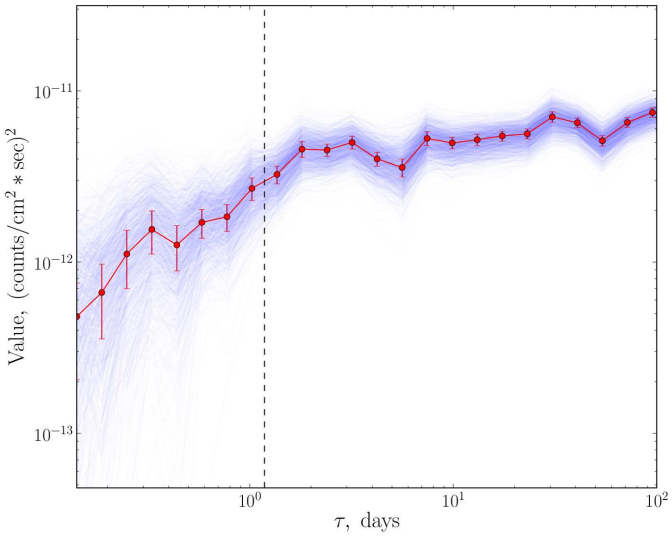

Figure 59: Structure function of the light curve of 3C 273, partially shown in Fig. 60. Error bars correspond to 68% confidence ranges. The structure functions from the simulated light curves, used to determine the error bars, are shown in light blue. The minimum detected variability time scale – ≈ 1.18 days – is marked by the vertical dashed line. A dip in the structure function is seen at $\tau \sim 5$ days.

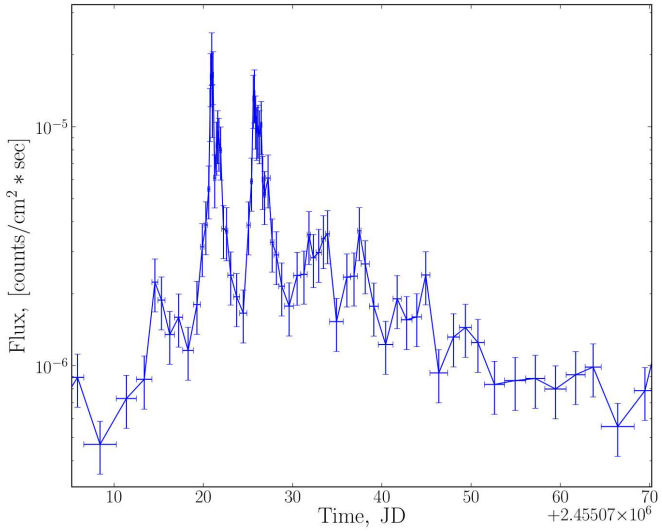

Figure 60: Part of the light curve of 3C 273 in September–November 2009, which shows a possible quasi-periodicity in it.

3.2.6 Discussion

The minimum variability time scale provides information on the size and location of the γ-ray emission region and/or on the physical process responsible for the emission. In the case of blazars, the high-energy γ-ray emission might originate from a "blazar emission zone" in the jet at large distance from the central SMBH or, alternatively, from the direct vicinity of the black hole. We have proposed a method to distinguish between these two scenarios via the study of the correlation of the minimum variability time scale of γ-ray emission with the mass of the SMBH. In the former case, no such correlation is expected, because the shortest variability time scales are determined by the size scales and/or Lorentz factors of small inhomogeneities in the blazar jets (possibly formed via development of plasma instabilities or magnetic reconnection events). In the latter scenario, a correlation is generally expected because the shortest variability time scale is determined by the size of the blazar central engine.

We have attempted to verify the existence of the "minimum time scale – black hole mass" correlation, using the Fermi/LAT data. Our analysis shows that the LAT sensitivity is sufficient to detect variability time scales as short as the SMBH light crossing time and/or period of rotation around the last stable circular orbit for a number of bright flaring blazars; see Fig. 56. From this figure one could see that ~ 10 blazars (out of the 86 considered in the analysis) exhibit variability on the "fundamental" SMBH time scales. At the same time, none of the sources is variable on time scales shorter than the black hole light crossing time.

From the same figure, one could see that most of the sources are variable at least on the time scales within an order of magnitude from the period of rotation around the last stable orbit around a Schwarzschild black hole. For most of the sources, the minimum variability time scale measured by LAT is determined by the low statistics of the signal in LAT, rather than by the physics of the γ-ray emission intrinsic to the source. This is clear from Fig. 57, in which a trend of decreasing minimum measured variability time scale with increasing peak flux is observed. Only three sources in our sample (3C 273, 4C +21.35 and PKS 1510-089) deviate from the formal sensitivity limit due to the finite γ-ray count rate in the LAT, shown by the dashed line in Fig. 57.

In these three sources the measured minimum variability time scale might be determined by the physics of the source, rather than by LAT performance. In this case the measurement of the minimum variability time scale would provide important information on the nature of the γ-ray emission. Indeed, the estimates of the masses of black holes in 4C +21.35, PKS 1510-089 and 3C 273 differ by more than an order of magnitude, but in all three sources the minimal variability time scale derived from the LAT data is close to the light crossing time of the SMBH. This provides a support for the hypothesis of a relation between the minimum variability time scale and the size of the blazar central engine. It is clear, however, that accumulation of a larger sample of blazars, for which the intrinsic minimum variability time scale is measured, is needed before definitive conclusions on the validity of this hypothesis could be drawn.

One possible caveat of the measurement of the minimum variability time scale in 4C +21.35, PKS 1510-089 and 3C 273 could be in the peculiarity of the observation mode of the LAT. LAT images each particular direction on the sky for the time spans of ~ 0.5 hr once every 3.2 hours. Detection of variability on the time scales between 0.5 and 3.2 hours could, therefore, be affected by the irregularity of the LAT exposure. In the cases of PKS 1510-089 and 4C +21.35, the minimum detectable variability time scales are shorter than 0.5 hr and so, in principle, the variability could be measured within a single 0.5 hr exposure (with several time bins contained in this exposure). However, in the case of 3C 273, the minimum measurable variability time scale is close to 0.5 hr, and so the variability on this time scale might be missed if a particular flare of the source is not fully contained within a single 0.5 hr exposure. At the same time, 3C 273 produced a number of bright flares over the three year exposure with LAT, so it is perhaps unlikely that a half-hour scale variability has been missed in all of them. Clarification of the issue of the instrumental 3.2 hr and 0.5 hr scales in the search for the minimum variability time scales will become possible with the accumulation of more flaring sources with minimum detectable variability time scales in this range.

If the observed minimum variability time scales are indeed related to the time scales of the SMBH in the blazar central engine, they provide a direct measurement of the size of the central engine without any uncertainty related to the Doppler factor of the emitting plasma ([194]). Indeed, as the black hole and the observer are located in the same rest frame, the variability produced by the black hole will be seen by the observer at the very same time scale, independently of what happens on the way with the medium

carrying the emission. Thus, the only difference between the intrinsic and observed time scales comes from the cosmological redshift of the source, which lengthens the observed time scales by $(1 + z)$ with respect to the intrinsic ones. Thus, γ-ray observations could potentially provide independent estimates of the masses of SMBHs in the cores of AGNs, providing an important tool in the context of the study of the formation and evolution of the SMBHs. Indeed, in our analysis only 86 sources with known estimates of the SMBH masses were included (see Table 1). However, the LAT AGN catalogue [208] includes a much larger number of variable sources for which measurements of the minimum variability time scales could be obtained, resulting in estimates (or upper limits) of the masses of SMBHs. The γ-ray tool for estimating black hole masses would be only usable after accumulating larger statistics of the measurements of the intrinsic minimum variability time scales of γ-ray emission from blazars and verification of the possible correlation between the black hole mass and variability time scale shown in Fig. 56.

As mentioned before, current instruments, such as Fermi/LAT, allow only the brightest objects to be studied at the sufficient level of details. The question of whether the minimum variability time scale is indeed limited by the size of the central black hole, thus, might need to wait for the new generation of γ-ray instruments to become operational.

4 Measurement of the IGMF using the γ-ray observations of blazars

4.1 Methodology: how do we measure magnetic field with γ-ray data

Blazars are powerful emitters of high-energy radiation, visible from large distances. This fact allows to study their evolution with the redshift and opens a possibility to study the intergalactic medium, irradiated by blazars. Over the last decade γ-ray observations of distant blazars were used to estimate the amount of the Extragalactic Background Light (EBL) through the measurements of the apparent absorption of VHE γ-ray emission in interactions with the low energy EBL photons (see Sect. 1.3.1). An interesting extension of this is a possibility to measure the Intergalactic Magnetic Field (IGMF) (see Sect. 1.3.2) via the observations in the high energy γ-ray domain.

The method of detection of the IGMF using the observation of cosmological sources of TeV γ-rays was first described in [223] and developed in [93, 200, 201]. It was noted, that emission of the sources of multi-TeV photons does not reach the Earth unaffected. In fact, these photons are absorbed because of the interaction with the lower energy photons of the diffuse electromagnetic background. This background can be divided into two separate parts – Cosmic Microwave Background (CMB) and EBL (see Sect. 1.3.1). CMB spectrum has one peak around $\sim 10^{-3}$ eV corresponding to its temperature of 2.7 K. In its turn EBL constitutes of all the light emitted by the galaxies over the history of the Universe and, as main emitters of light in the galaxies are stars and dust, its spectral energy density distribution features two distinct peaks at characteristic energies of the photons emitted by the stars ($\sim$ 1 eV) and the dust ($\sim 10^{-2}$ eV).

Interaction of multi-TeV γ-ray photons with diffuse background leads to production of e^+e^--pairs in the intergalactic medium. The mean free path of this photons can be written as:

$$D_{\gamma\gamma}(E'_\gamma, z) = \langle n_{bkg}(z)\sigma_{\gamma\gamma}(s)\rangle^{-1} \tag{14}$$

where n_{bkg} is the number density of the background photons and $s = E'_\gamma E_{bkg}(1 - cos(\theta))/(m_e^2c^4)$ with θ being the angle between the directions of propagation of the γ-ray and background photons. Here prime denotes that the energy of the primary γ ray is written in the rest frame of the emitting source. The pair production cross-section $\sigma_{\gamma\gamma}(s)$ can be represented in the following analytical form ([29]):

$$\sigma_{\gamma\gamma} = \frac{3\sigma_T}{2s^2}\left[\left(s + \frac{1}{2}\ln s - \frac{1}{6} + \frac{1}{2s}\right)\ln\left(\sqrt{s} + \sqrt{s-1}\right) - \left(s + \frac{4}{9} - \frac{1}{9s}\right)\sqrt{1 - \frac{1}{s}}\right] \tag{15}$$

Pair production cross-section $\sigma_{\gamma\gamma}$ sharply depends on s and has a peak around $s = 4m_e^2c^4$ (see Fig. 61), so most of interaction happens for:

$$E'_\gamma E_{bkg} \sim 2m_e^2c^4 \tag{16}$$

for head-on collisions. In this way the peak in the background photon number density distribution directly connects to the γ-ray photon energy it will primarily absorb. It is easy to see that absorption on CMB will happen for γ-ray photons with energies $\sim$ 1000 TeV, whereas the two peaks in the EBL spectrum will cause an absorption at $\sim$ 100 TeV and $\sim$ 1 TeV.

As these $e^+ - e^-$-pairs are produced, they gradually loose their energy emitting secondary photons. These photons can in their turn be absorbed, leading to deposition of a new generation of pairs in the medium these photons propagate through. In this way, an electromagnetic cascade of subsequent photon absorption, pair production and photon re-emission develops, stopping only when the last generation secondary photons can no longer pair-produce. As it can be seen from the Eq. 16, the lower is the energy of the γ-ray photon, the more energetic the background photon should be. Maximal energy of the background photons corresponds to the EBL peak around 1 eV, which produces the absorption of γ rays of $\sim$ 1 TeV energies. The mean free path of this multi-TeV photons with respect to the absorption on EBL is ([201]):

$$D_\gamma(E'_\gamma, z) = 80\frac{k}{(1+z)^2}\left[\frac{E'_\gamma}{10\ \mathrm{TeV}}\right]^{-1}\ \mathrm{Mpc}\ , \tag{17}$$

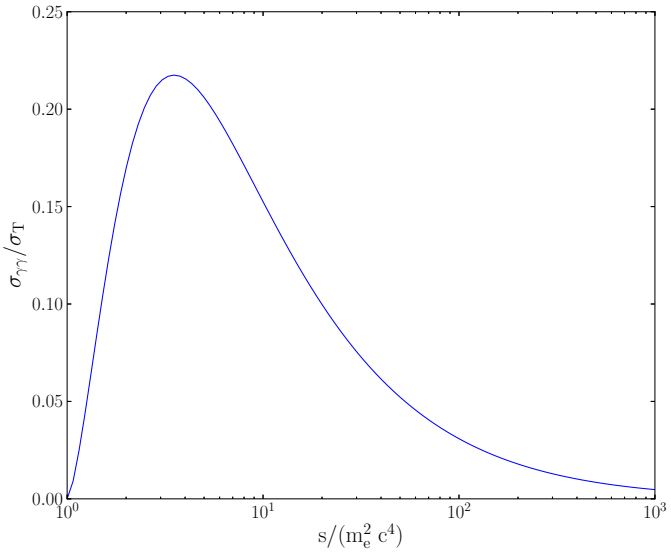

Figure 61: Pair production cross-section in units of Thomson cross-section

where numerical factor $k = k(E'_\gamma, z)$ accounts for the uncertainties in the EBL modelling.

For multi-TeV energies $D_\gamma \gtrsim 100$ Mpc the development of the cascade takes place predominantly in the intergalactic medium. As magnetic field in the intergalactic medium in extremely weak (see Sect. 1.3.2), synchrotron losses are largely sub-dominant, and these particles cool mainly through the Inverse Compton (IC) scattering of the CMB and EBL photons. Corresponding energies of the secondary photons for IC scattering are:

$$E'_{IC} = \frac{4}{3} E_{bkg} \left(\frac{E_e}{m_e c^2} \right)^2 \tag{18}$$

Here E_e is the energy of the electron preforming the scattering, and, as the energy of the incoming γ-ray photon is much larger than the energy of the background photon it interacts with, $E_e \simeq E'_\gamma/2$.

Since the efficiency of IC scattering depends on the number density of the target photons, scattering primarily occurs on the CMB photons, that largely outnumber more energetic EBL ones (see Fig. 14 in [90]). The resulting energy of the secondary photons in this case is:

$$E'_{IC} = 0.88 \left(\frac{E'_\gamma}{1 \text{ TeV}} \right)^2 \text{ GeV} \tag{19}$$

As the last generation electrons have energies close to 1 TeV (they are coming from ~ 1 TeV photons), they are relativistic with Lorentz-factors $\Gamma \sim 10^6$. This means that secondary photons are emitted almost in the direction of the movement of the electrons within small angle $1/\Gamma \sim 10^{-6}$, i.e. almost parallel to them.

If a magnetic field is present in the region $e^+ - e^-$-pair are born into, it may deflect electrons and positrons from their initial directions and, as a result, the direction of emission of the secondary photons may be different from the direction of the initial ones. Deflection angle δ depends on the energy of the electron (or positron) E_e, its cooling distance D_e, strength B and correlation length λ_B of the magnetic field, which sets the scale at which the magnetic field can no longer be treated as homogeneous. Schematic representation of the geometry of the process is depicted in Fig. 62. For the following simplified description of the observational effects, induced by the presence of magnetic field, here I will assume the approach of [201].

Cooling distance of electrons with energy E'_e with respect to the IC scattering can be written as:

$$D_e = \frac{3 m_e^2 c^3}{4 \sigma_T U'_{CMB} E'_e} \simeq 10^{24} (1+z_{\gamma\gamma})^{-4} \left(\frac{E'_e}{1 \text{ TeV}} \right)^{-1} \text{ cm } \simeq 0.3 (1+z_{\gamma\gamma})^{-4} \left(\frac{E'_e}{1 \text{ TeV}} \right)^{-1} \text{ Mpc} \tag{20}$$

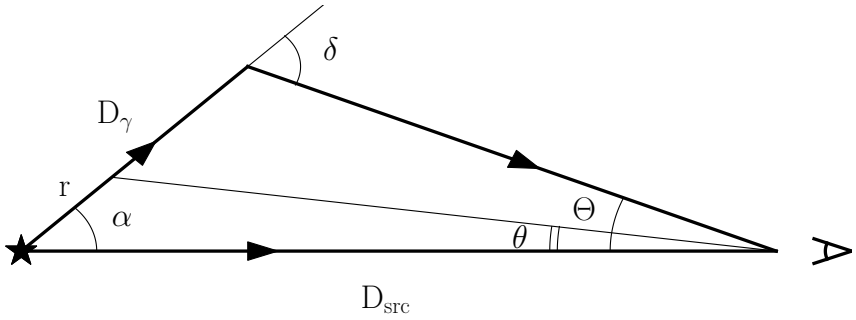

Figure 62: Schematic representation of the situation with the deflection of the e^+e^- beam by the magnetic field. Source of the emission is at the left, observer is at the right.

For the simplicity of discussion, I will further consider two limiting cases: the case of a large correlation length ($\lambda_B \gg D_e$) and the case of a small correlation length ($\lambda_B \ll D_e$).

If $\lambda_B \gg D_e$, the motion of electrons and positrons can be described as a motion in a homogeneous field. In this case:

$$\delta \simeq D_e/R_L \simeq 3\times10^{-2}(1+z_{\gamma\gamma})^{-4}\left(\frac{B'}{10^{-16}\text{ G}}\right)\left(\frac{E'_e}{1\text{ TeV}}\right)^{-2}\ , \tag{21}$$

where R_L is the Larmor radius of electron:

$$R_L = \frac{E'_e}{eB'} \simeq 3\times10^{25}\left(\frac{E'_e}{1\text{ TeV}}\right)\left(\frac{B'}{10^{-16}\text{ G}}\right)^{-1} \tag{22}$$

In the opposite case of the small correlation length the motion of electron can be described as a diffusion in angle, and the deflection angle becomes:

$$\delta = \frac{\sqrt{D_e\lambda_B}}{R_L} \simeq 5\times10^{-5}(1+z_{\gamma\gamma})^{-2}\left(\frac{B'}{10^{-16}\text{ G}}\right)\left(\frac{E'_e}{10\text{ TeV}}\right)^{-3/2}\left(\frac{\lambda'_B}{1\text{ Kpc}}\right)^{1/2} \tag{23}$$

If initial γ rays were emitted not in the direction towards the observer, the deflection of electrons in the magnetic field can point secondary photons to the Earth (see Fig. 62). This would lead to the formation of an extended emission region near the primary point-like source ([93]), which shape would depend on a particular orientation of the primary γ-ray beam ([192]). For the simplicity, here I will assume an isotropically emitting source of the primary γ rays; this description also remains valid for the jets of distant blazars for as long as the deflection angle δ is smaller than the jet opening angle. In this case, the size of the cascade extended emission region can be written in the following way (see Fig. 62):

$$\sin\Theta = D_\gamma(E'_{\gamma0})\frac{\sin\delta}{D_{src}} \tag{24}$$

Under the assumption of small Θ and δ this becomes:

$$\Theta(E'_\gamma) = \frac{D_\gamma(E'_{\gamma0})}{D_{src}}\delta = \frac{\delta}{\tau(E'_{\gamma0})}\ , \tag{25}$$

where $\tau = D_{src}/D_\gamma(E'_{\gamma0}) > 1$ is the optical depth with respect to the absorption of photons of $E'_{\gamma0}$ energy. Substituting the expressions for the deflection angle δ one gets:

$$\Theta(E'_\gamma) \simeq \begin{cases} 0.5^\circ(1+z_{\gamma\gamma})^{-4}\left(\frac{\tau}{10}\right)^{-1}\left(\frac{E'_\gamma}{1\text{ GeV}}\right)^{-1}\left(\frac{B'}{10^{-16}\text{ G}}\right), & \lambda'_B \gg D_e \\ 0.02^\circ(1+z_{\gamma\gamma})^{-2}\left(\frac{\tau}{10}\right)^{-1}\left(\frac{E'_\gamma}{1\text{ GeV}}\right)^{-3/4}\left(\frac{B'}{10^{-16}\text{ G}}\right)\left(\frac{\lambda'_B}{1\text{ kpc}}\right)^{1/2}, & \lambda'_B \ll D_e \end{cases} \tag{26}$$

As secondary and direct emission travel over different paths, the time delay between their arrival times is introduced. This delay can be estimated as the difference of the direct distance to the source and the sum of travel distances of the primary and the secondary photons. The travel distance of the secondary photon can be calculated from Fig. 62:

$$D_{secondary} = \sqrt{D_\gamma^2 + D_{src}^2 - 2D_\gamma D_{src}\cos(\delta - \Theta)} \tag{27}$$

Then the difference in paths becomes:

$$\Delta D \approx \frac{1}{2} D_\gamma(E'_{\gamma 0}, z)\delta^2 \left(1 - \frac{D_\gamma(E'_{\gamma 0}, z)}{D_{src}}\right) , \tag{28}$$

and the time delay can be expressed as:

$$T_{delay} \approx \frac{1}{2}(1+z)\frac{D_\gamma(E'_{\gamma 0}, z)\delta^2}{c} \left(1 - \frac{D_\gamma(E'_{\gamma 0}, z)}{D_{src}}\right) , \tag{29}$$

or, substituting the numbers:

$$T_{delay}(E'_\gamma) \approx \begin{cases} 7\times 10^{14} k(1-\tau)^{-1}(1+z)^{-1}\left(\frac{E'_\gamma}{1\text{ GeV}}\right)^{-5/2}\left(\frac{B'}{10^{-16}\text{ G}}\right)^2 s, & \lambda'_B \gg D_e \\ 10^{12} k(1-\tau)^{-1}(1+z)^{-1}\left(\frac{E'_\gamma}{1\text{ GeV}}\right)^{-2}\left(\frac{B'}{10^{-16}\text{ G}}\right)^2\left(\frac{\lambda'_B}{1\text{ kpc}}\right) s, & \lambda'_B \ll D_e \end{cases} \tag{30}$$

Extended halos and time delays in the light curves, induced by the presence of the IGMF, can be distinguished from other processes via their characteristic dependence of the energy of the incoming photons. Observations of these appearances of the cascade can be used to constrain the strength and correlation length of the intergalactic magnetic field.

In the above equations the strength and correlation length of the magnetic field always come together, and, as a result, any detection of a time delay or a halo will constrain just their combination, not the values separately. The solution here would be to scan over different energies, looking for a specific energy $E_{\gamma,br}$ at which the electron cooling distance D_e is equal to the magnetic field coherence scale λ_B, $D_e \sim \lambda_B$.

Indeed, as a deflection mode of electrons is different for $E_\gamma < E_{\gamma,br}$ and $E_\gamma > E_{\gamma,br}$, it is natural to expect that the angular profile of the halo and temporal profiles of the light curves will be different in this two cases. For the case of the source emitting directly towards the observer this is described in my publication [204]. In the following I briefly present the corresponding calculations.

I assume that the source is emitting within a narrow cone with an opening angle of α_{jet}. Geometry of the situation is the same as at the Fig. 62.

Let's first consider a line within this cone, and call r the coordinate along this line. Interaction with EBL leads to absorption of the primary photons, their number decrease with r as $N(r) = N_0 \exp(-r/D_\gamma)$. As each absorption of the primary γ-ray photon produces an e^+e^--pair, rate of the injection of these particles along the line under consideration is:

$$\frac{dN_e}{dr} = \frac{2N_0}{D_\gamma}\exp\left(-\frac{r}{D_\gamma}\right) \tag{31}$$

From the energy conservation condition it follows, that the power of the IC emission of the electrons and positrons, deposited along the line, should be equal to the power, removed from the primary γ-ray beam:

$$\frac{dP_{IC}}{dr} = \frac{E_{\gamma_0} N_0}{D_\gamma}\exp\left(-\frac{r}{D_\gamma}\right) \tag{32}$$

The distribution of electrons at each point along the beam can be written in the following way:

$$\frac{\partial^2 N_e(\delta)}{\partial r \partial \Omega} = \frac{\partial N_e(\delta)/\partial r}{2\pi\delta\partial\delta} = \frac{dN_e/dr \cdot f_\delta d\delta}{2\pi\delta d\delta} \tag{33}$$

In the above expression the number of electrons that are deflected within the range of angles $[\delta; \delta + d\delta]$ is denoted by $N_e(\delta)$, and their fraction from the total number is given by $f_\delta d\delta$. Under the assumption,

that the probability density function f_x is constant over the electron trajectory and quenches at $x = D_e$ (here x is a coordinate along the trajectory), its dependence on the deflection angle can be written as:

$$f_\delta d\delta = f_x dx = f_x \frac{dx}{d\delta} d\delta = const \frac{dx}{d\delta} d\delta \tag{34}$$

The constant here is defined by the requirement that $\int_0^{D_e} f_x dx = 1$. Eq. 33 can now be rewritten as:

$$\frac{\partial^2 N_e(\delta)}{\partial r \partial \Omega} \sim \frac{dN_e/dr \cdot \frac{d\delta}{dx} d\delta}{2\pi\delta d\delta} = \frac{dN_e/dr}{2\pi\delta(d\delta/dx)} = = \frac{dN_e/dr}{2\pi c} \begin{cases} R_L/\delta, & \lambda_B \gg D_e \\ 2R_L^2/\lambda_B, & \lambda_B \ll D_e \end{cases} \tag{35}$$

The energy of the electrons drops with the distance coordinate x as $E_e(x) = E_0/(1 + x/D_e)$ with E_0 being their initial energy at the moment of injection. As the IC emission power scales as E_e^2, one can now write:

$$\begin{aligned} \frac{\partial^2 P_{IC}(\delta)}{\partial r \partial \Omega} &\sim \frac{\partial^2 N_e(\delta)}{\partial r \partial \Omega} E_e^2(x[\delta]) \\ \frac{\partial^2 P_{IC}(\delta)}{\partial r \partial \Omega} &= \frac{E_{\gamma_0} N_0 R_L}{2\pi D_e D_{\gamma_0}} \exp\left(-\frac{r}{D_{\gamma_0}}\right) \times \begin{cases} \frac{1}{\delta\left(1 + R_L\delta/D_e\right)^2}, & \lambda_B \gg D_e \\ \frac{2R_L}{\lambda_B} \frac{1}{\left(1 + R_L^2\delta^2/(D_e\lambda_B)\right)^2}, & \lambda_B \ll D_e \end{cases} \end{aligned} \tag{36}$$

Here the normalization is obtained requiring that $\int_0^{\delta_{max}} f_{IC}(\delta) 2\pi\delta d\delta = dP_{IC}/dr$ with the limit of integration $\delta_{max} = D_e/R_L$ in the case $\lambda_B \gg D_e$ and $\delta_{max} = \sqrt{\lambda_B D_e}/R_L$ in the case $\lambda_B \ll D_e$.

The observer looking at beam at the angle α will only see the emission of the e^+e^--pairs if the required deflection angle $\delta < \delta_{max}$ (see Fig. 62). The flux reaching the observer depends on the angular distance Θ of the emission point from the source. As it can be seen from Fig. 62, $r = D \sin\theta / \sin\delta$ and we can write:

$$\begin{aligned} \frac{dF}{d\theta} &= \frac{dF}{dr}\frac{dr}{d\theta} = \frac{1}{d^2}\frac{\partial^2 P_{IC}(\delta)}{\partial r \partial \Omega}\frac{dr}{d\theta} \\ \frac{dF}{d\theta} &= \frac{E_{\gamma_0} N_0 R_L}{2\pi\alpha D^2 D_e D_{\gamma_0}} \times \exp\left(-\frac{D\theta}{\delta D_{\gamma_0}}\right) \begin{cases} \frac{1}{\delta\left(1 + R_L\delta/D_e\right)^2}, & \lambda_B \gg D_e \\ \frac{2R_L}{\lambda_B} \frac{1}{\left(1 + R_L^2\delta^2/(D_e\lambda_B)\right)^2}, & \lambda_B \ll D_e \end{cases} \end{aligned} \tag{37}$$

where $\delta = \alpha + \theta$.

The surface brightness profile of the jet can be found by integrating Eq. 37 over the α:

$$\frac{d\mathcal{F}}{d\theta} = \frac{1}{2\pi\theta} \int_{\alpha_{min}}^{\alpha_{jet}} 2\pi\alpha d\alpha \frac{dF}{d\theta} \tag{38}$$

The upper limit of integration is set by the opening angle α_{jet} of the jet, whereas the lower limit α_{min} is given by the requirement that maximal value of r (which corresponds to the minimal α, see Fig. 62) is equal to D_γ, so that $\alpha_{min} = \theta(\tau - 1)$. Substituting $dF/d\theta$ from Eq. 37 and integrating one finds in the limit of small θ:

$$\frac{d\mathcal{F}}{d\theta} \sim \begin{cases} \theta^{-1}(1 + \ln(\tau\theta)), & \lambda_B \gg D_e \\ \text{const}, & \lambda_B \ll D_e \end{cases} \tag{39}$$

Comparison of the angular profiles, derived here using an analytical approach, with the results of the full Monte Carlo simulation of the development of the cascade is shown in Fig. 63.

The difference in the angular profiles for the two cases ($\lambda_B \gg D_e$ and $\lambda_B \ll D_e$) allows to measure the correlation length of the intervening magnetic field, the corresponding photon energy $E_{\gamma,br}$ happens to be in the energy range accessible by the currently existing or future γ-ray telescopes.

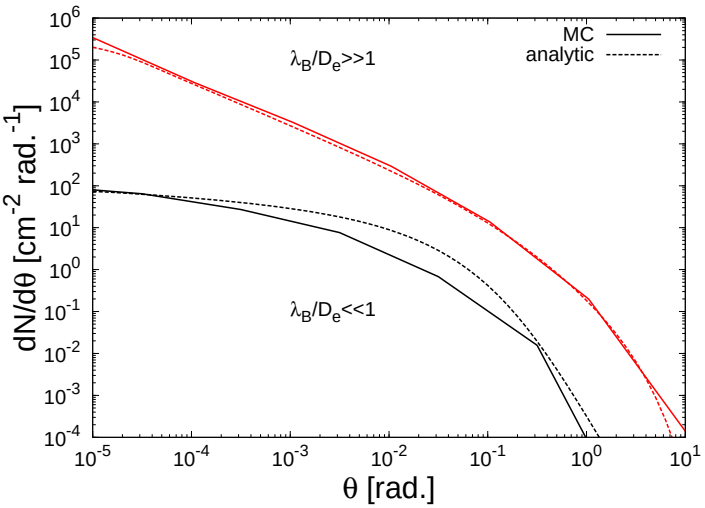

Figure 63: The angular profile of the arriving γ-ray flux obtained with both Monte Carlo and analytic (Eq. 39) methods. The angles shown are measured relative to the centre of the blazar. For this plot, the angular profile of 1-10 GeV photons in a cascade from a source at $z = 0.13$ for a 10^{-15} G IGMF with coherence lengths 10 kpc (black lines) and 10 Mpc (red lines) are shown. Source: [204]

4.2 Lower bound on the strength of the Intergalactic Magnetic Field

The availability of the instruments working in both GeV and TeV domain made it possible to apply the previously described method of the measurement of the IGMF to real data. Indeed, in the absence of a magnetic field the IC emission from the cascade will contribute to the primary source point-like flux ([82, 188, 223]), whereas the presence of a non-negligible IGMF on the line of sight would spread the secondary emission, leading to the formation of an extended emission region around the point-like source ([46, 88, 93, 200, 201]). This means that, instead of coming all from the direction of the point-source, the secondary flux will be smeared over the whole area of the extended emission region, thus reducing, possibly significantly, the point-source flux in the domain where the secondary flux should appear. In particular, as the last generation of the cascade particles is born out of the γ-rays of TeV energies, for which the secondary photons would have GeV energies, the presence of IGMF could change the balance between the observed amount of emission in this two domains.

The size of the extended emission region Θ_{ext} depends on the energy and is larger for lower energies, as corresponding electrons are more significantly deviated. The energy of the secondary cascade photons $E_{\gamma,min}$, below which the extended halo becomes larger than the point spread function (PSF) of the instrument, depends on the magnetic field strength and coherence length. In the case of the Fermi/LAT telescope, the PSF depends on the incoming photon energy and 95% of the signal are contained within a radius ([230])

$$\Theta_{\rm PSF} \simeq 2^\circ \, (E_\gamma/1 \text{ GeV})^{-0.8} \tag{40}$$

Taking $E_\gamma \sim 10$ GeV as a reference, one finds that $\Theta_{ext} > \Theta_{PSF}$ if

$$B \geq B_{PSF} \simeq \begin{cases} 6 \times 10^{-17} \tau \, [E_{\gamma,min}/10 \text{ GeV}] \text{ G}, & \lambda_B > D_e \\ 8 \times 10^{-16} \tau \, [E_{\gamma,min}/10 \text{ GeV}]^{3/4} \, [\lambda_B/1 \text{ kpc}]^{-1/2} \text{ G}, & \lambda_B < D_e \end{cases} \tag{41}$$

A search for the magnetic field induced suppression of the GeV flux would require a sample of observable sources of VHE γ-ray emission – blazars – located as far as possible, to maximize the effect of γ ray absorption on EBL and, thus, to maximize the amount expected cascade emission in the lower γ-ray band. Not only these sources should be distant ones, they should also have relatively hard spectra in the GeV-TeV band to minimize the presence of the intrinsic spectrum in the domain the cascade emission should appear and thus make the analysis less sensitive to its exact shape. In my publication [205] we used a sample of four blazars, satisfying the above criteria – 1ES 0229+200 ($z = 0.14$), H 2356-309 ($z = 0.165$), 1ES 1101-232 ($z = 0.186$) and 1ES 0347-121 ($z = 0.188$) ([33, 34, 38, 39, 41]).

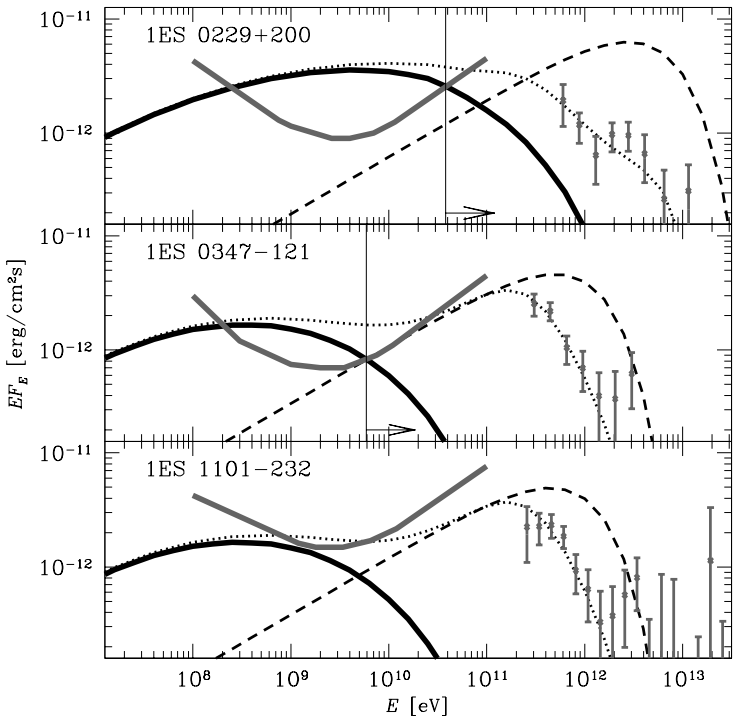

Figure 64: A comparison of models of cascade emission from TeV blazars (thick solid black curves) with Fermi/LAT upper limits (grey curves) and HESS data (grey data points). Thin dashed curves show the primary (unabsorbed) source spectra. Dotted curves show the spectra of electromagnetic cascade initiated by pair production on EBL. Vertical lines with arrows show the energies below which the cascade emission should be suppressed. HESS data points are taken from [33, 34, 41].

At the time when this analysis was carried out – spring 2010 – none of these sources was detected in the GeV band with Fermi/LAT and only upper limits on their fluxes could have been derived. To analyse Fermi/LAT data we used the *Fermi Science Tools* package, following the instructions in the Fermi/LAT data analysis threads ([189]). The point sources visible in Fermi/LAT images, as well as isotropic and galactic diffuse backgrounds were included in the analysis. The analysed field of view for each source was centred on it and had radius of 14°.

The upper limits in the LAT band were obtained in the following way. Assuming that the spectra of the sources in the 0.1-100 GeV band had power law shape $dN_\gamma/dE = N_0\,(E/0.1\text{ GeV})^{-\Gamma}$, we computed the upper bound on the normalization factor N_0 for each value of Γ. For this for each value of Γ we computed the value of the Test Statistics (TS) ([179]) as a function of N_0 to derive the 95% confidence level upper bound $N_{0,95}(\Gamma)$, following the procedure described in [179]. The resulting upper limits in the sources fluxes are the envelopes of the entire set of these power law spectra and are shown in Fig. 64.

To calculate the bounds on the parameters of the initial sources spectra, we have fitted the available HESS measurements in the $0.1 - 10$ TeV domain with the model spectra with the different E_{cut} and Γ. For each set of these two parameters the normalization of the model spectrum was found by fitting the model to the data using the minimal χ^2 criterion. The values of the χ^2_{min} and the total flux above 0.1 GeV were recorded as function of E_{cut} and Γ. This allowed us to calculate the 68% and 95% confidence level for the combination of the last to variables. These levels, together with the flux levels, are shown in Fig. 65.

To be conservative and minimize the presence of the cascade component one needs to minimize the amount of the primary source emission in the more energetic domain. To do so we have chosen the combination of E_{cut} and Γ that would give the minimal integral flux above 0.1 TeV while lying within the 95% confidence region. We considered a restriction of $\Gamma \geq 1.5$, which is commonly adopted for the modelling of blazar spectra in the VHE domain (see e.g. [33, 39, 107]). We have also verified that the

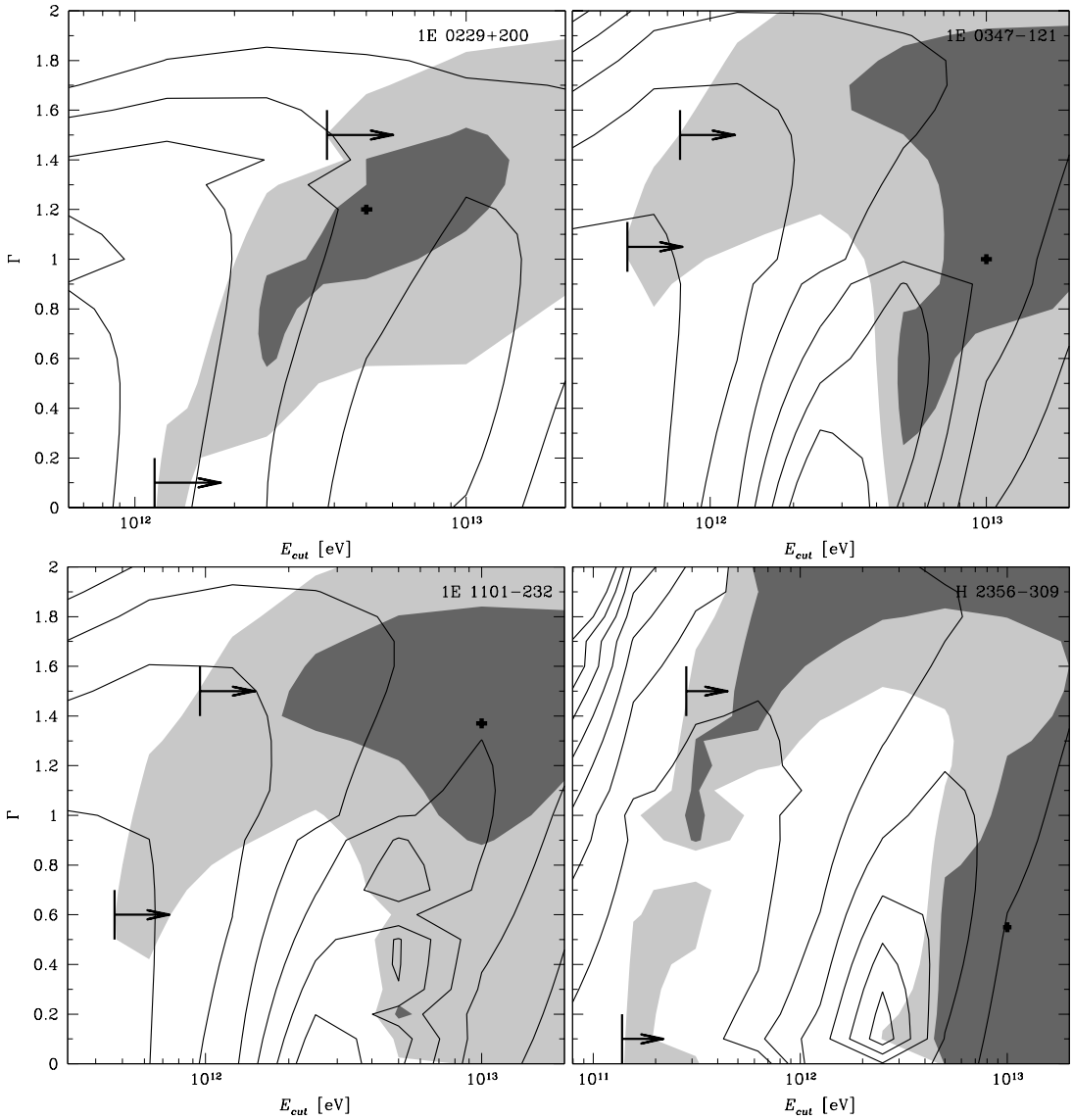

Figure 65: Greyscale: 68 and 95% confidence levels for the cut-off energy E_{cut} and photon index Γ found from the fitting of HESS spectra. Crosses mark the best-fit parameter values. Contours show the levels of integral energy flux above 0.1 TeV for the fitted spectra at each E_{cut} and Γ, with the increments of 2.5×10^{-12} erg/cm^{2}s. Arrows show the 95% confidence level lower bounds on the cut-off energy for the photon index $\Gamma \geq 1.5$ (upper arrows) and absolute lower bounds on E_{cut} (lower arrows).

	$\Gamma \geq 1.5$			all Γ		
Source	$E_{cut,min}$	$E_{\gamma,min}$	$B_{\rm PSF}(\lambda \gg D_e)$	$E_{cut,min}$	$E_{\gamma,min}$	$B_{\rm PSF}(\lambda \gg D_e)$
1ES 0229+200	3.8 TeV	39 GeV	3×10^{-16} G	1.2 TeV	30 GeV	3×10^{-16} G
1ES 0347-121	0.8 TeV	6 GeV	2×10^{-17} G	0.5 TeV	6 GeV	2×10^{-17} G
1ES 1101-232	1.0 TeV	-	-	0.5 TeV	-	-
H 2356-309	0.3 TeV	-	-	0.14 TeV	-	-

Table 9: Parameters of the model spectra and limits on IGMF for the analysed sources.

relaxation of this constraint doesn't change the results of the analysis (existence of the lower bound on the IGMF strength). The lower bounds on the cut-off energy E_{cut} of the sources in our sample are given in the Tab. 9.

The minimal possible cascade flux for 1ES 1101-232 and H 2356-309, derived as described above, is below the Fermi/LAT upper bounds. For the illustration, predicted cascade spectrum and LAT upper limits for 1ES 1101-232 are shown at the bottom panel of the Fig. 64. At the same time, non-detection of the emission from 1ES 0229+200 and 1ES 0347-121 imposes constraints on the cascade contribution in the Fermi/LAT energy band. In order to determine these constraints we used a numerical model of the development of the electromagnetic cascade in the intergalactic space, initiated by the absorption the VHE γ-rays on the EBL. This model solves one-dimensional kinetic equation for the concentrations of photons and electron-positron pairs, taking into account production of e^+e^- via the absorption of TeV photons and cooling of the resulting pairs via the IC emission of the secondary γ rays. In this model $e^+ - e^-$-pair interact with the photon background, represented by CMB and EBL. The EBL model was taken from [107].

The initial source spectra were chosen in the form of the cut-off power law $dN_\gamma/dE \sim E^{-\Gamma} \exp(-E/E_{cut})$ with the parameters Γ and E_{cut} chosen to minimize the contribution of cascade the GeV band, as described above. These spectra are shown at Fig. 64 with dashed lines. The power of the cascade emission is equal to the power removed from the initial γ-ray beam at TeV energies. As emission in the TeV domain is almost completely absorbed, the cascade luminosity is roughly equal to the source luminosity above ~ 100 GeV.

As it can be seen from Fig. 64, assumption of negligible magnetic field along the line of sight towards the blazars we have used is in contradiction with the Fermi/LAT upper limits on the sources fluxes. Even though predicted source spectra in the GeV domain deviate from the power law shape, these deviations are small and comparison with the LAT upper limits is applicable.

As it is seen from Fig. 64, cascade emission should be suppressed below energy $E_{\gamma,min}$, marked with vertical lines on the top two plots. This suppression can be achieved, if e^+e^--pairs, responsible for the secondary emission, are deviated from their initial trajectories by the magnetic field. Cascade emission wouldn't contribute to the source flux below $E_{\gamma,min}$, if intergalactic magnetic will be stronger than B_{PSF}, defined in Eq. 41. The values of B_{PSF}, derived for each of the sources, are given is Tab. 9.

The best limit on the strength of the IGMF comes from observations of 1ES 0229+200 (see Fig. 64) and is presented at Fig. 66. This limit suffers from the number of uncertainties and should be considered only as an order of magnitude estimate.

Suppression of the cascade emission below $E_{\gamma,min}$ leads to the change in the shape of the source spectrum and expected deviation from the power law. This means that upper limits on the source fluxes, shown at Fig. 64, give only a rough estimate of $E_{\gamma,min}$ and, thus, B_{PSF}. Another uncertainty is introduced by the uncertainty in the measurements of the EBL spectrum, which leads to the uncertainty of the mean free path in Eq. 17. Further uncertainty comes from the fact that observations in the GeV and TeV domains were not carried out simultaneously, with Fermi/LAT observing in 2008-2009 and HESS measurements taken in the 2005-2007 period ([33, 39, 41]). Moreover, measurements in the GeV band provide a flux limits, averaged over whole period of observations (1.5 years), whereas TeV observations are performed in the separate nights and give estimates of the flux only at these dates. However, up to know, no long term variability was found in the HESS observations ([33, 35, 39, 41]).

The size of the largest structures in the Universe – galaxy clusters – is of the order of a few megaparsecs. With the mean free path of the primary photons being of the order of 100 Mpc (Eq. 17), most of the

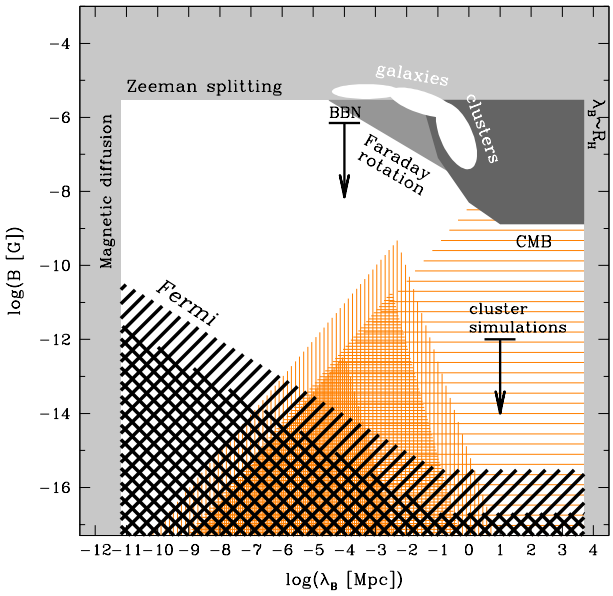

Figure 66: Light, medium and dark grey: known observational bounds on the strength and correlation length of IGMF, summarized in [201]. The bound from Big Bang Nucleosynthesis, marked "BBN", is from [124]. The black hatched region shows the lower bound on the IGMF derived in this paper. Orange hatched regions show the allowed ranges of B, λ_B for magnetic fields generated at the epoch of Inflation (horizontal hatching) the electroweak phase transition (dense vertical hatching), QCD phase transition (medium vertical hatching), epoch of recombination (rear vertical hatching) [201]. White ellipses show the range of measured magnetic field strengths and correlation lengths in galaxies and galaxy clusters.

absorption and subsequent development of the electromagnetic cascade happens in the intergalactic space in the voids of the Large-Scale Structure. This indicates that the magnetic field, responsible for the suppression of the cascade emission is primarily located in the intergalactic space.

Evidence for the presence of a magnetic field in the voids of the Large-Scale Structure gives a strong argument in favour of the cosmological origin of the fields, that played the role of seeds for the subsequent amplification in the galactic dynamos. Models of magnetic fields produced in the early Universe predict that these weak fields should fill the whole Universe, being also present in the voids. On contrary, if the seed fields were produced by young (proto)galaxies, they are expected to concentrate around them and be almost absent in a more distant regions.

Models of the cosmological magnetogenesis consider the magnetic fields with the coherence length and energy density not exceeding the size of the horizon and critical energy density at the epoch of the magnetogenesis. Several broad classes of cosmological models are considered: magnetogenesis at the epoch of inflation, electroweak phase transition, quantum chromodynamics (QCD) phase transition, at the epoch of recombination ([83, 85, 124, 155, 228, 231, 243, 264, 268, 279]). The lower limit, shown at Fig. 66, excludes significant part of the parameter space for all these models.

4.3 Dependence of the lower bound on the variability of the used sources

4.3.1 Introduction

As it was shown in the previous section, even in the simplest settings of the cascade development the lower bound on the strength of IGMF at the level 10^{-15} G is derived. This bound adopts a simplifying assumption that the measured spectra of the blazars used to derive the bound, provide a correct estimate of the time-averaged flux in the GeV and TeV domains. This can be, in principle, tested via the systematic observations of these sources simultaneously in the GeV and TeV energy bands.

Here I present the work done by me and collaborators ([260]), where we consider a set of blazars, that were simultaneously observed by the Fermi/LAT and ground based Cherenkov telescopes. We found

that in the cases of blazars RGB J0710+591 and 1ES 1218+304 the measured flux in the GeV domain is below the predictions for zero IGMF and thus implies a lower bound on its strength, similarly to the bound found for 1ES 0229+200 and 1ES 0347-121 ([205]), that were discussed in the previous section. However, contrary to the bounds for 1ES 0229+200 and 1ES 0347-121, derived before, no assumption on the absence of the variability is needed because of the simultaneous nature of observations.

The term "simultaneous observations" should be clarified here. As the effective area of the Fermi/LAT instrument is much smaller than that of any of the Cherenkov telescopes, to achieve the required level of photon statistics at the time scales these telescopes operate on, it has to observe a bright source. In the sample of blazars used here only 3C 66A is bright enough in the GeV band to be detectable by LAT on the time scale of several days. For this reason we used Fermi/LAT spectra, averaged over the whole period of observations (~ 2 years). The term "simultaneous" here denote the fact, that observations in the TeV domain were performed sometime during the period of observations of the LAT. We therefore assume, that these spectra – in the TeV domain and time-averaged in the GeV domain – are representative of the source spectra during the period of observations of LAT.

Simultaneous observations in the GeV-TeV domain enables us to test two alternative reason for the suppression of the cascade component in the GeV domain – suppression of the cascade signal contribution to the point-source flux due to the extended nature of the cascade emission vs. its dilution because of the time delay after the period of the enhanced activity of the source.

4.3.2 Source selection and data analysis

Detailed calculation of the cascade spectrum requires the knowledge of the initial, unabsorbed spectrum of the source in the TeV domain. If magnetic field in the intergalactic space is negligibly small, secondary γ rays arrive almost simultaneously with the primary emission. Only a small time delay of a ~ 10 hr is induced because of the magnetic field-independent angular scatter of the electrons and positrons in the pair-production process ([201]). In this way, the prediction of the cascade spectrum in the GeV domain requires the simultaneous observations of the primary spectrum in the TeV band.

Fermi/LAT observations started on August 4, 2008 and any observations in the TeV band, performed by one of the Cherenkov telescopes HESS, VERITAS or MAGIC after this date automatically becomes simultaneous with the LAT measurements. Several blazars have been reported to have TeV observation since that date: Mrk 501 ([140]), PKS 2155-304 ([30]), 3C 66A ([235]), RGB J0710+591 ([19]) and 1ES 1218+304 ([22]), 1ES 0229+200 ([84, 221]) and PKS 1424+240 ([18]). In this work we used available GeV-TeV data for all these blazars.

For each of the sources, listed above, we obtained the spectrum using the publicly available Fermi/LAT observations in the 0.1-100 GeV band and combined it with the published spectrum in the TeV domain. We used the LAT data, received between the August 4, 2008 and November 30, 2010. To analyse them we used the *Fermi Science Tools* package version v9r17p0 – a standard software package for the analysis of the Fermi/LAT data. The spectra were derived using the unbinned likelihood method, and all the sources mentioned in the first year Fermi catalogue ([12]) within 10° were included in the analysis. The last step is necessary as the Fermi/LAT PSF strongly depends on the energy and is several degrees wide in the 0.1-1 GeV band. As usual distances between the sources in the first year Fermi/LAT catalogue are smaller than the width of the LAT PSF at the lowest energies, their images often overlap. To disentangle the contribution from each source a simultaneous fit of all the sources within a field of view is required. For each of the sources we further split 0.1-100 GeV interval into several smaller bins with their number depending on the average source flux – the brighter is the source, the larger is the number of bins. In each bin we then performed the spectral analysis in order to get an estimate of the flux. Detection significance in each bin was characterized by the value of the Test Statistics (TS) ([179]). As it was indicated by [179], the value of TS and the detection significance σ are connected as $\sigma = \sqrt{TS}$. In our analysis we required that TS in each bin should be greater than 10 ($\sigma > 3$), otherwise a 99% confidence level upper limit on the source flux in this bin was computed. The broad-band (0.1 GeV - 10 TeV) spectra were then modelled with a two-component model, that consisted of the intrinsic source emission and the component arising from the electromagnetic cascade, initiated by the absorption of the intrinsic spectrum photons on the EBL.

For 1ES 1424+240 the uncertainty on the redshift doesn't allow firm prediction on the spectral appearance of the cascade component, for this reason it was excluded from further analysis. For three

sources – Mrk 501, 3C 66A and PKS 2155-304 – the slopes of the intrinsic spectra, found by our fitting procedure, are relatively soft, having photons indices $\Gamma \simeq 2$. Under these conditions, the expected cascade contribution to the source flux in the GeV domain is sub-dominant with respect to the intrinsic spectrum and, thus, hard to constrain. For this reason these blazars were also excluded from our analysis. The remaining three sources are shown in Tab. 10.

Name	RA	Dec	z	Γ	$E_{\rm cut}$
RGB J0710+591	07:10:30.0	+59:08:20	0.13	1.7	1.2
1ES 0229+200	02:32:48.6	+20:17:17	0.14	1.2	5.0
1ES 1218+304	12:21:21.9	+30:10:37	0.18	1.7	2.5

Table 10: Blazars considered in the analysis. Γ and $E_{\rm cut}$ are the limiting values of photon index and the cut-off energy derived from the fit of the Fermi and TeV data with the direct emission (cut-off power law attenuated by the pair production on EBL) plus cascade model, under the requirement of the minimal cascade contribution.

We noted that, as a result, we were left with just three sources that lie in a quite narrow redshift range. Blazars and radio galaxies (BL Lac parent AGN population) exhibit general positive evolution with the cumulative power of the sources increasing as $(1+z)^k$, $k > 0$ ([135, 236, 247]). So the probability to find a hard spectrum blazar per given redshift bin size increases with the redshift; at the same time the chances to see the source are smaller for larger z. For this reason the expectation is that only the sources in some narrow redshift bin should be available for our analysis – which is exactly what we see. We thus believe that this selection effect is responsible for the small number of sources in the Tab. 10 and their redshift location. The analysis of these three sources is used below to constrain the IGMF.

4.3.3 Monte Carlo simulations

Extragalactic electromagnetic cascades, in the presence of non-negligible IGMF ($> 10^{-20}$ G), evolve both spatially and energetically as the propagation front of the emission moves away from the source. The nature of the constraints on the IGMF derived from the timing and imaging analysis of the signal produced by electromagnetic cascades, developing in intergalactic space, can be qualitatively understood from the decomposition of the cascade signal in space and time, which we illustrate using Monte-Carlo simulations.

In order to convey the key features introduced by the spatial evolution of the cascade, we started with a consideration of simplified situation of a collimated primary gamma-ray beam (i.e. neglecting the finite jet opening angle). To further simplify the consideration, we considered an idealized situation in which a distant source injects primary gamma-rays at a fixed energy $E_0 = 100$ TeV. The energy E_0 is chosen in such a way that the optical depth with respect to pair production on the EBL is $\tau(E_0) \gg 1$. The resulting spectra of the cascade emission depend only weakly on E_0 as soon at $\tau(E_0) \gg 1$. In these illustrative calculations we assume the source redshift $z = 0.13$, equal to the redshift of RGB J0710+591. Later we introduce the non-zero intrinsic jet opening angle $\theta_{jet} > 0$ and broad band emission spectrum and describe how our simplified results are altered.

We show the results of our calculation in Fig. 67. In both panels of this figure the arriving spectrum, calculated for the negligibly small IGMF, is shown with long dash, short dash line. In fact the results of the our calculation utilising the Monte Carlo description of the cascade (for more details see [259]) are in a good agreement with the "kinetic equation" description of the zero B-field case, used in the previous section.

Throughout this work we used the EBL model, proposed by [107], in which the evolution of the EBL with redshift is taken into account. Furthermore, we adopted the following values for the cosmological parameters of our model: $H_0 = 70$ km s^{-1} Mpc^{-1}, $\Omega_M = 0.3$, and $\Omega_\Lambda = 0.7$.

In all the calculations in this work we assumed, that the IGMF consists of patches of uniform magnetic field, each patch being $\lambda_B = 1$ Mpc in size. At the same time different patches have completely random field orientations. Such description effectively puts all the power in the magnetic field power spectrum to the longest length scales. In reality this is not the case, which will lead to a slightly weaker deflections, so our result can be considered conservative. We have also verified that the limits on the IGMF, derived

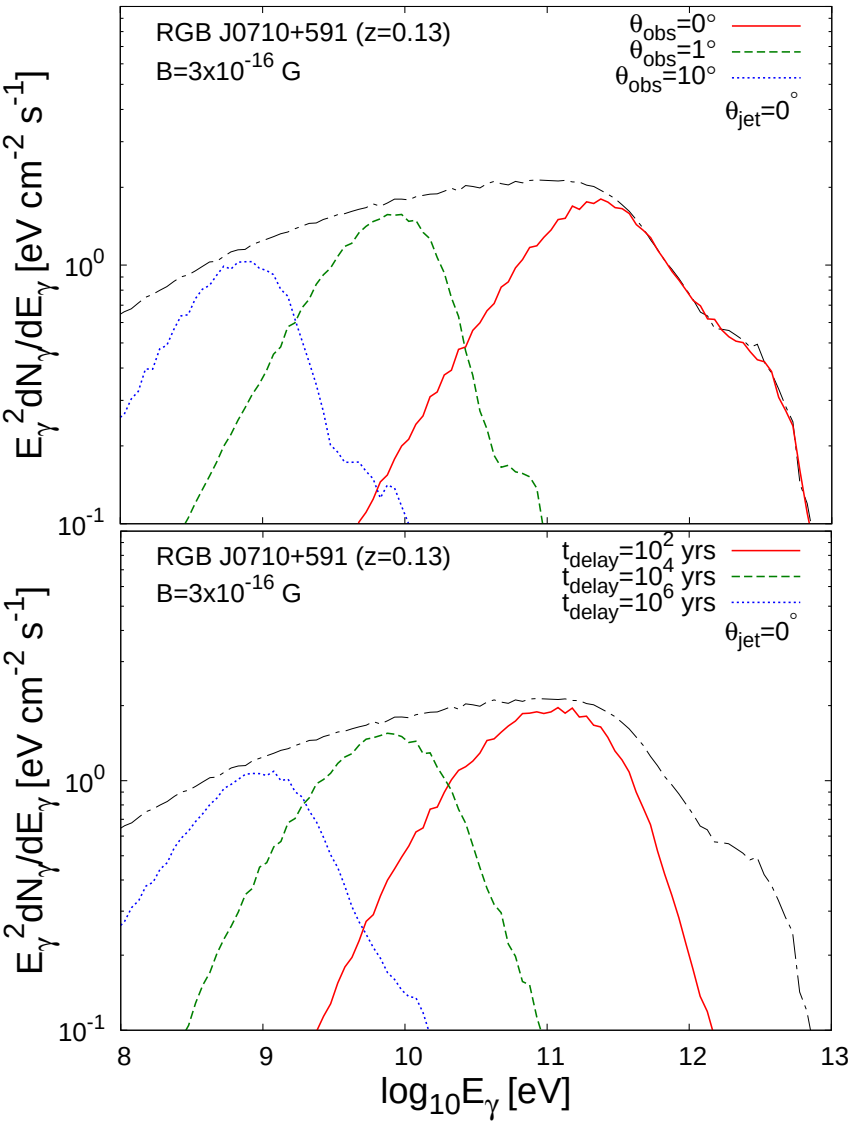

Figure 67: The arriving energy fluxes following the injection of a 100 TeV photon flux from a source at redshift $z = 0.13$, with an intervening IGMF=3×10^{-16}G. Top: The arriving flux is decomposed into that observed from different observer angles, $\theta_{\rm obs}$. Bottom: The arriving flux is decomposed into that arriving with different delay times, $t_{\rm delay}$. In both plots, the long-short dash line represents the envelope flux containing the non-decomposed spectrum.

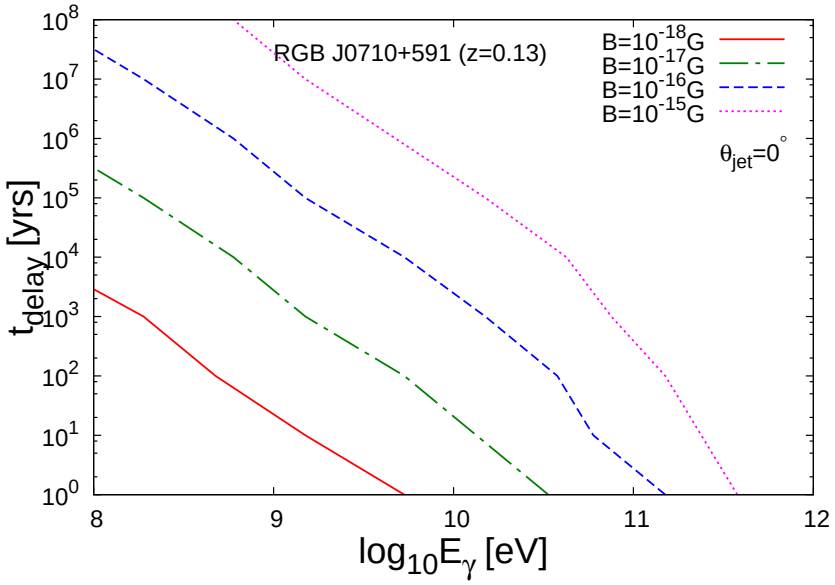

Figure 68: The mean time delay incurred by a photon energy flux following its injection at 10^{14} eV from a source at redshift $z = 0.13$, for different intervening IGMF in the range $10^{-18} - 10^{-15}$ G.

here, do not depend on λ_B for as long as $\lambda_B \geq 1$ Mpc by the comparison of the results of calculations for the $\lambda_B = 1$ Mpc and $\lambda_B = 30$ Mpc cases. As the cooling distance of the electrons produced from the absorption of multi-TeV photons is smaller than 1 Mpc (see Eq. 20), the assumption of $\lambda_B = 1$ Mpc means each electron cools within a single, homogeneous patch of the magnetic field. Although this was considered throughout the calculations in this work, this result can be easily generalized on the case of $\lambda_B \ll D_e$ – similarly to the findings in the previous section, due to the change in the electron deflection mode, the lower bound on the strength of the IGMF will scale as $\lambda_B^{-1/2}$.

Non-negligible magnetic field introduces both spatial spread of the cascade in angle, away from the initial beam direction, and significantly increases the cascade front depth, resulting in the spread of the arrival times ([223]). We show both spatial and temporal decomposition of the cascade, arising in presence of the non-negligible IGMF, in Fig. 67.

For the calculation, presented at the top panel of Fig. 67, we put the observer at a small off-axis angle θ_{obs} with respect to the γ-ray beam at a distance D from the source. In this calculation observer detects only photons arriving at sphere of a radius $R = D$ at a small incident angle $\theta \leq \theta_{PSF}$. θ_{PSF} here represents the point spread function of the Fermi/LAT instrument and throughout this work we used the following approximation for it:

$$\theta_{\rm PSF} \approx 1.7^\circ \left(E_{\gamma,\rm GeV}\right)^{-0.74} \left[1 + \left(\frac{E_{\gamma,\rm GeV}}{15}\right)^2\right]^{0.37}, \quad (42)$$

where $E_{\gamma,GeV}$ is the energy of the photon in GeVs. The above approximation gives the 95% confidence range radius for the energies in the range 30 MeV to 300 GeV[21]. Bin widths of 0.1° (i.e. photons are collected from a ring $\theta_{obs} \pm 0.1^\circ$) were used for the observer position. The bottom panel of Fig. 67 shows only the photons, that arrive with particular time delay with respect to propagation time of the direct photons from the source. The width of the time bins is half a decade around the reference $t_{\rm delay}$ value.

In Fig. 68 the dependence of the time delay on the incoming photon energy is shown for different strengths of the IGMF. A bin size of 1 per logarithmic decade in time is used in this figure. As it can be seen from it, the time delay scales with the photon energy E_γ as $\sim E_\gamma^{-2}$ or $\sim E_\gamma^{-2.5}$, in agreement with analytical calculations of [201]. The slope of the curves changes at highest energies because of the energy dependence of the mean free path for the corresponding initial γ rays.

[21] See http://www-glast.slac.stanford.edu/software/IS/glast_lat_performance.htm

A realistic description of development of the cascade should take into account intrinsic angular spread of the beam due to the non-zero opening angle of the jet, as well as the spread of the initial photon energies E_0, arising from the non-monochromatic nature of the blazar emission.

The first point is taking into account in our calculation by assuming, that blazar emits within a jet with an opening angle $\theta_{jet} = 5^\circ$, which is a typical opening angle observed in radio galaxies and is also a typical opening angle $\theta_{jet} \simeq \Gamma^{-1}$ inferred from the bulk Lorentz factors $\Gamma \sim 10$, estimated from the gamma-ray observations of blazars. We somewhat arbitrarily put the observer at $\theta_{obs} = 2^\circ$.

The spread of initial photon energies is taken into account by assuming that the blazar emits as power law with exponential cut-off in the GeV-TeV band:

$$\frac{dN_\gamma}{dE_\gamma} \propto E_\gamma^{-\Gamma} \exp\left(-\frac{E_\gamma}{E_{\rm cut}}\right), \tag{43}$$

The spectral appearance of the blazars in the GeV-TeV band is defined by the combination of the intrinsic spectrum and the reprocessed cascade component. It was even shown ([49]) for the case of Mrk 501, that the cascade can give a dominant contribution in source flux in the GeV-TeV domain. In our calculation the overall spectrum is given by the sum of the intrinsic spectrum and the cascade component. On top of this, we consider two different limiting cases, to which we refer to as the "minimal" and "maximal" cases.

In the "minimal" case the parameters of the spectral model in the Eq. 43 are chosen to minimize the expected contribution of the cascade in the GeV domain, while giving a good fit to the entire multi-wavelength (GeV and TeV) data set. The "maximal" case adopts different possibility – that the intrinsic spectrum is so hard and with such a large cut-off energy $E_{\rm cut}$, that the observed spectrum in the GeV-TeV domain is a pure cascade emission. In this case the exact shape of the intrinsic spectrum is not important any more, what matters is only the absorbed power. For this reason for the maximal case we arbitrarily fix the intrinsic spectral index to $\Gamma = 1$ and cut-off energy to $E_{\rm cut} = 100$ TeV. The results for the observed GeV-TeV band spectrum in the maximal cascade model are similar to those derived by [49] for the case of negligible IGMF.

4.3.4 Results: minimal and maximal cascade model fits to the spectra

Comparing the spectra, obtained by Fermi/LAT, with the results of the ground-based telescopes, we found, that they perfectly match each other at the transition energies ~ 100 GeV. This indicates that no "intercalibration factor" is needed, and the combination of these spectra can be used for the global fit in the 0.1 GeV-10 TeV energy band.

For Mkr 501, PKS 2155-304 and 3C 66A the observed spectra in the 0.1-100 GeV band have spectral indices close to $\Gamma = 2$ with almost no signature of the curvature over the entire energy band. The spectrum of the cascade component, although being generally close to power law, still deviates from it significantly, so the assumption that the GeV spectra of these sources are primarily of the cascade origin is inconsistent with the data. For such soft intrinsic spectra, cascade contribution is at most comparable with the direct flux from the source. At the same time, for Mrk 501 and PKS 2155-304 the cut-off energies, inferred from the analysis of the $0.1 - 10$ TeV part of the spectra, are close to 1 TeV. As a result, the expected amount of the cascade emission from these sources in the GeV band is sub-dominant with respect to the direct emission and does not notably modify the apparent spectrum. This all suggests that dominant contribution to the observed source spectra of these sources comes from the direct γ rays from the sources and not from the cascade component, as is shown at Fig. 69.

For the other three sources, RGB J0710+591, 1ES 0229+200 and 1ES 1218+304, situation is different. The analysis of the TeV part of the spectra, where the contribution of the cascade emission in the "minimal" case is negligible, indicates that their intrinsic spectra are hard, with photon indices $\Gamma < 2$. As a result, the power output of the intrinsic spectrum in the TeV domain is order of magnitude larger than the corresponding output in the GeV band (see Fig. 70). As a significant part of the TeV emission is absorbed and preprocessed into the GeV energy band, the cascade emission in the $0.1 - 10$ GeV energy range dominates over the direct flux from the source, as it is shown in Fig. 70.

Fitting the model in Eq. 43 alone to the observed spectra we found the reduced χ^2 close to 1 for both RGB J0710+591 and 1ES 1218+304. For 1ES 0229+200 only an upper bound on the source flux in the

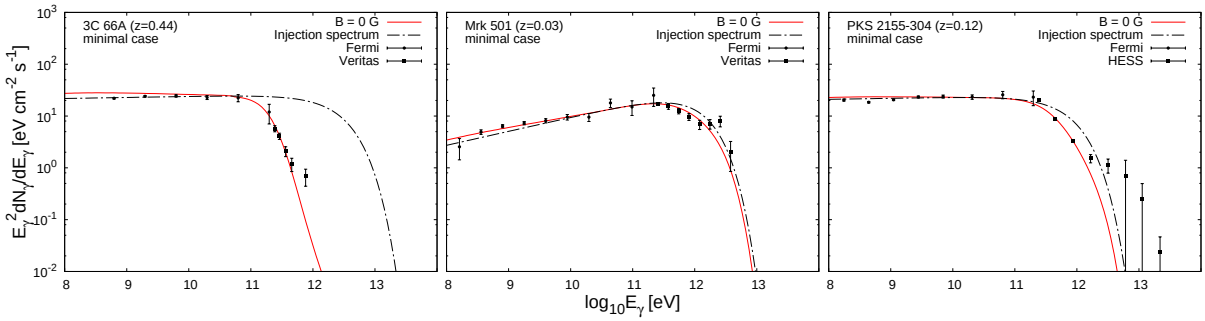

Figure 69: The arriving photon energy flux, resulting from the "minimal cascade" model for Mrk 501 (top), PKS 2155-304 (middle) and 3C 66A (bottom). Long-dash-dotted line shows the intrinsic source spectra. Red solid lines show the spectra with account for the cascade component.

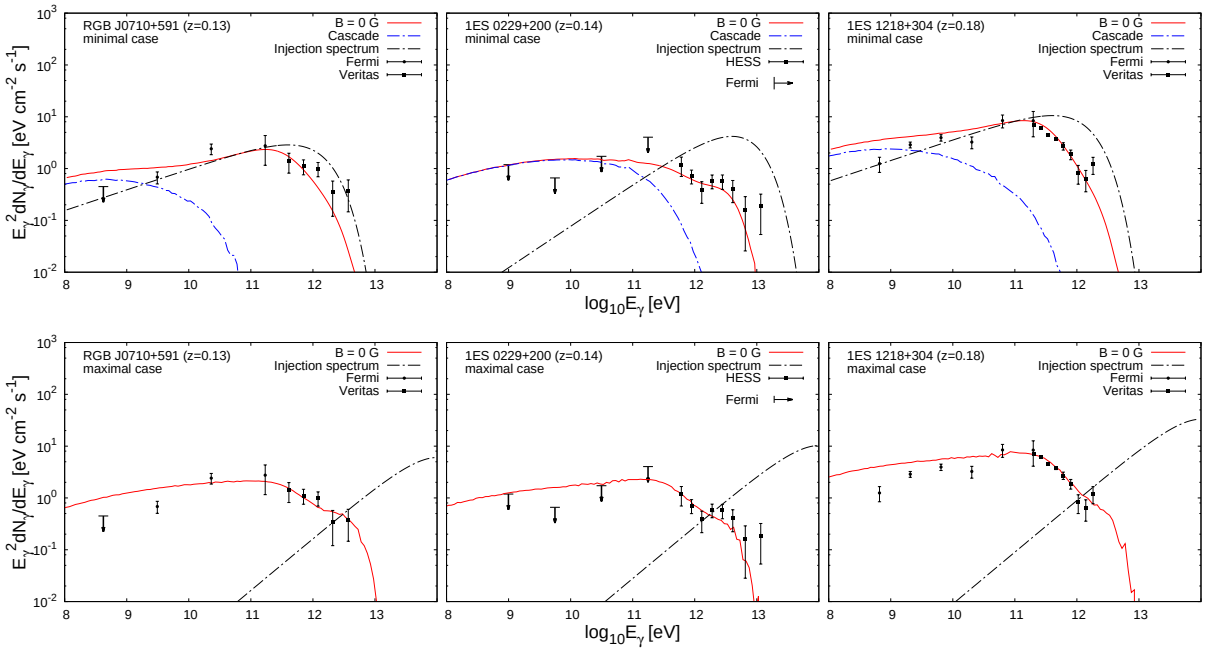

Figure 70: Top: The arriving photon energy flux, resulting from the "minimal cascade" model for RGB J0710+591 (left), 1ES 0229+200 (center) and 1ES 1218+304 (right). Fermi upper bounds are at the 99% confidence level. Notations are the same as in Fig. 69. Blue dash-dotted line shows the cascade component of the spectrum. Bottom: the results for the "maximal cascade" model.

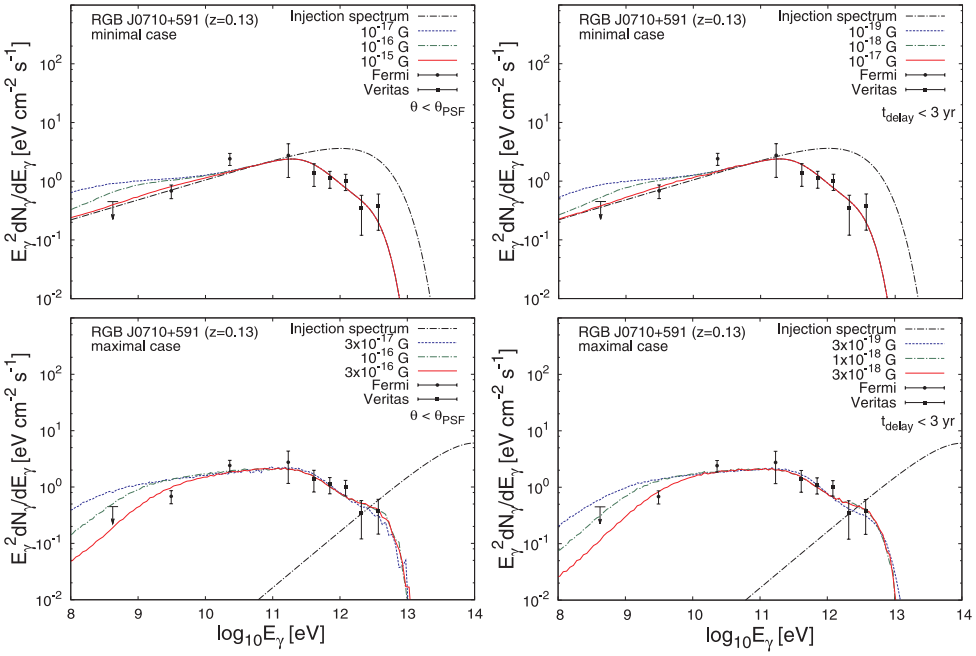

Figure 71: The effects of the presence of the IGMF on the arriving cascade from the blazar RGB J0710+591. Two top panels show the results for the case of the "minimal cascade" model of the γ-ray spectrum, for the two possibilities of suppression of the cascade flux: via extension of the cascade source and via the time delay of the cascade emission. Two bottom panels show the results for the "maximal cascade" model.

GeV band could be derived from the Fermi/LAT data. Account of the cascade contribution to the source spectra, which has to be present for the case of zero IGMF, violates the upper bound on the GeV band source flux in the case of 1ES 0229+200. In the case of RGB J0710+591 and 1ES 1218+304 account of the cascade contribution leads to the worsening of the fit to the spectrum from $\chi^2 = 8$ (7 d.o.f.) to $\chi^2 = 18$ (RGB J0710+591) and from $\chi^2 = 17$ (13 d.o.f.) to $\chi^2 = 57$ (1ES 1218+304). This implies that the model with cascade component calculated under the assumption of zero IGMF is ruled out at 98.8% and $> 99.99\%$ confidence levels for RGB J0710+591 and 1ES 1218+304, respectively.

The parameters of the minimal model for the case of 1ES 0229+200 can not be firmly defined, as the source is not detected in the Fermi/LAT energy band. Following [205], we chose $E_{\rm cut}$ and Γ in order to minimize the cascade flux in the GeV domain. The corresponding values are $E_{\rm cut} \sim 5$ TeV and $\Gamma \sim 1.2$, so, as a result, the "minimal" and "maximal" models for this source are not very different.

The problem of inconsistency of the predicted cascade flux with the Fermi/LAT measurements in the GeV band is also encountered in the "maximal" model shown in Fig. 70. Assuming that the cascade emission dominates over the direct source emission in the TeV band, one finds that the expected cascade flux level in the 0.1-10 GeV band is higher than the observed source flux if IGMF strength is $B = 0$ (solid red curves in Fig. 70).

4.3.5 Results: implications for IGMF

The fits to the combined GeV-TeV band spectra found in the minimal and maximal models for the cascade contribution under the $B = 0$ assumption are shown in Fig. 70 for RGB J0710+591, 1ES 0229+200 and 1ES 1218+304. For these sources, both minimal and maximal models, calculated under the assumption of zero IGMF, are not acceptable. The main source of discrepancy between the model predictions and the data is an over-prediction of the low energy flux, $E_\gamma \lesssim 10$ GeV, due to the presence of the cascade contribution to the total source flux.

As discussed in section 4.3.3, a decrease in the cascade contribution to the arriving flux at low energies

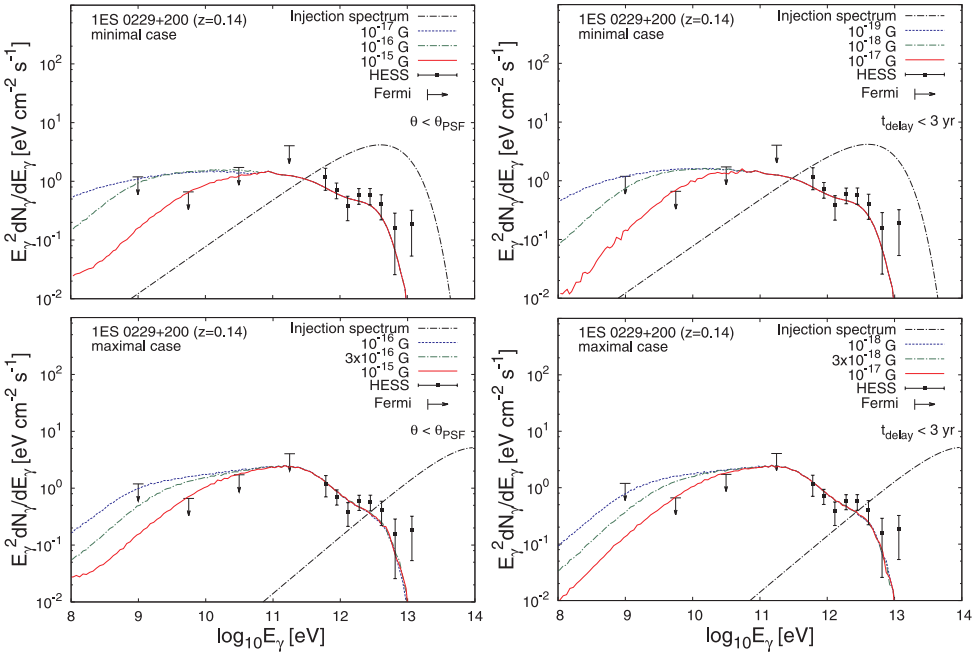

Figure 72: Same as in Fig. 71 but for 1ES 0229+200.

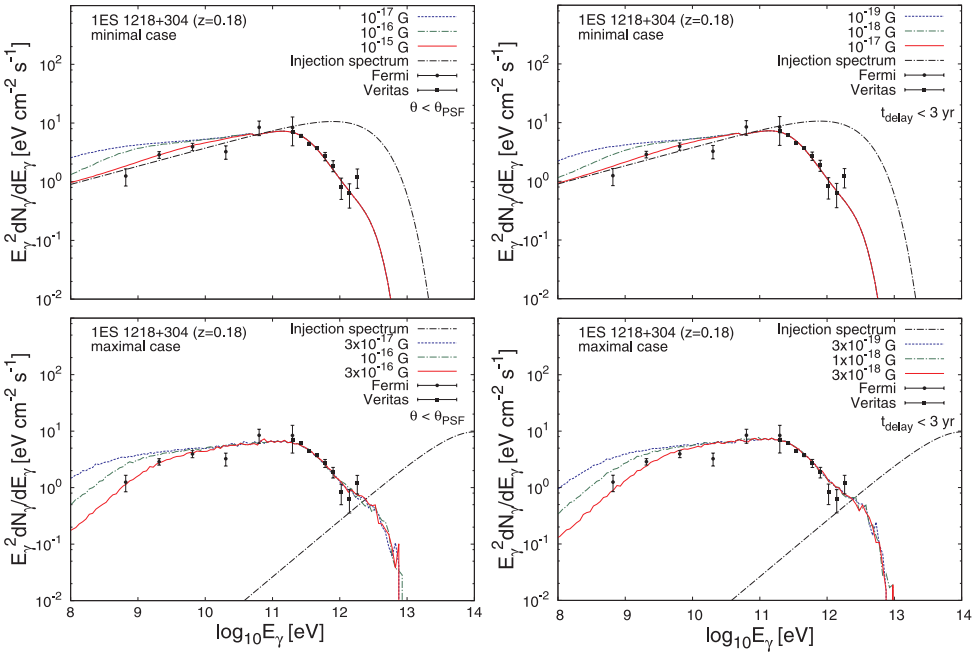

Figure 73: Same as in Fig. 71 but for 1ES 1218+304.

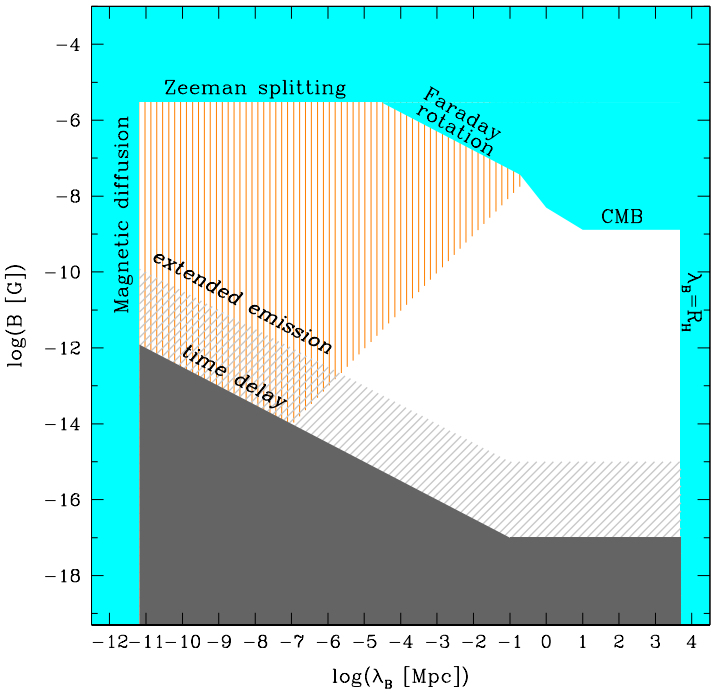

Figure 74: Bounds on magnetic field derived from the simultaneous GeV-TeV data. Blue shaded regions show the previously known bounds on B and λ_B, summarized by [201]. Orange shading shows the upper bound on B, λ_B which could be generated before the epoch of recombination, derived in [58].

can be achieved through the introduction of a non-zero magnetic field in the cascade development region. The effect of a non-zero magnetic field on the cascade component is shown in Figs. 71, 72, and 73 for the cases of suppression of the cascade flux due to the large extension of the cascade source and due to the time delay of the cascade signal.

For the case of the suppression due to the extended nature of the cascade source, the presence of magnetic field modifies the cascade spectrum at GeV energies only if the magnetic field strength is $B \gtrsim 10^{-16}$ G, for the case of RGB J0710+591, 1ES 0229+200, and 1ES 1218+304. The minimal magnetic field strengths needed to make the model source spectra consistent with the data can vary between 10^{-16} and 10^{-15} G, depending on the adopted model of the source (from "minimal" to "maximal", through all the "intermediate" possibilities) and the model of the EBL. The tightest bound is derived from the data on 1ES 0229+200, at the level of 10^{-15} G, which is consistent with the bounds found under similar assumptions about the cascade suppression mechanism by [89, 205, 257]. We stress that the bound should be considered only as an order-of-magnitude estimate, due to the significant uncertainty of the shape and overall normalization of the cascade introduced by the uncertainty of the normalization and spectral shape of the EBL.

For the case of the suppression of the cascade emission due to the time delay of the cascade signal, one assumes that the primary source is active only during a limited period of time, just about the time span of gamma-ray observations ($t_{\rm source} \sim 1$ yr). Time delay of the cascade signal by $t_{\rm delay} > t_{\rm source}$ would lead to the suppression of the cascade flux by a factor $t_{\rm delay}/t_{\rm source}$. Figs. 71, 72, and 73 show that the time delay of the cascade signal starts to influence the cascade emission at GeV energies when the magnetic field strength reaches $\sim 10^{-18}$ G. Similar to the case of suppression due to the extended emission, the precise value of B necessary to suppress the cascade emission depends on the adopted source and EBL models. The tightest lower bound is again derived from the data on 1ES 0229+200, at the level of 10^{-17} G. This bound should also be considered as an order-of-magnitude estimate because of the remaining uncertainty in the measurements of the EBL spectrum.

Note that the bound $B \geq 10^{-17}$ G, derived assuming suppression of the cascade emission due to the

time delay of the cascade signal in the case of 1ES 0229+200, is by 1.5 orders of magnitude stronger, than the bound derived from a similar analysis of the same source by [84]. We believe that the main source of discrepancy between the result obtained in the present work and that of [84] is the simplified analytical treatment of the cascade emission adopted in [84]. The simplified treatment of the cascade has led to an under-estimate of the cascade flux at high energies $E_\gamma \gtrsim 10$ GeV and an over-estimate of the strength of suppression of the cascade emission due to the time delay at low energies $E_\gamma \lesssim 10$ GeV.

Furthermore, we note that our limit of $B > 10^{-17}$ G from the time delay of the cascade signal is consistent with the results of a similar analysis by [89], who found somewhat tighter bound $B > 10^{-16}$ G, assuming a larger minimal possible time delay, $t_{\rm delay} > 100$ yr in the cascade emission from 1ES 0229+200.

A summary of the limits on magnetic fields in the intergalactic medium, which can be derived from the simultaneous GeV-TeV band observations is shown in Fig. 74. In our analysis we have considered the bound on the IGMF strength assuming a fixed magnetic field correlation length $\lambda_B = 1$ Mpc. If the IGMF correlation length is $\lambda_B \gtrsim 1$ Mpc, the lower bound on IGMF strength does not depend on λ_B because the cooling distance of e^+e^- pairs is much shorter than the typical size of regions in which IGMF is correlated. We have explicitly verified this by making a control run of Monte-Carlo simulations with $\lambda_B = 30$ Mpc and comparing the results with the case $\lambda_B = 1$ Mpc shown above. On the other hand, if $\lambda_B \lesssim 1$ Mpc, the inverse Compton cooling distance becomes larger than the size of the regions with correlated IGMF. This means that electrons and positrons pass through regions with different magnetic field orientations during their cooling. As a result, the deflection angle scales proportionally to the square root, rather than linearly with the propagation distance on the distance scales comparable to the inverse Compton cooling length. This explains the improvement of the lower bound on the IGMF strength $B \sim \lambda_B^{-1/2}$ at $\lambda_B \lesssim 1$ Mpc: stronger magnetic field is required to deviate electron trajectories by a given angle.

4.3.6 Conclusion

In the present work we have derived constraints on the strength of magnetic fields in the intergalactic medium from simultaneous observations of blazars in the GeV band (by Fermi/LAT telescope) and TeV band (by ground-based γ-ray telescopes). The constraints stem from the requirement that the GeV band signal from electromagnetic cascade initiated by the absorption of the primary TeV γ-rays in interactions with Extragalactic Background Light should be suppressed by deflections of electron-positron pairs by magnetic fields in the intergalactic medium. Non-observation of the cascade emission by Fermi/LAT telescopes imposes a lower bound on the cascade flux suppression factor which could be converted to a correlation length dependent lower bound on the strength of magnetic field.

We have found that constraints on the magnetic field strength could be derived from the γ-ray data on three blazars, 1ES 0229+200, RGB J0710+591 and 1ES 1218+304 (out of seven, for which simultaneous GeV-TeV data are available). The difference between this work and previous analysis of 1ES 0229+200 ([205]), presented in section 4.2, is the availability of the TeV re-observations of this source, performed in 2009 by VERITAS ([84]), which confirm the stability of the source emission in the TeV domain at the $\sim$ 3-yr time scale. For all three sources, we have performed detailed modelling of the spectral characteristics in the broad (0.1 GeV to 10 TeV) energy range. We have fitted the observed γ-ray spectra with a two-component spectral model which consists of both direct absorbed emission from the blazar and a cascade emission component calculated using detailed Monte-Carlo simulations of the cascade development. The observational data are inconsistent with the models in which the cascade emission is calculated assuming zero magnetic field strength in the cascade development region (extending to $\sim$ 100 Mpc distance from the source along the line of sight).

The minimal magnetic field strength required to achieve sufficient suppression of the cascade signal depends on the assumption about the mechanism of suppression of the cascade signal. If the suppression is due to the time delay of the cascade emission following a period of enhanced activity of the source in the TeV band (with duration $\sim$ 1 yr), then the minimal required field strength is $B \sim 10^{-17}$ G in the case of the field with large correlation length $\lambda_B \gtrsim 1$ Mpc. If the (unknown) correlation length is $\lambda_B \lesssim 1$ Mpc, the minimal needed magnetic field strength is larger by a factor $(\lambda_B/1\ {\rm Mpc})^{-1/2}$. If the suppression of the cascade emission is due to the fact that the size of the cascade source is much larger than the point spread function of *Fermi*/LAT telescope, rather than due to the time delay of the cascade

signal, the lower bound is $B \geq 10^{-15}$ G, with the same dependence of the correlation length λ_B.

The two possibilities for suppression of the cascade emission could be distinguished via a search of the delayed GeV γ-ray emission following strong TeV band flares of blazars or of the extended emission around TeV blazars in the GeV-TeV band. The distinguishing feature of the delayed cascade emission is the characteristic energy dependence $t_{\rm delay} \sim E_\gamma^{-2.5}$ or $\sim E_\gamma^{-2}$, as shown in Fig. 68. If the real magnetic field strength is close to $B \sim 10^{-15}$ G, the extended emission around TeV blazars should be detectable with *Fermi*, while the time delay of the cascade emission might be detectable at higher energies (~ 100 GeV) by the ground-based γ-ray telescopes.

We have investigated the dependence of the derived limit on the assumptions about the intrinsic spectrum of the sources by considering the extreme cases of "minimal" and "maximal" cascade contributions. In the "minimal" case the parameters of the intrinsic spectrum of the source are chosen in such a way that they minimize the total flux in the cascade component (at zero magnetic field strength). In the "maximal" cascade model the cascade flux dominates over the intrinsic source flux at all energies up to the TeV range. Surprisingly, the lower bound on the magnetic field strength is practically independent on the choice of the model used to fit the observed GeV – TeV band spectra. This is explained by the fact that the amount of power transferred by the cascade from the TeV to the GeV energy band is determined only by the measured TeV flux from the direction of the source and is not sensitive to the origin of the TeV γ-rays (if they are intrinsic to the source or produced in the course of development of electromagnetic cascade close to the source). Since "minimal" and "maximal" cascade models represent the two extreme possibilities for the possible amount of cascade contribution to the source flux, we conclude that the uncertainty of the modelling of the observed source spectrum introduces a negligible uncertainty in the derived lower bound on IGMF strength.

4.4 Dependence of the lower bound on the level of the Extragalactic Background Light

4.4.1 Introduction

Constraints on the Intergalactic Magnetic Field (IGMF), presented in Sections 4.2 and 4.3, are significantly dependent on the assumptions on the shape and overall level of the Extragalactic Background Light (EBL). Indeed, the amount of the EBL and its spectral energy distribution defines the strength and energy dependence of the absorption of VHE photons, which is then translated into the lower energy cascade emission.

The lower limits on the IGMF, presented before, are derived assuming a certain level of EBL density (a low EBL density derived by [107] is used in most of the publications on the IGMF in order to derive conservative bounds). However, a variety of EBL models do exist ([116, 152, 248]), which spans the full range of the present uncertainty in the EBL density. This uncertainty therefore introduces an uncertainty into the bounds on the IGMF derived from the γ-ray data. Higher(lower) EBL density leads to stronger(weaker) absorption of the primary γ-ray flux along with a stronger(weaker) cascade contribution to the observed flux in the GeV range. The suppression of such stronger(weaker) cascade contribution would require a stronger(weaker) IGMF.

As it was mentioned in section 1.3.1, γ-ray observation were also used to constrain the level of the EBL. In fact, these measurements have an underlying assumption of the IGMF behind them (IGMF should be strong enough to completely suppress the contribution of the cascade at the energies below $\lesssim 100$ GeV). Thus, the limits on the EBL derived from the γ-ray data depend on the assumptions made about the IGMF strength and vice versa. This implies that the correct procedure for the derivation of limits on the EBL from the γ-ray data should include marginalization over the possible IGMF values. Conversely, the correct procedure for the derivation of the limits on the IGMF should include marginalization over the possible EBL densities and spectra.

Practical implementation of this correct procedure for the derivation of the EBL and IGMF bounds, however, presents a challenging task since the quality of the γ-ray data is usually insufficient for the exploration of the entire EBL-IGMF parameter space. Exploration of this parameter space requires the measurement of the source spectra both in the TeV and GeV energy ranges.

Here I present the results of the work [274] I've performed with my collaborators on the observations of blazar 1ES 0229+200 in the 1-300 GeV energy range using Fermi/LAT data with three years of exposure.

The detection of the source below 100 GeV provides the information necessary for the correct analysis of the IGMF-dependent upper bound on the EBL density and of the EBL-dependent lower bound on the IGMF strength. We present such bounds in the form of a two-dimensional exclusion plot in the "EBL density" vs. "IGMF strength" parameter space.

4.4.2 Analysis

In this work we use publicly available data of the LAT instrument collected over the period from August 2008 till November 2011. We use the Pass 7 data and analyse them using the Fermi Science Tools v9r23p1 software package, with the patches as of the November 1st 2011. We limit ourselves with the class 2 events, as is recommended by the Fermi/LAT team[22]. We select only photons with energies in the 1-300 GeV range for the analysis. During the spectral fitting, we include in the analysis all the sources listed in the Fermi second year catalogue ([208]) within 5°-circle around the position of 1ES 0229+200.

The fluxes in separate energy bins are computed with the spectral indices of all sources frozen at the values quoted in the Fermi/LAT second year catalogue; the spectral index of 1ES 0229+200 is fixed at the best-fit value in the 1-300 GeV band. For energies where 1ES 0229+200 is not detected in the bin, we compute the 90%-confidence upper limit.

To compute the "spectral butterfly" we scan the value of the likelihood in the "index-normalization" parameter space and select the corresponding 68% confidence region.

We employ a Monte-Carlo description of the electromagnetic cascades in order to determine the arriving spectra observed for the case of different strength of the IGMF. The simulations we use are similar to the ones that were described in section 4.3 (see also [260] for the details). The shape of the EBL spectrum is assumed to follow that derived by [107], while the normalization of the EBL is left free. A lower bound on the normalization of the EBL from the direct source counts (as summarized by [91]) is $\simeq 15\%$ lower than the normalization of the EBL model of [107]. Recent analysis of GeV to TeV spectra of several blazars ([216]), however, suggested that the EBL level is somewhat higher, reaching $\simeq 60\%$ of the EBL model of [107] at the 2σ confidence level. Both these bounds are taken into account in our analysis.

In our calculations we consider the suppression of the cascade emission by time delay effects ([223]). The TeV γ-ray emission from the source is observed to be stable on the time scale of ≥ 3 yr, from the initial HESS observations of the source ([33]) till the recent re-observation by the Veritas telescope ([84]). We do not consider the alternative possibility for the suppression of the cascade flux due to the extended nature of the cascade emission region. The generalization of our analysis to this case, however, is straightforward, the main difference being that the suppression of the cascade emission due to the source extension would result in a somewhat higher bound on the IGMF strength ([260]).

4.4.3 Results

1ES 0229+200 is detected by LAT in the 1-300 GeV energy band with significance $\simeq 7\sigma$. The test statistics (TS) value found in the likelihood analysis is $TS = 45$. Modelling the source spectrum as a power law we find the slope of the spectrum $\Gamma = 1.36 \pm 0.25$ and normalization at 20 GeV $(1.4 \pm 0.5) \times 10^{-15}$ (MeV·cm^2·sec)$^{-1}$ (at the 68% confidence level). The spectrum of the source found from the LAT data is shown in Fig. 75 together with the HESS spectrum at higher energies. The source is not detected below $\simeq 3$ GeV, only an upper limit on the source flux can be derived in this energy band.

The source spectrum in the 3-300 GeV energy band can have two contributions: the direct γ-ray signal from the primary source and emission from the electromagnetic cascade developing in the IGM. It is not clear a-priori if the measured spectral slope, consistent with $\Gamma \simeq 1.5$, characterizes the intrinsic source spectrum, the spectrum of the cascade component, or comprises a summed spectrum of the two (similar in strength) contributions. For instance, a spectral index harder then 1.5, as found in the analysis of [249] in the TeV band, would be indicative of a GeV spectrum which results from the sum of both the intrinsic spectrum and that of the cascade. Different possibilities for the dominance of one of the two components in the spectrum are illustrated in the two panels of Fig. 75. In both models the normalization of the intrinsic spectrum is chosen to fit the HESS measurements in the TeV band. We also assume that the

[22] http://fermi.gsfc.nasa.gov/ssc/data/analysis/documentation/Cicerone/Cicerone_Data_Exploration/Data_preparation.html

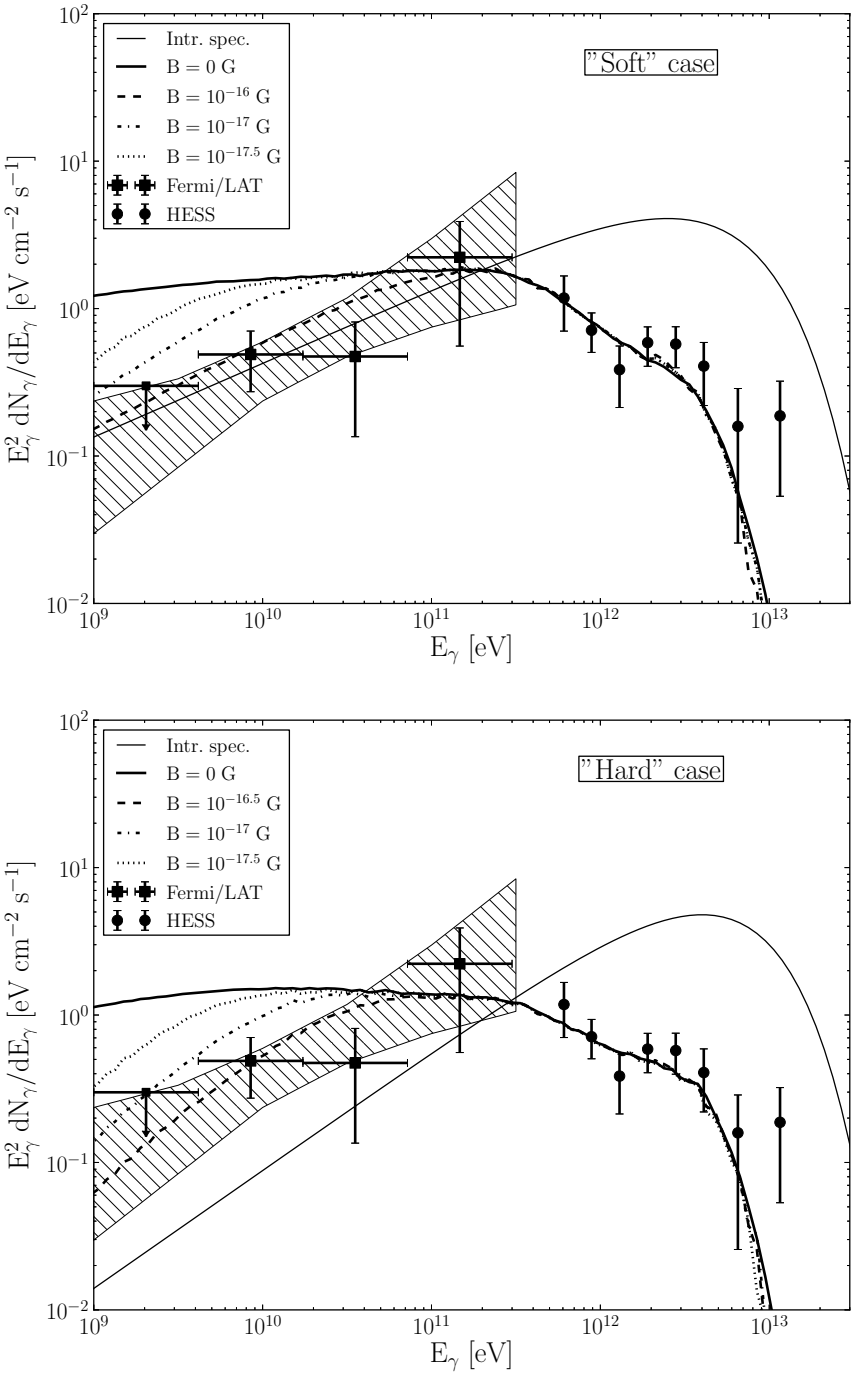

Figure 75: Top panel: the GeV-TeV SED under the assumption of a soft ($\Gamma = 1.5$) intrinsic source spectrum. Bottom panel: the GeV-TeV SED under the assumption of a hard ($\Gamma = 1.2$) intrinsic source spectrum. Lines for different values of IGMF strengths represent the sums of the intrinsic spectrum and the corresponding predicted cascade emission. In both cases the Fermi/LAT flux "butterfly" shown corresponds to the 68% confidence region.

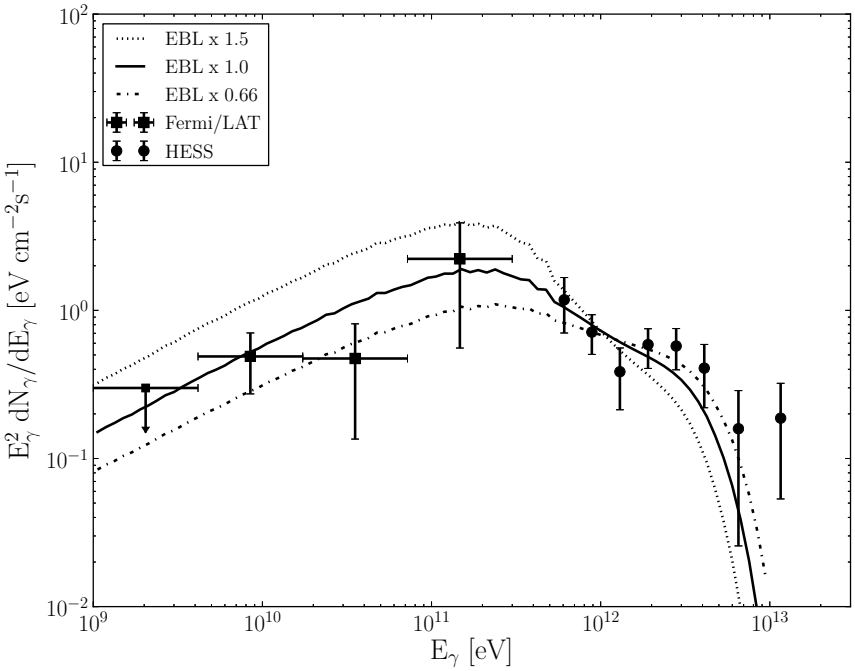

Figure 76: GeV-TeV SED under the assumption of a soft ($\Gamma = 1.5$) intrinsic spectrum for a different EBL scales. The IGMF strength of 10^{-16} G is adopted here, and the normalization of the spectra is chosen to fit the HESS data. The reference EBL scale is that of [107].

intrinsic source spectrum has a high-energy cut-off at $E_{cut} = 5$ TeV. As it was shown in section 4.3, this choice minimizes the strength of the cascade contribution in the Fermi/LAT energy band.

In the upper panel the main contribution to the 3-300 GeV source flux is given by the direct flux of the primary source, shown by the thin solid line. This is possible only if the cascade component is suppressed by the influence of a strong enough IGMF. If the IGMF is negligible, the flux of the direct and cascade emission (thick solid line) will largely dominate over the direct emission. Strong IGMF ($\geq 10^{-17}$ G) is needed to sufficiently suppress the cascade emission down to the level of the error bars of the LAT measurements in the 3-300 GeV range.

If the IGMF is weaker than $\sim 3 \times 10^{-17}$ G, the cascade emission provides the dominant contribution to the source spectrum, as is illustrated in the lower panel of Fig. 75. The only possibility to make the LAT measurement consistent with observations is to assume that the intrinsic spectrum of the primary source has a slope harder than $\Gamma = 1.5$. The hardness of the intrinsic source spectrum depends on the IGMF strength. For the particular example shown in the lower panel of Fig. 75, the assumption that the IGMF strength $B \leq 3 \times 10^{-17}$ G imposes a constraint on the intrinsic source spectrum $\Gamma \leq 1.2$. In fact, if the intrinsic source spectrum is even harder, the intrinsic source flux contribution to the 3-300 GeV band flux becomes negligible and the flux is completely dominated by the cascade emission.

The overall normalization of the cascade emission is determined by the density of the EBL. An increase of the EBL density leads to the stronger absorption of multi-TeV γ rays and, consequently, to stronger cascade emission. To the contrary, reducing the EBL normalization down to the level of the lower bound from the direct source counts opens up the possibility of a weaker IGMF, down to $\sim 6 \times 10^{-18}$ G. The effect of changing the EBL normalization is illustrated in Fig. 76. In this figure a spectral slope of $\Gamma = 1.5$ and IGMF of 10^{-16} G have been adopted, and three different (66%, 100% and 150% in terms of the EBL level reported by [107]) levels of EBL have been used.

The maximal normalization of the EBL which can still be consistent with the data depends on the strength of the IGMF. Too strong an EBL can result in a large over-prediction of the strength of the cascade emission, even after taking into account the suppression of this emission by the IGMF effects. Thus, the upper bound on the EBL derivable from the γ-ray observations of 1ES 0229+200 is IGMF-dependent.

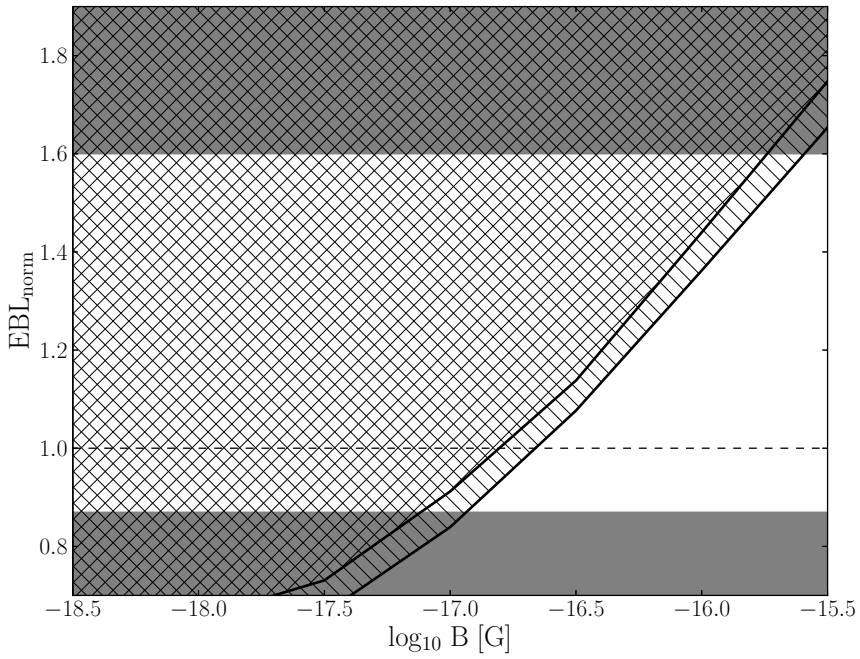

Figure 77: Allowed normalizations of the [107] EBL spectrum, as a function of the IGMF strength. Dark grey shaded regions are restrictions from [91] and [216]. The single stroke (cross) hatched region is excluded by the analysis presented here at the 95% (99.7%) confidence level.

In order to find this bound, we compute the allowed ranges of the EBL normalization for a set of IGMF strengths and intrinsic spectrum spectral indices. The IGMF strengths scanned over lay in the range 3×10^{-19} G to 10^{-14} G, while the spectral indices were varied within the range from 1.5 to 0. We then find the best-fit set of values in this "IGMF-EBL-Γ"parameter space, and chose an appropriate confidence region. The projection of this region onto the "IGMF-EBL"plane is shown in Fig. 77 and comprises the not hatched part of the plot. The hatched part thus represents the EBL-dependent bound on the IGMF (or, equivalently, the IGMF-dependent bound on the EBL).

One can see from this figure that for IGMF strengths $B \sim 10^{-17}$ G the upper bound on the EBL normalization sits at the level derived by [107]. If the IGMF is at the level of $\sim 10^{-15}$ G, the allowed EBL normalization is by a factor of 2 higher than that of the [107] and [91] models.

4.4.4 Conclusion

Following our investigations into the newly detected blazar 1ES 0229+200 with Fermi/LAT we find that, if the [107] EBL level is adopted, an IGMF strength of at least 10^{-17} G is required in order for the inevitable GeV cascade spectral component to be consistent with observations. However, we find that, more generally, the IGMF lower bound is dependent on the EBL level adopted, as demonstrated in Fig. 77.

One should keep in mind that this bound is derived for large ($\lambda_B > 1$ Mpc) correlation lengths of the IGMF, and scales approximately as $\lambda_B^{-1/2}$ for $\lambda_B \lesssim 1$ Mpc. Our result lies in agreement with previous findings of [139] and the result presented in the section 4.3. Under the assumption that the source is stable on a time scale much longer than 3 years, a larger bound on the IGMF is obtained (see sections 4.2, 4.3 and [89, 258]).

We also find that an intrinsic blazar spectral index of $\Gamma = 1.5$ is able to sit in agreement with observations of 1ES 0229+200 by Fermi/LAT ($\Gamma = 1.36 \pm 0.25$). Thus our results can find agreement with the underlying assumptions behind previous EBL constraint calculations by [39]. However, the remaining uncertainty in the origin of the blazar's spectral shape in the GeV domain leaves open the possibility for a harder intrinsic spectrum ($\Gamma < 1.5$).

We note, that in previous works of [39] and [216] the authors made the implicit assumption for the absence of the cascade contribution in the GeV-TeV domain, which is equivalent to the presence of the strong IGMF with $B \gtrsim 10^{-15}$ G. As can be seen from Fig. 77, for such a strong field our result is also compatible with the level of EBL found by [216]. For weaker fields, $B \sim 10^{-17}$ G, we are also compatible with the findings of [91]. However, for such weak fields a proper account should be given of the GeV-TeV cascade component contribution.

Future observations with ground-base Cherenkov telescopes, such as MAGIC Stereo, HESS 2 and CTA, will dramatically improve the measurements of blazar spectra below ~ 100 GeV, allowing much better constraints on the IGMF and EBL. In the particular case of 1ES 0229+200, if the intrinsic spectrum is hard, the presented IGMF lower bound may be transformed to a *measurement*, helping to better understand the nature of the intergalactic magnetic field.

5 Summary and concluding remarks

The beginning of operation of a new instrument always bring lots of new data and observational facts, and Fermi/LAT is not an exception is this case. Owing to its large field of view and higher sensitivity than its predecessors, it has shed a new light onto the AGNs in the 100 MeV–300 GeV energy domain.

Owing to its high sensitivity, Fermi/LAT has enabled the study of blazar variability on the time scales down to a fraction of an hour. Results, presented in Section 3, demonstrate that for several blazars this translates into the variability on the central black hole light crossing time scales. This opens the possibility of distinguishing between different emission sources in binary SMBH systems (see Section 3.1) and testing the hypothesis on the γ-ray emission site (Section 3.2). In the case of the blazars with binary SMBHs, such as OJ 287, which was the target of the study in the Section 3.1, a comparison of the observed variability time scales with the characteristic time scales of the system, like the SMBHs light crossing times or periods of the last stable orbits, can be used to tell which of the two black holes is responsible for the observed γ-ray emission. This argument is based on the assumption, that the γ-ray emission site is located close to the black hole and its variability is governed by the black hole related time scales. An attempt to test this assumption via the study of the variability properties of a sample of blazars, presented in Section 3.2, unfortunately didn't provide a firm conclusion on the matter. It turns out, that the sensitivity of the Fermi/LAT is after all not sufficient to detect the variability of blazars on the time scales smaller than the light crossing time of their central SMBHs, which is necessary for the arguments in Section 3.2 – the minimal variability of the majority of the observed blazars is limited by the count rate, measured by the Fermi/LAT. As a consequence, a larger effective area instrument is needed to be able to tell if the blazar γ-ray emission is indeed produced close to the central black hole or is rather formed in more distant regions of the jet. As an all-sky scanning instrument, larger than Fermi/LAT, is not planned in the foreseeable future, deeper studies of the blazar γ-ray variability will have to be carried out with the ground based Cherenkov telescopes, which have a large effective area but, unfortunately, small field of view. This instruments can be used to study the most variable blazars seen by Fermi/LAT, improving the lower part of the figure 56 and, probably, providing a conclusive argument on the location of the blazar γ-ray emission zone.

The Fermi/LAT energy range – 100 MeV–300 GeV – overlaps with that of the existing ground-based Cherenkov telescopes. This is particularly important, as blazar emission in the multi-TeV band, where most of the Cherenkov instruments operate, is affected by the absorption on the EBL. Observations at lower, GeV, energies, accessible to Fermi/LAT, allow to measure the intrinsic spectrum of a blazar, as γ-ray photons of these energies are not absorbed on the EBL. As Fermi/LAT has much smaller effective area than the Cherenkov telescopes, it detects only few photons at its highest energies, which in turn are the lowest energies accessible to the ground-based instruments such as HESS, VERITAS and MAGIC. But advantage of the Fermi/LAT is that at this energies it is almost background-free, as galactic and extragalactic backgrounds have soft spectra and die off at high energies. As a result, even a single photon, detected by Fermi/LAT at energies $\sim$ 100 GeV may indicate a significant detection of a γ-ray source. This approach is used in Section 2 to look for the new VHE sources, potentially accessible to the currently existing and future Cherenkov telescopes. Another advantage of the Fermi/LAT is its large field of view – ~ 2.4 sr, which allows it to observe the whole sky in just two spacecraft revolutions. As a consequence, LAT is able to preform an all-sky search for the VHE candidates – something that is very difficult to do with the small-field Cherenkov telescopes. A catalogue of $\gtrsim$ 100 GeV sources, presented in Section 2.2, contains 75 sources, among which 50 are new, previously unknown extragalactic VHE emitters. Among these there are also high-redshift sources with the z up to 2. Observations of such sources in the multi-TeV domain could provide an information on the redshift evolution of the EBL, which in turn would provide additional information on the star-formation history of the Universe. A dedicated search for such blazars, presented in Section 2.3, revealed 13 sources with redshifts greater than 0.5, which could be potentially detectable in the VHE domain by the current and/or future atmospheric Cherenkov telescopes. The comparison of the sensitivity of these instruments with Fermi/LAT, performed in Section 2.3, indicates, that these sources constitute almost a complete sample of blazars, that can be used to study the redshift evolution of the EBL in the coming years. As it was outlined in Section 2.3, this sample already indicates some inconsistency between observations and theoretical predictions of the γ-ray transparency of the Universe. But this inconsistency may be not connected to the discrepancy between the models and the

real level of the EBL. One of the possible explanations of it is the improperly determined redshifts of some sources in the sample. To discard this possibility, the redshifts of the suspicious sources in this sample need to be carefully verified.

γ-ray observations of distant blazars can be used not only for the studies of the blazars themselves. Measurement of the Intergalactic Magnetic Field with the help of the γ-ray observations is a relatively new topic, although the idea of this measurement is almost 20 years old ([223]). The sensitivity of the modern ground based Cherenkov telescopes, combined with that of the space-born lower energy γ-ray detectors, provided the first evidences of the presence of a relatively strong magnetic field in the voids of the Large-Scale Structure. These measurements are based on the non-detection of secondary γ-ray emission, which should be produced by the electromagnetic cascade, initiated by the absorption of the primary γ-rays on the EBL (see Section 4 for details), and rely on several assumption concerning the source emission and the background photons spectrum.

Analyses, presented in sections 4.3, 4.4, subsequently address different uncertainties, related to the lower limit on the IGMF, derived in Section 4.2. The analysis setup of the Section 4.2 considered a simplified scenario of an isotropically emitting, stable in time blazar and one of the lowest EBL densities [107], predicted by models. As the intrinsic spectrum of the source was not known, the spectral slope and the cut-off energy were scanned over to account for a different possible combinations. The values of spectral slope and cut-off energy, which provided the minimal amount of the cascade emission while still being consistent with the observed TeV spectrum, were then used to compute the spectrum of the secondary emission. Further simplification in this analysis was that the spectrum of the cascade emission was calculated using a one-dimensional numerical model (see section 4.2 for details), rather than a full Monte Carlo description of the development of the cascade. Even though providing a trustworthy conclusion on the necessity of the suppression of the cascade emission by the presence of a strong IGMF, the value of the lower bound on the strength of the IGMF, obtained in this work, could have been changed, if different assumption on the source emission spectrum and variability were made.

The question of variability of the blazars, used to constrain the IGMF, is addressed in Section 4.3. To account for the possible variability, there we use the sample of blazars, simultaneously observed in GeV and TeV domains. A Monte Carlo simulation of the cascade development is also used in this section. This allows to more accurately predict cascade spectral appearance and to take into account the effects, related to the presence of the non-negligible IGMF. Results, presented in Section 4.3, show that possible variability of the blazars, which provide the best constraints on the IGMF, relaxes the lower limit on its strength from 10^{-15} G to 10^{-17} G. This clearly demonstrates, that the source variability is an extremely important question in the derivation of the IGMF constraints, capable of drastically changing the resulting lower limit on its strength. For this reason, a dedicated campaign of observations of several most promising sources in the TeV domain, lasting for a year or so, would be very important for the verification of the results, presented in Section 4.3. Observations with instruments like HESS II, MAGIC Stereo and, in future, CTA have another important advantage: they have lower energy threshold and can go down to energies below 100 GeV. This has a direct consequence for the IGMF constraints, as part of their uncertainty comes from the energy range between several tens of GeV and $\sim 150 - 200$ GeV, which is the low-energy threshold for HESS and VERITAS, provided the TeV data, used in Sections 4.2, 4.3 and 4.4. In this energy range Fermi/LAT detects a small number of photons from the source, which then translates in large uncertainty on the source spectrum and, thus, large uncertainty on the presence of the cascade component. Lowering the energy threshold of the TeV telescopes would help to significantly reduce this uncertainty and would lead to improvement of the currently existing bounds.

Technique, described in sections 4.1, 4.2 and 4.3, in actuality allows to constrain the electron deflection angle in the presence of IGMF and, thus, provides constraint on the combination of the IGMF strength B and correlation length λ_B. This is expressed in the λ_B-dependent lower bound on the IGMF strength, shown in Figs. 66 and 74. The value of the correlation length λ_B can indicate the origin of the IGMF, as the IGMF produced in the galaxies should have a correlation length comparable to the size of a galaxy or, possibly, a galaxy cluster, whereas the IGMF of a cosmological origin doesn't have this restriction. Thus, splitting the $B - \lambda_B$ degeneracy is an important task, potentially capable to tell apart these two possible scenarios of the IGMF generation.

A way to estimate the correlation length of the IGMF was proposed in Section 4.1. This idea is based on the fact that electrons and positrons deflect differently in the magnetic fields with very small

and very large correlation lengths. Indeed, as was outlined in Section 4.1, for a λ_B much larger than the election cooling distance D_e, e^+e^--pairs cool in the homogeneous patches of the field, whereas if $\lambda_B \ll D_e$ deflection mode changes to the diffusion in angle. These two different deflection regimes lead to differently shaped angular profiles of the cascade emission, as it is from Eq. 39. Thus, accurately measuring the angular profile of the cascade emission, one can tell how the correlation length of the IGMF compares with the cooling distance of the corresponding electrons. As the cooling distance depends on the electron energy (see Eq. 20), in principle, a transition from one deflection mode to another can be observed within the energy band of one instrument. In this case, a direct measurement of the λ_B can be derived from the observations. Such analysis would require an observation of a distant blazar with the accumulation of a significant number of photons to allow the accurate reconstruction of the cascade emission angular profile. Ground-based Cherenkov telescopes have an advantage here, as, owing to their much larger effective area, they are able to collect much more photons from the chosen blazar than the Fermi/LAT. On the other hand, while having better than the Fermi/LAT angular resolution, these instruments have much smaller field of view of $\lesssim 1^\circ$. As a result, Fermi/LAT and Cherenkov instruments are suited for the detection of the extended cascade emission, corresponding to different configurations (strengths) of the IGMF.

Overall, in the days of the Fermi/LAT our knowledge of blazars has enriched itself with lots of new observational data. These data gave us new clues about the location of the blazar γ-ray emission site, allowed to broaden the population of the VHE-sources and provided with the first observational evidence of the presence of the Intergalactic Magnetic Field. An injection of new information, a positive momentum, given by the Fermi/LAT to the scientific community, will be, hopefully, maintained and result in further advances in the field of the extragalactic astrophysics.

References

[1] http://www.mpi-hd.mpg.de/hfm/CT/. [Online].

[2] http://heasarc.gsfc.nasa.gov/docs/sas2/sas2.html, 2003. [Online; updated in 2003].

[3] https://heasarc.gsfc.nasa.gov/docs/cgro/, 2005. [Online; updated in 2005].

[4] http://veritas.sao.arizona.edu/whipple-10m-topmenu-117, 2011. [Online; updated in 2011].

[5] http://magic.mppmu.mpg.de/, 2012. [Online; updated in 2012].

[6] http://veritas.sao.arizona.edu/, 2012. [Online; updated in 2012].

[7] http://www.cta-observatory.org/, 2012. [Online; updated in 2012].

[8] http://sci.esa.int/cos-b, 2013. [Online; updated in 2013].

[9] http://www.mpi-hd.mpg.de/hfm/HESS/, 2013. [Online; updated in 2013].

[10] A. A. Abdo, M. Ackermann, I. Agudo, et al. The Spectral Energy Distribution of Fermi Bright Blazars. *ApJ* , 716:30–70, June 2010.

[11] A. A. Abdo, M. Ackermann, M. Ajello, et al. The First Catalog of Active Galactic Nuclei Detected by the Fermi Large Area Telescope. *ApJ* , 715:429–457, May 2010.

[12] A. A. Abdo, M. Ackermann, M. Ajello, et al. Fermi Large Area Telescope First Source Catalog. *ApJS* , 188:405–436, June 2010.

[13] A. A. Abdo, M. Ackermann, M. Ajello, et al. Fermi Large Area Telescope Constraints on the Gamma-ray Opacity of the Universe. *ApJ* , 723:1082–1096, November 2010.

[14] A. A. Abdo, M. Ackermann, M. Ajello, et al. The on-orbit calibration of the Fermi Large Area Telescope. *Astroparticle Physics*, 32:193–219, October 2009.

[15] A. A. Abdo, M. Ackermann, M. Ajello, et al. The Fermi-LAT High-Latitude Survey: Source Count Distributions and the Origin of the Extragalactic Diffuse Background. *ApJ* , 720:435–453, September 2010.

[16] A. A. Abdo, M. Ackermann, M. Ajello, et al. Spectrum of the Isotropic Diffuse Gamma-Ray Emission Derived from First-Year Fermi Large Area Telescope Data. *Physical Review Letters*, 104(10):101101, March 2010.

[17] A. Abramowski, F. Acero, F. Aharonian, and et al. VHE γ-ray emission of PKS 2155-304: spectral and temporal variability. *A&A* , 520:A83, September 2010.

[18] V. A. Acciari, E. Aliu, T. Arlen, et al. Discovery of Very High Energy Gamma Rays from PKS 1424+240 and Multiwavelength Constraints on Its Redshift. *ApJL* , 708:L100–L106, January 2010.

[19] V. A. Acciari, E. Aliu, T. Arlen, et al. The Discovery of γ-Ray Emission from the Blazar RGB J0710+591. *ApJL* , 715:L49–L55, May 2010.

[20] V. A. Acciari, E. Aliu, T. Arlen, et al. Radio Imaging of the Very-High-Energy γ-Ray Emission Region in the Central Engine of a Radio Galaxy. *Science*, 325:444–, July 2009.

[21] V. A. Acciari, E. Aliu, T. Arlen, et al. Veritas Observations of a Very High Energy γ-Ray Flare From the Blazar 3C 66A. *ApJL* , 693:L104–L108, March 2009.

[22] V. A. Acciari, E. Aliu, M. Beilicke, et al. Discovery of Variability in the Very High Energy γ-Ray Emission of 1ES 1218+304 with VERITAS. *ApJL* , 709:L163–L167, February 2010.

[23] M. Ackermann, M. Ajello, A. Allafort, et al. The Second Catalog of Active Galactic Nuclei Detected by the Fermi Large Area Telescope. *ApJ* , 743:171, December 2011.

[24] M. Ackermann, M. Ajello, A. Allafort, et al. The Imprint of the Extragalactic Background Light in the Gamma-Ray Spectra of Blazars. *Science*, 338:1190–, November 2012.

[25] M. Actis, G. Agnetta, F. Aharonian, et al. Design concepts for the Cherenkov Telescope Array CTA: an advanced facility for ground-based high-energy gamma-ray astronomy. *Experimental Astronomy*, 32:193–316, December 2011.

[26] J. K. Adelman-McCarthy, M. A. Agüeros, S. S. Allam, et al. The Sixth Data Release of the Sloan Digital Sky Survey. *ApJS* , 175:297–313, April 2008.

[27] J. K. Adelman-McCarthy and et al. The SDSS Photometric Catalog, Release 7 (Adelman-McCarthy+, 2009). *VizieR Online Data Catalog*, 2294:0, June 2009.

[28] V. L. Afanas'Ev, S. N. Dodonov, A. V. Moiseev, et al. Spectral Studies with the Special Astrophysical Observatory 6 m and RATAN-600 Telescopes. *Astronomy Reports*, 49:374–389, May 2005.

[29] F. Aharonian. *Very High Energy Cosmic Gamma Radiation*. World Scientific Publishing Co. Pte. Ltd., 2004.

[30] F. Aharonian, A. G. Akhperjanian, G. Anton, et al. Simultaneous Observations of PKS 2155-304 with HESS, Fermi, RXTE, and Atom: Spectral Energy Distributions and Variability in a Low State. *ApJL* , 696:L150–L155, May 2009.

[31] F. Aharonian, A. G. Akhperjanian, G. Anton, et al. Discovery of Very High Energy γ-Ray Emission from Centaurus a with H.E.S.S. *ApJL* , 695:L40–L44, April 2009.

[32] F. Aharonian, A. G. Akhperjanian, K.-M. Aye, et al. A New Population of Very High Energy Gamma-Ray Sources in the Milky Way. *Science*, 307:1938–1942, March 2005.

[33] F. Aharonian, A. G. Akhperjanian, U. Barres de Almeida, et al. New constraints on the mid-IR EBL from the HESS discovery of VHE γ-rays from 1ES 0229+200. *A&A* , 475:L9–L13, November 2007.

[34] F. Aharonian, A. G. Akhperjanian, U. Barres de Almeida, et al. Discovery of VHE γ-rays from the distant BL Lacertae 1ES 0347-121. *A&A* , 473:L25–L28, October 2007.

[35] F. Aharonian, A. G. Akhperjanian, U. Barres de Almeida, et al. Upper limits from HESS active galactic nuclei observations in 2005-2007. *A&A* , 478:387–393, February 2008.

[36] F. Aharonian, A. G. Akhperjanian, U. Barres de Almeida, et al. Discovery of VHE γ-rays from the high-frequency-peaked BL Lacertae object RGB J0152+017. *A&A* , 481:L103–L107, April 2008.

[37] F. Aharonian, A. G. Akhperjanian, A. R. Bazer-Bachi, et al. An Exceptional Very High Energy Gamma-Ray Flare of PKS 2155-304. *ApJL* , 664:L71–L74, August 2007.

[38] F. Aharonian, A. G. Akhperjanian, A. R. Bazer-Bachi, et al. Discovery of very high energy γ-ray emission from the BL Lacertae object H 2356-309 with the HESS Cherenkov telescopes. *A&A* , 455:461–466, August 2006.

[39] F. Aharonian, A. G. Akhperjanian, A. R. Bazer-Bachi, et al. A low level of extragalactic background light as revealed by γ-rays from blazars. *Nature* , 440:1018–1021, April 2006.

[40] F. Aharonian, A. G. Akhperjanian, A. R. Bazer-Bachi, et al. The H.E.S.S. Survey of the Inner Galaxy in Very High Energy Gamma Rays. *ApJ* , 636:777–797, January 2006.

[41] F. Aharonian, A. G. Akhperjanian, A. R. Bazer-Bachi, et al. Detection of VHE gamma-ray emission from the distant blazar 1ES 1101-232 with HESS and broadband characterisation. *A&A* , 470:475–489, August 2007.

[42] F. Aharonian, A. G. Akhperjanian, A. R. Bazer-Bachi, et al. Fast Variability of Tera-Electron Volt γ Rays from the Radio Galaxy M87. *Science*, 314:1424–1427, December 2006.

[43] F. Aharonian, A. G. Akhperjanian, A. R. Bazer-Bachi, and et al. An Exceptional Very High Energy Gamma-Ray Flare of PKS 2155-304. *ApJL* , 664:L71–L74, August 2007.

[44] F. Aharonian, J. Buckley, T. Kifune, and G. Sinnis. High energy astrophysics with ground-based gamma ray detectors. *Reports on Progress in Physics*, 71(9):096901, September 2008.

[45] F. Aharonian, W. Essey, A. Kusenko, and A. Prosekin. TeV gamma rays from blazars beyond z=1? *ArXiv e-prints*, June 2012.

[46] F. A. Aharonian, P. S. Coppi, and H. J. Voelk. Very high energy gamma rays from active galactic nuclei: Cascading on the cosmic background radiation fields and the formation of pair halos. *ApJL* , 423:L5–L8, March 1994.

[47] F. A. Aharonian, D. Khangulyan, and L. Costamante. Formation of hard very high energy gamma-ray spectra of blazars due to internal photon-photon absorption. *MNRAS* , 387:1206–1214, July 2008.

[48] F. A. Aharonian, A. K. Konopelko, H. J. Völk, and H. Quintana. 5@5 - a 5 GeV energy threshold array of imaging atmospheric Cherenkov telescopes at 5 km altitude. *Astroparticle Physics*, 15:335–356, August 2001.

[49] F. A. Aharonian, A. N. Timokhin, and A. V. Plyasheshnikov. On the origin of highest energy gamma-rays from Mkn 501. *A&A* , 384:834–847, March 2002.

[50] J. Albert, E. Aliu, H. Anderhub, et al. Very High Energy Gamma-Ray Observations of Strong Flaring Activity in M87 in 2008 February. *ApJL* , 685:L23–L26, September 2008.

[51] J. Albert, E. Aliu, H. Anderhub, et al. Detection of Very High Energy Radiation from the BL Lacertae Object PG 1553+113 with the MAGIC Telescope. *ApJL* , 654:L119–L122, January 2007.

[52] J. Albert, E. Aliu, H. Anderhub, and et al. Variable Very High Energy γ-Ray Emission from Markarian 501. *ApJ* , 669:862–883, November 2007.

[53] M. Amenomori, S. Ayabe, D. Chen, et al. A Northern Sky Survey for Steady Tera-Electron Volt Gamma-Ray Point Sources Using the Tibet Air Shower Array. *ApJ* , 633:1005–1012, November 2005.

[54] J. R. P. Angel and H. S. Stockman. Optical and infrared polarization of active extragalactic objects. *ARA&A* , 18:321–361, 1980.

[55] R. Antonucci. Unified models for active galactic nuclei and quasars. *ARA&A* , 31:473–521, 1993.

[56] R. Atkins, W. Benbow, D. Berley, et al. TeV Gamma-Ray Survey of the Northern Hemisphere Sky Using the Milagro Observatory. *ApJ* , 608:680–685, June 2004.

[57] W. B. Atwood, A. A. Abdo, M. Ackermann, and et al. The Large Area Telescope on the Fermi Gamma-Ray Space Telescope Mission. *ApJ* , 697:1071–1102, June 2009.

[58] R. Banerjee and K. Jedamzik. Evolution of cosmic magnetic fields: From the very early Universe, to recombination, to the present. *Phys. Rev. D* , 70(12):123003, December 2004.

[59] J. M. Bardeen, W. H. Press, and S. A. Teukolsky. Rotating Black Holes: Locally Nonrotating Frames, Energy Extraction, and Scalar Synchrotron Radiation. *ApJ* , 178:347–370, December 1972.

[60] W. A. Barkhouse and P. B. Hall. Quasars in the 2MASS Second Incremental Data Release. *AJ*, 121:2843–2850, May 2001.

[61] J. D. Barrow, P. G. Ferreira, and J. Silk. Constraints on a Primordial Magnetic Field. *Physical Review Letters*, 78:3610–3613, May 1997.

[62] F. E. Bauer, J. J. Condon, T. X. Thuan, and J. J. Broderick. RBSC-NVSS Sample. I. Radio and Optical Identifications of a Complete Sample of 1556 Bright X-Ray Sources. *ApJS* , 129:547–562, August 2000.

[63] R. A. Bernstein. The Optical Extragalactic Background Light: Revisions and Further Comments. *ApJ* , 666:663–673, September 2007.

[64] S. Berta, B. Magnelli, D. Lutz, et al. Dissecting the cosmic infra-red background with Herschel/PEP. *A&A* , 518:L30, July 2010.

[65] M. Béthermin, H. Dole, A. Beelen, and H. Aussel. Spitzer deep and wide legacy mid- and far-infrared number counts and lower limits of cosmic infrared background. *A&A* , 512:A78, March 2010.

[66] R. D. Blandford and D. G. Payne. Hydromagnetic flows from accretion discs and the production of radio jets. *MNRAS* , 199:883–903, June 1982.

[67] R. D. Blandford and R. L. Znajek. Electromagnetic extraction of energy from Kerr black holes. *MNRAS* , 179:433–456, May 1977.

[68] P. Blasi, S. Burles, and A. V. Olinto. Cosmological Magnetic Field Limits in an Inhomogeneous Universe. *ApJL* , 514:L79–L82, April 1999.

[69] R. Bordoloi, S. J. Lilly, C. Knobel, et al. The Radial and Azimuthal Profiles of Mg II Absorption around $0.5 < z < 0.9$ zCOSMOS Galaxies of Different Colors, Masses, and Environments. *ApJ* , 743:10, December 2011.

[70] M. Böttcher, C. D. Dermer, and J. D. Finke. The Hard VHE γ-Ray Emission in High-Redshift TeV Blazars: Comptonization of Cosmic Microwave Background Radiation in an Extended Jet? *ApJL* , 679:L9–L12, May 2008.

[71] W. Brinkmann, J. Siebert, E. D. Feigelson, et al. Radio-loud active galaxies in the northern ROSAT All-Sky Survey. II. Multi-frequency properties of unidentified sources. *A&A* , 323:739–748, July 1997.

[72] L. Cambrésy, W. T. Reach, C. A. Beichman, and T. H. Jarrett. The Cosmic Infrared Background at 1.25 and 2.2 Microns Using DIRBE and 2MASS: A Contribution Not Due to Galaxies? *ApJ* , 555:563–571, July 2001.

[73] A. Cannon. Fermi LAT detection of increasing gamma-ray activity of blazars PKS 0537-441 and PKS 0301-243. *The Astronomer's Telegram*, 2591:1, April 2010.

[74] A. Celotti, A. C. Fabian, and M. J. Rees. Limits from rapid TeV variability of MRK 421. *MNRAS* , 293:239, January 1998.

[75] R. Chary, S. Casertano, M. E. Dickinson, et al. The Nature of Faint 24 Micron Sources Seen in Spitzer Space Telescope Observations of ELAIS-N1. *ApJS* , 154:80–86, September 2004.

[76] S. Ciprini, D. Gasparrini, L. C. Reyes, et al. Fermi LAT and GASP detections of a concurrent GeV and optical flare from the blazar OJ 287. *The Astronomer's Telegram*, 2256:1, October 2009.

[77] P. Coles. Primordial Magnetic Fields and the Largescale Structure of the Universe. *Comments on Astrophysics*, 16:45, 1992.

[78] P. Colin, D. Borla Tridon, E. Carmona, et al. Performance of the MAGIC telescopes in stereoscopic mode. *ArXiv e-prints*, July 2009.

[79] L. Costamante and G. Ghisellini. TeV candidate BL Lac objects. *A&A* , 384:56–71, March 2002.

[80] F. D'Ammando, N. Gehrels, E. Hoversten, P. Romano, and S. Vercellone. Swift detection of a bright X-ray flare from OJ 287. *The Astronomer's Telegram*, 2267:1, October 2009.

[81] C. W. Danforth, B. A. Keeney, J. T. Stocke, J. M. Shull, and Y. Yao. Hubble/COS Observations of the Lyα Forest Toward the BL Lac Object 1ES 1553+113. *ApJ* , 720:976–986, September 2010.

[82] P. D'Avezac, G. Dubus, and B. Giebels. Cascading on extragalactic background light. *A&A* , 469:857–860, July 2007.

[83] V. Demozzi, V. Mukhanov, and H. Rubinstein. Magnetic fields from inflation? *Journal of Cosmology and Astroparticle Physics*, 8:25, August 2009.

[84] C. D. Dermer, M. Cavadini, S. Razzaque, et al. Time Delay of Cascade Radiation for TeV Blazars and the Measurement of the Intergalactic Magnetic Field. *ApJL* , 733:L21, June 2011.

[85] A. Díaz-Gil, J. García-Bellido, M. García Pérez, and A. González-Arroyo. Magnetic Field Production during Preheating at the Electroweak Scale. *Physical Review Letters*, 100(24):241301, June 2008.

[86] B. L. Dingus and D. L. Bertsch. The highest energy emission detected by EGRET from blazars. In S. Ritz, N. Gehrels, and C. R. Shrader, editors, *Gamma 2001: Gamma-Ray Astrophysics*, volume 587 of *American Institute of Physics Conference Series*, pages 251–255, October 2001.

[87] S. S. Doeleman, V. L. Fish, D. E. Schenck, et al. Jet-Launching Structure Resolved Near the Supermassive Black Hole in M87. *Science*, 338:355–, October 2012.

[88] K. Dolag, M. Kachelrieß, S. Ostapchenko, and R. Tomàs. Blazar Halos as Probe for Extragalactic Magnetic Fields and Maximal Acceleration Energy. *ApJ* , 703:1078–1085, September 2009.

[89] K. Dolag, M. Kachelriess, S. Ostapchenko, and R. Tomàs. Lower Limit on the Strength and Filling Factor of Extragalactic Magnetic Fields. *ApJL* , 727:L4, January 2011.

[90] H. Dole, G. Lagache, J.-L. Puget, et al. The cosmic infrared background resolved by Spitzer. Contributions of mid-infrared galaxies to the far-infrared background. *A&A* , 451:417–429, May 2006.

[91] A. Domínguez, J. R. Primack, D. J. Rosario, et al. Extragalactic background light inferred from AEGIS galaxy-SED-type fractions. *MNRAS* , 410:2556–2578, February 2011.

[92] D. Donato. Fermi LAT observed another strong GeV flare from 4C 21.35 (PKS 1222+21). *The Astronomer's Telegram*, 2584:1, April 2010.

[93] A. Elyiv, A. Neronov, and D. V. Semikoz. Gamma-ray induced cascades and magnetic fields in the intergalactic medium. *Phys. Rev. D* , 80(2):023010, July 2009.

[94] D. Emmanoulopoulos, I. M. McHardy, and P. Uttley. On the use of structure functions to study blazar variability: caveats and problems. *MNRAS* , 404:931–946, May 2010.

[95] W. Essey and A. Kusenko. A new interpretation of the gamma-ray observations of distant active galactic nuclei. *Astroparticle Physics*, 33:81–85, March 2010.

[96] A. C. Fabian, M. J. Rees, L. Stella, and N. E. White. X-ray fluorescence from the inner disc in Cygnus X-1. *MNRAS* , 238:729–736, May 1989.

[97] R. Falomo, J. K. Kotilainen, N. Carangelo, and A. Treves. Black Hole Masses and the Fundamental Plane of BL Lacertae Objects. *ApJ* , 595:624–630, October 2003.

[98] R. Falomo, J. K. Kotilainen, and A. Treves. The Black Hole Mass of BL Lacertae Objects from the Stellar Velocity Dispersion of the Host Galaxy. *ApJL* , 569:L35–L38, April 2002.

[99] J.-H. Fan, Y.-H. Yuan, Y. Liu, and et al. The estimations of four basic parameters for gamma-ray loud blazars. *Research in Astronomy and Astrophysics*, 9:538–546, May 2009.

[100] B. L. Fanaroff and J. M. Riley. The morphology of extragalactic radio sources of high and low luminosity. *MNRAS* , 167:31P–36P, May 1974.

[101] P. Favre, T. J.-L. Courvoisier, and S. Paltani. AGN variability time scales and the discrete-event model. *A&A* , 443:451–463, November 2005.

[102] G. G. Fazio, M. L. N. Ashby, P. Barmby, et al. Number Counts at 3 μm ¡ λ ¡ 10 μm from the Spitzer Space Telescope. *ApJS* , 154:39–43, September 2004.

[103] D. P. Finkbeiner, M. Davis, and D. J. Schlegel. Detection of a Far-Infrared Excess with DIRBE at 60 and 100 Microns. *ApJ* , 544:81–97, November 2000.

[104] J. D. Finke, S. Razzaque, and C. D. Dermer. Modeling the Extragalactic Background Light from Stars and Dust. *ApJ* , 712:238–249, March 2010.

[105] L. Foschini, G. Ghisellini, F. Tavecchio, G. Bonnoli, and A. Stamerra. Search for the shortest variability at gamma rays in flat-spectrum radio quasars. *A&A* , 530:A77, June 2011.

[106] G. Fossati, L. Maraschi, A. Celotti, A. Comastri, and G. Ghisellini. A unifying view of the spectral energy distributions of blazars. *MNRAS* , 299:433–448, September 1998.

[107] A. Franceschini, G. Rodighiero, and M. Vaccari. Extragalactic optical-infrared background radiation, its time evolution and the cosmic photon-photon opacity. *A&A* , 487:837–852, September 2008.

[108] D. T. Frayer, M. T. Huynh, R. Chary, et al. Spitzer 70 Micron Source Counts in GOODS-North. *ApJL* , 647:L9–L12, August 2006.

[109] J. A. Gaidos, C. W. Akerlof, S. Biller, et al. Extremely rapid bursts of TeV photons from the active galaxy Markarian 421. *Nature* , 383:319–320, September 1996.

[110] J. P. Gardner, T. M. Brown, and H. C. Ferguson. Ultraviolet Galaxy Counts from Space Telescope Imaging Spectrograph Observations of the Hubble Deep Fields. *ApJL* , 542:L79–L82, October 2000.

[111] J. Germain, P. Barai, and H. Martel. Anisotropic Active Galactic Nucleus Outflows and Enrichment of the Intergalactic Medium. I. Metal Distribution. *ApJ* , 704:1002–1020, October 2009.

[112] G. Ghisellini and F. Tavecchio. Rapid variability in TeV blazars: the case of PKS2155-304. *MNRAS* , 386:L28–L32, May 2008.

[113] G. Ghisellini, F. Tavecchio, G. Bodo, and A. Celotti. TeV variability in blazars: how fast can it be? *MNRAS* , 393:L16–L20, February 2009.

[114] G. Ghisellini, F. Tavecchio, L. Foschini, and G. Ghirlanda. The transition between BL Lac objects and flat spectrum radio quasars. *MNRAS* , 414:2674–2689, July 2011.

[115] D. Giannios, D. A. Uzdensky, and M. C. Begelman. Fast TeV variability in blazars: jets in a jet. *MNRAS* , 395:L29–L33, May 2009.

[116] R. C. Gilmore, P. Madau, J. R. Primack, R. S. Somerville, and F. Haardt. GeV gamma-ray attenuation and the high-redshift UV background. *MNRAS* , 399:1694–1708, November 2009.

[117] R. C. Gilmore, R. S. Somerville, J. R. Primack, and A. Domínguez. Semi-analytic modelling of the extragalactic background light and consequences for extragalactic gamma-ray spectra. *MNRAS* , 422:3189–3207, June 2012.

[118] P. Giommi, M. T. Menna, and P. Padovani. The sedentary multifrequency survey - I. Statistical identification and cosmological properties of high-energy peaked BL Lacs. *MNRAS* , 310:465–475, December 1999.

[119] P. Giommi, S. Piranomonte, M. Perri, and P. Padovani. The sedentary survey of extreme high energy peaked BL Lacs. *A&A* , 434:385–396, April 2005.

[120] D. S. Gorbunov, P. G. Tinyakov, I. I. Tkachev, and S. V. Troitsky. Identification of extragalactic sources of the highest energy EGRET photons by correlation analysis. *MNRAS* , 362:L30–L34, September 2005.

[121] V. Gorjian, E. L. Wright, and R. R. Chary. Tentative Detection of the Cosmic Infrared Background at 2.2 and 3.5 Microns Using Ground-based and Space-based Observations. *ApJ* , 536:550–560, June 2000.

[122] R. J. Gould and G. Schréder. Opacity of the Universe to High-Energy Photons. *Physical Review Letters*, 16:252–254, February 1966.

[123] R. J. Gould and G. P. Schréder. Opacity of the Universe to High-Energy Photons. *Physical Review*, 155:1408–1411, March 1967.

[124] D. Grasso and H. R. Rubinstein. Magnetic fields in the early Universe. *Phys. rep.* , 348:163–266, July 2001.

[125] G. Greenstein. Primordial Helium Production in "Magnetic" Cosmologies. *Nature* , 223:938–939, August 1969.

[126] J. L. Greenstein. Red-Shift of the Unusual Radio Source: 3C 48. *Nature* , 197:1041–1042, March 1963.

[127] R. C. Hartman. Gamma-ray Variability in Blazars. In H. R. Miller, J. R. Webb, and J. C. Noble, editors, *Blazar Continuum Variability*, volume 110 of *Astronomical Society of the Pacific Conference Series*, page 333, 1996.

[128] M. G. Hauser, R. G. Arendt, T. Kelsall, et al. The COBE Diffuse Infrared Background Experiment Search for the Cosmic Infrared Background. I. Limits and Detections. *ApJ* , 508:25–43, November 1998.

[129] C. Hazard, M. B. Mackey, and A. J. Shimmins. Investigation of the Radio Source 3C 273 By The Method of Lunar Occultations. *Nature* , 197:1037–1039, March 1963.

[130] T. M. Heckman. An optical and radio survey of the nuclei of bright galaxies - Activity in normal galactic nuclei. *A&A* , 87:152–164, July 1980.

[131] J. Heidt. Intraday Variability Statistics of Radio-Selected and X-Ray Selected BL Lac Objects. In R. D. Ekers, C. Fanti, and L. Padrielli, editors, *Extragalactic Radio Sources*, volume 175 of *IAU Symposium*, page 246, 1996.

[132] J. Heidt, M. Tröller, K. Nilsson, et al. Evolution of BL Lacertae host galaxies. *A&A* , 418:813–825, May 2004.

[133] C. Heiles and T. H. Troland. The Millennium Arecibo 21 Centimeter Absorption-Line Survey. III. Techniques for Spectral Polarization and Results for Stokes V. *ApJS* , 151:271–297, April 2004.

[134] H.E.S.S. Collaboration, A. Abramowski, F. Acero, et al. Measurement of the extragalactic background light imprint on the spectra of the brightest blazars observed with H.E.S.S. *A&A* , 550:A4, February 2013.

[135] J. A. Hodge, G. R. Zeimann, R. H. Becker, and R. L. White. Faint, Evolving Radio Active Galactic Nuclei in SDSS Luminous Red Galaxies. *AJ*, 138:900–910, September 2009.

[136] W. Hofmann. Very High Energy gamma-ray emission from AP Lib detected by H.E.S.S. *The Astronomer's Telegram*, 2743:1, July 2010.

[137] R. Hopwood, S. Serjeant, M. Negrello, et al. Ultra Deep Akari Observations of Abell 2218: Resolving the 15 μm Extragalactic Background Light. *ApJL* , 716:L45–L50, June 2010.

[138] F. Hoyle, G. R. Burbidge, and W. L. W. Sargent. On the Nature of the Quasi-stellar Sources. *Nature* , 209:751–753, 1966.

[139] H. Huan, T. Weisgarber, T. Arlen, and S. P. Wakely. A New Model for Gamma-Ray Cascades in Extragalactic Magnetic Fields. *ApJL* , 735:L28, July 2011.

[140] D. Huang, A. Konopelko, and for the VERITAS collaboration. VERITAS Observations of Mkn 501 in 2009. *ArXiv e-prints*, December 2009.

[141] S. D. Hunter, D. L. Bertsch, B. L. Dingus, et al. Detection of high-energy gamma rays from quasar PKS 0528 + 134 by EGRET on the Compton Gamma Ray Observatory. *ApJ* , 409:134–138, May 1993.

[142] A. Imran and for the VERITAS Collaboration. VERITAS Discovery of Variability in the VHE Gamma-Ray Emission of 1ES 1218+304. *ArXiv e-prints*, August 2009.

[143] D. L. Jauncey, A. E. Wright, B. A. Peterson, and J. J. Condon. Redshifts of southern radio sources. III. *ApJL* , 219:L1–L5, January 1978.

[144] T. W. Jones, S. L. O'dell, and W. A. Stein. Physics of Compact Nonthermal Sources. I. Theory of Radiation Processes. *ApJ* , 188:353–368, March 1974.

[145] T. W. Jones, S. L. O'dell, and W. A. Stein. Physics of Compact Nonthermal Sources. II. Determination of Physical Parameters. *ApJ* , 192:261–278, September 1974.

[146] T. Kahniashvili, Y. Maravin, and A. Kosowsky. Faraday rotation limits on a primordial magnetic field from Wilkinson Microwave Anisotropy Probe five-year data. *Phys. Rev. D* , 80(2):023009, July 2009.

[147] S. Kaspi, P. S. Smith, H. Netzer, and et al. Reverberation Measurements for 17 Quasars and the Size-Mass-Luminosity Relations in Active Galactic Nuclei. *ApJ* , 533:631–649, April 2000.

[148] K. Katarzyński, G. Ghisellini, F. Tavecchio, J. Gracia, and L. Maraschi. Hard TeV spectra of blazars and the constraints to the infrared intergalactic background. *MNRAS* , 368:L52–L56, May 2006.

[149] R. Keenan, A. Barger, L. Cowie, and W. H. Wang. The Resolved Near-Infrared Extragalactic Background. In M. Raue, T. Kneiske, D. Horns, D. Elsaesser, and P. Hauschildt, editors, *Cosmic Radiation Fields: Sources in the early Universe (CRF 2010)*, page 7, 2010.

[150] A. D. Kerrick, C. W. Akerlof, S. D. Biller, et al. Outburst of TeV photons from Markarian 421. *ApJL* , 438:L59–L62, January 1995.

[151] E. E. Khachikian and D. W. Weedman. A spectroscopic study of luminous galactic nuclei. *Astrofizika*, 7:389–406, 1971.

[152] T. M. Kneiske, T. Bretz, K. Mannheim, and D. H. Hartmann. Implications of cosmological gamma-ray absorption. II. Modification of gamma-ray spectra. *A&A* , 413:807–815, January 2004.

[153] D. A. Kniffen, D. L. Bertsch, C. E. Fichtel, et al. Time variability in the gamma-ray emission of 3C 279. *ApJ* , 411:133–136, July 1993.

[154] A. Kosowsky and A. Loeb. Faraday Rotation of Microwave Background Polarization by a Primordial Magnetic Field. *ApJ* , 469:1, September 1996.

[155] P. P. Kronberg. Extragalactic magnetic fields. *Reports on Progress in Physics*, 57:325–382, April 1994.

[156] P. P. Kronberg and M. Simard-Normandin. New evidence on the origin of rotation measures in extragalactic radio sources. *Nature* , 263:653–656, October 1976.

[157] R. M. Kulsrud and E. G. Zweibel. On the origin of cosmic magnetic fields. *Reports on Progress in Physics*, 71(4):046901, April 2008.

[158] G. Lagache, L. M. Haffner, R. J. Reynolds, and S. L. Tufte. Evidence for dust emission in the Warm Ionised Medium sing WHAM data. *A&A* , 354:247–252, February 2000.

[159] H. Landt. Optical spectroscopy of the γ-ray bright blazars PKS 0447-439 and PMN J0630-24. *MNRAS* , 423:L84–L86, June 2012.

[160] E. Lefa, F. A. Aharonian, and F. M. Rieger. "Leading Blob" Model in a Stochastic Acceleration Scenario: The Case of the 2009 Flare of Mkn 501. *ApJL* , 743:L19, December 2011.

[161] E. Lefa, F. M. Rieger, and F. Aharonian. Formation of Very Hard Gamma-Ray Spectra of Blazars in Leptonic Models. *ApJ* , 740:64, October 2011.

[162] H. J. Lehto and M. J. Valtonen. OJ 287 Outburst Structure and a Binary Black Hole Model. *ApJ* , 460:207, March 1996.

[163] L. R. Levenson and E. L. Wright. Probing the 3.6 μm CIRB with Spitzer in Three DIRBE Dark Spots. *ApJ* , 683:585–596, August 2008.

[164] H. T. Liu and J. M. Bai. Absorption of 10-200 GeV Gamma Rays by Radiation from Broad-Line Regions in Blazars. *ApJ* , 653:1089–1097, December 2006.

[165] P. Madau, A. Ferrara, and M. J. Rees. Early Metal Enrichment of the Intergalactic Medium by Pregalactic Outflows. *ApJ* , 555:92–105, July 2001.

[166] P. Madau and L. Pozzetti. Deep galaxy counts, extragalactic background light and the stellar baryon budget. *MNRAS* , 312:L9–L15, February 2000.

[167] MAGIC Collaboration, J. Albert, E. Aliu, et al. Very-High-Energy gamma rays from a Distant Quasar: How Transparent Is the Universe? *Science*, 320:1752–, June 2008.

[168] M. Mariotti. Discovery of Very High Energy gamma-ray emission from 1FGL J2001.1+4351 by MAGIC. *The Astronomer's Telegram*, 2753:1, July 2010.

[169] M. Mariotti. MAGIC detects a VHE flare from 4C +21.35 (PKS 1222+21). *The Astronomer's Telegram*, 2684:1, June 2010.

[170] M. Mariotti. MAGIC detects VHE gamma-ray emission from IC 310. *The Astronomer's Telegram*, 2510:1, March 2010.

[171] M. Mariotti and MAGIC Collaboration. Discovery of Very High Energy Gamma-Ray Emission from NGC1275 by MAGIC. *The Astronomer's Telegram*, 2916:1, October 2010.

[172] J. Masbou. *Étude de la sensibilité de H.E.S.S. 2 en dessous de 300 GeV et recherche indirecte de matière noire dans les données de H.E.S.S.* PhD thesis, 2010.

[173] E. Massaro, P. Giommi, S. Sclavi, et al. A Multifrequency Blazar catalog (Roma-BZCAT). In S. Ritz, P. Michelson, and C. A. Meegan, editors, *The First GLAST Symposium*, volume 921 of *American Institute of Physics Conference Series*, pages 349–350, July 2007.

[174] J. J. Matese and R. F. O'Connell. Neutron Beta Decay in a Uniform Constant Magnetic Field. *Physical Review*, 180:1289–1292, April 1969.

[175] J. J. Matese and R. F. O'Connell. Production of Helium in the Big-Bang Expansion of a Magnetic Universe. *ApJ* , 160:451, May 1970.

[176] T. Matsumoto, S. Matsuura, H. Murakami, et al. Infrared Telescope in Space Observations of the Near-Infrared Extragalactic Background Light. *ApJ* , 626:31–43, June 2005.

[177] S. Matsuura, M. Shirahata, M. Kawada, et al. Detection of the Cosmic Far-infrared Background in AKARI Deep Field South. *ApJ* , 737:2, August 2011.

[178] T. A. Matthews and A. R. Sandage. Optical Identification of 3c 48, 3c 196, and 3c 286 with Stellar Objects. *ApJ* , 138:30, July 1963.

[179] J. R. Mattox, D. L. Bertsch, J. Chiang, et al. The Likelihood Analysis of EGRET Data. *ApJ* , 461:396, April 1996.

[180] J. R. Mattox, D. L. Bertsch, J. Chiang, et al. The EGRET detection of quasar 1633 + 382. *ApJ* , 410:609–614, June 1993.

[181] J. R. Mattox, S. J. Wagner, M. Malkan, et al. An Intense Gamma-Ray Flare of PKS 1622-297. *ApJ* , 476:692, February 1997.

[182] D. Mazin and M. Raue. New limits on the density of the extragalactic background light in the optical to the far infrared from the spectra of all known TeV blazars. *A&A* , 471:439–452, August 2007.

[183] R. J. McLure and J. S. Dunlop. On the black hole-bulge mass relation in active and inactive galaxies. *MNRAS* , 331:795–804, April 2002.

[184] A. A. Meiksin. The physics of the intergalactic medium. *Reviews of Modern Physics*, 81:1405–1469, October 2009.

[185] L. Metcalfe, J.-P. Kneib, B. McBreen, et al. An ISOCAM survey through gravitationally lensing galaxy clusters. I. Source lists and source counts for A370, A2218 and A2390. *A&A* , 407:791–822, September 2003.

[186] A. Mirizzi, G. G. Raffelt, and P. D. Serpico. Signatures of axionlike particles in the spectra of TeV gamma-ray sources. *Phys. Rev. D* , 76(2):023001, July 2007.

[187] K. Murase, C. D. Dermer, H. Takami, and G. Migliori. Blazars as Ultra-high-energy Cosmic-ray Sources: Implications for TeV Gamma-Ray Observations. *ApJ* , 749:63, April 2012.

[188] K. Murase, K. Takahashi, S. Inoue, K. Ichiki, and S. Nagataki. Probing Intergalactic Magnetic Fields in the GLAST Era through Pair Echo Emission from TeV Blazars. *ApJL* , 686:L67–L70, October 2008.

[189] J.D. Myers. `http://fermi.gsfc.nasa.gov/ssc/data/analysis/scitools/`, 2012. [Online; updated 14-August-2012].

[190] R. Narayan and T. Piran. Variability in blazars: clues from PKS 2155-304. *MNRAS* , 420:604–612, February 2012.

[191] A. Neronov and F. A. Aharonian. Production of TeV Gamma Radiation in the Vicinity of the Supermassive Black Hole in the Giant Radio Galaxy M87. *ApJ* , 671:85–96, December 2007.

[192] A. Neronov, D. Semikoz, M. Kachelriess, S. Ostapchenko, and A. Elyiv. Degree-scale GeV "Jets" from Active and Dead TeV Blazars. *ApJL* , 719:L130–L133, August 2010.

[193] A. Neronov, D. Semikoz, and S. Sibiryakov. Constraints on masses and spins of black holes in blazars from fast TeV variability. In F. A. Aharonian, W. Hofmann, and F. Rieger, editors, *American Institute of Physics Conference Series*, volume 1085 of *American Institute of Physics Conference Series*, pages 545–548, December 2008.

[194] A. Neronov, D. Semikoz, and S. Sibiryakov. Measuring parameters of active galactic nuclei central engines with very high energy γ-ray flares. *MNRAS* , 391:949–958, December 2008.

[195] A. Neronov, D. Semikoz, and A. M. Taylor. Very hard gamma-ray emission from a flare of Mrk 501. *A&A* , 541:A31, May 2012.

[196] A. Neronov, D. Semikoz, and I. Vovk. Discovery of VHE gamma-ray emission from 4C +21.35 with Fermi. *The Astronomer's Telegram*, 2617:1, May 2010.

[197] A. Neronov, D. Semikoz, and I. Vovk. Discovery of VHE gamma-ray emission from PKS 0301-243 with Fermi. *The Astronomer's Telegram*, 2610:1, May 2010.

[198] A. Neronov, D. Semikoz, and I. Vovk. Very high-energy γ-ray emission from IC 310. *A&A* , 519:L6, September 2010.

[199] A. Neronov, D. Semikoz, and I. Vovk. High Galactic latitude Fermi sources of γ-rays with energies above 100 GeV. *A&A* , 529:A59, May 2011.

[200] A. Neronov and D. V. Semikoz. A method of measurement of extragalactic magnetic fields by TeV gamma ray telescopes. *JETP Lett*, 85:473, 2007.

[201] A. Neronov and D. V. Semikoz. Sensitivity of γ-ray telescopes for detection of magnetic fields in the intergalactic medium. *Phys. Rev. D* , 80(12):123012, December 2009.

[202] A. Neronov and D. V. Semikoz. Extragalactic Very High Energy Gamma-Ray Background. *ApJ* , 757:61, September 2012.

[203] A. Neronov, D. V. Semikoz, A. M. Taylor, and I. Vovk. Very-high-energy gamma-ray emission from high-redshift blazars. *ArXiv e-prints*, July 2012.

[204] A. Neronov, A. M. Taylor, C. Tchernin, and I. Vovk. Measuring the correlation length of intergalactic magnetic fields from observations of gamma-ray induced cascades. *A&A* , 554:A31, June 2013.

[205] A. Neronov and I. Vovk. Evidence for Strong Extragalactic Magnetic Fields from Fermi Observations of TeV Blazars. *Science*, 328:73–, April 2010.

[206] A. Neronov and I. Vovk. Fast variability of γ-ray emission from supermassive black hole binary OJ 287. *MNRAS* , 412:1389–1393, April 2011.

[207] P. Nilson. *Uppsala general catalogue of galaxies*. 1973.

[208] P. L. Nolan, A. A. Abdo, M. Ackermann, et al. Fermi Large Area Telescope Second Source Catalog. *ApJS* , 199:31, April 2012.

[209] R. A. Ong. Discovery of VHE Gamma-Ray Emission from the Fermi-LAT Source 1ES 0502+675. *The Astronomer's Telegram*, 2301:1, November 2009.

[210] R. A. Ong. Discovery of VHE Gamma-Ray Emission from the Fermi-LAT Source PKS 1424+240. *The Astronomer's Telegram*, 2084:1, June 2009.

[211] R. A. Ong. VERITAS discovery of a new VHE Gamma-ray Source, VER J0521+211. *The Astronomer's Telegram*, 2260:1, October 2009.

[212] R. A. Ong. VERITAS discovery of a new VHE Gamma-ray Source, VER J0521+211. *The Astronomer's Telegram*, 2260:1, October 2009.

[213] R. A. Ong and P. Fortin. Discovery of High-Energy Gamma-Ray Emission from the BL Lac Object RBS 0413. *The Astronomer's Telegram*, 2272:1, October 2009.

[214] R. A. Ong, VERITAS Collaboration, D. Paneque, and Fermi Large Area Telescope. VERITAS Discovery of Very High-Energy Gamma-Ray Emission from 1FGL J0648.8+1516. *The Astronomer's Telegram*, 2486:1, March 2010.

[215] M. ORR. VERITAS Observations of the BL Lac Object PG 1553+113 Between May 2010 and May 2011. In *International Cosmic Ray Conference*, volume 8 of *International Cosmic Ray Conference*, page 119, 2011.

[216] M. R. Orr, F. Krennrich, and E. Dwek. Strong New Constraints on the Extragalactic Background Light in the Near- to Mid-infrared. *ApJ* , 733:77, June 2011.

[217] P. Padovani and P. Giommi. The connection between x-ray- and radio-selected BL Lacertae objects. *ApJ* , 444:567–581, May 1995.

[218] S. Paltani and M. Türler. The mass of the black hole in 3C 273. *A&A* , 435:811–820, June 2005.

[219] C. Papovich, H. Dole, E. Egami, et al. The 24 Micron Source Counts in Deep Spitzer Space Telescope Surveys. *ApJS* , 154:70–74, September 2004.

[220] J. S. Perkins, H. M. Badran, G. Blaylock, et al. TeV Gamma-Ray Observations of the Perseus and Abell 2029 Galaxy Clusters. *ApJ* , 644:148–154, June 2006.

[221] J. S. Perkins and VERITAS Collaboration. Probing the Extragalactic Background Light with Very High Energy Blazars. In *AAS/High Energy Astrophysics Division #11*, volume 42 of *Bulletin of the American Astronomical Society*, page 708, February 2010.

[222] S. Pinsonneault, H. Martel, and M. M. Pieri. Anisotropic Galactic Outflows and Enrichment of the Intergalactic Medium. II. Numerical Simulations. *ApJ* , 725:2087–2100, December 2010.

[223] R. Plaga. Detecting intergalactic magnetic fields using time delays in pulses of γ-rays. *Nature* , 374:430–432, March 1995.

[224] R. M. Plotkin, S. F. Anderson, P. B. Hall, et al. a Large Sample of BL Lac Objects from the SDSS and First. *AJ*, 135:2453–2469, June 2008.

[225] C. Porciani and P. Madau. The Origin of Intergalactic Metals around Lyman Break Galaxies. *ApJL* , 625:L43–L46, May 2005.

[226] R. E. Pudritz, M. J. Hardcastle, and D. C. Gabuzda. Magnetic Fields in Astrophysical Jets: From Launch to Termination. *Space Science Reviews*, 169:27–72, September 2012.

[227] M. Punch, C. W. Akerlof, M. F. Cawley, et al. Detection of TeV photons from the active galaxy Markarian 421. *Nature* , 358:477, August 1992.

[228] J. M. Quashnock, A. Loeb, and D. N. Spergel. Magnetic field generation during the cosmological QCD phase transition. *ApJL* , 344:L49–L51, September 1989.

[229] J. Quinn, C. W. Akerlof, S. Biller, et al. Detection of Gamma Rays with E ¿ 300 GeV from Markarian 501. *ApJL* , 456:L83, January 1996.

[230] R. Rando, E. Charles, S. Digel, and L. Baldini. `http://www.slac.stanford.edu/exp/glast/groups/canda/lat_Performance.htm`, 2011. [Online; updated 27-October-2011].

[231] B. Ratra. Cosmological 'seed' magnetic field from inflation. *ApJL* , 391:L1–L4, May 1992.

[232] T. A. Rector, J. T. Stocke, and E. S. Perlman. A Search for Low-Luminosity BL Lacertae Objects. *ApJ* , 516:145–162, May 1999.

[233] R. A. Remillard and J. E. McClintock. X-Ray Properties of Black-Hole Binaries. *ARA&A* , 44:49–92, September 2006.

[234] R. B. Rengelink, Y. Tang, A. G. de Bruyn, et al. The Westerbork Northern Sky Survey (WENSS), I. A 570 square degree Mini-Survey around the North Ecliptic Pole. *A&AS* , 124:259–280, August 1997.

[235] L. C. Reyes, for the Fermi LAT collaboration, and the VERITAS collaboration. Simultaneous Observations of Flaring Gamma-ray Blazar 3C 66A with Fermi-LAT and VERITAS. *ArXiv e-prints*, July 2009.

[236] E. M. Sadler, R. D. Cannon, T. Mauch, et al. Radio galaxies in the 2SLAQ Luminous Red Galaxy Survey - I. The evolution of low-power radio galaxies to z ˜ 0.7. *MNRAS* , 381:211–227, October 2007.

[237] C. L. Sarazin. *X-ray emission from clusters of galaxies*. 1988.

[238] T. Sbarrato, L. Foschini, G. Ghisellini, and F. Tavecchio. Study of the variability of blazars gamma-ray emission. *Advances in Space Research*, 48:998–1003, September 2011.

[239] D. J. Schlegel, D. P. Finkbeiner, and M. Davis. Maps of Dust Infrared Emission for Use in Estimation of Reddening and Cosmic Microwave Background Radiation Foregrounds. *ApJ* , 500:525, June 1998.

[240] M. Schmidt. 3C 273 : A Star-Like Object with Large Red-Shift. *Nature* , 197:1040, March 1963.

[241] H. Seta, N. Isobe, M. S. Tashiro, et al. Suzaku and Multi-Wavelength Observations of OJ 287 during the Periodic Optical Outburst in 2007. *PASJ* , 61:1011–, October 2009.

[242] C. K. Seyfert. Nuclear Emission in Spiral Nebulae. *ApJ* , 97:28, January 1943.

[243] G. Sigl, A. V. Olinto, and K. Jedamzik. Primordial magnetic fields from cosmological first order phase transitions. *Phys. Rev. D* , 55:4582–4590, April 1997.

[244] D. Sijbring and A. G. de Bruyn. Multifrequency radio continuum observations of head-tail galaxies in the Perseus cluster. *A&A* , 331:901–915, March 1998.

[245] A. Sillanpaa, S. Haarala, M. J. Valtonen, B. Sundelius, and G. G. Byrd. OJ 287 - Binary pair of supermassive black holes. *ApJ* , 325:628–634, February 1988.

[246] J. H. Simonetti, J. M. Cordes, and D. S. Heeschen. Flicker of extragalactic radio sources at two frequencies. *ApJ* , 296:46–59, September 1985.

[247] V. Smolčić, G. Zamorani, E. Schinnerer, et al. Cosmic Evolution of Radio Selected Active Galactic Nuclei in the Cosmos Field. *ApJ* , 696:24–39, May 2009.

[248] F. W. Stecker, M. A. Malkan, and S. T. Scully. Intergalactic Photon Spectra from the Far-IR to the UV Lyman Limit for $0 < z < 6$ and the Optical Depth of the Universe to High-Energy Gamma Rays. *ApJ* , 648:774–783, September 2006.

[249] F. W. Stecker and S. T. Scully. The spectrum of 1ES0229 + 200 and the cosmic infrared background. *A&A* , 478:L1–L3, January 2008.

[250] C. C. Steidel. The Nature and Evolution of Absorption-Selected Galaxies. In G. Meylan, editor, *QSO Absorption Lines*, page 139, 1995.

[251] W. A. Stein, S. L. Odell, and P. A. Strittmatter. The BL Lacertae objects. *ARA&A* , 14:173–195, 1976.

[252] M. Stickel, J. W. Fried, and H. Kuehr. Optical spectroscopy of 1 Jy BL Lacertae objects and flat spectrum radio sources. *A&AS* , 80:103–114, October 1989.

[253] M. Stickel, P. Padovani, C. M. Urry, J. W. Fried, and H. Kuehr. The complete sample of 1 Jansky BL Lacertae objects. I - Summary properties. *ApJ* , 374:431–439, June 1991.

[254] J. T. Stocke and T. A. Rector. An Excess of Mg II Absorbers in BL Lacertae Objects. *ApJL* , 489:L17, November 1997.

[255] P. A. Strittmatter, K. Serkowski, R. Carswell, et al. Compact Extragalactic Nonthermal Sources. *ApJL* , 175:L7, July 1972.

[256] M. Tavani and J. Arons. Theory of High-Energy Emission from the Pulsar/Be Star System PSR 1259-63. I. Radiation Mechanisms and Interaction Geometry. *ApJ* , 477:439, March 1997.

[257] F. Tavecchio, G. Ghisellini, G. Bonnoli, and L. Foschini. Extreme TeV blazars and the intergalactic magnetic field. *MNRAS* , 414:3566–3576, July 2011.

[258] F. Tavecchio, G. Ghisellini, L. Foschini, et al. The intergalactic magnetic field constrained by Fermi/Large Area Telescope observations of the TeV blazar 1ES0229+200. *MNRAS* , 406:L70–L74, July 2010.

[259] A. M. Taylor and F. A. Aharonian. Spectral shape and photon fraction as signatures of the Greisen-Zatsepin-Kuzmin cutoff. *Phys. Rev. D* , 79(8):083010, April 2009.

[260] A. M. Taylor, I. Vovk, and A. Neronov. Extragalactic magnetic fields constraints from simultaneous GeV-TeV observations of blazars. *A&A* , 529:A144, May 2011.

[261] The MAGIC Collaboration, J. Aleksić, L. A. Antonelli, et al. Rapid and multi-band variability of the TeV-bright active nucleus of the galaxy IC 310. *ArXiv e-prints*, May 2013.

[262] D. J. Thompson, D. L. Bertsch, B. L. Dingus, et al. The Second EGRET Catalog of High-Energy Gamma-Ray Sources. *ApJS* , 101:259, December 1995.

[263] S. Tremaine, K. Gebhardt, R. Bender, and et al. The Slope of the Black Hole Mass versus Velocity Dispersion Correlation. *ApJ* , 574:740–753, August 2002.

[264] M. S. Turner and L. M. Widrow. Inflation-produced, large-scale magnetic fields. *Phys. Rev. D* , 37:2743–2754, May 1988.

[265] M.-H. Ulrich, L. Maraschi, and C. M. Urry. Variability of Active Galactic Nuclei. *ARA&A* , 35:445–502, 1997.

[266] C. M. Urry. An Overview of Blazar Variability. In H. R. Miller, J. R. Webb, and J. C. Noble, editors, *Blazar Continuum Variability*, volume 110 of *Astronomical Society of the Pacific Conference Series*, page 391, 1996.

[267] C. M. Urry and P. Padovani. Unified Schemes for Radio-Loud Active Galactic Nuclei. *PASP* , 107:803, September 1995.

[268] T. Vachaspati. Magnetic fields from cosmological phase transitions. *Physics Letters B*, 265:258–261, August 1991.

[269] M. J. Valtonen, H. J. Lehto, K. Nilsson, et al. A massive binary black-hole system in OJ287 and a test of general relativity. *Nature* , 452:851–853, April 2008.

[270] M. J. Valtonen, H. J. Lehto, A. Sillanpää, et al. Predicting the Next Outbursts of OJ 287 in 2006-2010. *ApJ* , 646:36–48, July 2006.

[271] M. J. Valtonen, K. Nilsson, C. Villforth, et al. Tidally Induced Outbursts in OJ 287 during 2005-2008. *ApJ* , 698:781–785, June 2009.

[272] M.-P. Véron-Cetty and P. Véron. A catalogue of quasars and active nuclei: 13th edition. *A&A* , 518:A10, July 2010.

[273] I. Vovk and A. Neronov. Variability of Gamma-Ray Emission from Blazars on Black Hole Timescales. *ApJ* , 767:103, April 2013.

[274] I. Vovk, A. M. Taylor, D. Semikoz, and A. Neronov. Fermi/LAT Observations of 1ES 0229+200: Implications for Extragalactic Magnetic Fields and Background Light. *ApJL* , 747:L14, March 2012.

[275] R. M. Wagner. Synoptic studies of 17 blazars detected in very high-energy γ-rays. *MNRAS* , 385:119–135, March 2008.

[276] I. Wasserman. On the origins of galaxies, galactic angular momenta, and galactic magnetic fields. *ApJ* , 224:337–343, September 1978.

[277] T. C. Weekes, M. F. Cawley, D. J. Fegan, et al. Observation of TeV gamma rays from the Crab nebula using the atmospheric Cerenkov imaging technique. *ApJ* , 342:379–395, July 1989.

[278] T. C. Weekes, H. F. Helmken, and J. L'Heureux. The MT. Hopkins Sky Survey for Gamma Rays of Energy 100-1000 GEV. II. Point Sources. In *International Cosmic Ray Conference*, volume 1 of *International Cosmic Ray Conference*, page 126, 1979.

[279] L. M. Widrow. Origin of galactic and extragalactic magnetic fields. *Reviews of Modern Physics*, 74:775–823, 2002.

[280] A. M. Wolfe, R. A. Jorgenson, T. Robishaw, C. Heiles, and J. X. Prochaska. An 84-μG magnetic field in a galaxy at redshift z = 0.692. *Nature* , 455:638–640, October 2008.

[281] Z.-Z. Wu, M.-F. Gu, and D.-R. Jiang. The debeamed luminosity, sychrotron peak frequency and black hole mass of BL Lac objects. *Research in Astronomy and Astrophysics*, 9:168–178, February 2009.

[282] G. Z. Xie, H. T. Liu, G. W. Cha, and et al. Spectrophotometry and Photometry for Five Blazars and Their Central Black Hole Masses. *AJ*, 130:2506–2512, December 2005.

[283] C. K. Xu, J. Donas, S. Arnouts, et al. Number Counts of GALEX Sources in Far-Ultraviolet (1530 Å) and Near-Ultraviolet (2310 Å) Bands. *ApJL* , 619:L11–L14, January 2005.

[284] A. A. Zdziarski, A. Neronov, and M. Chernyakova. A compact pulsar wind nebula model of the γ-ray-loud binary LS I +61$\circ$303. *MNRAS* , 403:1873–1886, April 2010.

[285] A. Zech, B. Behera, Y. Becherini, et al. Discovery of VHE emission from PKS 0447-439 with H.E.S.S. and MWL studies. *ArXiv e-prints*, May 2011.